Design, Calibration and Use of Quantitative Alpha-Induced Radioluminescence Detectors

A thesis submitted in partial fulfilment of the requirements for the degree of Doctor of Philosophy and the Diploma of the Imperial College

by

Benjamin Charles Pearce

Centre for Environmental Policy

Imperial College London

The work presented in this thesis is my own and all contributions from others are referenced.

The copyright of this thesis rests with the author. Unless otherwise indicated, its contents are licensed under a Creative Commons Attribution-Non Commercial-No Derivatives 4.0 International Licence (CC BY-NC-ND).

Under this licence, you may copy and redistribute the material in any medium or format on the condition that; you credit the author, do not use it for commercial purposes and do not distribute modified versions of the work.

When reusing or sharing this work, ensure you make the licence terms clear to others by naming the licence and linking to the licence text.

Please seek permission from the copyright holder for uses of this work that are not included in this licence or permitted under UK Copyright Law.

Crown Copyright © 2019

Abstract

The detection of alpha-emitting radioactive materials using UV radioluminescence methods has been subject to increasing attention in recent years. By detecting the UV photons emitted when alpha particles interact with nitrogen and other molecules in air, this method provides the opportunity to detect alpha-emitting radionuclides at distances beyond the small path length of alpha particles in air.

To date – while detectors have been shown to detect alpha-emitting materials at large distances, in low quantities and in short duration – the capability of such detectors to produce accurate, repeatable, quantitative measurements of alpha-emitting sources has not been comprehensively explored. This lack means that comparison of the technique with others employed by industry has not been possible and little work has considered how devices' analytical performance might be assessed.

This thesis presents methods for the calibration of alpha-induced radioluminescence detectors against traceable sources of known activity to enable the quantitative estimation of sources of unknown activity.

The design of a novel, portable detector capable of such measurements over a range of distances is presented, along with findings about the ideal design of detectors for quantitative measurement. This detector was shown to perform effectively in a wide variety of operating environments, ranging from light tight boxes to operational lighting in one of Sellafield's active laboratories.

The detector was used to develop four calibration methods – manual calibration, microprocessor-controlled confinement of a source, conveyor-based scanning and imaging by varying the pan/tilt angle of the detector. Using these methods, it was shown that the detector's response scales linearly with the activity of americium-241 sources measured.

Through the analysis of performance of two methods, it was shown that calibrations should only be applied to measurements obtained using the same acquisition process. This method of performance analysis provides a framework the for comparison of both methodological and detector performance.

Acknowledgements

I would like to express my sincere thanks and appreciation to my supervisors – Professors Susan Parry and Kym Jarvis – for their enduring guidance, support and advice throughout the course of the project. I am especially grateful for your patience and understanding while I was completing this thesis. Without your experience, knowledge and support none of this work would have been possible, for which I am very thankful. I hope that this PhD goes some small way to assist your exciting endeavours at Viridian Consultants.

I have had the pleasure to work with many collaborators, technicians and other interested people during the project. To those from Viridian Consultants, Imperial College Reactor Centre, Blackett Laboratory, National Nuclear Laboratory, National Physical Laboratory, RUSI, AWE and CEP with whom I have shared this journey, thank you for your friendship, interest and enthusiasm, which has bought this project to life.

I would like to thank Her Majesty's Government through the Nuclear Decommissioning Authority for funding the project and my studentship. I would also like to thank National Nuclear Laboratory for enabling the experimental trials on the Sellafield site and for administering the project on behalf of the NDA.

To my friends – your intellect, humour and camaraderie have provided the most wonderful memories and made these years the best of my life.

Finally, to my family – to those who have passed, to those who stand on and to that most special one who has since joined – my heart is yours and this journey has been for you.

Table of Contents

Abstract 5

Acknowledgements 7

Table of Contents 9

List of Tables and Figures 13

Tables 13

Figures 15

Chapter 1 Introduction 23

1.1 Detecting radiological contamination 23

1.2 Alpha-emitting radioactive materials in nuclear decommissioning 25

1.3 Alpha-induced radioluminescence detectors 26

1.4 From detection to measurement 27

1.5 Towards an industrial application 29

Chapter 2 Literature Review 31

2.1 Mechanisms of alpha decay and nuclear contamination 31

2.2 Energy deposit in matter 38

2.3 Molecular Spectroscopy and Fluorescence 45

2.4 Current radioluminescence detection devices 59

Chapter 3 Simulated Emission and Detection Characteristics 73

3.1 Modelling photon emission processes 74

3.1.1 Modelling Energy Deposit in Space: Bethe Formula 74

3.1.2 Modelling Energy Deposit in Time: Temporal Bethe Formula 77

3.1.3 Photon Emission Events 80

3.2 Modelling detector performance 84

3.2.1 Detection Geometries 84
3.2.2 Range, Detection Region and Photon Flux 88
3.2.3 Angular Phenomena 95
3.3 Modelling decay energies 102
3.3.1 The impact of decay energy on angular effects 102
3.3.2 Parametric fitting of angular emission distributions 105
3.3.3 Comparison to experiment 112
3.4 Conclusion 114
Chapter 4 Equipment Design: Detector System 117
4.1 Detector design 118
4.1.1 Components of detector 118
4.1.2 Detector design parameters 121
4.1.3 Optical detection devices 123
4.1.4 Optical modelling for lens design 126
4.1.5 Optical filters 127
4.1.6 Theoretical combined efficiency 129
4.1.7 Mechanical casing design: additive manufacturing 131
4.2 Data acquisition equipment design and selection 133
4.2.1 Electronic controller design 133
4.2.2 Microprocessor firmware design 135
4.2.3 Choice of photomultiplier DAQ unit 136
4.2.4 After pulsing correction 137
4.3 Conclusion 140
Chapter 5 Development of Calibration and Operational Methods 143
5.1 Motivation for calibration 145
5.1.1 Established calibration methods 145
5.1.2 Establishing a calibration for UV fluorescence 146

5.1.3 Attenuation over distance 147
5.2 Method development 148
5.2.1 Manual Remote Calibration 148
5.2.2 Mechatronic UV confinement 150
5.2.3 Development of an automated actuator system 155
5.2.4 Conveyor Scanning 165
5.2.5 Imaging method 175
5.3 Conclusion 188
Chapter 6 Methods for Quantitative Analysis of Detector Performance 191
6.1 Establishing relative detector response over distance 191
6.2 Measurements of sources of known activity 196
6.3 Activity calibration over distance 204
6.4 Detection Limits 208
6.5 Calculating Detection Limits for the UV Confinement Method 212
6.6 Conclusion 221
Chapter 7 Conclusions and future work 225
7.1 Review of research problem 225
7.2 Conclusions 226
7.3 Future work 232
Bibliography 237
Appendix 1 Eckert & Ziegler Calibration Certificate 247
Reference: 139716 – SX 214 247
Appendix 2 Eckert & Ziegler Calibration Certificate 251
Reference: 027744 D-K-15203-01-00 251
Appendix 3 Permissions to Reproduce Copyrighted Material 255

List of Tables and Figures

Tables

2.1 Alpha-emitting radionuclides with large quantities recorded in the UK NDA's Waste Inventory (2013). ……..……... 37

2.2 Stopping ranges for 5.5MeV alpha-particles in a number of relevant materials. ... 41

2.3 Major transitions in the fluorescence emission spectrum of Nitrogen with corresponding Einstein coefficients and origin. ……. 54

3.1 Comparison of alpha particle ranges over different energies predicted by SRIM and the numerical method presented here (equation 3.5) at air density of 1.225kgm-3. Results demonstrate that the Bethe formula provides accurate data to uncertainty of approximately 0.3mm. ..……... 77

3.2 Variables generated upon the generation of a photon by this numerical simulation; from this data the detection-side geometries can be introduced, thus offering the possibility to quantitatively evaluate the number of photons detected in various scenarios. ……..……... 81

4.1 This table shows the parameters utilised in the detector design process, derived from the modelling and survey of past literature on alpha UV detectors. …….. 122

4.2 Optical components incorporated into final detection system. ……... 128

5.1 UV photons from manual calibration of six americium-241 sources at 68mm. …. 148

5.2 Compiled results of the measurement of two americium sources using the actuated UV confinement method. ……. 158

5.3 Data obtained for six americium sources using the actuated UV confinement method. ……... 163

5.4 Observations using the conveyor scanning method of the individual sources labelled 1-6 at 50mm measurement distance. ……. 170

5.5 Comparison of the sum of individual measurement net count rates compared to those measured by sources in combination, all at 50mm measurement distance. .. 174

6.1 Data extracted from the summing of exposed and confined segments of the measurement of a 221Bq americium source. …….. 199

6.2 Calculation of the detector's response to a (221±13)Bq americium source at two distances, as measured by the UV confinement method …… 199

6.3 Calibration data obtained from three sources using the imagining method and a five point analysis as outlined in the previous chapter. …….. 201

6.4 Calculation of the attenuation calibration parameter A. ……. 204

6.5 Calculation of the critical limit, limit of detection and the limit of quantification using the replication variance-based standard uncertainty in the background of ±10 counts. …….. 206

6.6 Calculation of the critical limit, limit of detection and the limit of quantification for measurements obtained using the imaging method based on the replication variance-based standard uncertainty in background (±10 counts). …..……... 209

6.7 Sampled minimum activities required to reach the threshold decision limit, detection limit and limit of quantification in a 10s/point image of americium sources. ……... 211

6.8 Logistic fitting parameters obtained from actuated UV confinement data evaluated for the periods indicated. …… 214

6.9 Calculation of the y-intercept of the calibration function for the UV confinement method using a point calibration performed using a 221Bq americium-241 source. ……..……... 214

6.10 Calculation of the error weighted mean for the two calculated values of the model parameter A. …… 215

6.11 Evaluation of the background variance associated with measurements using the UV confinement method of various measurement periods. ……... 218

6.12 Calculation of the decision limit, detection limit and limit of quantification for the UV confinement method for a measurement of 10s, 60s and 300s. ……. 219

6.13 Minimum activity at the limits of determination, detection and quantification for the UV confinement technique measured for paired measurements of 300s duration for each active and background segment. …… 220

Figures

2.1 Average binding energy per nucleon of naturally occurring isotopes. ……... 32

2.2 Number of protons plotted against the number of neutrons for radioactive nuclei. 34

2.3 The Geiger-Nuttall relation which describes the relationship between half-life and alpha particle energy. …..……. 36

2.4 The function of an alpha particle's stopping power over distance in air as described by the Bethe formula. ……. 39

2.5 Stopping power versus particle energy for alpha particles in air. ……... 40

2.6 Top: Simulation of UV radioluminescence emissions in air for 6.5 10^5 decays of americium-241, cobalt-60 and phosphorus-32. Bottom: 2D spatial distribution of photon emissions for each radionuclide. ……...……. 44

2.7 The near-UV (300-400nm) fluorescence emission spectrum of nitrogen in dry air at 101.3 kPa induced by electrons. ……. 47

2.8 Left: Potential energy curves for various low electronic states of the O_2 molecule. Right: Schematic of the process in which, due to an electronic excitation, the molecule results immediately in a higher vibrational energy state. 49

2.9 A schematic representation of the processes of diatomic molecular fluorescence. 51

2.10 The most intense emissions in the near-UV region for dry air correspond to the first negative (1N) and second positive (2P) band systems of nitrogen molecules. 53

2.11 Spectrally resolved fluorescence yield of dry air induced by electrons giving an indicative total yield across the region of 29 photons/MeV. …….. 56

2.12 (a) Real image of a telemanipulator gripper in a nuclear facility produced using a normal camera. (b) As for (a) with the 'alpha image', obtained using a UV-sensitive CCD camera exposed for 5 minutes, overlaid to expose relative degrees of contamination on the grip. ……. 60

2.13 A schematic of the HUAVA device produced by STUK. …….. 65

2.14 Coincidence measurements between two photomultipliers connected by a TCSPC unit to analyse the delay between two pulses received by either detector. 66

3.1 Rate of energy loss per unit time, *dE/dt*, of a 5.5MeV alpha particle traversing air of density 1.225kgm^{-3} over time. …….…….. 79

3.2 Visual representation of the photons emitted from an alpha particle. Factoring all considerations discussed above this gives the spatio-temporal profile of alpha decay. …….. 82

3.3 Histogram plots of the temporal profile of radioluminescence caused by 5.5 MeV alpha particles, averaged over 300,000 decays. …… 84

3.4 Simple geometric case used for modelling the detection of radioluminescence photons. ……... 86

3.5 The detection characteristics of a square detector of width 0.8cm for 50,000 5.5MeV alpha particles emitted in a pencil beam per point, averaged over 35 sets of 50,000 decays to give indicative uncertainty values to one standard deviation. Inset: relationship with range displayed on a linear scale. ……. 88

3.6 The variation of photon flux detected from a pencil beam of 5.5MeV alpha particles compared to the width of the detection region (detection diameter) at a range of 20cm. Inset: overall proportion of radioactive decays producing coincidence compared to detection diameter. ……. 89

3.7 Variation of the median time of photon emission relative to the radioactive decay of the alpha-emitting nucleus (5.5MeV, pencil beam) for a detector of diameter 0.8cm, averaged over 30 sets of 50,000 radioactive decays, over distance. …….. 91

3.8 Variation of photons detected per decay over distance for detectors of widths varying from 0.8 (bottom curve) to 22.5cm (top). …….……. 92

3.9 A more complicated geometry used for modelling the detection of photons emitted during the radioluminescence process incorporating off-axis alpha particle emissions. ……... 94

3.10 Left: The number of photons arriving at a square detector, width 2.5cm, from a source emitting at angle $\delta\Omega$ relative to the detector face over a hemisphere. Right: The normalised contribution of each of the 41 measurements to the overall number of photons detected. …….…….. 97

3.11 The median emission time of photons detected from sets of 50,000 particle emissions over a hemispherical radius. …….. 98

3.12 The profile of detection over the full circular angle range of δΩ demonstrating the periodicity of this function over the interval of 2π as expected geometrically. 99

3.13 Representation of the proportion of the angular emission curve "seen" by the detector while positioned at different angles. ……. 100

3.14 The angular emission profile of a semicircular alpha-emitting source, viewed from the angular perspectives over the full semicircle [-π/2,π/2] at ranges of 5, 6, 7, 10, 15 and 20cm, by a square detector of width 2.5cm. ……. 101

3.15 Three-dimensional analysis of the number of photons detected by a detector of equivalent solid angle to a 7.90mm square photocathode resulting from 200,000 alpha particle emissions of each energy, emission angle and range. …….. 103

3.16 Number of photons intersecting a 7.9mm square detector for 10,000 emissions of various alpha particle energies (from 2.5MeV to 5.5MeV) at 5cm source-to-detector distance. …… 104

3.17 A further geometry used to model the rotation of a source relative to the detector for a source emitting into a defined angular range. ...……. 107

3.18 Graphical representation of the regression analysis of the fit function for a rotated source of differing emission energies. …… 109

3.19 Representation of the number of photons detected by an 8mm circular detector from angular perspectives from 0 to 360 degrees around an alpha-emitting source. ……...….. 111

3.20 Photon intensity (I) detected during the rotation of four 241Am sealed radioactive sources attached to a motor displaced 5cm from a photomultiplier tube. ……...…… 113

3.21 Schematic representation of the rotating source experiment. …….. 114

4.1 Left: Interior of the first edition of the detector prototype. Right: Conceptual representation of a non-imaging alpha-UV optical detector. …….. 119

4.2 Quantum efficiency of the photomultiplier tube used in the detector (dashed) versus peak emission wavelengths in the nitrogen 2P and 1N band systems. ….... 124

4.3 Change in count rate versus supply voltage for photomultiplier tubes operating in analogue and photon counting modes. ……... 125

4.4 Percentage transmission versus wavelength for the components incorporated into the final detector system. …… 130

4.5 Component layout of the detector casing, illustrating the photomultiplier tube, Edmond Optic 337nm filter (F1), convex lens (CL), Hoya U340 filter (F2) and plano-convex lens (PCL). ……... 131

4.6 CAD drawing of final detector casing layouts displayed illustrating the adjoining edges of the top and bottom half and the cross section of the casing. …… 132

4.7 Schematic representation of the H10721 photosensor module. ……. 133

4.8 Circuit diagram of components used to control power and level of sensitivity of photomultiplier tube. ……... 134

4.9 An interface made in Visual Studio using the C# programming language to control elements of the detector system. ……. 136

4.10 Binned interarrival periods of two americium sources measured using the final detection system illustrated using a log-normal axis. ……. 139

4.11 A photograph of the final detector system developed for use in experiments presented in later chapters. ……. 141

5.1 Computer aided design representation of the first edition, modular UV confinement device. …… 151

5.2 Conceptual representation of the UV confinement method showing radioactive emissions (purple) producing photons (arrows) which are either (a) confined or (b) allowed to propagate into the external environment. …… 153

5.3 Adapted lower circular platform of UV confinement device incorporating grooves to fit two limit switches, activated once the upper platform is in positions (a) and (b). ……... 154

5.4 Conceptual illustration of the actuated UV confinement measurement system. … 155

5.5 Illustration of the detector output of the actuated UV confinement system. Measurements are taken over a set interval (40 minutes) with a background measurement (source confined) followed by a measurement of the same period with the source exposed. …..…….. 156

5.6 The count rates observed over background for two Americium sources produced using the actuated UV confinement system. ……... 159

5.7 Analysis of trends within the segments of 40 minute measurements of UV photons detected from two americium sources (background and exposed). ……. 160

5.8 Three measurements using the actuated UV confinement method for measuring the attenuation of observed counts due to two americium sources. ……... 162

5.9 Measurement of the UV photons detected at various distances using the actuated UV confinement technique for six americium sources. ……. 164

5.10 Conceptual representation of a conveyor-style calibration measurement in which a source is passed by motor under a fixed detector at a fixed distance. ……. 165

5.11 Analysis of detection characteristics of 6 individual sources sampled at 0.1mm intervals using the conveyor detection method. ……. 167

5.12 Extracted net count rates due to the individual sources labelled 1-6 at a measurement distance of 50mm. …… 169

5.13 Measurements performed on the set of six sources in combination using the conveyor scanning method. …… 172

5.14 The mean net UV photon count rates observed when measuring several sources in combination (black) using the conveyor scanning method, compared to the sum of those sources measured individually (red) under the same conditions. ….. 173

5.15 Equipment setup for the imaging calibration method. …… 176

5.16 Flowchart illustrating the procedure for measurement using the imaging method. 177

5.17 Illustration of the sequence of measurements performed using the imaging method for the example of θmax = 10°. …….. 179

5.18 Raw data obtained by using the imaging method over a range of 69mm to 339mm in 10 iterations. …….. 180

5.19 The image resulting from measurements performed over a 27x27 grid at 69mm measurement distance over an angular range of -13 degrees to 13 degrees. 181

5.20 UV measurement of six americium-241 sources at 69mm distance from source to detector illustrating a sampling method incorporating five points about the centre, derived from a 2D Gaussian non-linear least squares fitting algorithm. 184

5.21 Four models of data extraction performed on 47 images of six sources at various distances under 1m distance. …….. 185

5.22 Measurements obtained from 47 images over 8 measurement sessions showing repeatability of measurements. ……... 186

5.23 Comparison of net count rate measurements obtained using the four alpha-induced radioluminescence calibration methods presented in chapter 5. ……... 187

6.1 Measurements of the set of six americium-241 sources using the imaging calibration method, fitted with logistic and exponential fit functions using a non-linear least squares regression analysis. ……..... 193

6.2 Left: Generalised form of the parametrised net count rate distribution for the set of six sources. Right: The relative net count rate observed over measurement distances compared to a fixed y-intercept of 1, resulting from the fixing of parameter A. 195

6.3 UV confinement calibration measurement using a 221Bq source positioned at (51±2)mm measurement distance. …….. 197

6.4 UV confinement calibration measurement using (221±13)Bq source at (59.5±1)mm measurement distance. ……... 198

6.5 Image calibration measurements for (a) (912±27)Bq source at 71.5mm measured with 6s/point; (b) (1429±280)Bq americium source at 68mm at 5s/point and (c) (3±1)kBq americium source at 75mm at 5s/point. ……. 202

6.6 Data obtained across measurements of 4 sources using the imaging and confinement methods to obtain calibration factors ……. 203

6.7 Using the parametrised model of relative net count rate attenuation over distance it was possible, using point calibration, to calculate the attenuation of the detector's response using the imaging method over distance. …… 205

6.8 The minimum activity required for a net count rate in excess of the limit of quantification, Sq , limit of detection, Sd, and the critical limit, Sc, for an image-based measurement of an americium source. ……. 211

6.9 Attenuation curve for the confinement method obtained using two americium-241 sources. The data is fit using a logistic function. Net count rates were obtained from 2400s (40 minute) signal-background segments. …..……. 212

6.10 Actuated UV confinement measurements of two americium sources modelled using a logistic fit function. Measurements were obtained over paired 40 minute, 1 minute and 20s measurements to assess repeatability. …… 213

6.11 Comparison of the detector performance using the UV confinement method and the imaging method. ……... 217

6.12 Minimum detectable activities at the limits of determination, detection and quantification for the UV confinement method. ……. 221

Chapter 1
Introduction

1.1 Detecting radiological contamination

The challenge of detecting alpha-emitting radioactive material was first brought to public attention in 2006 in the aftermath of the poisoning of Alexander Litvinenko. Litvinenko was poisoned with polonium-210, an alpha-emitting material with short half-life. This radioactive isotope caused catastrophic internal radiation damage which ultimately led to his death. Nineteen days elapsed between the poisoning and the first diagnosis of radiation poisoning, with the full prognosis of polonium poisoning not being established until he had passed away [1]. Once polonium-210 had been identified, a decontamination programme was commenced by government agencies including the Health Protection Agency, AWE and DSTL, across London at the expense of £2,000,000. Given polonium's volatility, its containment medium and its high activity, contamination was spread broadly across a large regions of London [2][3].

The problems faced in the aftermath of the poisoning were indicative of the difficulties in detecting alpha-emitting radionuclides in other contexts. Alpha particles typically travel only short distances, reaching a depth of only 2-3cm in air and a few microns in solids and liquids. This makes the detection of alpha-emitting contaminants a considerable technical challenge in all environments, and not least outside of the laboratory.

The current method for the in-situ detection of some of the most common alpha-emitting materials relies on a secondary signature. Gamma-rays are occasionally emitted by alpha-emitting radioisotopes directly, or else by other radionuclides in their decay chains. This means that the measurement of a gamma spectrum can sometimes be used to infer the presence of a quantity of alpha-emitting material. Given that gamma-rays have a considerably greater mean free path in air, this proxy measurement can be performed at a safe distance from the material. This method is currently deployed in the nuclear industry for the detection of alpha-emitting materials with detectible gamma emissions, such as americium-241.

This method has a number of limitations. The majority of alpha-emitting materials of relevance to the nuclear industry tend to emit only low energy gamma emissions, which are difficult to detect at a distance using gamma detectors [4].

Other radionuclides, including polonium-210, have branching fractions which make detection by gamma emission time consuming and prone to error. Polonium-210 in its decay into lead-206 emits an accompanying gamma-ray photon only once in every 80,000 decays [5]. This means that were an operator to seek to identify regions of contamination using a conventional gamma probe then the minimum detectable quantity of polonium would be considerably less than if measured by an equivalent alpha probe.

The risk that an unacceptably large quantity of polonium-210 could be missed led the decontamination team to use alpha-sensitive probe detectors. However, this presented the team with the arduous task of sweeping, within 1-2 centimetres, every surface which the involved parties might have come into contact over a period of weeks to identify possible regions of contamination [6].

The Litvinenko case led to an uplift in research focussed on new methods to detect such alpha-emitting contaminants. From 2007 onwards efforts focussed on emerging methods for detection which were not reliant on gamma emissions and which could be performed remotely. During this period National Physical Laboratory [7], Radiation and Nuclear Safety Authority of Finland [8], the Australian Department of Defence [9], and Defence Research and Development Canada [10], Idaho National Laboratory [11][12], and others each independently produced devices capable of remotely detecting alpha-emitting radionuclides by observing UV light emitted during the interaction of alpha particles with the surrounding air.

This work, motivated by the need to prevent the recurrence of such an attack, produced new detection methods with great potential for application within the nuclear industry. In the UK this is true of the mission to decommission various sites involved in the production of nuclear weapons, the reprocessing of nuclear materials and the production and handling of nuclear fuel. Indeed on the Sellafield site a 2013 review of technical challenges, needs and opportunities in decommissioning identified remote characterisation and imaging techniques to locate alpha hot spots as a need in all but three facilities on the Sellafield site [13]. The

demand for new techniques capable of remotely measuring alpha-emitting materials is considerable and motivated by a wide range of potential uses [13].

1.2 Alpha-emitting radioactive materials in nuclear decommissioning

The nuclear decommissioning industry has a particular need for techniques to produce analytically robust measurements of alpha-emitting radioactive material. Before being prepared for long term storage or disposal, radioactive waste is differentiated into a "classification" based on its composition [14]. Classifications range from material which can be disposed of similarly to conventional waste material (exempted) to waste which must be segregated and stored in geologically stable repositories indefinitely (high level waste). A major determinant of this classification is the proportion and overall activity of alpha-emitting radionuclides in a waste package, with those containing high quantities of alpha-emitting material requiring longer term, secure storage [14].

Wastes containing alpha-emitting material are distinguished due to a variety of their physical and radiological properties. Alpha-emitting radioactive materials often tend to have a very long lifetime, meaning any storage method must be robust over long periods before material can return to safe levels of overall activity.

Alpha-emitting radionuclides also release 3-9 MeV of energy with every decay. This energy is mostly retained within and dissipated throughout the surrounding material. If not sufficiently cooled, then this release of heat can lead to fissures and cracks in the matrix of the containment medium [14].

Alpha particles themselves can also present challenges in long term storage. The product of alpha decay is an energetic helium nucleus. Once this particle is released and its energy dissipated, the nucleus combines with electrons from atoms in the surrounding material, resulting in a helium atom. When a large quantity of alpha-emitting waste is stored for long periods the resulting helium gas can build up within a waste containment matrix [15]. Wastes with a significant fraction of alpha-emitting materials thus require a containment matrix made from specially designed materials to ensure the robustness of the package over time [16].

These factors mean that there is a significant cost associated with the disposal of waste containing a significant fraction of alpha-emitting material (high- and intermediate-level waste) compared to other wastes (low- and very low-level waste). It is therefore important that wastes are accurately assessed - a process which cannot easily be performed in-situ or at pace using the techniques currently used by industry.

Other industrial environments with a need for in-situ, remote monitoring of alpha-emitting materials include facilities handling plutonium, such as reprocessing and MOX fabrication plants. Such facilities, containing hot cells, glove boxes and chemical processing equipment, are at risk of leaks, spills and contamination of alpha-emitting materials and may be under safeguard. Operation of such active facilities would normally include the regular monitoring and assessment of contamination.

1.3 Alpha-induced radioluminescence detectors

An area of research seeking to overcome these difficulties is the development of detectors designed to identify alpha-induced radioluminescence. Such detectors are sensitive to light which is emitted as alpha particles interact with air.

As alpha particles travel through air the electrostatic interaction between the helium nucleus and orbital electrons results in deceleration of the particle and transfer of decay energy. This transfer causes the liberation of energetic electrons which in turn interact with and transfer energy to molecules in their path [17].

This dissipation of alpha decay energy results in a cascade of electrons with sufficiently low energy to produce excitation of nitrogen and other molecules in air. The processes of de-excitation (when a molecule returns to a lower energy state) and recombination (when a low energy electron recombines with an ionised molecule) result in the emission of photons [18]. For nitrogen, the largest constituent of air, these processes result in the emission of a spectrum of photons in the ultraviolet spectrum.

These fluorescence photons can then be detected by sensors which are able to detect photons of those wavelengths. UV photons have a considerably greater mean free path in air than alpha particles, meaning the radioluminescence emissions can be detected far beyond the path of the alpha particle by sensors capable of detecting these photons. Furthermore for each

alpha particle emitted a greater number of UV photons is emitted; in normal atmospheric conditions, for example, a 5.49MeV alpha particle emitted by Americium-241 has been shown to result in the emission of an average of 98.7 UV photons [18].

The systems developed to exploit this phenomenon are in two broad categories:

- Camera-like devices producing images of contamination[10][4][19][20][21][22]; and
- Single-pixel photon counting detectors [7][23][24][25][26].

The former devices offer an operator with the relative positioning of contaminants to a resolution roughly corresponding to the alpha particle's mean free path. Time scales associated with such measurements tend to be relatively long (hours) depending on the desired resolution and signal-to-noise ratio. The outputs of these systems are also often not relatable to the quantities of radioactive material present. Such devices are principally intended for use in the identification of possible regions of contamination.

The second category represents a promising alternative for use in applications requiring quantitative assessment. Using devices capable of detecting and counting individual photons, such as photomultiplier tubes, combined with optics designed to maximise the collection of light from a particular target area, these devices tend to operate in a manner similar to conventional radiometric counting detectors. These devices differ in terms of their particular optical configuration; radioluminescence wavelength targeted; methods employed to reduce background interference; and sensitivity of the type of photosensitive device.

1.4 From detection to measurement

While much work has focused on the development of devices and the testing of their ability to detect particular sources, to date little work has considered the analytical validity of measurements produced by these systems and how the relative performance of such devices could be assessed. This has been exaggerated by a lack of established methods to calculate basic parameters of device performance for alpha-induced radioluminescence detectors in all but the simplest cases. These parameters include: limits of detection, minimum detectable activity and the detector response at different measurement distances.

This thesis explores the principal considerations for the design, calibration and use of alpha-induced radioluminescence detectors designed specifically for the quantitative assessment of alpha-emitting radioactive materials. Beginning with the fundamental physical processes, in chapter 3 a model is presented and used to assess the basic detection geometries associated with the alpha radioluminescence phenomenon. This was then used to analyse the optimal efficiency which could be obtained for various detector geometries.

The results of numerical simulation and the findings of the literature review were used to inform the design and development of a novel device, presented in chapter 4. The design process produced a conceptual framework of considerations which must be made in the design of a detector system, depending on the intended operating environment, performance characteristics and available resources. A detector design is presented based on an intended operation in scenarios encountered in decommissioning. Specifically these were: a fixed detector on top of a conveyor belt; a fixed detector performing measurements on a fixed source; and a detector scanning an environment with unknown levels of contamination. This section outlines the technical parameters of the device, which forms the basis of experimental measurements obtained later.

Chapter 5 presents the development of new methods for calibration based on these priority scenarios. The chapter begins with an assessment of the compatibility of International Organisation for Standardisation methods for the calibration of contamination monitors to the alpha-induced radioluminescence technique. Moving from the simplest possible method (manually performing two measurements, one with a radioactive source present and one without) the chapter looks at increasingly refined methods and experimental configurations to eliminate possible sources of uncertainty while seeking to increase repeatability. The conveyor-style method was then used to demonstrate the linearity of the detector's response function vs the total alpha activity under measurement - a key finding for the use of the detector to produce quantitative measurements of alpha activity. A series of measurements were then performed to assess the extent to which the results obtained using different methods can be compared. It was found that the level of systematic error introduced between methods means that any device calibration must be applied to a particular method of operation, rather than to the device itself independent of the method used.

Two of these methods were then put into practise to calculate detection parameters using sources of known activity traceable to national and international standards. Chapter 6 demonstrates the practical application of these methods to derive a device calibration for measurements over source-to-detector distances under one metre. The measurements were used to derive some important parameters of device performance under different modes of operation. A comparison between two modes is presented to illustrate how the performance of two detectors could be quantitatively compared using this methodology. Specifically, a method to calculate the minimum detectable activity of alpha-emitting material is presented.

1.5 Towards an industrial application

This work seeks to address several barriers limiting the introduction of alpha-induced radioluminescence detection methods for industrial use. Without a comprehensive understanding of a device's analytical performance, any investment into the development of such detectors is likely to be speculative, limiting the pace of adoption by industry. Through the establishment of methods to compare device performance it is hoped that it will be possible for device designers to more accurately reflect the characteristics of their systems, leading to greater confidence in results.

When considering the adoption of a new device, both operators and Site Licence Companies require a thorough understanding of the potential limitations of devices before deployment. This is particularly true where devices are to be used in active facilities, where a reliable understanding of the levels of contamination which could be missed using a technique is as important as being able to identify a contaminant. The results of this work outline a method for the establishment of traceable measures of the minimum detectable activity using several modes of measurement.

To our knowledge this work presents the first use of alpha-induced radioluminescence to quantitatively assess the activity of sources using a calibration against international standards. This demonstration expands the possible uses of these detectors in an industrial context to areas such as operational planning, cost estimation for remediation and dose estimation.

Through this developed understanding, methodology and capability it is hoped that the technique can step closer to adoption in industry.

Chapter 2
Literature Review

A thorough review of alpha-induced radioluminescence detection need consider aspects of several disciplines including physics, engineering (nuclear, industrial and electronic) and analytical science. This review focuses on the physical mechanisms underlying this method of detection - the emission of alpha particles, interactions between charged particles and matter and the emission of photons through molecular fluorescence and radioluminescence - before surveying the range of devices which have been produced to exploit this phenomenon in the detection of alpha-emitting radionuclides. Details of the various mechanisms employed by device developers to overcome issues of sensitivity and noise (both internal to the device and from other sources) are presented. This section concludes, in agreement with the findings of several other research papers, that the absence of established methods for detector operation, for calibration of detectors and quantitatively assessing performance between devices are major limitations for the broader use of the technique in industry.

As outlined in the introduction alpha-emitting materials are of great significance for the nuclear industry, and their accurate characterisation is of paramount importance to the site licence companies and operators working on decommissioning sites. The significance of alpha-emitters to the nuclear industry can be understood through a number of their physical properties exhibited during decay.

2.1 Mechanisms of alpha decay and nuclear contamination

The theoretical basis of alpha decay was first comprehensively described in terms of quantum mechanics by three independent researchers simultaneously: Gamow, Gurney and Condon [27][28]. Their explanation considers that relative to other small nuclei, as shown in figure 2.1, the helium nucleus has very large binding energy compared to other nuclei of a similar mass. This means that helium can effectively establish itself as a quasi-stable particle, as a collection of bound nucleons, within the nucleus of a larger element. This quasi-stable entity within the nucleus could be thought of as existing in equilibrium, balancing the attractive

strong nuclear forces – between the quasi-particle and the remaining nucleus – and the repulsive electrostatic forces.

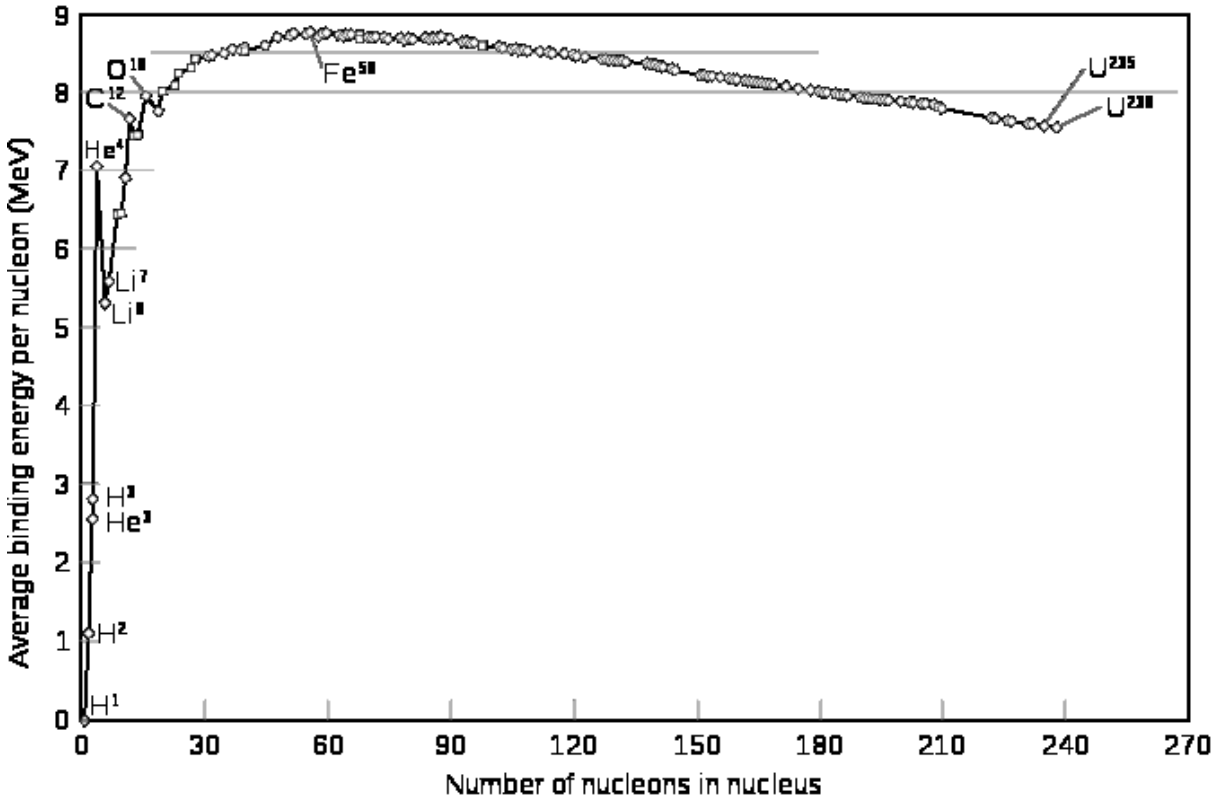


Figure 2.1: Average binding energy per nucleon of naturally occurring elements. The helium nucleus represents a stable decay product because of its high binding energy per nucleon relative to those of similar mass, enabling the formation of quasi-stable states within large nuclei. Heavier nuclei benefit in energetic terms from the processes of radioactive decay and fission as their disintegration causes an increase in binding energy per nucleon [29].

In a stable, light nucleus such a particle could continue to exist in this equilibrium with no probability of being ejected. However, for heavier nuclei the sum of the binding energy of the products of an alpha decay (a helium nucleus and a nucleus with its atomic mass and charge reduced accordingly) mean that it could be possible for an alpha decay to occur. If the binding energy (B) of a parent nucleus (proton number Z, atomic number A) were

considerably greater than the decay products ($B(Z,A) < B(Z - 2,A - 4) + B(2,4)$) [30], then the decay is not energetically possible. Where the sum of the binding energy of the decay products are greater than (or close to) the parent nucleus then decay is possible. In common with all forms of nuclear decay, for a decay to occur the sum of the binding energies of the decay products must exceed that of the initial state.

This criterion imposes an intrinsic limit on elements which can decay by alpha-emission. Nuclei must be large, on the right side of the figure 2.1 where the gradient of binding energy vs number of nucleons is negative, for decay to a lighter nucleus by alpha-emission to result in a larger total binding energy. The lightest element known to decay by alpha-emission is tellurium-106. As shown in figure 2.2 the majority of alpha emitters are found after the largest, known, stable isotope, lead-208, where fissionable radionuclides are also located.

The principle outlined above, that for decay to occur the sum of binding energies of the decay products must be greater than that of the parent nucleus, also applies to the products of fission. Some nuclei which are susceptible to alpha decay because of the factors outlined above are also susceptible to fission because of these properties. This illustrates one of the connections between alpha-emitting radionuclides and nuclear fission, and the connection between alpha-emitters and the nuclear industry.

Examples of such alpha-emitting substances include some isotopes of uranium, plutonium (used to fuel nuclear reactors) and americium, curium and neptunium (by-products of fissile materials which are prevalent in nuclear reprocessing facilities and decommissioning).

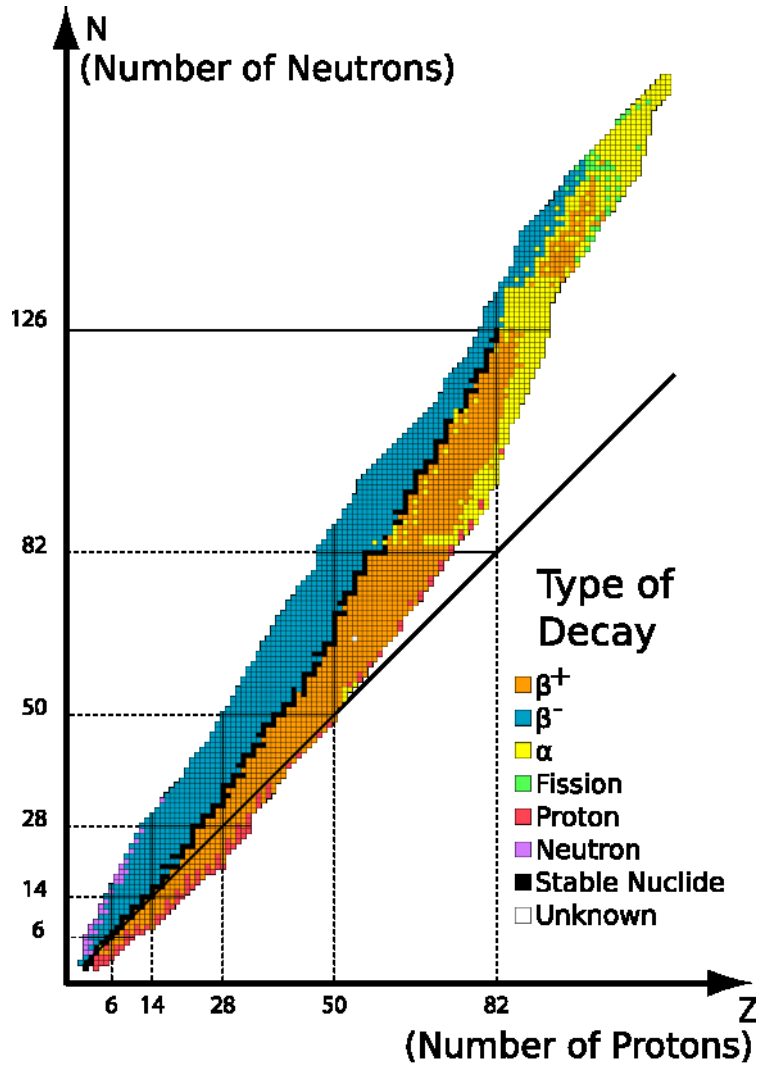


Figure 2.2: Most alpha-emitters are found in the high Z region of the periodic table. This is due to the energetic balance of the high binding energy of the quasi-stable helium state and the decreasing binding energy of the heavier elements. Beta decay, however, dominates for neutron rich radioisotopes. The heaviest observationally stable nucleus is lead-208 at Z=82 [31].

Consideration of the quantum mechanics of a helium quasi-particle inside a parent nucleus leads to a theoretical explanation of alpha decay. In classical mechanics, consideration of a quasi-particle state would render alpha decay impossible, as the energy required to overcome the attraction of the strong nuclear force would not be internally

provided; instead the particle would exist in continuous equilibrium and thus remain stable. When considered in terms of quantum mechanics tunnelling phenomena must also be considered. In this model such a helium nucleus could acquire energy for a very brief period, as governed by the Heisenberg uncertainty relation [32].

This effect also has physical consequences. When comparing radioisotopes of the same element, if more energy is required in one nucleus to push a quasi-stable alpha particle over the potential barrier then this process has a lesser probability of occurring, and the resulting alpha particle will have less energy itself. This fact leads to the interesting conclusion that there is a relationship between the half-life of an isotope and an alpha particle's decay energy. The equation describing this process is the Geiger-Nuttall relation [30]:

$$\log_{10}(t_{1/2}) = a + bZE_{\alpha}^{-1/2} \tag{2.1}$$

Which shows that the log of the radioactive half-life of an isotope, $t_{½}$ is proportional to the inverse square root of the decay energy of the alpha particle, E_{α}. The constant a is related to the element of the isotopic nucleus, atomic number Z, undergoing the decay and b is constant across all nuclei. This is shown in figure 2.3 for isotopes of uranium, radium and polonium.

The Geiger-Nuttall relation is useful in the characterisation of radiological contamination as the isotopic composition of a material can, in a limited number of cases, be inferred from the level of activity of a sample. Uranium for example is distinctive in its appearance and can be visually identified by personnel experienced in uranium characterisation. A useful indicator of the enrichment of a sample of uranium is its alpha activity. Highly-enriched uranium has an activity approximately 100x that of a similar mass of low-enriched or natural uranium[6], meaning that the alpha activity (or surface emission rate) of a sample can be used as a proxy measure of a sample's enrichment.

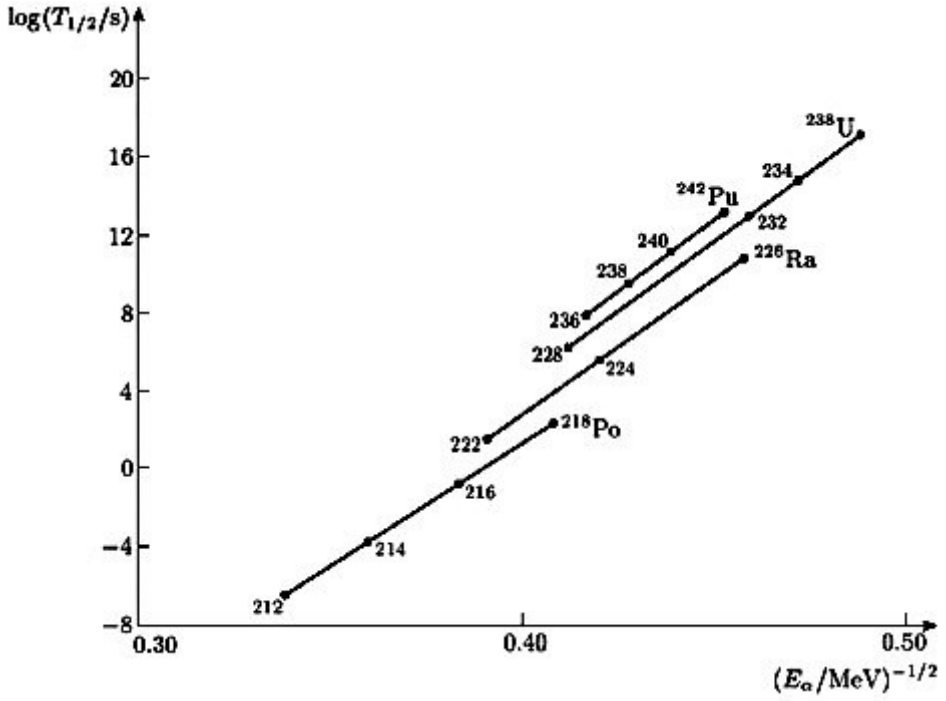


Figure 2.3: The Geiger-Nuttall relation, first proven experimentally and later theoretically, describes the relationship between half-life and alpha particle energy. This relation explains the great variation of half-life compared to energy: the relationship is logarithmic. Subtle differences in the energy and half-life of isotopes of an element can be used to deduce isotopic composition [33].

Many fissionable nuclei are also alpha-emitters, for example uranium-233, 235, 238, neptunium-237 and plutonium-238, 239, 240 and 242 [34], and the decay products of fissionable materials are often also alpha-emitting. Fission is the basis of conventional nuclear power generation and as such large amounts of alpha-emitting contamination and waste is encountered in the decommissioning of nuclear facilities. Some of the major constituents of the UK's nuclear decommissioning legacy, documented the UK Radioactive Waste Inventory by activity, are: curium, americium, neptunium, uranium and plutonium (see Table 2.1) [35]. These elements are therefore the primary focus of the work being undertaken in this study and are the major focus of decommissioning projects on alpha-induced radioluminescence.

Radionuclide	$t_{1/2}$ (years)	$E_{\alpha,max}$ (MeV)	NDA Inventory (TBq)
^{233}U	1.59 E+5	4.908	1.6 E+0
^{234}U	2.45 E+5	4.857	1.7 E+1
^{235}U	7.04 E+8	4.678	5.6 E-1
^{236}U	2.34 E+7	4.573	1.5 E+0
^{238}U	4.47 E+9	4.270	1.7 E+1
^{237}Np	2.14 E+6	4.959	1.1 E+2
^{239}Pu	2.41 E+4	5.244	9.3 E+3
^{240}Pu	6.56 E+3	5.256	1.0 E+4
^{242}Pu	3.75 E+5	4.985	7.3 E+0
^{241}Am	4.33 E+2	5.637	4.0 E+5
^{243}Am	7.37 E+3	5.349	1.9 E+3
^{242}Cm	3.47 E-1	6.216	1.4 E+3
^{243}Cm	2.91 E+1	6.169	1.3 E+3
^{244}Cm	1.81 E+1	5.901	1.2 E+5

Table 2.1: Alpha-emitting radionuclides with large quantities recorded in the UK Nuclear Decommissioning Authority's Waste Inventory (2013). As shown, when measured by activity the most significant quantities of alpha-radionuclides present in the UK are americium, curium and plutonium. Due to their long half life uranium isotopes have lower total activity, but represent a considerable contribution by volume. Data obtained from: [35][36].

Following the decay of an alpha-emitting nucleus several further physical processes determine the dissemination and transfer of energy from the alpha particle to its surroundings. The following section outlines these interactions.

2.2 Energy deposit in matter

The energy loss of charged particles has been studied extensively since the beginning of the twentieth-century. A major finding was Hans Bethe's application of quantum perturbation theory to ion stopping power [17].

Developing work conducted by Bohr [37], Bethe created a formula to describe the rate of energy loss per unit length ("stopping power") of a charged particle entering a medium of net neutral charge composed of charged particles (in this case nuclei and electrons). The Bethe formula in its entirety is:

$$-\frac{dE}{dx} = \left(\frac{ze^2}{4\pi\epsilon_0}\right)^2 \frac{4\pi Z\rho N_A}{Am_e v^2}\left[\ln\left(\frac{2m_e v^2}{I}\right) - \ln\left(1-\beta^2\right) - \beta^2\right] \quad (2.2)$$

Where β represents the particle's speed as a proportion of the speed of light ($\beta = \frac{v}{c}$); ze its electronic charge ($2e$ for α-particles); m_e is the electron mass; N_A is Avogadro's constant; Z, ρ A and I are the target material's atomic number, density, atomic mass and ionization potential. The ionization potential, I, is the average energy required to singularly ionise an atom in the target material; in practise this quantity is difficult to estimate for mixtures of various elements such as air, but an approximation of $I = 11Z$eV is often used in media with Z <20 [32][30].

Equation 2.2 is valid for high-energy relativistic effects where the velocity of the ion, v, approaches the speed of light. An elementary classical calculation of the speed of the highest energy alpha-particle listed in Table 2.1, curium-242, shows that the maximum possible ejection velocity is $1.7 \cdot 10^7 ms^{-1}$, approximately 6% of the speed of light, so relativistic effects can be neglected for the purpose of this study of alpha-particles. This leads to the following simplified form:

$$-\frac{dE}{dx} = \left(\frac{ze^2}{4\pi\epsilon_0}\right)^2 \frac{4\pi Z\rho N_A}{Am_e v^2}\left[\ln\left(\frac{2m_e v^2}{I}\right)\right] \tag{2.3}$$

The Bethe formula's calculation of stopping power, $\frac{dE}{dX}$, is consistent with experimental data in the range from the energy of alpha emission to the energy at which the nucleus is able to recombine with electrons. The lower limit corresponds to the point at which there is a possibility of recombination with the electrons with which an alpha particle collides, thus neutralising its charge and changing the nature of its energy loss (see figure 2.5) [38]. This point in the case of alpha-particles lies in the region of 178keV for alpha particles in air, after which the stopping power, $\frac{dE}{dX}$, calculated by the formula reaches zero, and becomes increasingly negative. This is clearly not in accordance with physical reality, and so defines the boundaries of accuracy of the expression (see figure 2.5). This defines the low velocity limit of the Bethe formula, upon which corrections were built by subsequent scholars [38].

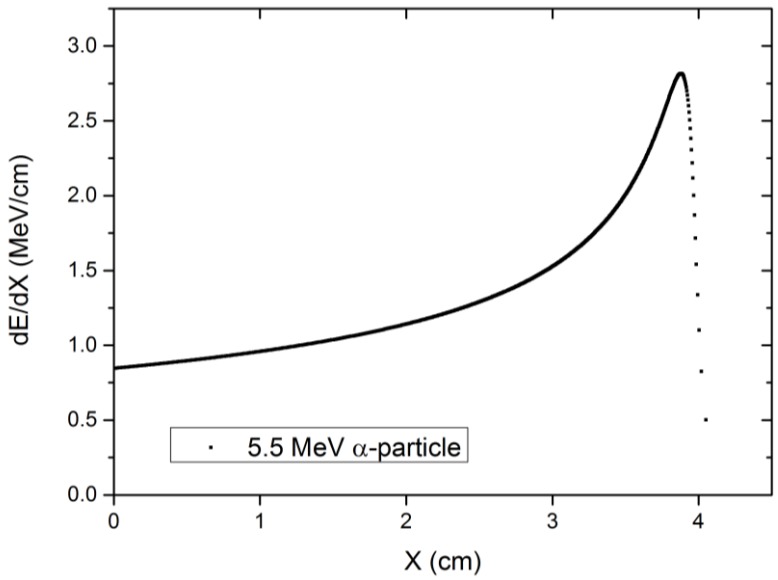


Figure 2.4: The function of an alpha particle's stopping power over distance in air as described by the Bethe formula. As shown clearly the majority of the particle's energy is deposited in the outer reaches of its path. This leads to the so called 'Bragg Peak'.

Various programming libraries have been developed for modelling this process. SRIM [39], 'Stopping Range of Ions in Matter', is a program designed to model efficiently energy deposit profiles of energetic particles in matter which considers both theoretical models and experimental data, allowing the user to build depth profiles of various materials into which ions traverse. Data is output offering the user information upon the sputtering (deviation from the charged particle's straight path over its transit), energy deposit and ionisation events. Such programs are a useful tool for approximate models, however small disparities exist with experimental data and international standard values from the International Commission on Radiation Units and others [40]. Experimental data has also been published by NIST in the ASTAR database, with data drawn from the International Commission on Radiation Units and Measurements (ICRU) [41].

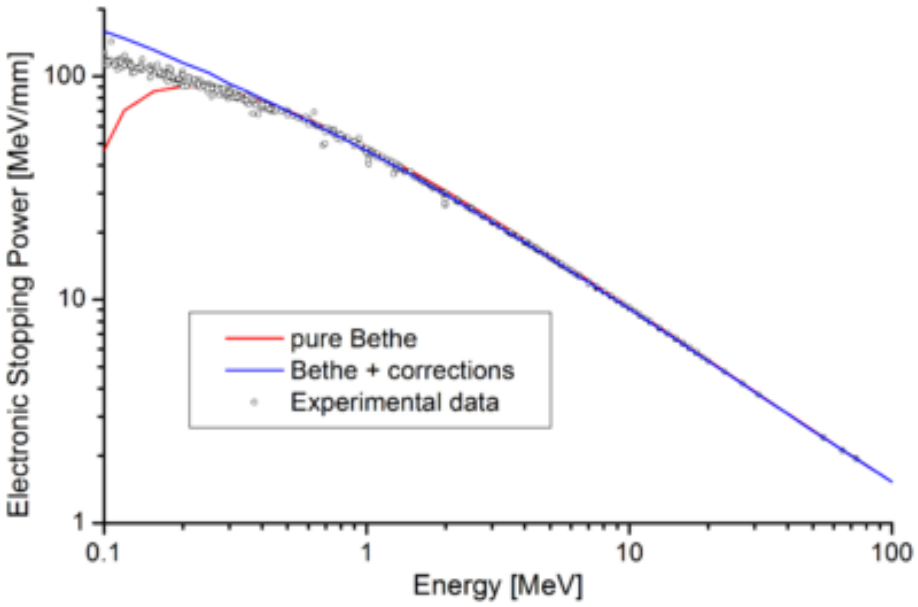


Figure 2.5: Stopping power versus particle energy for alpha particles in air. At velocities comparable to that of orbital electrons the possibility of the incident ion combining with the electrons which it encounters arises. This neutralisation of ionic charge, and other low velocity phenomena, impacts the stopping power of the ion and causes variation between the Bethe formula and experimental data [33].

One significant result from the Bethe formula is the relationship between energy and range of alpha particles. Once an alpha particle slows to an adequately low velocity ionisation no longer occurs and it is at rest. One can then write the expression:

$$R = \int_0^R \mathrm{d}x = \int_{E_{initial}=\frac{1}{2}mv^2}^{0} \left[-\frac{dE}{dx}\right]^{-1} \mathrm{d}E \tag{2.4}$$

for the range of an ion in air, with initial kinetic energy $E_{initial}$. In practise, if using equation 2.3 the discontinuity discussed at 178keV means that the limits of integration must be modified to limit the integration to a non-zero value at which the stopping power, $\frac{dE}{dx}$, is non-negative. This modification has little overall effect on range calculations, with numerical simulations presented in chapter 3, using the uncorrected Bethe formula, estimating an alpha particle range of (41.4±0.4)mm in air compared to the SRIM-derived value of (41.48±0.05)mm at 1.2kgm^{-3}.

Material	Density (gcm^{-3})	Phase	Range
Uranium	19.04	Solid	9.76μm
Thorium	11.66	Solid	15.31μm
Lead	11.34	Solid	15.69μm
Polonium	9.25	Solid	19.60μm
Carbon	2.25	Solid	21.25μm
Beryllium	1.85	Solid	28.47μm
Radium	5.02	Solid	34.30μm
Water	1.00	Liquid	42.05μm
Air	0.0012	Gas	41.48mm

Table 2.2: Stopping ranges for 5.5MeV alpha-particles in a number of relevant materials. Data reproduced from [39].

The rate energy loss for alpha particles is significant factor in alpha-particle spectroscopy. In this technique measurements are made of the energy of alpha particles emitted by a sample. The spectrum of energies acquired in analysis can then provide details of the isotopic and elemental composition of the radionuclides [42]. These studies are sensitive, analysing the specific energies to a precision of a few keV. Problems can arise where an alpha particle's energy is lost while traversing a medium before striking the detector (especially in dense materials and those in solid phase). If a nucleus does not lie on the immediate surface of a material, instead say 100 atomic layers down, then the energy of the particle when it emerges from the surface will be considerably attenuated. Over time, rather than a sharp peak corresponding precisely to an emission energy, a continuum of values – all corresponding to the specific surface distances from which they originated – will emerge [43]. This means that the spectrum obtained will have a considerably lower resolution. As such, in alpha-particle spectroscopy samples are specifically prepared to be very thinly distributed on planchets [42].

For in-situ measurements there is little-to-no opportunity to prepare samples and as such the energy spectrum of alpha particle emissions from unprepared, contaminated surfaces are largely uninterpretable. This presents difficulty to analyst when performing in-situ measurements and means that the only in-situ measurement possible is an estimate of the overall surface emission rate per unit area ($s^{-1}cm^{-2}$). Samples can instead be taken for analysis in a radiochemical laboratory environment to obtain isotopic and elemental data. Some exceptions do exist, such as the uranium case discussed on page 35 [6].

A significant feature of the alpha-induced radioluminescence technique is the spatial distribution of energy deposited by alpha particles compared to that of β and γ radiations. β and γ radiations interact less strongly, depositing on average less energy per unit length travelled than α radiation. The cross sections associated with these radiations are therefore considerably smaller. For illustration, the stopping power associated with a 0.5MeV electron in air is $1.81 MeVgcm^{-2}$ compared with $1964 MeVgcm^{-2}$ for an alpha particle of equivalent energy; the rate of energy loss per unit length is therefore more than 1000x greater for an alpha particle [41].

This property was explored in a paper by Thompson et al. who performed numerical simulations of the UV radioluminescence emissions of alpha-, beta- and gamma-emitting radionuclides in air using Geant4. Using their model they concluded that, compared to beta-

and gamma-emitting radionuclides, alpha-emitters had an improved localisation, supporting the view that the technique is well suited for the detection and localisation of alpha emitters [18].

Figure 2.6 shows the spatial distribution of UV photons emitted for illustrative radioisotopes predicted by their model within a 20m cubic geometry [18].

Clearly visible in the trace for americium-241 (red) are characteristic components arising from the alpha and gamma contributions. At 40mm the Bragg peak is clearly resolved, followed by a small region of straggling from 40-70mm. The straggling region can be understood as being composed of both straggling of the alpha particle and drift of the electrons liberated through ionisation. In the region beyond than path length of alpha particles a contribution from the low energy americium-241 gamma photons can be observed, primarily arising due to Compton scattering.

For both cobalt-60 (blue) and phosphorus-32 (green) the contributions due to the interaction of beta radiation with air are visible as a continuum from the point of emission to a maximum distance. The continuum for ^{32}P extends for a larger distance (approximately 2500mm vs 800mm) corresponding to its higher average emission energy (695keV vs 97keV).

The cobalt-60 distribution shows a higher magnitude at short distances compared to phosphorous-32. This is due to the contributions of the high energy gamma emission (a weighted average of 2.51MeV) of ^{60}Co. These are clearly resolved in the tail of the distribution beyond 600mm, but also offsets the curve at shorter distances.

Their results show that the radioluminescence emissions arising due to alpha particles are concentrated into a considerably smaller, more confined area than the respective beta and gamma radioluminescence contributions.

In the case of americium-241 the paper also shows that the contribution due to the low energy gamma emissions is present but very small. This contribution is not visible on the spatially resolved figure for ^{241}Am (lower left).

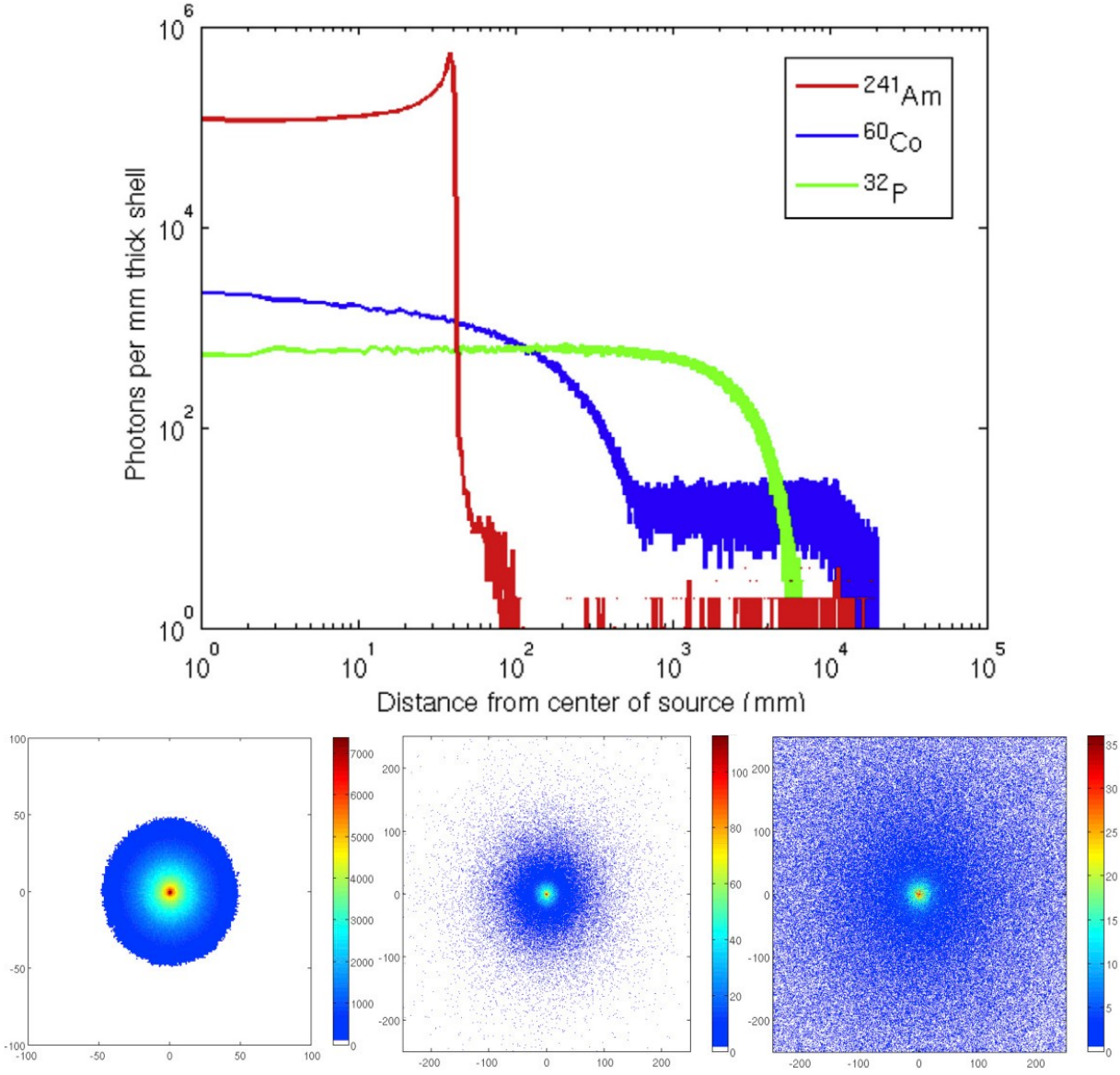


Figure 2.6: Top: Simulation of UV radioluminescence emissions in air for 6.5 10^5 decays of americium-241 (5.48MeV α; 21.3keV γ), cobalt-60 (97keV β; 2.51MeV γ) and phosphorus-32 (695keV β). The quoted decay energies were averaged across all emissions for each isotope by the authors. Bottom: 2D spatial distribution of photon emissions for each radionuclide illustrating localisation of fluorescence from ^{241}Am (left) compared to ^{60}Co (centre) and ^{32}P (right). Reproduced with permission of the rights holder from: [18].

The distinct characteristics of contributions from alpha, beta and gamma provide an opportunity to distinguish radioluminescence resulting from each type of radiation. Within a conveyor scanning scenario contributions from beta and gamma sources could be distinguished based on their width and lower relative intensity (if relative activity were known, for example by a beta/gamma measurement).

During the imaging of sources of known geometry, any contribution from beta or gamma would extend beyond the boundaries of the physical casing of the source. This could be identified by analysis of the width of the distribution around the source, allowing the distinction between alpha contributions (confined to a few centimetres around the source) and others (which stretch far beyond).

In an engineered solution intended for measurement of mixed radiation types (for example in a decommissioning environment) the optimisation of such a mechanism is likely to be one of the most significant challenges.

The spatial distribution of luminescence emissions has also been explored for electrons and X-rays in an experiment using therapeutic radiation beams [44], with results obtained from the luminescence spectra of x-rays and electrons analysed with an electron multiplying charged coupling device (EMCCD). The paper demonstrated the impact of straggling on electron beams over various energies (6, 12 and 20MeV), with photons emitted from a smaller lateral region for higher energy beams. This is because electrons at higher energies have a lesser chance of being scattered at significant angles (straggling) as their interaction cross section is smaller and momentum transfer is less. So while photons are emitted by the same process of excitation, ionisation and fluorescence, they are more diffuse toward the end of the particle's path.

2.3 Molecular Spectroscopy and Fluorescence

The physics underpinning the observation of highly energetic particles using UV light photons was first explored in the study of cosmic ray air showers. When cosmic rays enter the upper atmosphere, they collide with molecules which result in the emission of energetic secondary particles including pions and other subatomic particles. In turn these produce other particles which also interact with molecules in air. The outcome of these interactions the

release an enormous cascade of liberated electrons. After reaching energies comparable to those of orbital electrons these electrons go on to recombine with ionised molecules or cause the emission of photons through excitation. The initial cosmic ray event is therefore observed on earth as an enormous release of light photons [45], with the magnitude of the light shower proportional to the initial energy of the cosmic ray particle.

The fluorescence released following an alpha decay is governed by the same principals. The alpha particle causes the liberation of many energetic secondary electrons, which in turn induce the release of photons from the molecular constituents of air through de-excitation and recombination [18]. This section explores the mechanisms of fluorescence generation through radioactive decays and considers the spectrum emitted as a result.

Extensive studies of the spectrum of wavelengths produced during the deposition of energy by charged particles in air have been conducted. Most studies were motivated by the observation of extensive air shower events produced by the interactions of highly energetic (10^{12} - 10^{15}eV/particle) cosmic rays in the upper atmosphere [45]. To simulate this process in the laboratory environment, spectral emissions of highly energetic electrons (one product of extensive air showers) across energy scales have also been analysed [46]. These studies were important in the development of the field of alpha-induced radioluminescence but are different in their length and energy scales. As a result a small body of work, largely motivated by nuclear safeguards and forensics, emerged analysing alpha emission and its resultant fluorescence phenomena, however the body of work remains small by comparison.

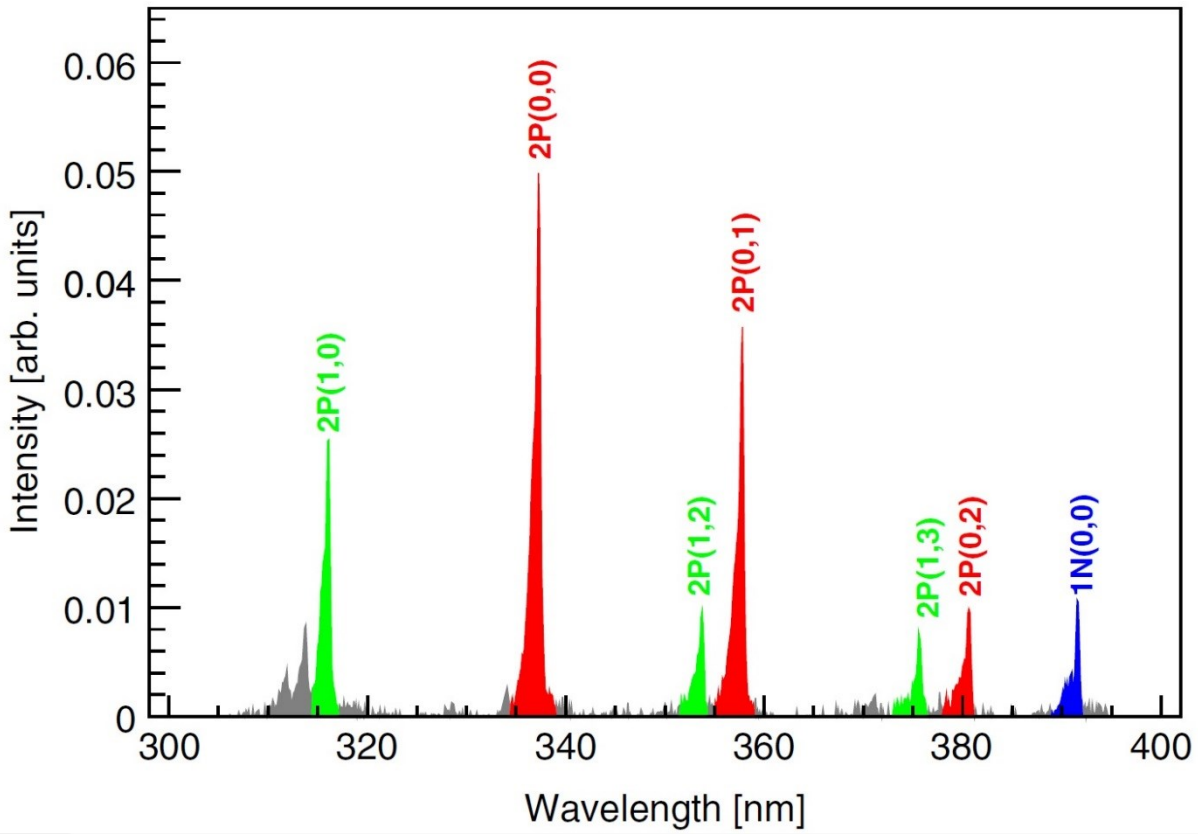


Figure 2.7: The near-UV (300-400nm) fluorescence emission spectrum of nitrogen in dry air at 101.3 kPa induced by electrons. Additional features shaded in grey are composed from additional constituents of dry air such as oxygen and argon. Labelled are the respective electronic molecular states of nitrogen from which emission occurs [46].

The first characterisation of alpha-induced radioluminescence was by Lord and Lady Huggins in 1903 [47]. By comparison of a spectroscope spectrum obtained on photographic film to nitrogen and radium the authors identified that luminous emissions of radium bromide arose not from the excitation and emission of radium itself but from nitrogen and other constituents in air. This, it was proposed, was the reason that radium was seen to glow when observed in the dark.

The processes of excitation and fluorescence of air are governed by the principles of diatomic molecular spectroscopy. Fluorescence of air in the 300-400nm range primarily originates from the emission spectrum of nitrogen, the largest constituent of air, shown in red,

blue and green in figure 2.7 compared to other constituents in grey. Nitrogen and oxygen are homonuclear diatoms which simplifies several considerations (such as molecular dipoles) in their emission and absorption spectrum.

Emission and absorption spectra originate from the electronic structure of atoms or molecules [48][49]. Molecular emission spectra are considerably more complex than atomic ones. In addition to the electronic contributions of individual atoms, the combination of atoms provides greater degrees of freedom, which complicate structures. These extra degrees of freedom, such as motion of nuclei relative to one another in rotation and vibration, produce substructure, typically of lesser magnitude, which contribute heavily in consideration of molecular emission spectra.

The vibrational structure of homonuclear diatomic molecules includes the relative motion of one nucleus compared to the other. A useful mechanism implemented in analysis of molecular energy structures is the Born-Oppenheimer approximation. This approximation separates the contributions to the total molecular wavefunction, Ψ, into its respective components: electronic, $\psi_{electronic}$, and nuclear (vibrational and rotational), $\psi_{nuclear}$:

$$\Psi = \psi_{electronic} \times \psi_{nuclear} \tag{2.5}$$

Correspondingly for energy, considering the action of the Schrödinger equation on 2.5:

$$E = E_{electronic} + E_{nuclear} \tag{2.6}$$

Where the nuclear component of both E and ψ can similarly be decomposed into the vibrational and rotational subcomponents. This approximation is possible as the timescales associated with changes in nuclear and electronic motion, according to their respective inertias, are significantly different. An indicative scale of contribution from these terms can be semi-classically derived [49][50]:

$$E_{electronic} \gg E_{vibrational} \gg E_{rotational} \tag{2.7}$$

Indicating the relative significance in the structure of excitation-emission spectra.

The Born-Oppenheimer approximation is not valid where a change of a vibrational state effects the electronic state of the molecular wavefunction; this so called 'vibronic coupling' is a challenge in spectroscopy and proves key to the analysis of some fluorescence spectra.

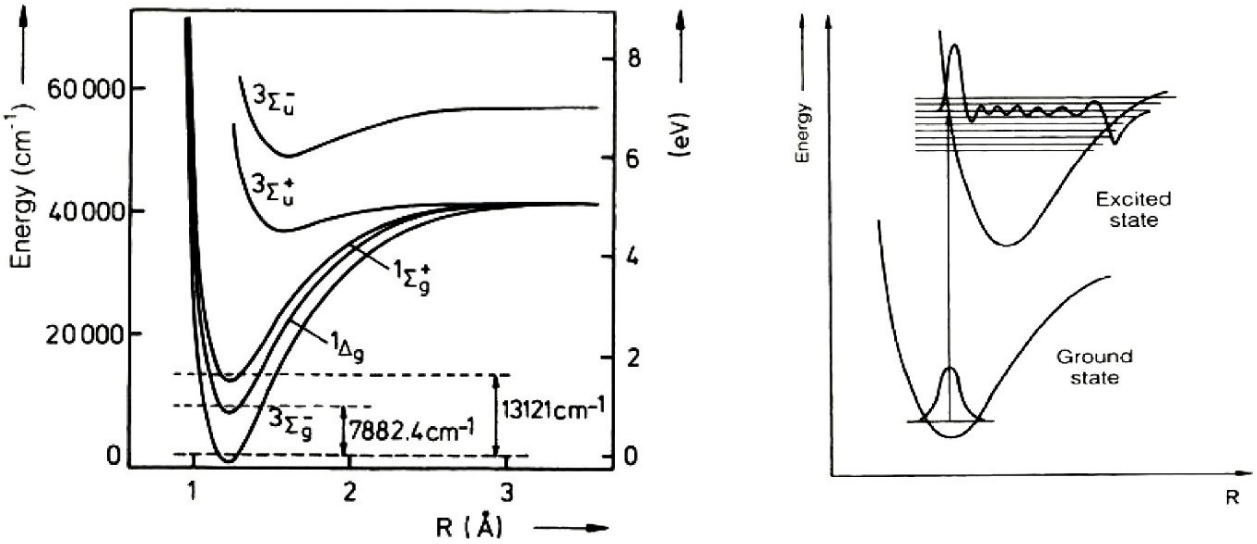


Figure 2.8: Left: Potential energy curves for various low electronic states of the O_2 molecule. The equilibrium internuclear distance (R) of the ground vibrational state (corresponding to the energy minima) of different electronic states can vary. As a result, given the relative timescale of nuclear motion, a change in electronic state can shift a molecule into a higher vibrational state with internuclear distance comparable to the original one. Right: Schematic of the process in which, due to an electronic excitation, the molecule results immediately in a higher vibrational energy state. Reproduced with permission of the rights holder from: [48].

The vibrational term arises as for each electronic state, an independent potential field exists between nuclei within the molecule, centred about their centre of gravity and with an associated equilibrium distance between them. If nuclei move either closer or further away from this distance, as in excited vibrational states, the potential energy of the nuclei in a molecule increases. The frequency at which nuclei resonate within a molecule is determined by the binding force between them; correspondingly a change in electronic state impacts the

resonant frequency and potential energy curve of the molecule, thus also often changing the equilibrium position (see figure 2.8).

When an electronic excitation occurs, due to the small timescale of electronic transition compared to nuclear motion, it is often accompanied by a change in vibrational state of the kind:

$$E''_{el}(v'') \rightarrow E'_{el}(v') \tag{2.8}$$

where E_{el} and v are the electronic and vibrational states before ($''$) and after ($'$) transition. The probability of transition from a ground state equilibrium position to a similar equilibrium position in another electronic state is thus larger than one with a corresponding change in nuclear position. As such, as shown on the right of figure 2.8, transitions will occur with highest probability vertically, without change in internuclear distance.

The formalism of this mechanism comes in the form of the Franck-Condon integral which determines the probability of transitions of the type in equation 2.8:

$$\int \chi_{v'}(\mathbf{R})\chi_{v''}(\mathbf{R})dV_{nuclear} = \langle \chi_{v'}(\mathbf{R})| \ |\chi_{v''}(\mathbf{R})\rangle \tag{2.9}$$

Where $\chi_v(\mathbf{R})$ is the vibrational wavefunction of the nuclei at position $\boldsymbol{R}$ for electronic state E before *(E'', v'')* and after *(E', v')* transition. The wavefunctions are integrated across the entire volume of the molecule in nuclear coordinates. Overlaid on the right of figure 2.8 is the one dimensional vibrational wavefunction of two electronic states; in evaluation of this integral, the regions of overlap between the wavefunctions contribute to its overall magnitude. Accordingly electronic and corresponding vibrational states (pre- and post-transition) which are large at the same internuclear distance produce the largest Franck Condon integral.

The probability of transition between states is related to equation 2.9 by the square:

$$q_{v'',v'} = |\langle \chi_{v'}(\mathbf{R})| \ |\chi_{v''}(\mathbf{R})\rangle|^2 \tag{2.10}$$

here $q_{v'',v'}$ is the Franck-Condon factor for the transition, used widely in spectroscopic calculations, which after normalisation between all available vibrational states can be used to quantitatively evaluate the relative intensity of the various transitions.

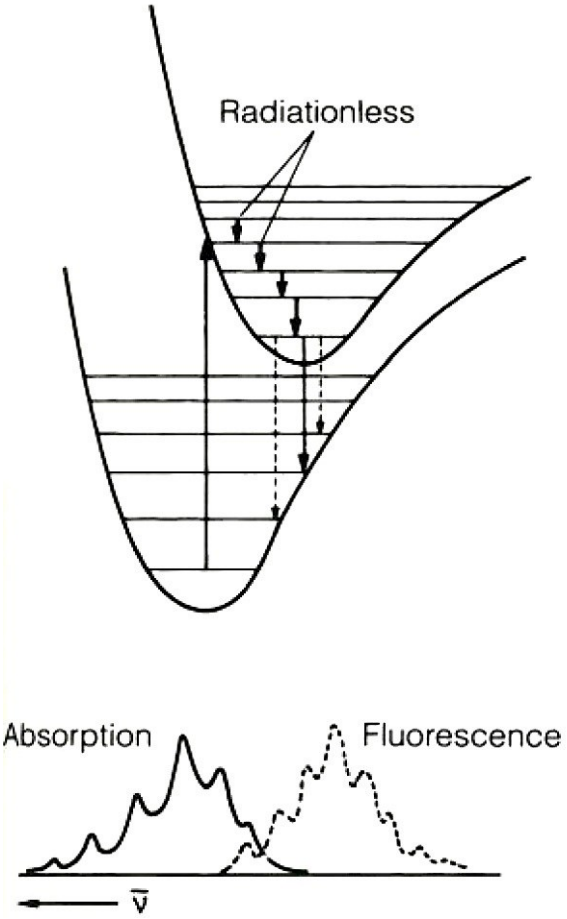


Figure 2.9: A schematic representation of the processes of diatomic molecular fluorescence. Photons are absorbed at a particular wavelength promoting electrons to higher electronic states; given the Franck-Condon Principle vibrational states with comparable internuclear distance are preferred. After a number of radiationless de-excitations in vibrational state causing the internuclear distance to increase, a change in electronic state occurs releasing a lesser amount of energy and thus a larger wavelength photon. Reproduced with permission of the rights holder from: [48].

Once a molecule is excited to a higher electronic and/or vibrational state through transfer of energy from either a photon or charged particle, photons can be emitted during the de-excitation which follows. Fluorescence is the process by which radiation is absorbed, exciting an atom or molecule to a higher energy state, and later re-radiated as photons at a different, higher wavelength. This phenomenon can be explained effectively by the model outlined above: radiation excites a molecule to a higher vibronic state, followed by a number of subsequent radiationless changes of vibrational quantum number (thus increasing the internuclear distance), followed by a change in electronic state to vibrational states of comparable internuclear distance. This process is displayed in figure 2.9; the energy of de-excitation, after the non-radiative changes of vibrational state, is less than the energy of excitation. The condition of this process of fluorescence is the time-scale associated with changes in internuclear distance. If electronic state decay is faster than the time-scale for changes in internuclear distance then fluorescence cannot occur: radiationless de-excitation between vibrational states causes the re-emission at a larger wavelength.

In the case of nitrogen, as displayed in figure 2.10, fluorescence processes exist and in the 300-400nm region these are primarily due to the 2P and 1N band systems, corresponding to the neutral and ionised molecule respectively. Due to its relative magnitude, the rotational substructure of nitrogen is of little relevance to consideration of such band systems in the context of radiation detection and as such is not explored in this review.

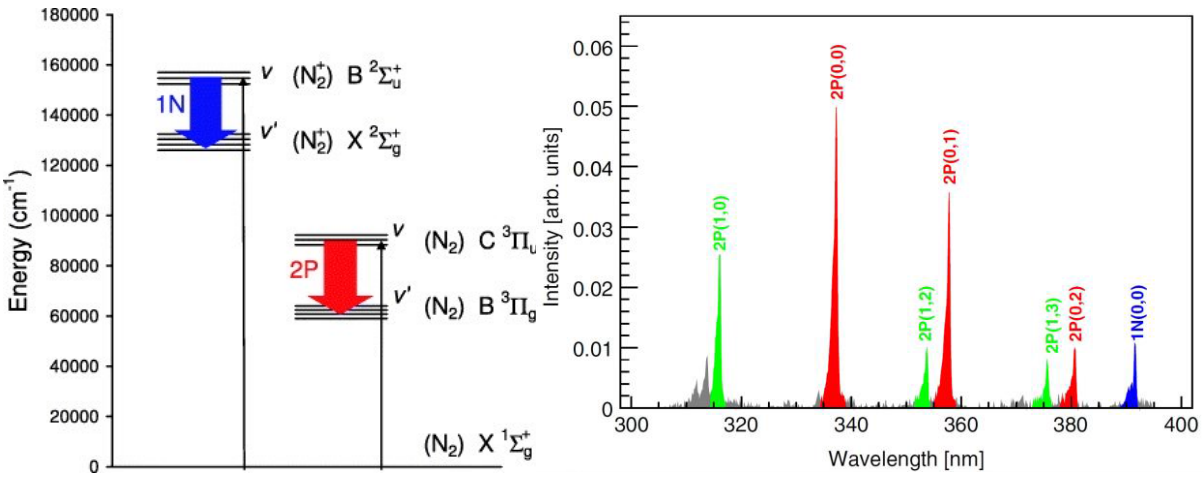


Figure 2.10: The most intense emissions in the near-UV region for dry air correspond to the first negative (1N) and second positive (2P) band systems of nitrogen molecules. Reproduced with permission of the rights holder from: [49][52].

A convenient metric for analysing molecular emission transmissions is the Einstein Coefficient. This coefficient refers to the rate at which molecular transitions occur spontaneously. By analogy of radioactive decay, if considering large numbers of molecules in the same, excited state then, if *de-excitation* is random and uncorrelated, the number of de-excitations per unit time will be proportional to the number of molecules in that state at time t. This can be written in terms of $N(t)$, number of molecules in a state:

$$\frac{\partial N(t)}{\partial t} = -A_{12}N(t) \tag{2.11}$$

With A_{12} being the constant of proportionality, the Einstein Coefficient, dependent on the originating and final state, which indicates a characteristic decay period of the state, 1, to a final state, 2. This factor is called the Einstein coefficient. From this differential equation a simple solution can be found for values of N at time t in terms of the original number of excited molecules ($N(0)$) in the form:

$$N(t) = N(0)e^{-A_{12}t} \tag{2.12}$$

Where A_{12} is related to the mean lifetime of the decay, t_{12} by its reciprocal:

$$A_{12} = \frac{1}{t_{12}} \tag{2.13}$$

λ (nm)	Band	v"	v'	$A_{v'',v'}$ (s^{-1})
391.44	1N	0	0	1.14 E+7
380.49	2P	0	2	3.56 E+6
375.54	2P	1	3	4.93 E+6
358.21	1N	1	0	5.76 E+6
357.69	2P	0	1	8.84 E+6
337.13	2P	0	0	1.31 E+7
315.93	2P	1	0	1.19 E+7
313.60	2P	2	1	1.01 E+7
311.67	2P	3	2	5.94 E+6

Table 2.3: Major transitions in the molecular nitrogen fluorescence emission spectrum with their corresponding Einstein coefficients[53] and origin [49]. Due to the quenching effects of oxygen in air the average decay periods tend to be shortened, leading to a greater Einstein coefficient than those presented.

In addition to the emission of a photon an excited state can also undergo de-excitation by other processes. In the context of fluorescence this process is called quenching, integrating all processes by which fluorescence intensity is reduced. The most common mechanism in gaseous media is collisional exchange of energy between molecules of different elements; specifically in the case of air, oxygen. The rate of quenching is affected by a number of variables including temperature and pressure, and this can reduce the overall number of photons which are emitted following the transfer of energy from an alpha particle. The overall variation of this effect over the range of temperatures and pressures encountered in terrestrial conditions is such that this can be neglected for this study, as it has in others [54].

The above factors combine to give a comprehensive view of the total fluorescence production mechanism, which culminates in the definition of the fluorescence yield, Y_f. The number of photons produced with a particular wavelength, per unit energy within air is described by:

$$Y_f(\lambda, T, p) = \frac{N_{photons}(\lambda)}{E_{deposited}} \tag{2.14}$$

Thus for a series transitions over a wavelength range:

$$Y_{total}(T, p) = \sum_{\lambda_{min}}^{\lambda_{max}} \frac{N_{photons}(\lambda)}{E_{deposited}} \tag{2.15}$$

This quantity has been studied extensively in the case of electron-fluorescence induction in air but to a lesser extent for alpha particles. Displayed in figure 2.11 is the fluorescence yield production itemised by spectral transition in dry air for electrons.

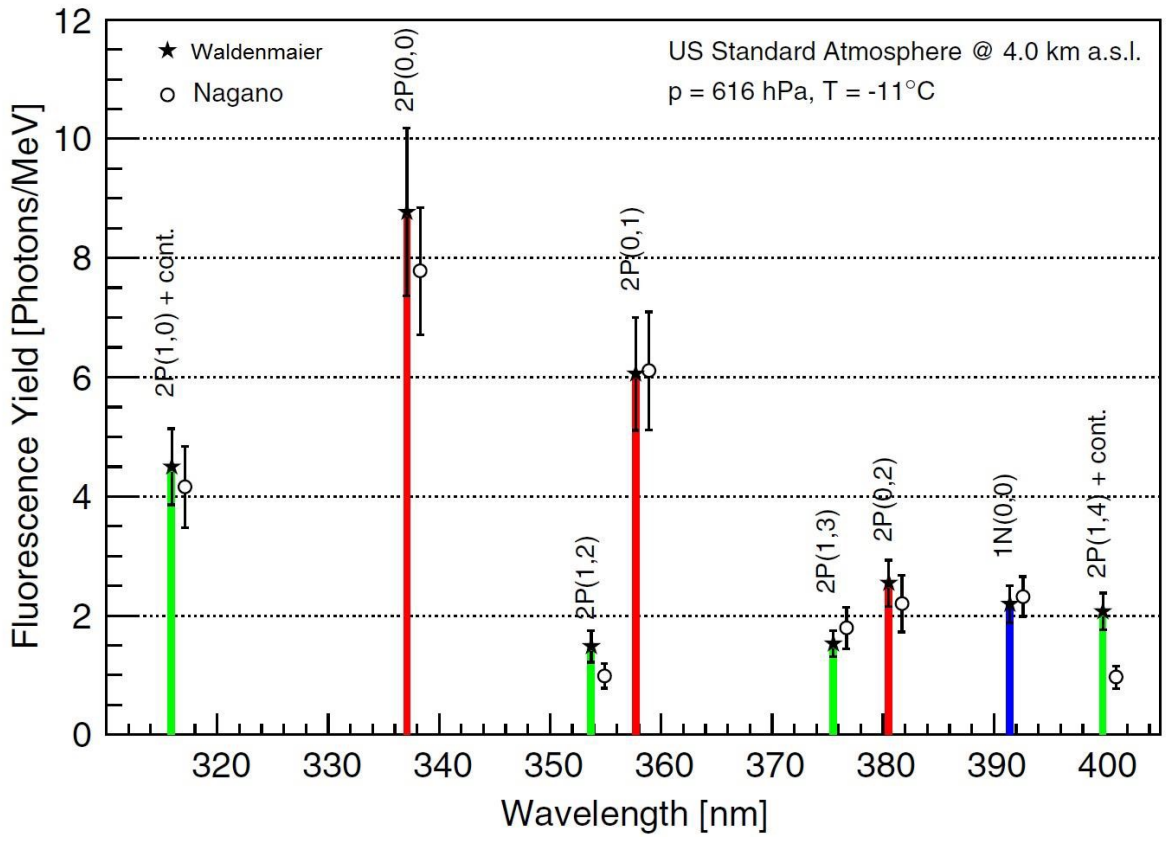


Figure 2.11: Spectrally resolved fluorescence yield of dry air induced by electrons giving an indicative total yield across the region of 29 photons/MeV. Reproduced with permission of the rights holder from: [46].

Work performed by the AIRFLY Collaboration has produced data supporting the thesis that fluorescence yield is constant across energy scales, meaning number of photons produced is proportional to the energy deposited in air [55]. Analysing individual emission spectra induced by electrons over energies between 500keV to 420MeV the study found that despite variation in the excitation cross section over this region the overall number of photons per unit energy remained largely constant. This is surprising, especially given the variation in cross section in the lower energy region of the spectrum (less than 1MeV), but this could be explained by statistical averaging effects in production of energetic secondary electrons, so called delta-rays, which in turn induce fluorescence in air [52]. The results of a number of studies with comparable methodology across various energy scales returned measurements

between 17.6 and 20.8 UV photons/MeV; these are, however, often difficult to compare due to differing methodologies, energy scales and wavelength ranges [56].

Interestingly even 337nm laser light has been shown to produce fluorescence yields of a similar order of magnitude [23].

A small body of work has emerged looking specifically at the radioluminescence induced by alpha particles in air. The first to quantitative study of the phenomenon was in 1960 shortly after the invention of the photomultiplier tube with a UV-transmitting quartz window [57], producing an estimate of 60 photons per 4.6MeV polonium-210 alpha particle. Later another study utilising UV-sensitive film[19] sought to measure the number of photons emerging from each decay, cumulatively producing an estimate of 30 photons/decay of plutonium-239 The analogue nature of the methodology means that it is difficult to assess the uncertainty in the measurement. Chichester and Watson[58] produced a further paper using a UV-sensitive CCD camera yielding an estimate of 20-200 near-UV (300-400nm) photons.

Arguably the most comprehensive experimental study of the light yield from alpha-induced radioluminescence in air was undertaken by STUK in Finland [54]. Using the Bethe formula's predictions of energy deposit, the authors quantitatively analysed photon emissions based on energy deposited over the particle's path. To achieve this the team used a mixed alpha source with plutonium-239 and lesser proportions of other plutonium isotopes and Am-241. The researchers characterised its composition using passivated implanted planar silicon (PIPS) and high purity germanium (HPGe) detectors to certainty of 3%. The source and detector were then arranged such that a small, variable gap was present between source and the PIPS detector. When radioactive decay occurred, an alpha particle traversed the air gap and lost a small proportion of its energy. The particle was then absorbed in the PIPS detector which analysed its residual energy. The amount of energy lost in air was calculated using experimental stopping power data [41] by considering the corresponding stopping power.

A low noise, UV-sensitive photomultiplier was placed planar to the source-detector set-up and was gated to the PIPS detector so that it could be activated when an alpha particle was detected. By calculating the energy loss the authors compared the probability of photon detection with the number of photons detected. This was then used to calculate the photon production rate (radioluminescence yield) which was measured to be (19±3) photons/MeV

between 300-400nm. This value is in agreement with many of the studies of electron-induced phenomena and supports the theory that fluorescence generation is largely independent of radiation type and principally dependent on the amount of energy deposit.

There were some minor limitations in the methodology. While uncertainty calculations are presented, the paper does not consider the possibility of a non-vertical alpha particle path from source to detector, which could have led to an overestimation of fluorescence yield. However, the paper represents the most comprehensive study of the emissions using alpha particles to date.

Further results were also presented for alpha, beta and gamma radionuclides in a paper by C. Thompson et al [18]. Their paper produced a model of the alpha-induced radioluminescence process in Geant4 consisting of three stages: propagation of the radiation; production of secondary electrons through ionisation; the excitation, emission and quenching of molecules in air and the emission of photons. Using their model they demonstrated that the relationship between the number of photons emitted and the energy of alpha particles was linear in the region below 5MeV, in agreement with experimental data. They found that for energy greater than 5MeV a power law (proportional to $E_{\alpha}^{0.92\pm0.01}$) more accurately modelled yield. These results were shown to agree with the experimental results presented by Sand et al [54].

In a comprehensive review paper by Crompton et al. the authors also agree that it can be asserted with some confidence that there was approximately 19 photons produced per MeV of energy deposited in air by alpha particles [59].

A number of other gases have also been studied in similar ways for their fluorescence characteristics under radiative stimulation. A pure atmosphere of nitrogen gas, for example, was found to have a fluorescence spectrum with a yield of 4x that of air due to the reduced quenching effects of oxygen [54]. Tetrafluoromethane, CF_4, while acting as a quenching agent in air has a yield of 2300 photons/MeV in a pure CF_4 atmosphere at STP [60]. Crompton et al. also found an enhanced radioluminescence yield in the UVC (180-280nm) wavelength range could be achieved by flowing gases (demonstrated with pure nitrogen, xenon, neon, krypton, P10 and argon) over an alpha emitting source. The paper showed that while enhancing the yield, the nature of the gas flow meant that results varied considerably

between experimental runs, leading to difficulty in producing quantitative measurements [61].

These papers form the basis of much of the later work presented in the thesis. From this review a number of key factors arise, most notably the need for effective collection optics and high efficiency detectors given the relatively small number of photons arising from each alpha decay, if low activity sources are to be detected.

2.4 Current radioluminescence detection devices

A wide range of detectors seeking to exploit the alpha-induced radioluminescence process have been developed, and many have been published [59]. Compared with conventional radiation detectors which rely on the direct interaction between radiation and detector, these detectors have to be specially designed to overcome the unique challenges of alpha-induced radioluminescence. These include:

- Producing a optical focussing device which either functions at a fixed distance, has a generic focus or a focussing device which adjusts the optical configuration to the subject being measured;
- The use of high sensitivity photosensor equipment, if the detection of small levels of activity is desired;
- A mechanism to reduce any background arising from other sources - e.g. sunlight, fluorescence tube lighting or beta/gamma radiation;
- Electronic systems to interpret photosensor outputs.

Given that these factors tend to vary depending on context (e.g. measurement distance or level/type of background), the majority of devices which have been produced tend to focus on operation within a particular environment [59].

Most devices developed to date fall into two categories. The first and simpler variant utilises photomultiplier tubes, exploiting their ability to quantitatively analyse photon fluxes; analysing the wavelength regions discussed earlier in this chapter these devices focus upon spectral filtering and others methods to deduce the presence of alpha-emitters by looking at the number of photons arriving at the photosensor. The devices produced by NPL[7],

STUK[8][24], the Australian Department of Defence [9], Oak Ridge National Laboratory [62], Crompton et al [25] [61] and Bubble Technology Industries [10] all fall into this category. These devices benefit from their ability to output quantitative data like count rates with high precision. A wide variety of photosensors of this type are in production, meaning considerations such as the distance from source to detector, desired photomultiplier quantum efficiency and operating environment can be used to optimise performance. These devices tend to be limited by their quantum efficiency in the UV region (typically less than 20% for 300-400nm or considerably less under 300nm [25]), dark count rate and difficulty localising sources. These factors mean that these detectors often incorporate other modular systems, such as distance sensors and light focussing optical assemblies to overcome them.

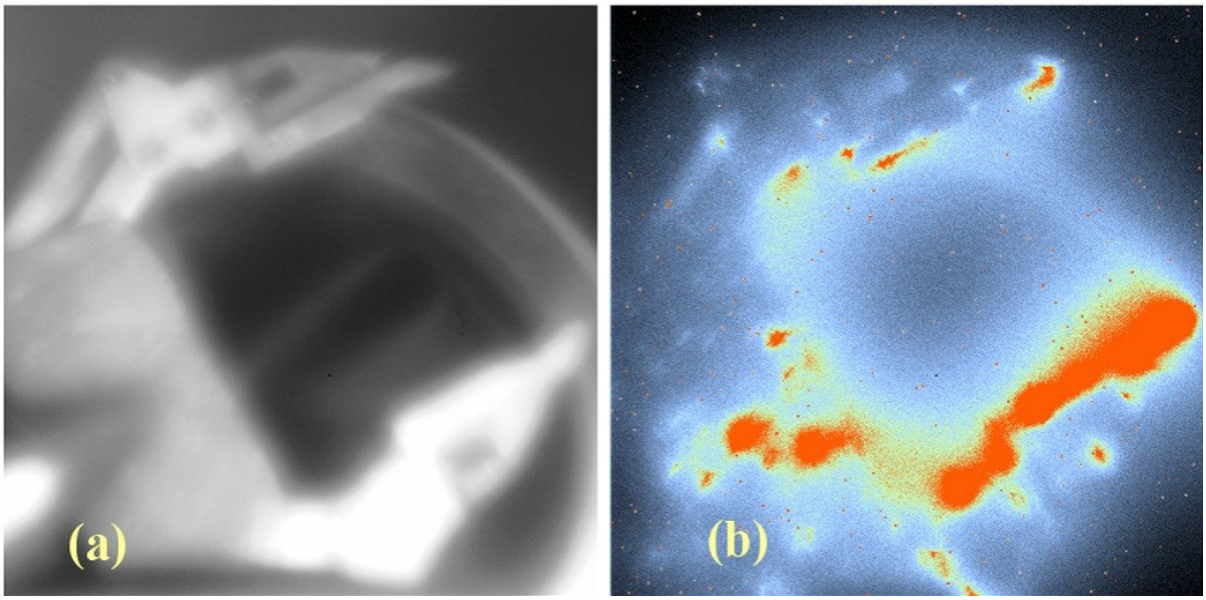


Figure 2.12: (a) Real image of a telemanipulator gripper in a nuclear facility produced using a normal camera. (b) As for (a) with the 'alpha image', obtained using a UV-sensitive CCD camera exposed for 5 minutes, overlaid to expose relative degrees of contamination on the grip. This image demonstrates the usefulness of the technique for decontamination operations; from this image it is possible to clean appropriately the contaminated region and once complete obtain another image to verify the result of decontamination. Reproduced with permission of the rights holder from [4]. © 2005, IEEE.

The second category of device produces ’images’ of radiological contamination using UV-sensitive CCD cameras of different types. Images are produced in the same way as normal cameras except that the light obtained originates from the fluorescence produced by radioactive energy. These devices use similar principles to PMT-based approaches, in focussing and detecting the photon flux produced in radioluminescence. However as CCDs tend not to be used to measure the number of photons incident on the sensor, and rather the relative intensity, producing quantitative measurements using these devices can be difficult. As shown in 2.12 the outputs of these devices are impressive and highly intuitive in an operational environment. Devices in this category have been produced by CEA[4][63][64], Idaho National Laboratory[58][11], the Kurchatov Institute[20][66], STUK [67, 26]and even applied to in and ex vivo imaging in a medical context[68][44].

While the case for such devices in a forensic or medical context is compelling, in decommissioning, and particularly in differentiation and characterisation of waste, the applicability of this technique is limited. Unless using prohibitively expensive EM-CCD systems, which are capable of producing quantitative count rates, then only the relative degree of contamination can be identified as photon signals are accumulated over a period, meaning estimates of activity are difficult to establish; furthermore all such systems so far rely on complete darkness and long acquisition periods due to the small nature of the signal and relative insensitivity of CCDs.

Photomultiplier tubes are effective in producing quantitative, analysable data from low intensity light sources. Photomultiplier tubes operate by the use of a photosensitive cathode which, after being impacted by a photon of an appropriate wavelength, ejects a photoelectron. This photoelectron is then drawn to and accelerated toward a series of increasingly positively charged anodes. Once a photoelectron collides with an anode, an avalanche effect occurs, amplifying the individual electron by liberating many further electrons from the anode itself. These are then attracted to the next anode in a similar process, and this is repeated until the final anode. At the final anode these electrons collectively form a pulse of charge with time characteristics corresponding to the geometry of the anodes. This accumulation of charge forms a current which once arriving at a resistor forms a considerably larger electrical potential - this is then analysed by subsequent electronics. Photomultiplier tubes, when operating in photon counting mode can be used to analyse the timing of photon absorption at

the cathode (with a small delay, ‘transit time’). Contemporary electronic systems allow the output of from photomultiplier tubes to be analysed in terms of the overall number of photoelectrons generated or the corresponding time stamp of arrival on a nanosecond scale.

Photomultipliers can be operated in several ways, mainly dictated by their gain and output electronics, but the two most prominent in this field are analogue and Geiger mode.

Analogue mode is a simpler technique used for high light environments with consistent intensity - the charge output by the photomultiplier is integrated across a transimpedence amplifier and quantified by an analogue to digital meter. The potential accumulated in the capacitor corresponds to the photon flux output from the photomultiplier tube in that period.

Photon counting (so called ‘Geiger mode’) is a digitalisation process in which each output from the photomultiplier tube is recorded with a corresponding timestamp. This is usually achieved by a system operating with a very high sampling rate which analyses the voltage at the photomultiplier tube’s anode compared to a threshold level. If the threshold is exceeded then a pulse is recorded with a timestamp. These individual records can then be analysed to extract count rates over time.

A number of limitations exist in photomultiplier operation; here I will focus on those most relevant to the temporal analysis of single photon counting.

- First, given the electronic properties of the photocathode, a frequent problem with photomultiplier tubes (especially when operating at high gain) is the tendency for electrons to be liberated at the cathode without a corresponding photon. These so called dark counts do not correspond to photons, so must be factored into any analysis of data produced by the system. By measuring the anode when the photocathode is not exposed to any light source it is possible to calculate the characteristic dark count rate for a particular photomultiplier tube, and it is possible to purchase items specifically designed for their low dark count rates.
- Secondly if exposed to a light source which is of strength greater than the manufactured limit then the intensity of electronic discharge through the photomultiplier tube can cause irreversible damage, potentially leading to higher dark count rates or complete malfunction. This problem is prevented by the use of a

feedback circuit between the controller and the photomultiplier tube which adjusts the gain level according to the light intensity: in high intensity environments the photomultiplier will then operate at a lower gain and vice versa.

- Thirdly, the electronics required to interpret the output of photomultipliers, especially in photon counting mode, is often complex and can be the significant expense associated with such systems.

While these limitations cause difficulty, effectively designed systems can overcome them and have resultantly produced the lowest detection limits[26], smallest integration periods required for detection (1kBq in 1 second [24]), largest source-to-detector distance measurement [12] (888kBq at 500 meters and 14.8GBq at over 1km [69]) and the ability to measure in the presence of other light sources [7][8] (typically sodium lamps or LEDs with nominal UV output). Photomultiplier-based detectors have even been shown to have low enough detection limits to detect concentrations of radon gas [70].

A review by Crompton et al [59] assessed a wide range of the devices which had been produced. They concluded that although many devices had been developed, the widely varying styles of presentation of results and methodologies employed made it difficult to fully assess progress which had been made. They recommended that a more systematic testing regime - looking only at the variation of a single variable, rather than several - would make comparison between devices simpler.

The ubiquitous presence of light in same wavelength regions from other sources, such as sunlight or fluorescence tube lighting, is arguably the biggest difficulty in exploitation of alpha-induced radioluminescence detection. Mechanisms for the reduction of or identification of background light sources are typically the major differentiator of devices. The most common mechanism, used most devices (even those operating in complete darkness), is the use of spectral filters. Such filters are typically transparent to wavelengths which exist in the fluorescence emission spectrum of air but opaque to visible and infrared wavelengths. One variation between devices is the specific wavelength range which is targeted: STUK for example utilise filters between the wavelengths of 280-340nm, targeting the segment of the near-UV wavelength range with the lowest background from other light sources while still including the most intense peaks at 337nm and 311-315nm [24]. Others[4] have used wide

bandpass filters from around 280-400nm or choose detectors which are insensitive to other ranges [20].

Some devices have attempted to detect alpha-emitting radioluminescence at wavelengths shorter than the near-UV region to reduce the presence of background. Crompton et al trialled a Hamamatsu UV TRON sensor, sensitive to UV-C wavelengths between 185-260nm, to detect a 6.95MBq source at 2cm distance in normal laboratory conditions [25]. However, later results showed that despite a promising reduction in background, observed at $(2.224 \pm 0.7)\cdot 10^{-3}$cps, the UV TRON was susceptible to interference from beta and gamma radiation [61] which limits its potential for use in a decommissioning environment. The significantly reduced radioluminescence yield and detection efficiency within this wavelength range, however, mean that detection is confined only to the most intense alpha sources at short distance.

The use of bandpass filters specific to the transition wavelengths offers more sophisticated mechanisms for background reduction. STUK [24] utilised this in their experimental set-up by combining the use of two photomultiplier tubes. This device (see figure 2.13) analyses a broad fluorescence spectrum (300-340nm) at one photomultiplier and an indicative background, not originating from alpha-induced fluorescence, between 298-303nm at the second photomultiplier tube (PMT2). Results from the device demonstrated the identification of a 1.2kBq point source (surface emission rate: $620s^{-1}$) at 40cm with one second integration time. Performance of the device could also be further enhanced by the use of more sensitive photomutlipliers, a larger photon collection aperture and performing measurements at a shorter distance from the source.

Another method to identify background signals is to use two gated photomultiplier tubes to analyse photos emitted from the same individual alpha decay. Using the figure presented earlier that (19±3)photons/MeV [54] are emitted in the near-UV (300-400nm) region, if all energy from an Am-241 decay is deposited (5.49MeV) in air the expected number of fluorescence photons per decay is 104. This means that if the source-detector distance is short then multiple photons from the same decay may reach the detector. This is useful as the photons originating from a single radioactive decay will all arrive in a short temporal window. This means individual radioactive decays will lead to a time distribution of photon emission, depending on at which point the nitrogen molecule is excited (at the beginning or

the end of de-excitation) and a randomly occurring fluorescence process as described by equation 2.12. This mechanism was explored by an experiment using two photomultiplier tubes arranged using a beam splitter and a single lens: the photomultipliers were connected to a time correlated single photon counting unit which, once one photomultiplier produced an electronic pulse, timed the duration until the other photomultiplier was activated. Once a radioactive decay had occurred, and fluorescence photons had been emitted, two or more photons from the same decay may reach the photomultipliers, thus giving an indicative delay. This was cumulated over many decays (100s of a 13kBq Am-241 source) without optical filtration and the results are displayed in figure 2.14.

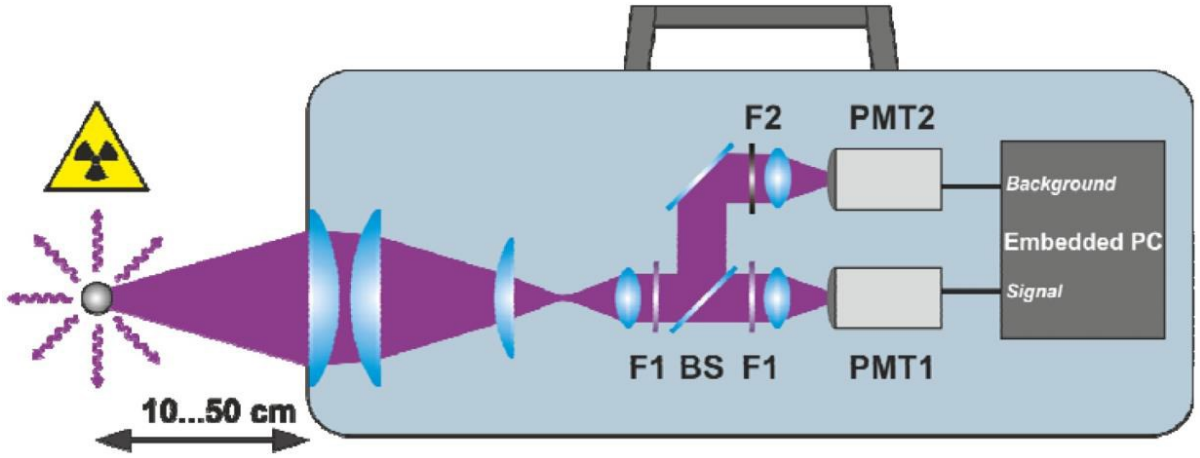


Figure 2.13: A schematic of the HUAVA device produced by STUK. Through a series of lenses the optical signal is collimated, first passes a 300-340nm bandpass filter and then reaches a beam splitter (BS) which divides the signal into two. From here at F1 and F2 the signals are filtered at different optical wavelengths. F1, the same as the previous filter, allows transmission of wavelengths between 300-340nm while F2 passes 298-303nm. This means at PMT1 photons between 300-340nm are present while at PMT2 only photons of wavelengths of approximately 298-303nm pass. This means that an effective background, not corresponding to nitrogen fluorescence signal and instead from background, can be accumulated at F2 while fluorescence photons are counted at PMT1. This allows the device to subtract the background from the actual signal and gain a more accurate indication of photon flux from fluorescence. Reproduced with permission from [24]. © IAEA, 2010.

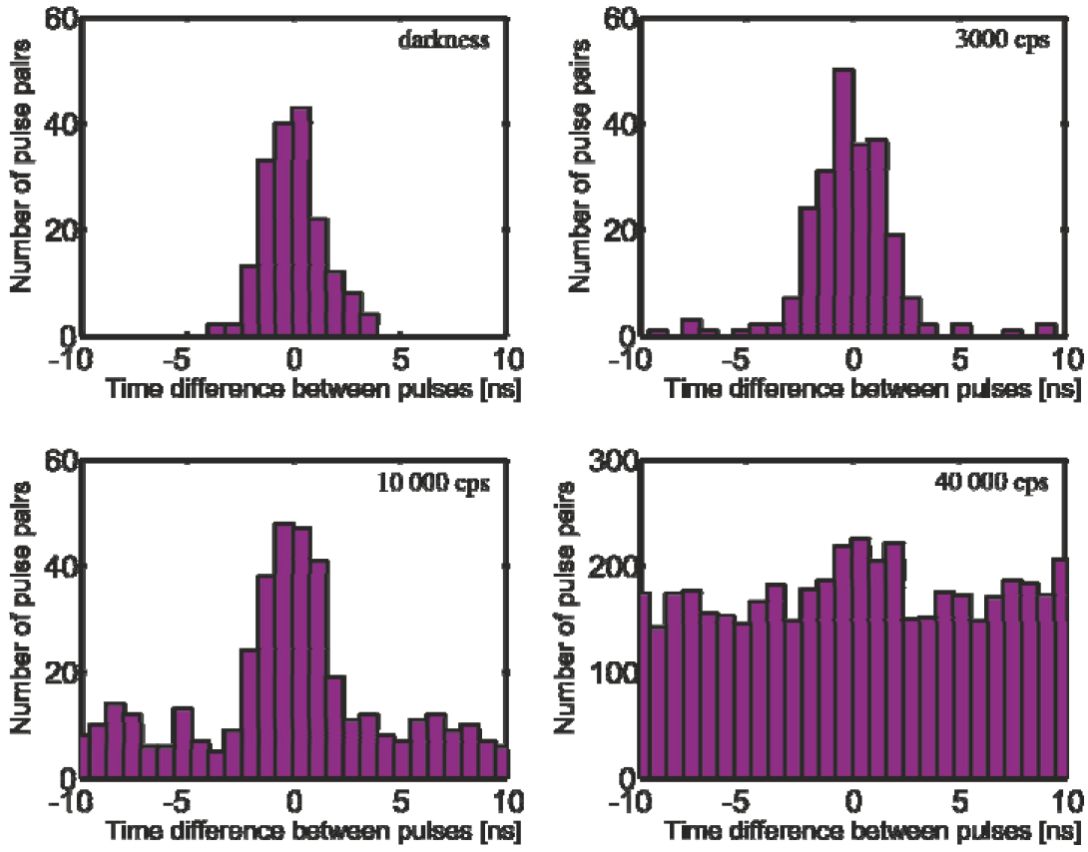


Figure 2.14: Coincidence measurements between two photomultipliers connected by a time correlated single photon counting (TCSPC) unit to analyse the delay between two photon pulses. Measurements were performed for a 13kBq Am-241 source at 20cm over a period of 100s with varying levels of background signal reaching the detectors (inset, upper right). The results demonstrate that half of the photons per decay (FWHM) are emitted in a period of 3.75ns. This property is explored more fully in chapter 3 through numerical simulation. Reproduced with permission from [24]. © IAEA, 2010.

Very little work to date has explored the ability of this technique to produce measurements which lead to quantitative measurements of the amount of activity present versus reference standards. This can primarily be explained by the focus of many teams being on forensic and safeguards applications of the detection method which do not necessarily require information on the activity of a sample and instead only whether it is *alpha-emitting or not.* This absence is one of the key areas which this thesis later seeks to address. Such measurements would be highly valuable in nuclear safeguards (e.g. quantifying holdup in

nuclear reprocessing facilities and reducing uncertainty budgets associated with reprocessing) and decommissioning (e.g. to understand the extent of contamination to reduce risk to operators).

An interesting area explored by a few developers hoping to produce devices capable of operation in outdoor conditions [9][20][25][26][61], influenced more heavily by consideration of the UV spectrum reaching earth from sunlight, is the use of an extended fluorescence spectrum including the solar blind region. The solar spectrum of photon emissions reaching earth reduce considerably below the 280nm range due to absorption by the earth's atmosphere.[9] As such the proposal presented by these groups is to analyse the 0.08 photons/MeV emitted in the solar blind region as background levels are considerably reduced.[9] However, the number of photons produced at these wavelengths and the low quantum efficiency of most detectors operating at those wavelengths mean that only extremely high activity sources at moderate distances could be detected.

Work performed using several imaging devices[22][26][63][67] has demonstrated a useful property of the technique: the ability to measure alpha-emitting materials remotely through UV-transmitting materials. Performing measurements through a number of industry-standard materials for containment and exclusion (primarily in glove boxes) they proved that Triplex, Polycarbonate and Plexiglass had a 90% transmission of the UV-fluorescence signal compared to air for a 1mm thick sample. Measurements have thus been performed in their analysis through the transparent containment walls of glove boxes, highlighting regions of contamination similarly to that displayed in figure 2.12. This has also been demonstrated in a variety of field environments. For the purposes of quantitative measurements of activity it is worth noting that any calibration would have to be performed using the specific material through which radionuclides are being measured, to ensure validity of the calibration to the measurement environment.

A number of interesting variations on the conventional alpha-induced radioluminescence method have also been developed. STUK for example has developed a technique utilising the fluorescence signal of alpha decays to produce new mechanisms for the analysis of alpha radionuclides with coincident gamma emission such as plutonium-239 and -240 [65][71][72][73]. Measurements of many of these isotopes is difficult as spectra can be

composed of many overlapping emissions from different isotopes. Gamma emissions, unlike alphas, penetrate from within a sample so emissions from below-surface level also influence spectra, meaning analysis of a particular region of a sample is difficult. To overcome this the team developed a gating technique where a photomultiplier tube measures fluorescence emissions and once stimulated this generates a microsecond gate at the data acquisition unit. Once gated by fluorescence, a HPGe gamma scintillation detector is activated to detect any coincident gamma-rays. This allows a small region of a surface to be analysed specifically as all other gamma-emissions are disregarded, meaning only those with an accompanying fluorescence signal are analysed. This technique very significantly reduces the time required to acquire equivalent minimum detectable activity (*MDA*) - an *MDA* of 3.8Bq for their detector under normal operation takes 40 hours of measurement while with the fluorescence gating method this can be achieved in just 4 hours, even with backgrounds from other gamma-emitters.[72]

The major advantage of this technique is the simultaneous deduction of activity levels and isotopic information derived from the gamma-spectrum of the emitter. The scalability of this technique to remote detection is yet to be proven and may be difficult due to the small solid angle occupied by both photomultiplier and scintillation detector. It does however have good prospects for decommissioning, forensics and safeguards in providing swift analysis of a sample's isotopic composition.

The final category of work in this field is the application of laser interrogation technologies to the remote detection of radioactive materials. This field is of a lesser relevance to the proposed research as it is mainly envisaged as a mechanism for very long range detection and also has a number of significant drawbacks.

After the passage of alpha particles through air, causing excitation and ionisation, a range of molecular energy states are present in the particle's wake. A new method focusses on the ability to use lasers to interrogate these molecular energy states. Detection of these higher energy states could be achieved in two ways. Firstly, by analysing the attenuation of laser beams passing through the ionised/excited region around an alpha emitter and comparing to their normal state [23]. This was demonstrated by using the 337nm transition of the nitrogen molecule; a 337nm laser beam was passed over a source of radioactivity and molecules which were in the $B^3\Pi_g$ state (see figure 2.10) were shown to absorb 337nm photons, placing them

in the $C^3\Pi_u$ state. As a result, the laser beam was attenuated by the various nitrogen molecules which absorbed the laser light and this was measured using a spectrometer. This was demonstrated experimentally but with very large sources of 1.48GBq and 2.96GBq (40 and 80mCi). These two sources produced a 20% and 40% attenuation of laser signal intensity respectively when compared to measurements not in the presence of the radioactive sources. This suggests there is some possibility that a source's activity might be calculable from the level of attenuation of the laser. A major drawback of this technique is that the laser and the detector must be placed in direct view of one another. This means that unless scanning a flat surface with access available to either side, detection in-situ would be problematic.

An alternative mechanism based on the same scenario would be to detect the subsequent re-emission of photons after the excited $B^3\Pi_g$ relaxes back to $C^3\Pi_u$, with the resulting emission of a photon at 337nm. These stimulated emissions would then be radiated randomly after the corresponding decay period (2.5ns on average [23]) - meaning a timed gate could be established between a pulsed laser and photomultiplier.

The alternative laser-based method, which has yet to be proven experimentally with radioactive sources, considers the effects of the greatly increased numbers of free electrons existing in proximity to radioactive emitters and thus the reduced laser energy density required to induce electromagnetic breakdown of air [74][75][76][77][78]. Electromagnetic breakdown and the formation of plasma is achieved more readily in gases with elevated numbers of free electrons: energy from the laser is transferred to these electrons, which in turn produce ionisation of other molecules, leading to a cascade of ionisation which results in electromagnetic breakdown. While the principle seems scalable and interesting, little work has produced results suggesting its validity beyond high activity forensic applications.

Alpha-induced radioluminescence detection has produced some interesting results to date, but there remain several issues preventing wider use of the technique in the nuclear industry and in nuclear decommissioning specifically. While many teams have produced devices capable of demonstrably detecting alpha-emitting radionuclides, there remains little work which has focused on the exploitation of the technique for the quantitative measurement of alpha-emitters by comparison to sources of known activity. Likewise few devices have

succeeded in operating in practical industrial environments (e.g. in daylight or ambient light conditions).

Through this review of the literature in the field of alpha-induced radioluminescence detection several core gaps have been identified:

- The absence of established methods of operation - both in methodological and practical terms - mean that the comparison of device performance is not possible.

- Few studies have attempted to relate measurements performed using the technique to the established methods for radiometric analysis. This has led to an absence of comprehensive data concerning detection limits and the minimum detectable activity, which will significantly inhibit application of the technique in an operational context.

- No work to date has sought to update, apply and modify methods established in ISOs for the measurement of alpha-emitting materials for use with alpha-induced radioluminescence detection.

- No identified studies have attempted to look at how device performance in different contexts could be generalised, and as such attempts to bring together detectors with other modular systems - such as conveyors, 3D measurement devices or distance metres - have been limited. This means that simple parameters - such as device sensitivity over different distances - have not been assessed.

- Most literature focusses on the three established modes of operation - a source being placed immediately in front of the detector, imaging a scene (both via optical focussing and “scanning” a photon counting device) and surveying a region using a photon counting device. None has attempted a “conveyor” style measurement as discussed in the introduction.

- No open literature has sought to use the technique to measure the activity of radioactive sources or samples of unknown activity. This could be achieved with reference to a device calibration measured using a traceable, calibrated standard

source.

- To my knowledge nobody has considered a method to produce such a calibration in realistic measurement scenarios – e.g. at various measurement distances or measured using different modes of measurement (scanning vs static).

- Considerations of measurement uncertainty and error in existing studies have been limited.

- Little work has focussed on the unique geometries resulting from the corona surrounding the alpha-emitting source and its impact on the characteristics of detection using the radioluminescence method.

This thesis seeks to address several of the core gaps identified in this chapter. Specifically those relating to the absence of methods of calibration, methods for the quantitative assessment of performance and use of international standard sources to assess detector performance. The next chapter seeks to address the final gap through consideration of the geometrical properties of detection using the radioluminescence method.

Chapter 3
Simulated Emission and Detection Characteristics

The spatial distribution of energy resulting from alpha decay around a source means that radioluminescence detection has the potential to exhibit distinct characteristics compared to conventional detection techniques. Around each source, alpha particles are emitted into some portion of a spherical region, with each source depositing energy into a coronal region described by the Bethe formula as described in section 2.2 of the previous chapter. This energy deposit subsequently results in the emission of photons, some proportion of which may be detected. These characteristics, and the relationship between the spatial distribution of energy from radioluminescence and the detection of photons in ideal conditions, will be explored in this chapter.

Considering the physics underpinning the spatial distribution of energy in alpha decay a model has been constructed for the emission of photons using finite difference and Monte Carlo methods. This has been used to explore various emission characteristics including the expected time between alpha particle emission and emission of 337nm photons.

Using this model as a basis for the physics governing photon emission along the path of alpha emission, the detection characteristics of a square faced detector is also considered for a 2D emission geometry. This geometry is combined with the emission model to produce a calculation of peak efficiency for detectors of various diameters. The characteristics of photon intensity over source-to-detector distance in this scenario are considered for detectors of various sizes.

These characteristics have been considered in the context of the design of the detector used later in the project and underpin a number of the proposals presented in the next chapter concerning the design of radioluminescence detectors.

3.1 Modelling photon emission processes

3.1.1 Modelling Energy Deposit in Space: Bethe Formula

Chapter 2 provided a theoretical basis upon which the numerical simulation of alpha-induced fluorescence can be considered. Most previous work presented in this field has considered alpha emitters as point sources of light [8][11] which radiate isotropically.

A notable exception is the paper presented by Thompson et al [18] which used a Geant4 framework to analyse photon emission processes. Their paper showed that on the contrary, the photons emitted by alpha radioluminescence are spread across a region of space depending on the type of radioactive decay which has occurred. For alpha decays, the dominant physical process governing this deposit was discussed in the previous chapter in relation to the Bethe formula, over an area of space depending on the source geometry. Models considering alpha sources as point light sources would be valid only in the approximation of large distance, with the distance between emitter and detector, R being far greater than the length of the alpha particle's path. Detection geometry and emission timing characteristics were also not considered in previous models.

This work focusses on detection characteristics in the region close to the source (under 1m) in which the assumption of large distance is not valid. For detection in this region these differences are significant and would considerably affect the performance of any detector seeking to make quantitative measurements. Through simulation data can be used to consider the effectiveness of various system designs. Other characteristics, such as the likelihood of detecting multiple photons from the same decay, can also be considered to give an indication of detector performance for different setups.

Numerical simulation is a useful tool in overcoming many of the factors discussed above and as such work proceeded in this direction before moving onto experimental, in-field detection of alpha-induced radioluminescence.

For the purposes of this work which seeks to produce an estimate of the emission characteristics of the source corona will be considered to be described by the Bethe formula, while noting the limitations described in the previous chapter. This has been reproduced here for clarity:

$$-\frac{dE}{dx} = \left(\frac{ze^2}{4\pi\epsilon_0}\right)^2 \frac{4\pi Z\rho N_A}{Am_e v^2}\left[\ln\left(\frac{2m_e v^2}{I}\right)\right] \tag{3.1}$$

Equation 3.1 can be evaluated over a range of values ranging from the initial alpha particle energy at emission, E_{decay}, and its rest energy, E_0. For the purposes of this study the initial energy being considered has been approximated across all decays at 5.500MeV, corresponding roughly to the major emission of americium-241 at 5.49MeV - this simplification means that all work presented corresponds to this decay energy and its corresponding energy deposit profile in air only. The results presented here, however, will scale linearly with initial energy as photon emission rate is assumed to be proportional to energy deposit.

In the process of de-energisation between E_{decay} and E_0 the energy of the alpha particle loses energy in collision with molecules and atoms in air; this process is by definition discrete, with every collision resulting in a small, individual loss of energy, $-dE$. The Bethe formula is thus an approximation: energy loss is assumed to be a continuous process described by the above differential equation. In this analysis the energy loss between elements is considered to be fixed, $-\delta E$, and this is defined to be 1keV. The alpha particle in this model thus assumes the discrete set of energy values:

$$E_\alpha = \{E_{decay}, E_{decay} - 1keV, E_{decay} - 2keV, \ldots, E_0\} \tag{3.2}$$

Given that the velocity of the alpha particle is related to its energy, v may be calculated at every point in this discrete set on the particle's path. This calculation is by the classical kinetic energy formula, $v = \sqrt{\frac{2E}{m_\alpha}}$, because as discussed earlier relativistic effects can be neglected at alpha particle velocities of relevant energy. As such, the stopping power can be found at a particular E by substituting v with this factor in equation 3.1. As such this becomes a function of only E_α of the form: $\frac{dE}{dx} = \frac{dE\ (E_\alpha)}{dx}$.

It is possible to establish a discrete set of values for the stopping power at alpha energies within the set, E_α, as:

$$-\frac{dE}{dx}(E_\alpha) = \left\{-\frac{dE}{dx}(E_{decay}), -\frac{dE}{dx}(E_{decay} - 1keV), ..., -\frac{dE}{dx}(E_0)\right\} \quad (3.3)$$

Resultantly the energy loss between elements of the discrete set, δE, can be defined as equal to 1keV. As such the corresponding change in position, δx can be found at every point in this set in the assumption that $\frac{dE}{dx}$varies nominally in the interval [E_α,E_α - δE]. This defines the set of values of δx as given by:

$$\delta x = \delta E \left[\frac{dE}{dx}(E_\alpha)\right]^{-1} \quad (3.4)$$

The limit of validity for the Bethe formula has been experimentally determined for alpha particles in air as (178 ± 0.5)keV, at which point the Bethe formula's approximation fails with stopping power assuming negative values at energies less than this value. Even in its unmodified form, however, the Bethe formula still has strong predictive power for values such as range and stopping power of alpha particles if the lower limit is applied.

δx, as described by equation 3.4, can be used to give an estimation of the overall range of an alpha particle's range by the summation of the component steps in position at the energies within E_α. This can be represented in terms of the particle's range, R_α, by the expression:

$$R_\alpha = \sum_{E_{decay}}^{E_0} \delta x(E_\alpha) = \sum_{E_{decay}}^{E_0} \delta E \left[\frac{dE}{dx}(E_\alpha)\right]^{-1} \quad (3.5)$$

For a comparison of data produced by this methodology and alternative data see table 3.1, showing that the method is accurate to within approximately 0.3mm of estimates by SRIM.

Additionally it is possible to analyse the stopping power, $\frac{dE}{dx}$, over the full length of the alpha particle's path by calculating each element in the set of values of E_α. This process exposes the so called Bragg peak discussed in the earlier sections of this report: an important consequence demonstrating that energy deposit is non-linear and is mostly skewed to the

latter regions of the alpha particle's path. The results of this, derived from the analysis displayed above, was presented in the previous chapter.

E_α (MeV)	R_α, SRIM (cm)	R_α, Simulation (cm)
5.5	4.080	4.081
5.0	3.531	3.564
4.5	3.020	3.032
4.0	2.545	2.538
3.5	2.109	2.086

Table 3.1: Comparison of alpha particle ranges over different energies predicted by Stopping Range of Ions in Matter (SRIM) [39] and the numerical method presented in this chapter (equation 3.5) at air density of 1.225kgm^{-3}. Results demonstrate that the Bethe formula provides accurate data to uncertainty of approximately 0.3mm.

3.1.2 Modelling Energy Deposit in Time: Temporal Bethe Formula

A novel result presented here is the temporal profile of alpha energy deposits described by the Bethe formula. This is a useful finding as it can be used to inform the gating period of measurements such as those presented in the paper by J Sand et al[24]. Such gated measurements can increase a system's ability to identify and distinguish background from other light sources.

In a similar manner to the creation of the set of values of stopping power, $\frac{dE}{dx}(E_\alpha)$, it is possible to find the velocity of the particle in each of the states within the set of energy values E_α. Considering the classical formula for the kinetic energy of an object:

$$v(E_\alpha) = \frac{dx}{dt}(E_\alpha) = \sqrt{\frac{2E_\alpha}{m_\alpha}} = \sqrt{\frac{2}{m_\alpha}\{E_{decay}, E_{decay} - 1keV, ..., E_0\}} \quad (3.6)$$

It is possible to see that *dt*, the infinitesimal time interval over which the energy of the alpha particle reduces, is related to the particle's velocity and the small position interval, *dx*. Given that over this interval the particle's velocity varies from an initial to final value as the particle decelerates, assuming that the velocity change is symmetric across dx, it is possible to calculate a finite time period over which the particle moves over the space *δx* by the average value between the initial and the final velocity:

$$\delta t = \frac{\delta x(E_\alpha)}{\frac{1}{2}(v(E_{\alpha,i}) + v(E_{\alpha,f}))} \quad (3.7)$$

Where *δx* is drawn from the corresponding value of E_α in the set described by equation 3.4. From this, using the fixed energy interval, *δE*, used across the range of values E_α, dividing *δE* by *δt* gives an indicative temporal stopping power, $\frac{dE}{dt}$:

$$\frac{\delta E}{\delta t} = \frac{dE}{dx}\left[\frac{1}{2}(v(E_{\alpha,i}) + v(E_{\alpha,f}))\right]^{-1} \quad (3.8)$$

By the same process of summation over the set of values, an indicative temporal dimension can be constructed from the component values of *δt*:

$$t(E_\alpha) = \sum_{E_{decay}}^{E_\alpha} \delta t(E_\alpha) \quad (3.9)$$

Thus by pairing corresponding values of $\frac{\delta E}{\delta t}(E_\alpha)$ and $t(E_\alpha)$ it is possible to establish an approximation of the distribution of energy over time for the alpha particle (see figure 3.1).

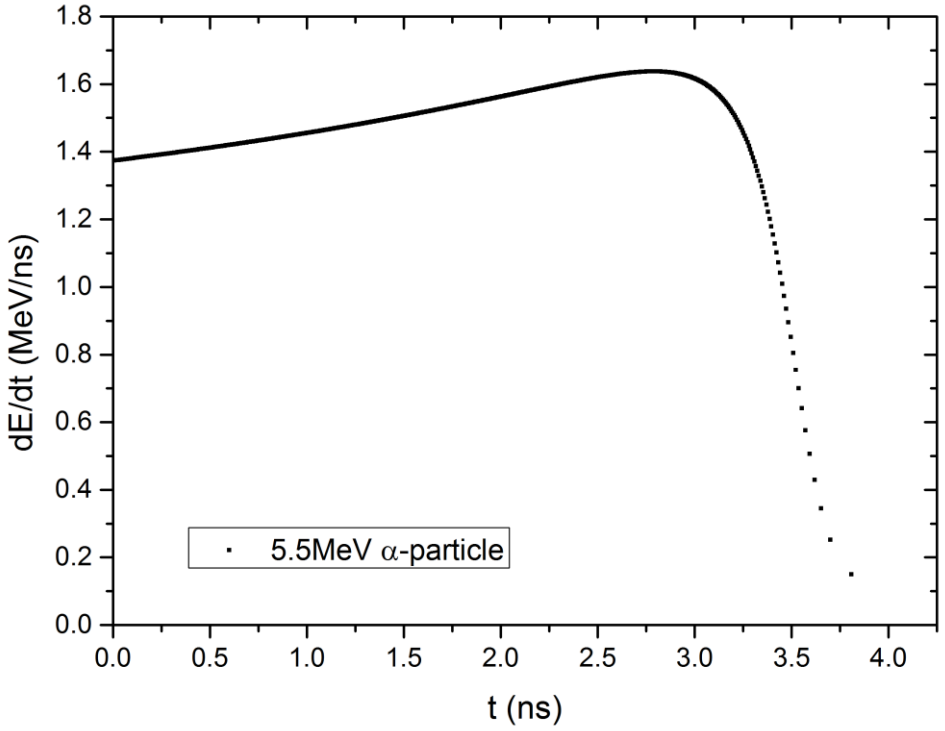


Figure 3.1: Rate of energy loss per unit time, $\frac{dE}{dt}$, of a 5.5MeV alpha particle traversing air of density 1.225kgm^{-3} over time, t. This distribution demonstrates the lack of an effective 'Bragg Peak' in the temporal domain compared to the spatial profile.

As shown, the time taken for the particle to slow is in the region of 3.5ns. This is convenient for detector systems seeking to use gating as this establishes a sufficiently short gating window to be effective in reducing background while not being so small that detectors are unable to perform.

The next step to consider is the generation of photons themselves, the focus of the next section.

3.1.3 Photon Emission Events

Within the numerical model outlined above we have access only to the energy deposit profile of an alpha decay. To expand this model to incorporate the statistical processes of photon emission and detection characteristics on the basis of the profiles discussed previously additional factors need to be added.

The first of these characteristics is to construct a stochastic photon emission process. This process follows from the model outlined above as each discrete element within E_α can be regarded as a distinct statistical event, each with an associated probability of photon emission.

In the assumption that the loss of energy by an alpha particle is proportional to the number of photons generated in that area, as discussed in the literature review, this means that the probability of photon emission is related to dE, energy loss between elements of E_α. Given the expectation value of number of photons per alpha particle emitted, $E(N_\gamma)$ = (19±3)photons / MeV , it is possible to establish an expectation value in each segment per alpha decay. This is achieved first by the normalisation of the elements within E_α:

$$\eta_\alpha = \sum_{E_{decay}}^{E_0} dE(E_\alpha) \tag{3.10}$$

where η_α is the sum of the energy steps between E_{decay} and E_0. Resultantly the normalised probability of photon emission, P_γ, of elements within the set E_α is given by:

$$P_\gamma(E_\alpha) = \frac{dE(E_\alpha)}{\eta_\alpha} \tag{3.11}$$

In the model dE is set as a constant across every element within E_α at 1keV , so P_γ is fixed depending only on the number of elements within E_α.

In order to establish whether or not a photon is emitted within a particular δE, a linear random variable, X, is used where $0 \leq X \leq 1$. This variable is itself normalised by the

expected number of photons, $E(N_\gamma)$, meaning an expectation value over all elements of E_α of $19 photons/MeV$. This can be written in terms of E_α as:

$$\gamma(E_\alpha) = \begin{cases} 1 & \frac{X}{E(N_\gamma)} < P_\gamma(E_\alpha) \\ 0 & \frac{X}{E(N_\gamma)} > P_\gamma(E_\alpha) \end{cases} \tag{3.12}$$

Thus if $\gamma(E_\alpha)$ is equal to 1 then a photon is emitted in the particular element of E_α, otherwise when equal to 0, no photon is recorded as emitted within that element.

This photon emission model allows the creation, from the various sets of values allocated and discussed earlier ($v(E_\alpha),x(E_\alpha),t(E_\alpha)$), of a full geometric model of photon emissions in both time and space. Additionally properties relating to the photons generated, such as their trajectory in spherical coordinates, positional and temporal origin, can be constructed to give a holistic view of the photon generation from alpha decay. See table 3.2 for a list of variables incorporated into the model, generated for each photon.

Variable	Description	Unit
$x(E_\alpha)$	Positional coordinate of the photon emission event.	cm
$t(E_\alpha)$	Time of excitation relative to the time of decay.	ns
t_{exp}	Time from the excitation event to the emission of a photon, as described by the exponential decay law.	ns
θ	Azimuthal angle of the emitted photon.	rad
ϕ	Polar angle of the emitted photon.	rad

Table 3.2: Variables generated upon the generation of a photon by this numerical simulation; from this data the detection-side geometries can be introduced, thus offering the possibility to quantitatively evaluate the number of photons detected in various scenarios.

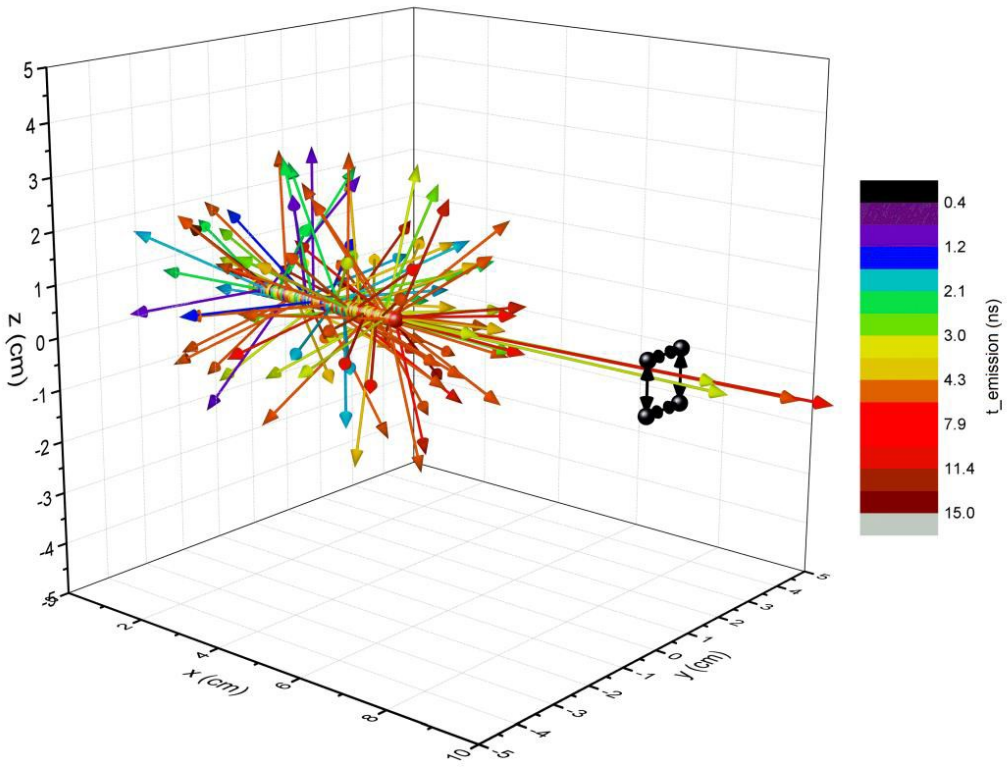


Figure 3.2: Visual representation of the photons emitted from an alpha particle; factoring all considerations discussed above this gives the spatio-temporal profile of alpha decay. Additionally shown is a schematic detector (black) demonstrating the power of this numerical technique. Not only can photon profiles be generated but also detection characteristics, including time, space and coincidence considerations. Photons reaching the detection region have been elongated for emphasis.

The final consideration incorporated into the model is the time delay between the excitation of nitrogen and the subsequent emission of a fluorescence photon. This was discussed in the literature review, concluding that the de-excitation of molecules follows an exponential decay law similarly to radioactive decay. To integrate this into the model, the exponential decay law is rearranged with logarithms to the form:

$$t_{exp} = \frac{\ln(N_0) - \ln(N(t))}{A_{12}} \tag{3.13}$$

N_0 is set to a value of 1 for ease of notation, meaning this term disappears from equation 3.13. With the use of another random variable, X_{exp}, where $0 < X_{exp} < 1$ in place of $N(t)$, the exponential decay relation of t_{exp} is maintained, with each t_{exp} corresponding to a single point of photon emission along the decay path with the corresponding Einstein coefficient, A_{12}. As shown in chapter 2, we can replace A_{12} with the reciprocal of the average lifetime, $\frac{1}{t_{12}}$. This means that the final expression takes the form:

$$t_{exp} = -\ln(X_{exp})t_{12} \tag{3.14}$$

This state lifetime can be added to the time at which the excitation occurred, $t(E_\alpha)$, to give the time of photon emission relative to the beginning of the decay itself.

This analysis concludes the photon-generation side of the numerical modelling. In summary the elements included in the temporal analysis are: time elapsed between the alpha particle being emitted and excitation of air and time taken for fluorescence processes to lead to emission of a photon. For alpha particles this temporal profile has not been explored explicitly before. The model can now be deployed to consider the characteristics of detection.

Figure 3.3 shows the full temporal profile of radioluminescence on an individual decay scale. The results are consistent with data from experiments presented in the previous chapter [24] (see figure 2.14). As displayed, the qualitative features of the numerical simulations, presented on the left of figure 3.3, are in agreement with those published by STUK. Shown clearly in both figures is the steep increase from the zero-point, representing decay, and the exponential decay-like character of the tail of time distribution. The two are slightly different in presentation, with STUK's work presenting coincidences between two photomutlipliers while the numerical simulation considers only absolute time from decay to emission: this is of no difference as axes are simply shifted back by approximately 3 to 4ns.

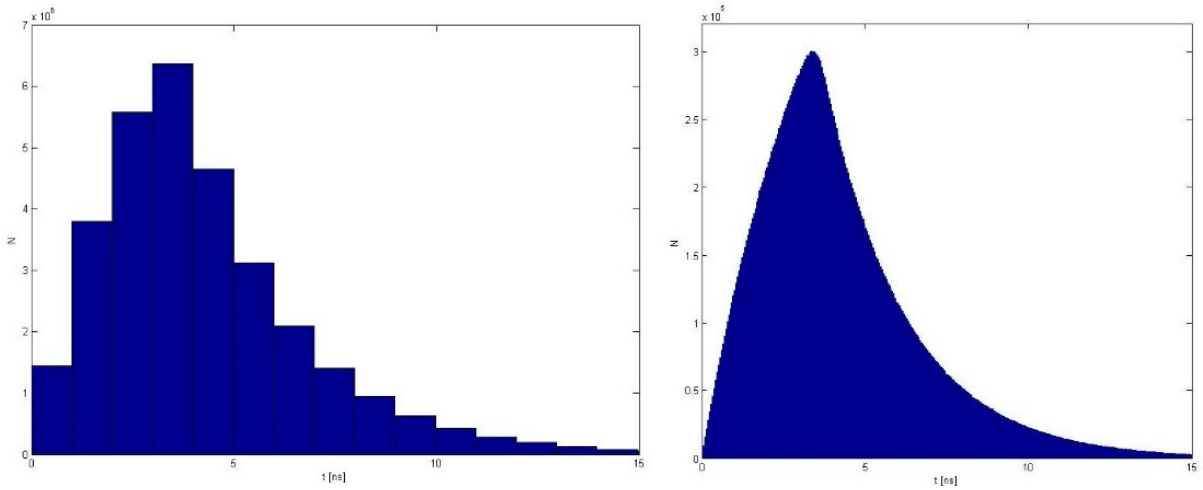


Figure 3.3: Histogram plots of the temporal profile of radioluminescence caused by 5.5 MeV alpha particles, averaged over 300,000 decays. This model incorporates both the temporal profile implied by the Bethe formula and an exponential decay curve originating from the excitation-emission delay due to fluorescence. This model incorporates an average excited state lifetime of 2.5ns, corresponding to the nitrogen 337nm state in air [23]. Both are drawn from the same dataset but displayed left is the nanosecond resolved profile for comparison with figure 2.14.

3.2 Modelling detector performance

3.2.1 Detection Geometries

To construct a model to analyse the detection characteristics of alpha-induced radioluminescence, and eventually provide a platform for comparison of empirical data to simulated data, the detection geometry must also be considered.

Many groups have considered the radioluminescence emission profile as emitted from a single point. More sophisticated models such as that presented by Thompson et al [18] looked at the spatial emission profile but did not move on to also consider the impact on detection characteristics. As has been demonstrated clearly above light is emitted over the full length of the alpha particle's path in a non-uniform way. The rationale for the omission of this consideration in others' models has been that the range of the alpha particle (3-4cm) is small

compared to the detection range of detection systems (20cm-1km). The focus of this section is to demonstrate that this assumption is invalid when considering detection characteristics below 1m, that it depends upon the optical collection diameter and demonstrates some interesting properties.

The rationale for the inverse-square approximation analogous to flux. For electromagnetic and gravitational fields as the distance from a body is increased, the solid angle subtended by a detector (or body, as per gravitational and electromagnetic forces) scales with the inverse-square of the distance from source to body. This model assumes two things which are invalid when analysing an anisotropic photon flux, namely: that the flux at zero distance is infinite and that the origin of the flux is a point. Evidently neither is true for alpha radioluminescence as there are a finite number of photons emitted per decay and photons are emitted from a finite space, the range of the particle's path.

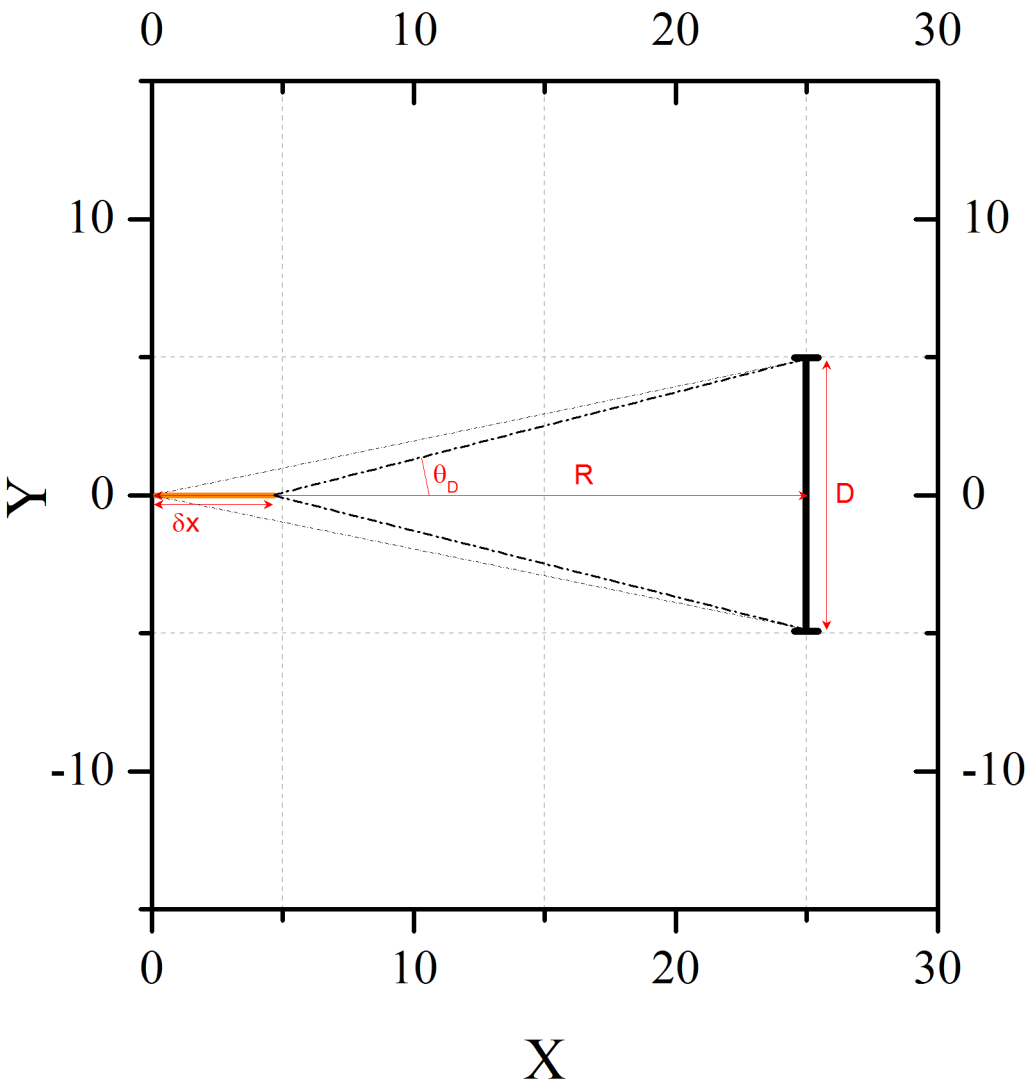


Figure 3.4: The simplest geometric case for detection is a detector, diameter D, planar to a source at a distance, R. Additionally shown is δx, the displacement of the point of emission, which represents a non-point light source (representative of a pencil beam of alpha particles) which emits a photon at this distance rather than at (0,0). This produces an angular region of $2\theta_D$ in which positive detection of photons occur. This is symmetric in the XZ plane. Dimensions are shown in arbitrary units.

Geometrically it is possible to describe the detection geometry by considering the length between a point source and a detection diameter. The angle θ between the point and the centre of the detector (of diameter D) at distance R can be shown to be:

$$\theta_D = \arctan\left(\frac{D/2}{R}\right) \tag{3.15}$$

Next, incorporating the displacement, δx, between the point of the radioactive decay and point of photon generation θ_D is now:

$$\theta_D = \arctan\left(\frac{D/2}{R - \delta x}\right) \tag{3.16}$$

This expression is only valid in the assumption that the alpha particle moves only perpendicular to the detector. If the detection region is assumed to be square-faced we can say that if both the azimuthal and polar angle of the emitted photon, defined by 3.12, lie in the intervals:

$$-\theta_D < \theta < \theta_D \tag{3.17}$$

And:

$$-\theta_D < \phi < \theta_D \tag{3.18}$$

Then the photon intersects the detector and can be considered to be detected by an ideal system. This simple geometric model allows the analysis of relationships between range, diameter and photon flux reaching a detector for simple, collimated alpha particle beams traversing air. Additionally with the temporal considerations discussed and derived earlier we can analyse the coincidence rate expected per decay, at particular ranges and detection diameter and finally consider the median emission time of photons from individual decays.

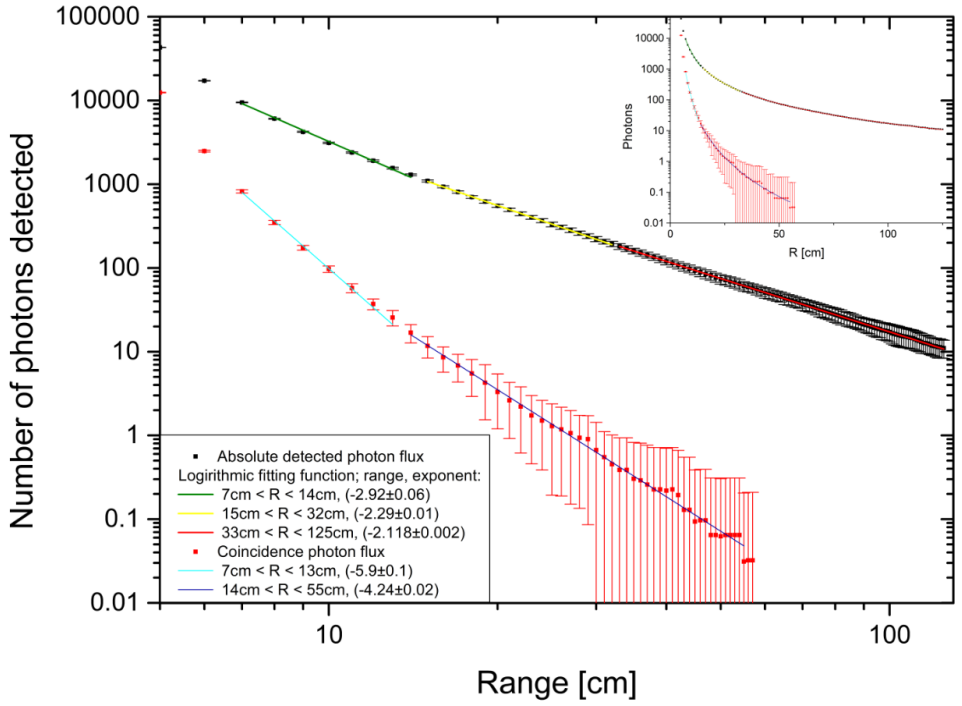


Figure 3.5: The detection characteristics of a square detector of width 0.8cm for 50,000 5.5MeV alpha particles emitted in a pencil beam per point, averaged over 35 sets of 50,000 decays to give indicative uncertainty values to one standard deviation. As displayed the fitting functions show a variation in gradient across the region shown. In the short distance case (7-14cm) this resembles more strongly an inverse cube law, before converging to an inverse square law relation at greater distances. The coincidence photons, as can be expected by the double probability required for the detection of two photons per decay, approximately demonstrate a gradient 2x that of the photon-range relationship. Inset: relationship with range displayed on a linear scale.

3.2.2 Range, Detection Region and Photon Flux

Figure 3.5 displays a simple case for a detector of diameter of 0.8cm, corresponding to the photomultiplier tube used for data acquisition in this thesis without any additional optics, showing the relationship between range and number of photons reaching this region. This demonstrates the complex relationship between range and number of photons detected; rather

than a simple square law the range-flux relationship's derivative itself varies over the detection range.

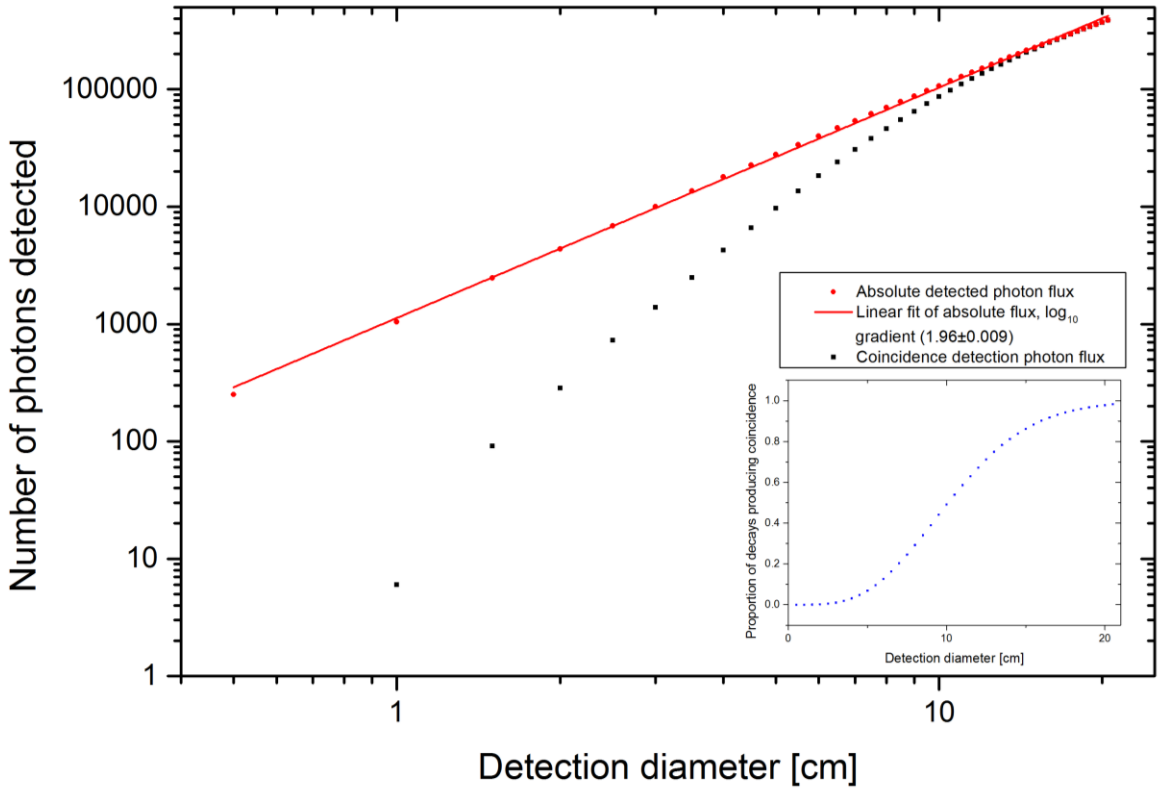


Figure 3.6: The variation of photon flux detected from a pencil beam of 5.5MeV alpha particles compared to the width of the detection region (detection diameter) at a source-detector distance of 20cm. Each point is product of 50,000 alpha decays with an expected total photon output of 5.225 million photons. Inset: overall proportion of radioactive decays producing coincidence compared to detection diameter; it is possible to resolve the point of saturation at which the expectation value of number of detected photons per decay exceeds 2 at diameter of 20cm.

Another consideration is the relationship between the detection diameter and photon flux detected. Displayed in figure 3.6 is the relationship between detection diameter and the photon flux at a fixed source-detector distance of 20cm. At this distance the relationship

between the two variables is simpler than range and displays only slight non-linear behaviour, with a derivative approximately corresponding to a square law. At larger diameters in this figure it is possible to resolve the point of saturation at which the overall number of photons converges with the curve for coincidence photons; this demonstrates the point at which all decays result in more than one photon reaching the detector. Shown inset is the relationship of the proportion of decays producing coincidence and detection diameter, slowing clearly that when detection diameter is approximately equal to range that the majority of decays result in coincidence (an example of which is represented in figure 3.2). Considering specifically the temporal profile of the detected photons it is possible to see directly the impact of the energy distribution described by the Bethe formula.

Displayed in figure 3.7 is the median emission time of detected photons for 30 sets of 50,000 radioactive decays over distance. The median emission time is indicative of the point at which the emitted photons, on average, originate from; a high median emission time corresponds to photons typically emitted in the latter sections of the alpha particle's path. Uncertainty in this measurement indicates how significant this median time is; a large uncertainty in median emission point corresponds to a larger spread of emission times. As displayed in the near-field region the median emission time affected by less uncertainty and larger relative to other values. This suggests that at in near-field detection photons arising from the end of the alpha particle's de-energisation dominate those detected due to the increase in the solid angle of detection. This demonstrates the significance of the non-point source model for near-field detection: if approximated to an inverse square law, this increased solid angle would not be accounted for and would lead to an underestimation of the reduction of intensity over distance.

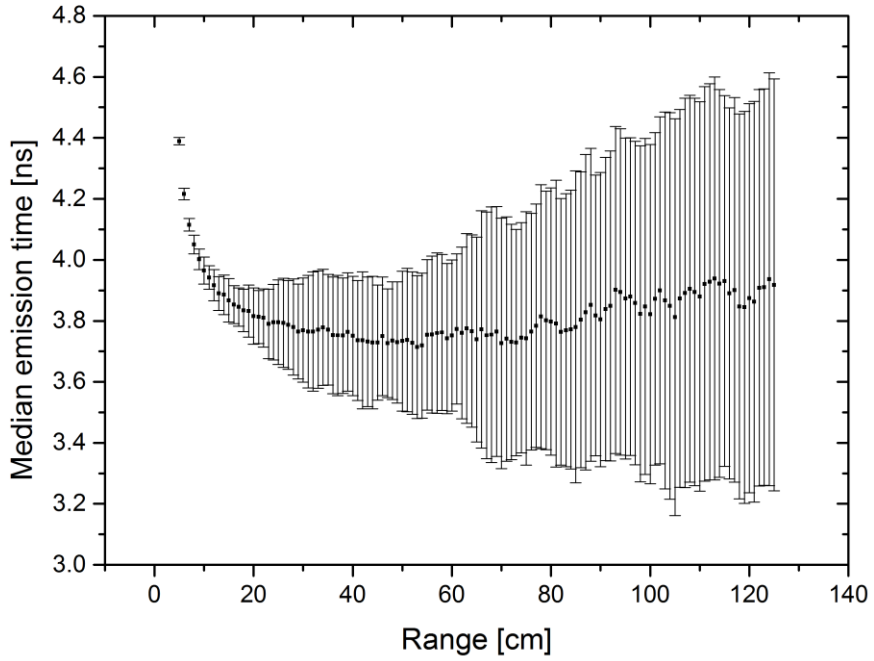


Figure 3.7: Variation of the median time of photon emission relative to the radioactive decay of the alpha-emitting nucleus (5.5MeV, pencil beam) for a detector of diameter 0.8cm, averaged over 30 sets of 50,000 radioactive decays, over distance. This figure shows the influence, in the near-field detection case (4.5-10cm), of the non-point source nature of the radioluminescence phenomenon. At ranges near to the particle's path the median emission time is higher, indicating that on average photons derive from the latter stages of the alpha particle's path. This is due to the higher detection solid angle for photons emitted nearer to the detector face. As range increases this effect becomes less pronounced and the uncertainty in emission time increases drastically as the median emission time depends less significantly on from which section of the alpha particle's path the photon derives.

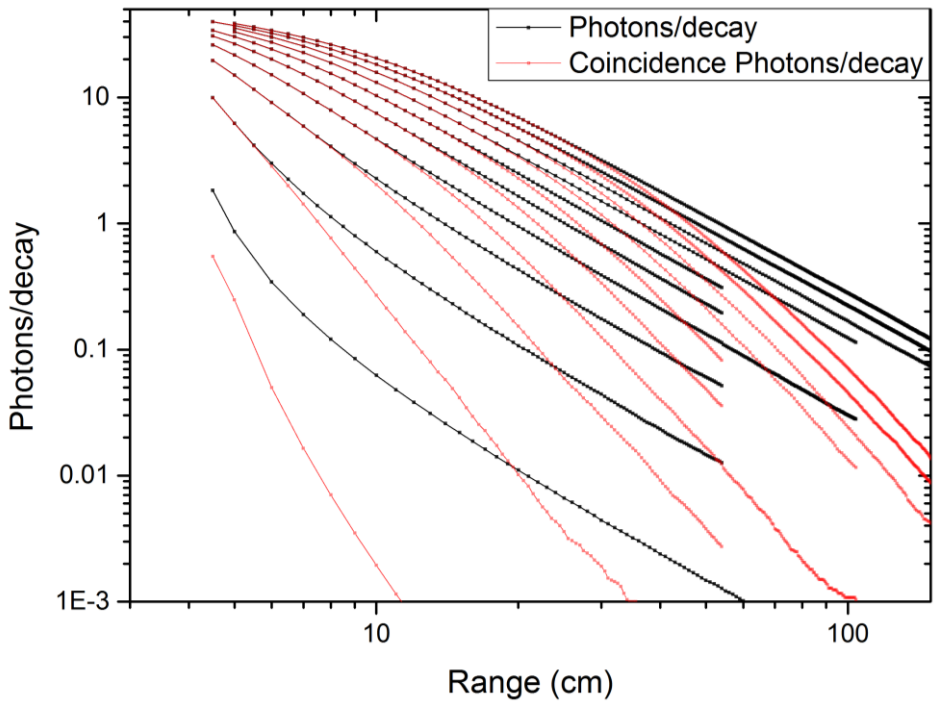


Figure 3.8: Variation of photons detected per decay over distance for detectors of widths varying from 0.8 (bottom curve) to 22.5cm (top). Each point represents the number of photons detected averaged over 50,000 decays. Displayed are the detection widths (bottom to top): 0.8, 2.5, 5, 7.5, 10, 12.5, 15, 17.5, 20 and 22.5cm.

Incorporating the variables considered previously, figure 3.8 displays the variation of photon flux detected per decay with range over a series of diameters within the range relevant to future detection systems. A number of interesting features emerge from this analysis. First is the qualitative shape of the various component curves; two different regimes emerge with variation of detection diameter and number of photons detected per decay. The first of these, discussed in relation to figure 3.5, is the simple case where photon flux decays at a reducing rate as the source-detector distance is increased. As described in the analysis of figure 3.5 this can be subdivided into regions corresponding to inverse cube and square laws. This is true, to a lesser extent at larger diameters, between 0.8 to 7.5cm detection width. The second group of curves, with widths between 10 to 22.5cm display a different characteristic; at short ranges little reduction of photon flux with distance is seen, after which the curve returns to a normal inverse square relation at larger distances.

This can be explained by considering the limiting case of detection diameter: a detector which spans from -∞ to +∞ in the YZ plane. Due to the parallel postulate, that if expanded indefinitely two lines whose two-dimensional angles sum to less than pi radians meet at a finite point, as the detector in this model is positioned perpendicular to the line of origin of the photons *any* photon with a projection lying in the hemispherical solid angle on the side of the detector will be detected. This means that in this limiting case the photon flux detected by a perfect, infinite detector would be independent of range and equal to half of the overall photon flux emitted over the full 4π solid angle. This value is equal to half of the expectation value of the emitted photons per unit energy multiplied by the energy of the emitted alpha particles. This is equal to $19\gamma/MeV \times 5.5MeV = 104.5\gamma$ per decay. Half of this value, 52.25γ, is the maximum possible value for the planar, square detection geometry. This factor is represented in figure 3.8 by the projected point of convergence of the curves of differing detection width. Data has not been included for ranges less than the length of the alpha particle's path due to the possible interaction of detector with the radiation itself.

Coincidence photons largely, in the region not corresponding to saturation (at which all decays result in more than two detected photons) appear again to follow a relationship similar to that discussed regarding figure 3.5, namely that the gradient is roughly double that for single photon detection. This is relevant to the work by STUK considering the coincident detection of multiple photons arising from the same decay [24].

Another interesting feature shown in figure 3.8 is the point at which the component curves become largely parallel in the limit of $D >> R$. The component parallel curves have been analysed and are found to tend, in the region beyond this limit, to converge to an inverse square law. This factor again defines the complexity of the inverse-square law approximation applied by other groups, be it through the detection width or the non-point source nature, to this phenomenon and defines loosely its applicability.

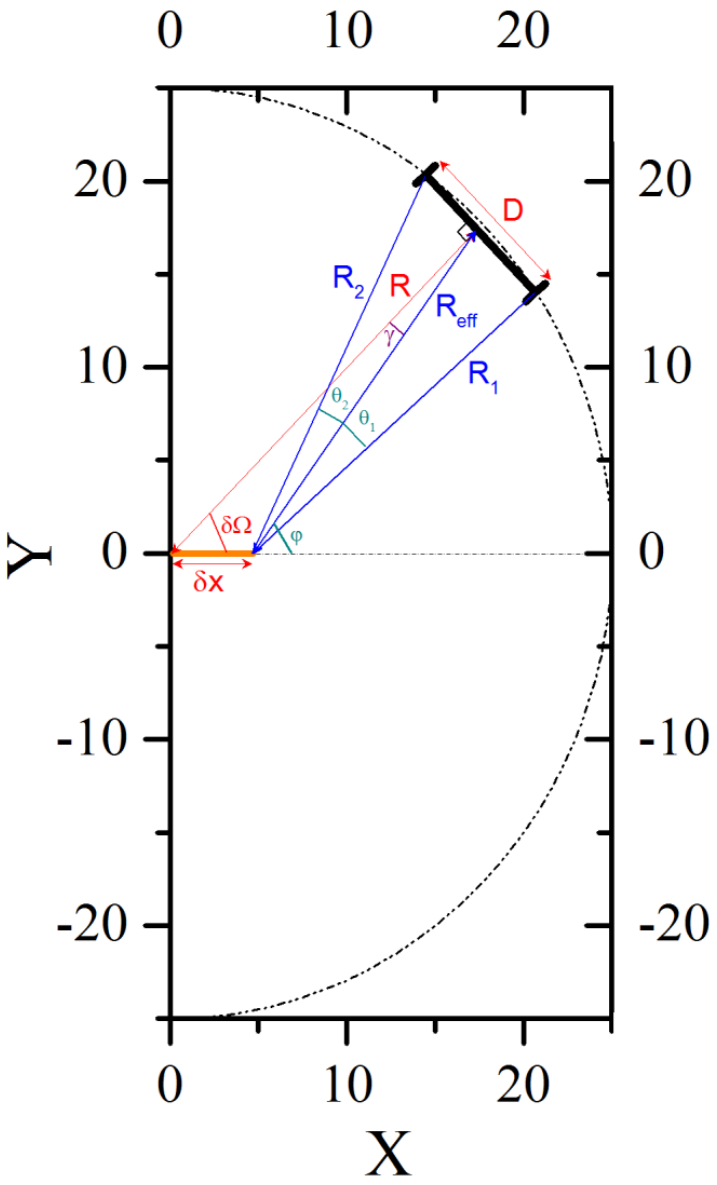


Figure 3.9: A more complicated geometry considers the rotation of a detection region, *D*, about a fixed radius, *R*, by an angle of $d\Omega$ from the origin, (0,0). The detector remains perpendicular to the radius of detection and is intersected at its centre by *R*. This creates the parametric quantities - dependent only on δx, $\delta\Omega$ and *R* - of R_{eff}, R_1, R_2, φ and γ to form the polar coordinates, relative to R_{eff}, of the edges of the detection region, θ_1 and θ_2. The detection interval is then described by the region $\varphi - \theta_1 < \theta < \varphi + \theta_2$. At an angular displacement of $\delta\Omega = 0$ this geometry converges to the simple case shown in figure 3.4, with $R_{eff} = R - \delta x$ and $\theta_1 = \theta_2 = \theta_D$.

3.2.3 Angular Phenomena

A consideration which was neglected from the previous model is the emission profile of the source itself; a point source alpha-emitter will emit alpha particles in a full 2π solid angle from the exposed surface of the source. In the context of the inverse-square law approximation this is interesting; photons derived from alpha particles emitted parallel to the detector (at an angle of $\pi/2$ to the source-detector line) will have a smaller solid angle to the detection area, in the near-field region, compared to those emitted perpendicular to the detector. This section focusses on analysing the effect of angularity of particle emission on photon flux and detection characteristics.

A more complicated geometry, represented in figure 3.9, demonstrates this angular effect. The figure shows a detection region rotated about an angle $\delta\Omega$ relative to the line of particle emission. Due to the rotational invariance of this configuration about the origin this model is a proxy for rotation of the source-emission angle. The region between $0 \leq \delta\Omega \leq \pi/2$ (the primary consideration in this work) is also symmetric in reflection.

The analysis of this geometry yields a number of parametric quantities, labelled on figure 3.9, which for ease of presentation and coherency have been left in their parametric form. The equations governing the rotation about $d\Omega$ can be represented:

$$R_{eff} = \sqrt{R^2 + \delta x^2 - 2\delta x R\cos(\delta\Omega)} \tag{3.19}$$

$$\cos\gamma = \frac{R^2 + R_{eff}^2 - \delta x^2}{2RR_{eff}} \tag{3.20}$$

$$R_1 = \sqrt{(D/2)^2 + R_{eff}^2 - DR_{eff}\sin\gamma} \tag{3.21}$$

$$R_2 = \sqrt{(D/2)^2 + R_{eff}^2 + DR_{eff}\sin\gamma} \tag{3.22}$$

$$\cos\theta_1 = \frac{-(D/2)^2 + R_1^2 + R_{eff}^2}{2R_1R_{eff}} \tag{3.23}$$

$$\cos\theta_2 = \frac{-(D/2)^2 + R_2^2 + R_{eff}^2}{2R_2R_{eff}} \tag{3.24}$$

Given that θ_1 and θ_2 represent the angles subtended between the effective radius, R_{eff} and the outer edges of the detector it is now possible to define the specific coordinates of the detector's edges relative to the source-emission line. This is achieved by considering φ, the angle between the emission angle and R_{eff}, to give the angular range analogous to equation 3.18 in terms of θ of the emitted photon:

$$\varphi - \theta_1 < \theta < \varphi + \theta_2 \tag{3.25}$$

$$\varphi = \delta\Omega + \gamma \tag{3.26}$$

$$\delta\Omega + \gamma - \theta_1 < \theta < \delta\Omega + \gamma + \theta_2 \tag{3.27}$$

Since rotation of the detector occurs in a circle about the origin in the XY plane, the angular limits for detection in the YZ plane, ϕ_D (the polar angle), change only slightly compared to equation 3.18; given that the distance from the point of photon evolution to the centre of the detector is no longer R - δx but instead R_{eff}, the angular region of detection between the edges of the detector is given by:

$$\phi_D = \arctan\left(\frac{D/2}{R_{eff}}\right) \tag{3.28}$$

$$-\phi_D < \phi < \phi_D \tag{3.29}$$

From these conditions, per the geometric case discussed in relation to equation 3.15, it is possible to construct data corresponding to values of $\delta\Omega$ and R. Variation of the angle of emission for the alpha particle produces some interesting results displayed graphically in figure 3.10. Varying the angle of emission over the region of a hemisphere, $-\pi/2$ to $\pi/2$, it is possible to see the significance of the angular variation over range. In the near-field case a 6-fold reduction in flux is seen across the hemispherical surface. This effect is lessened as the source-detector range is increased as it shown on the right figure, which is normalised with respect to the total number of detected photons. As the range increases this figure demonstrates that a convergence is reached at the value of 1⁄41 (0.0244) (shown by the line on figure 3.10) corresponding to the point at which each point contributes equally to the photon flux. This is not quite achieved at a detection distance of 75cm but clearly noise does begin to dominate at this point, hence the fluctuations about this value for the curves shown in green (50 and 75cm radius). The angle at which particles are emitted is very significant in the number of photons which are detected, especially at distances close to the detector.

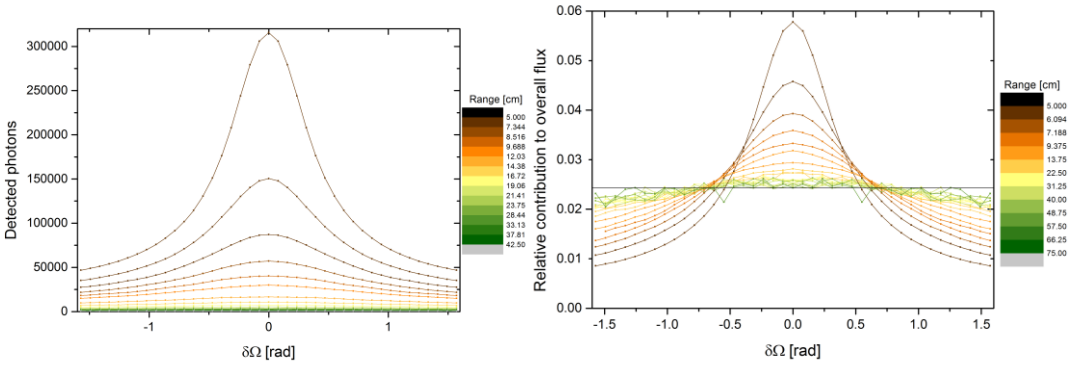


Figure 3.10: Left: The number of photons arriving at a square detector, width 2.5cm, from a source emitting at angle $\delta\Omega$ relative to the detector face over a hemisphere. Each point represents the sum of photon flux detected from 50,000 particle emissions. Results are displayed over the source-detector ranges of 5, 6, 7, 8, 9, 10cm; 12.5 to 42.5cm in 2.5cm intervals and 50 & 75cm. Right: The normalised contribution of each of the 41 measurements to the overall number of photons detected. The line shown at $1/41 = 0.244$ would represent the distribution were each angle to contribute equally. As shown, with increasing distance the curves tend toward a value of flux = 0.244. Each curve is normalised such that the integral between $-\pi/2$ and $\pi/2$ is equal to 1.

Displayed in figure 3.11 is the median emission time of photons reaching the detector at the various semicircular emission angles, $\delta\Omega$, and ranges, R. At small source-detector distances detected photons are emitted later on average similarly to figure 3.7. As the range increases it is also clear that the median emission time is a less significant factor, with noise dominating at larger values. For the near-field cases it is also possible to see that at the outer reaches of the hemisphere the median emission time reduces to values well below the overall median of the total photon flux represented by the line at 3.74ns. This can be explained by considering the smallest path between detector and emission source; when particles are emitted parallel to the detector, at values of $\pm\pi/2$, photons with the shortest path originates from the origin, the initial point of emission, so the median is reduced.

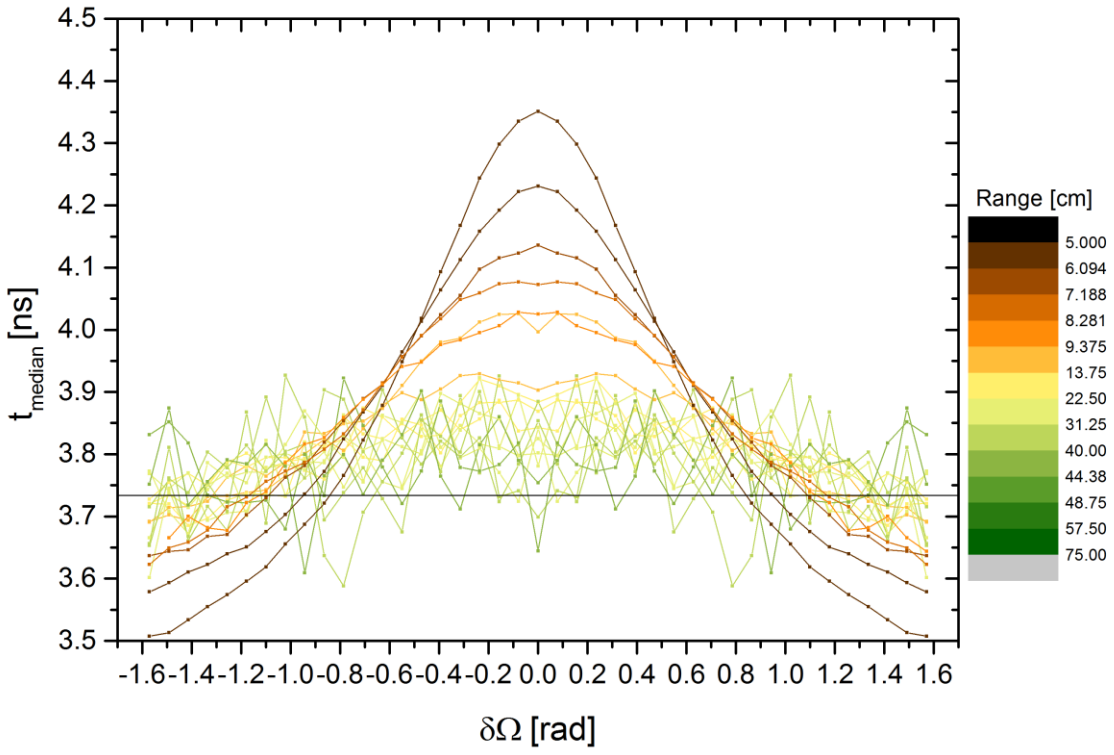


Figure 3.11: The median emission time of photons detected from sets of 50,000 particle emissions over a hemispherical radius. The detection diameter is also 2.5cm. The line, displayed at 3.74ns, is the overall median emission time of all photons arising from decays discounting detection characteristics. In the near-field region it is possible to see that photons are again clearly originating primarily from the latter stages of the particle's transit.

When expanding the considerations displayed in figure 3.10 to the full angular circular radius, with $\delta\Omega$ spanning over $[-\pi,\pi]$, it is possible to observe the periodicity in the angular photon detection function. Figure 3.12 shows the variation of photon flux as the emission angle is varied over this interval.

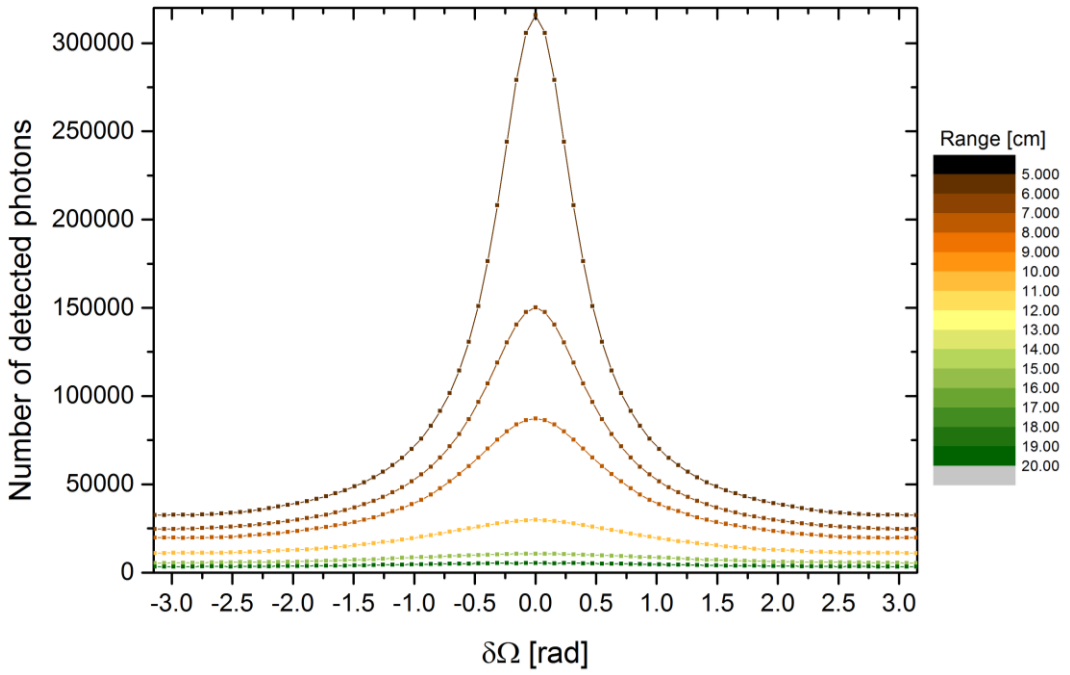


Figure 3.12: The profile of detection over the full circular angle range of $\delta\Omega$ demonstrating the periodicity of this function over the interval of 2π as expected geometrically. Each point is for 50,000 particle emissions at source detector ranges of 5, 6, 7, 10, 15 and 20cm for a square detector of width 2.5cm.

From these consideration it is now possible to construct a model of an alpha-emitting point source which emits over a semi-circular surface. Considering the 41 emission angles, $\delta\Omega$, over the 2π interval a detector placed off-axis at an angle $\delta\Omega_D$ will simply observe a flux equal to the sum of the components of emission angle $\delta\Omega$ which leave the surface. Clearly in all hemispherical scenarios an interval of $\delta\Omega$ equal in magnitude to π will be observed by the detector. Figure 3.13 shows the procedure to obtain the results displayed later. This can be intuitively understood by consideration of the regions of flux 'seen' by the detector at the various detection angles: at an angle of $\pi/2$ for example, corresponding to a detector lying in the XZ plane only, the values $\delta\Omega$ 'seen' will be between π and 0. As such these contributions

are summed. Likewise for $\delta\Omega_D = \pi/4$ the interval over which flux is summed lies between [$-\pi/4, 3\pi/4$].

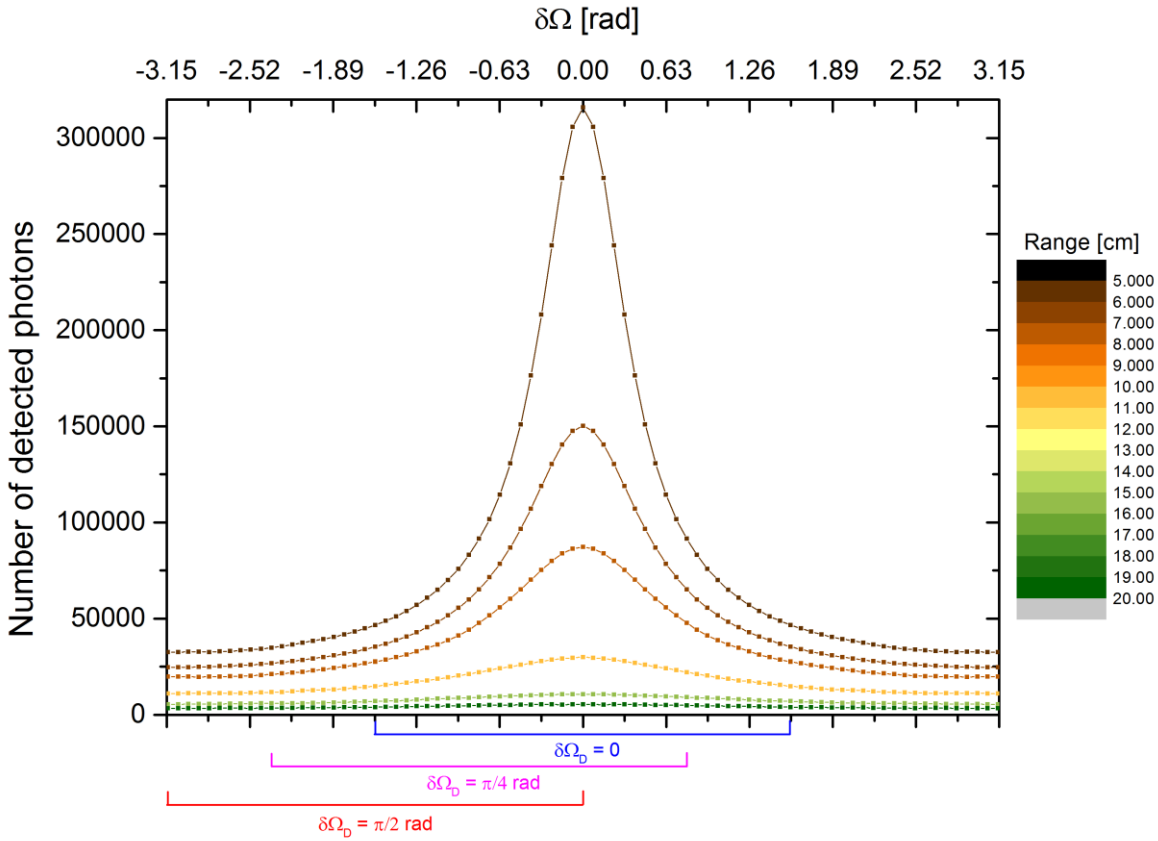


Figure 3.13: To calculate the contributions 'seen' by the detector placed at a detection angle $\delta\Omega_D$ the contributions from the various particle emission angles, $\delta\Omega$, which are not blocked by the point source's surface must be added. As we are considering a semicircular emission geometry this interval's full extent is always equal in to π. Shown are the examples of $\delta\Omega_D$ equal to 0, $\pi/4$ and $\pi/2$. All points present within this interval are summed to give the full emission profile from the particular detector angle, $\delta\Omega_D$.

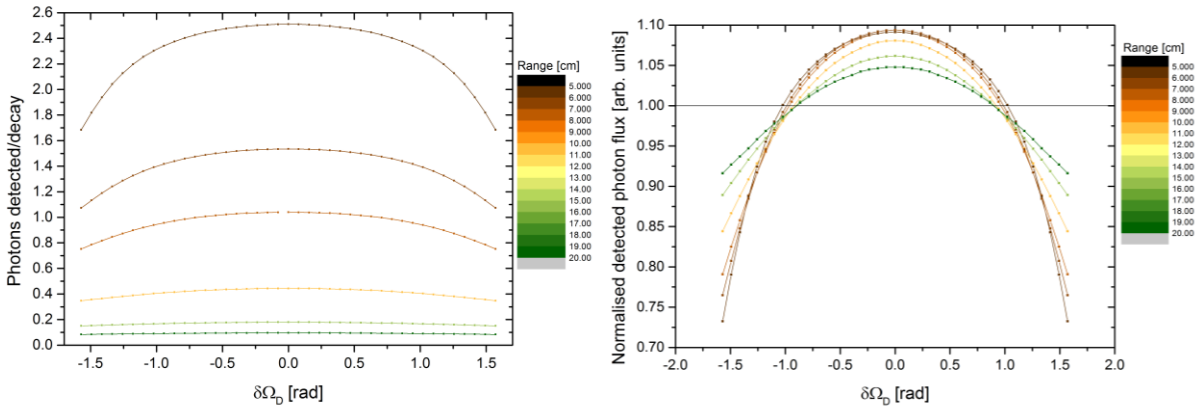


Figure 3.14: The angular emission profile of a semicircular alpha-emitting source, viewed from the angular perspectives over the full semicircle [$-\pi/2,\pi/2$] at ranges of 5, 6, 7, 10, 15 and 20cm, by a square detector of width 2.5cm. Each point is the summation of 41 angular emission angles each containing photon emissions from 50,000 decays. This total 2.05 million decays has been used in calculation of the photon/decay ratio used left. Displayed right is the normalised version, removing dependency on the absolute number of photons detected, giving the relative magnitude compared to the angularly invariant value of 1.

Displayed in figure 3.14 is the result of this calculation. When viewed from the angular perspectives $\delta\Omega_D$ at constant source-detector distance there is clearly an angular correlation of photon flux. As displayed on the right of this figure this effect clearly diminishes at larger source-detector distances. However, even at a distance 8x the detector width (20cm range) a reduction of 13 % is observed between the peak and trough value. This is even more defined at smaller ranges: at 5cm, almost corresponding to the alpha particle's path length, this effect leads to a reduction of approximately one third.

3.3 Modelling decay energies

3.3.1 The impact of decay energy on angular effects

Using the framework described above, an effective system for determining detector response to a given set of alpha particle emissions has been determined. Developing this further it is possible to explore the multivariate relationships between alpha particle energy, angle of emission and source-detector distance compared to number of photons detected. By construction of a four-dimensional matrix structure it has been possible to evaluate the effect of these variables on detection characteristics. In order to achieve this a number of performance optimisations had to be adopted into the algorithm to reduce computer memory allocation and to focus only on photons oriented toward the inside of or narrowly missing the detector face. The result of this simulation is displayed in figure 3.15 on a condensed basis: these calculations take into consideration the emission of particles across a full circular geometry (composed of 54 distinct points), 26 emission energies ranging in 0.1MeV intervals between 3 and 5.5MeV and 30 separate values of source-detector distance between 5 and 63cm. The slicing represented in this figure represents the difference between successive values of source-detector distance, with 5cm providing the highest photons intensity detected and 63cm the lowest.

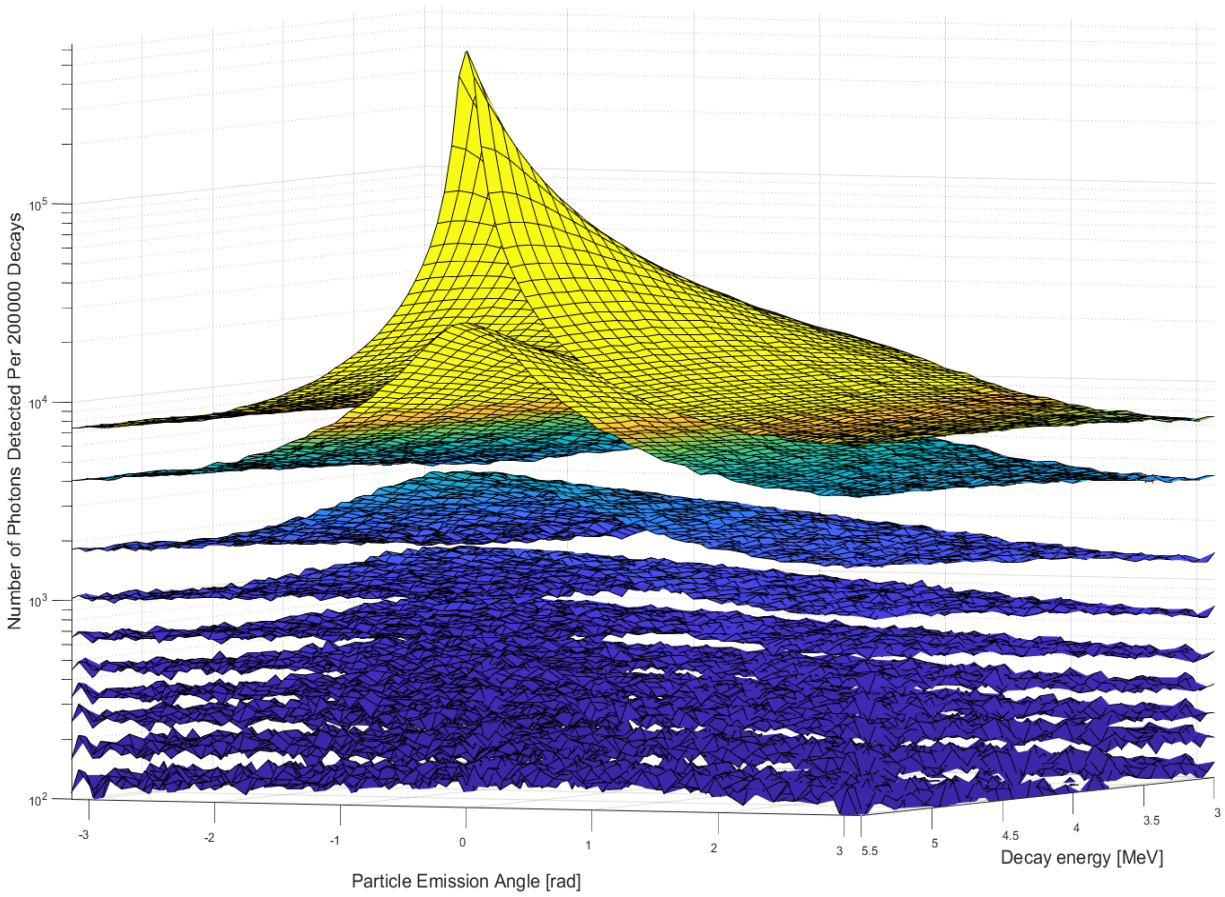


Figure 3.15: Three-dimensional analysis of the number of photons detected by a detector of equivalent solid angle to a 7.90mm square photocathode resulting from 200,000 alpha particle emissions of each energy, emission angle and range. Sliced surfaces on this plot represent the variation of source-detector distance across a range between 5cm (top layer) and 45cm (bottom layer) in 4cm intervals. Demonstrated is the coupled nature of particle emission energy, detection distance and number of photons received at the detector. It is also illustrative of the peak broadening for emissions occurring at larger distances.

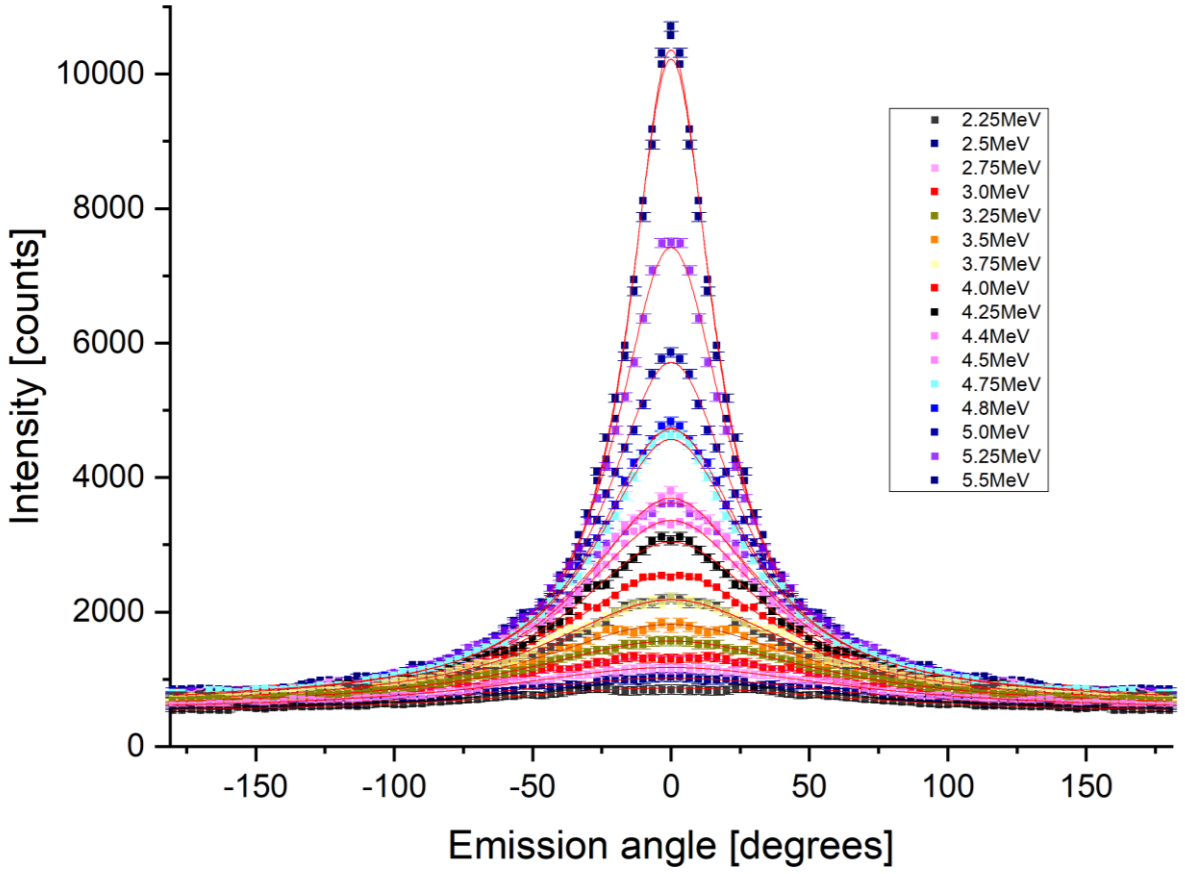


Figure 3.16: Number of photons intersecting a 7.9mm square detector for 10,000 emissions of various alpha particle energies (see legend, inset) at 5cm source-to-detector distance. Each curve has been fit using a Lorentzian fit function (red line). The emission angle represents the angle (relative to the normal of the centre of the detector face) at which the particles were emitted.

The results presented in this analysis demonstrate the interdependency of these variables: for source-to-detector distances where an alpha particle has sufficient energy to nearly reach the detector, a higher intensity will be measured for emissions perpendicular to the detector face. The magnitude of this effect is also determined by the energy of the particles themselves, with higher energy particles exhibiting a greater angular dependency.

Another interesting feature in figure 3.15 is that for a fixed distance, for example that of the top layer at 5cm, there are characteristic differences between the angular profiles of particles of different alpha particle energy. For example, for larger energy alpha emissions, say at 5.5MeV, there is a more strongly defined peak in intensity across the angular distribution when compared to say emissions at 3MeV.

This effect arises due to the larger effective solid angle for photons emitted nearer to the detector face, as discussed previously in this section.

3.3.2 Parametric fitting of angular emission distributions

Displayed in figure 3.16 is the data derived from the most intense slice of figure 3.15, corresponding to a source-detector distance of 5cm. Shown in the figure is a Lorentzian fit model compared to the data output by the numerical simulations described above. This function is of the form:

$$I = I_0 + \frac{2A}{\pi}\frac{\omega}{4(\theta-\theta_c)^2+\omega^2} \tag{3.30}$$

Where I_0, ω, A and θ_c can be interpreted as the minimum intensity for each curve (i.e. the count rate at $\theta = \pm 180°$), the full-width half-maximum, the area and the angle of maximum intensity of the distribution. Each of these factors are a function of the energy of the emissions of the radioactive source, E.

Using a similar method to that described in section 3.2.3 it is possible to explore the detection characteristics for emissions across the 2D geometry for different decay energies. To produce an estimate of the intensity due to emissions over a range of angles, it is convenient that the integral of this the Lorentzian fit model is readily obtained. If we assume that $\theta_c = 0$ for all E (see figure 3.16) the integral can be calculated:

$$\int_{\theta_1}^{\theta_2}\left(I_0 + \frac{2A}{\pi}\frac{\omega}{4(\theta-\theta_c)^2+\omega^2}\right)d\theta = \left[I_0\theta + \frac{A}{\pi}\tan^{-1}\left(\frac{2\theta}{\omega}\right)\right]_{\theta_1}^{\theta_2} \tag{3.31}$$

Here the limits of integration, θ_1 and θ_2, can be interpreted as the angular range over which alpha particles are emitted; for example for a simple source emitted from an infinitely thin slit, particles would be emitted over range from θ_1 = -180° to θ_2 = +180°. As discussed before, to obtain the detection characteristics for emissions over a range of angles the average was calculated over the relevant angles. The integral in equation 3.31 and the nature of the function mean that the mean value theorem can be used to calculate the mean intensity detected from a range of emission angles:

$$f(c) = \frac{1}{b-a}\int_a^b f(t)dt \tag{3.32}$$

Where $f(c)$ is the average value of the function $f(t)$ over the interval $[a,b]$.

The emission profile of a real alpha-emitting radioactive source can be considered equal for all emission angles, except where emissions are constrained some way - for example by a source casing. For the purposes of demonstration if we consider that the source: *i*) emits with the same probability in all angular directions over a range, *ii*) that angular range is centred on and symmetric about some angle, θ_s and *iii*) that emissions span over the angles $\pm\theta_E$ on either side of θ_s, then the limits θ_1 and θ_2 can be written instead as: $\theta_1 = \theta_s - \theta_E$ and $\theta_2 = \theta_s + \theta_E$. See figure 3.17 for a representation, based on the centre of a detector face being positioned normal to the red line at the top of the circle.

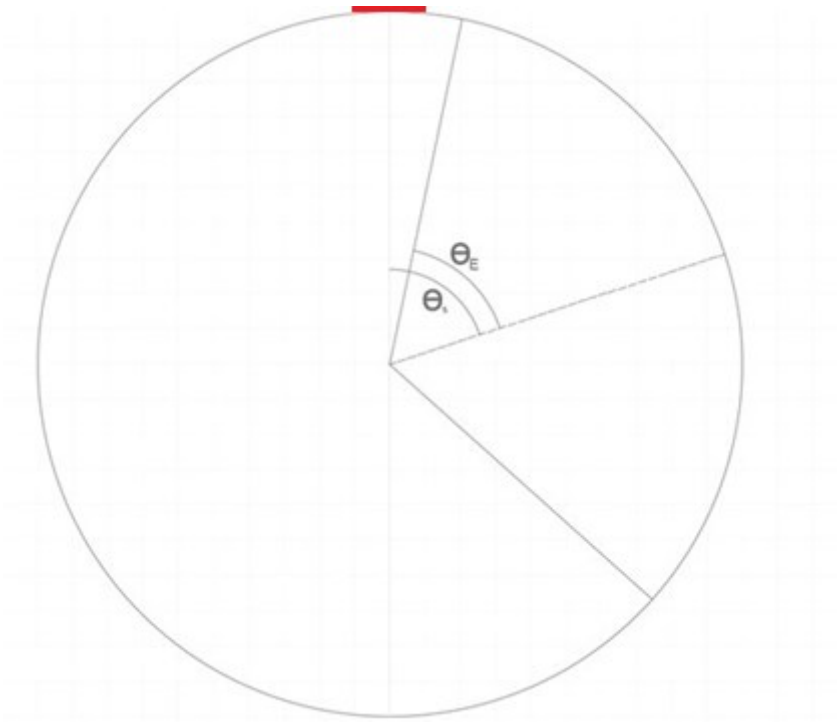


Figure 3.17: Where the centre of a detector face lies at line displayed in red at the top of the figure, the emission geometry of a radioactive source emitting symmetrically about a central point can be described by two factors: the central emission angle, θ_s and the half angle of the angular range, θ_E. As a source is rotated, θ_s varies and this can be used to infer the expected intensity of photons reaching the detector. Displayed is a radioactive source emitting into an angular region of 60 degrees oriented at angle θ_s relative to a detector.

Within this definition, rotation of the radioactive source relative to the detector (or the detector relative to the source) will change only the value of the central angle, θ_s. The mean intensity detected for a radioactive source oriented at an angle θ_s relative to a detector, emitting over the angular range $\theta = \theta_s \pm \theta_E$, can be calculated:

$$I_{detected}(A, \omega, I_0, \theta_s, \theta_E) = \frac{1}{2\theta_E}\left[I_0\theta + \frac{A}{\pi}\tan^{-1}\left(\frac{2\theta}{\omega}\right)\right]_{\theta_s-\theta_E}^{\theta_s+\theta_E} \quad (3.33)$$

To illustrate the behaviour of this equation it is possible to evaluate the relationship between the fitting parameters, A, I_0 and ω, calculated from the fitting models displayed in figures 3.15 and 3.16 for the scenario of a 7.9mm square faced detector placed at 5cm, with respect to the alpha particle emission energy. Figure 3.18 shows the results of this analysis. A variety of regression models were chosen to analyse the relationship between the fit parameters and decay energy (here displayed over a relevant range of energies, 2-6MeV) and those found to exhibit the lowest R^2 values were chosen to parametrise A, I_0 and ω in equation 3.33.

The parametric expressions found to most reliably represent these quantities were found to be:

$$I_0 = 19.5E(a_1 + b_1 e^{R_1 E}) \tag{3.34}$$

$$\omega = a_2 + b_2 E \tag{3.35}$$

$$A = a_3 + b_3 e^{R_3 E} \tag{3.36}$$

Where a, b and R 1, 2 and 3 are constants. Equation 3.33 for the intensity detected from a 8mm detector, $I_{detected}$ for emissions from a source spanning angular range θ_E at an orientation θ_s can now be expressed purely in terms of the angular characteristics of the source and energy of emission, E.

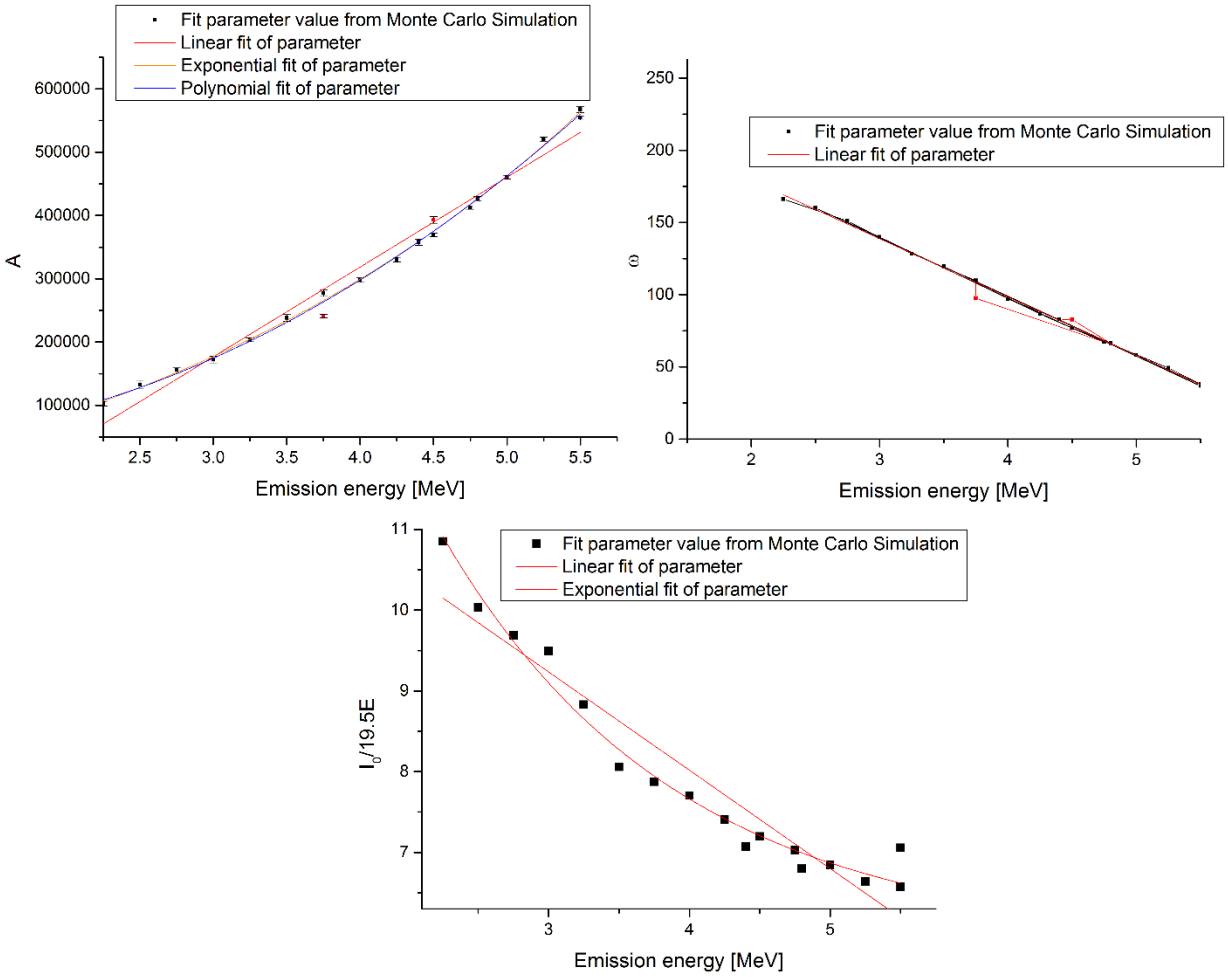


Figure 3.18: Graphical evaluation and regression analysis of the fit parameters defining the Lorentzian fitting function for the number of photons detected by an 8mm circular detector over varied emission angle and energy. Data is drawn from that presented in figure 3.16. Displayed are: (top left) area of distribution, A, against emission energy; (top right) full-width half maximum of distribution, ω; and (bottom) the baseline minimum number of photons detected, I_0, reduced by the overall number of photons emitted per particle, $\frac{I_0}{19.5E}$. A variety of fitting functions were tested and those with the highest R^2 value were selected to form the parametric rotational intensity function.

Replacing A, I_0 and ω in equation 3.33 with these parametric equations, the intensity can be calculated as a function of E, θ_s and θ_E:

$$I_{detected}(E,\theta_s,\theta_E) = \frac{1}{2\theta_E}\left[19.5E(a_1+b_1e^{R_1E})\theta + \frac{a_3+b_3e^{R_3E}}{\pi}\tan^{-1}\left(\frac{2\theta}{a_2+b_2E}\right)\right]_{\theta_s-\theta_E}^{\theta_s+\theta_E} \quad (3.37)$$

Equation 3.37, combined with the constants calculated using regression analysis, enables the calculation of intensity detected from a radioactive source rotated around a central point relative to a detector (square faced with diameter of 7.9mm at 5cm distance from the source). Figure 3.20 shows the results of this calculation for 3 values of energy, E (2.5, 3.75 and 5MeV) and three values of θ_E (90, 45 and 10°) over variation of the central angle over the range: $0° \leq \theta_s \leq 360°$.

The effect of variation of θ_s and the decay energy is clearly seen. A source emitting over a small angular range results in a higher intensity a narrower profile, with a greater angular dependency, with higher intensity detected at angles near the detector. Sources with a wider angular emission range (with higher values of θ_E) result in a broader, more evenly distributed profile.

Taken to its extreme that would mean that a point source emitting with equal probability in all directions (for example, a point-like alpha-emitting particle floating in air) would result in a circular profile given that rotation of the particle with respect to the detector would not affect the intensity observed by the detector.

The energy of the alpha particle emissions also has the effect of defining the magnitude of the intensity profile and its curvature as can be observed in figure 3.19.

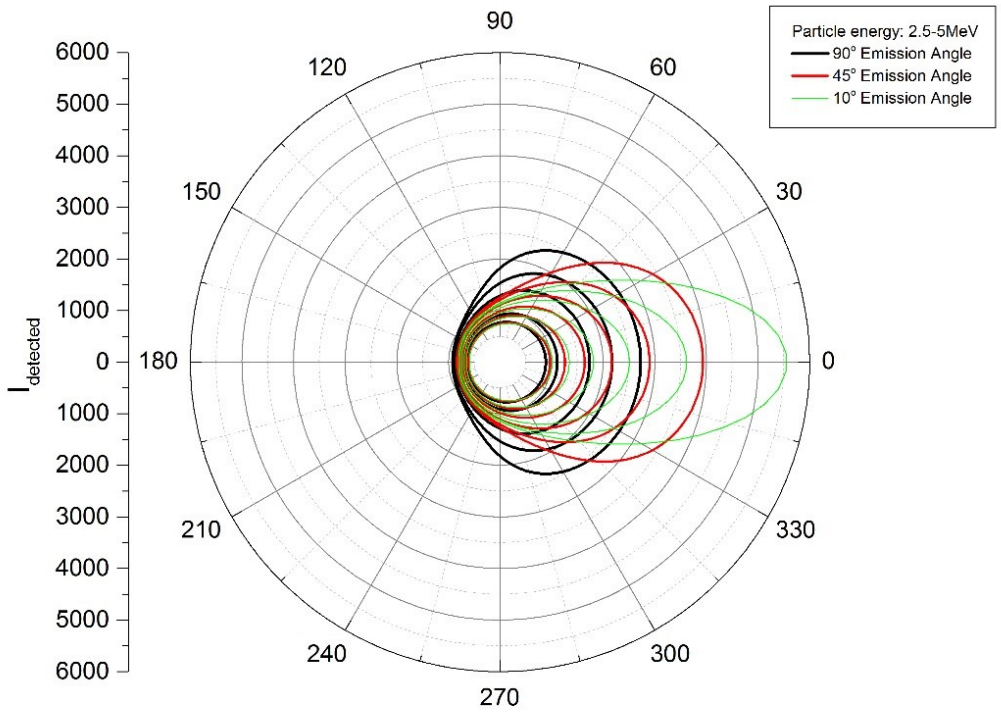


Figure 3.19: Representation of the number of photons detected by an 8mm circular detector from angular perspectives from 0 to 360 degrees. The radial scale represents the viewing angle (degrees) to the source; the black, red and green lines represent the intensity observed from that perspective relative to the intensity scale (see Y axis). The various values of θ_E, shown within the legend, demonstrate the effect of emission angle on the intensity observed from different angles. Lines of identical colour with increasing intensity represent emission energy values of 2.5, 3.0, 3.5, 4.0, 4.5 and 5MeV. For larger emission angles the distribution over the interval $[0, \pm 90]$ shows a lower decrease than for smaller emission angle. This would be most clearly indicated in the case of $\theta_E = 180°$, for which the corresponding distribution would be isotropic. The combination of the two factors, emission angle and decay energy, define the shape of the distribution.

3.3.3 Comparison to experiment

The scenario modelled in the previous section had several clear limitations which mean its testing by experiment would be difficult. Most radioactive sources in a laboratory do not emit in a two dimensional geometry, with electrodeposition onto a metal planchet being the most common method resulting in a hemispheric three dimensional emission. Any support which was used to safely position the source would inevitably block some proportion of the photons from reaching the detector, especially when the source was oriented in the opposite direction.

To test the hypothesis that orientation of a source in relation to the detector has an effect on the photon count rate observed, a simple experiment was designed. A schematic representation of the experiment is displayed in figure 3.21.

A small americium-241 source of unknown activity was placed on the rotating arm of a small 28BYJ-48 stepper motor which was in turn connected to microcontroller. The microcontroller was programmed to rotate the motor at a rate of one revolution per hour.

A Hamamatsu H10721-210 UV-sensitive photomultiplier tube was placed (5±0.2)cm in front of the source's face. A piece of Hoya U340 glass (UV-transmitting, visible-blocking) was placed in front of the 8mm circular photosensor aperture. The photomultiplier, motor and source were then enclosed within a light tight box to reduce interference from external light.

The photomultiplier tube was then powered up and its output was monitored, with counts measured per second. The motor was then set to commence its rotation and the detector measured for the hour of rotation.

Data from the photomultiplier tube was then analysed and the timing of the measured count rates was correlated to the angle of rotation of the source at that time. The results of this analysis are displayed in figure 3.20.

The figure shows an angular profile consistent with the characteristics predicted by the model. Displayed in red is a non-linear least squares fitting model applied to the observed data using equation 3.37. The fit converged and shows reasonable agreement with the measurements obtained in the experiment. The nonlinear least squares fitting method also produces a value for the emission energy, E, and the angular range parameter, θ_E. Given the

differences between the modelled scenario and the experimental setup it is not possible to assess the accuracy of these figures, but further work could consider the ability of this method to accurately assess source emission energy when modelled in greater detail.

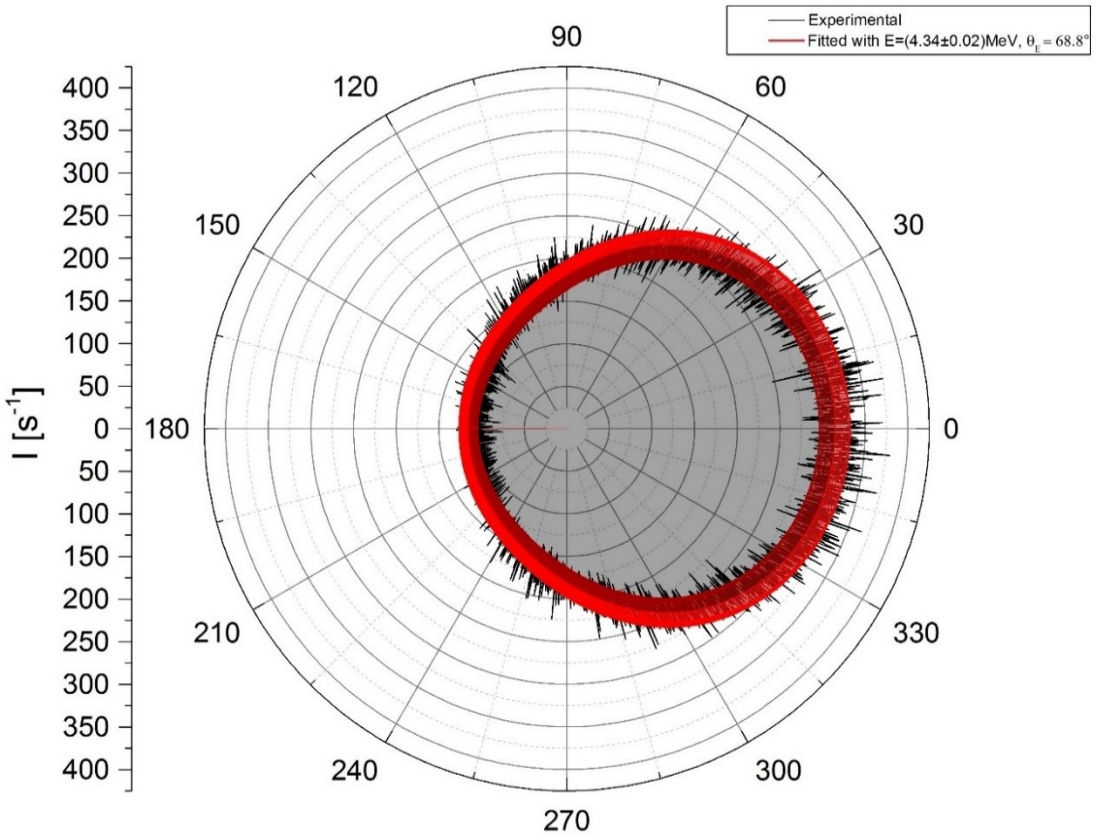


Figure 3.20: Photon intensity (I) detected during the rotation of four ^{241}Am sealed radioactive sources attached to a motor displaced 5cm from a photomultiplier tube. The photomultiplier was equipped with a broadband UV transmissive filter (Hoya U340 transmitting 300-400nm light at 90% efficiency) covering the photocathode. Shown in red is the fit function described in equation 3.37 with a Poisson distributed error corresponding to the averaging period of the experimental data (black). Shown in the legend are the resulting values of the floating fit parameters E and θ_E with values of (4.34 ± 0.02)MeV and 68.8° respectively. The excellent agreement between fit model and experimental data support the validity of the model despite difference in emission geometry.

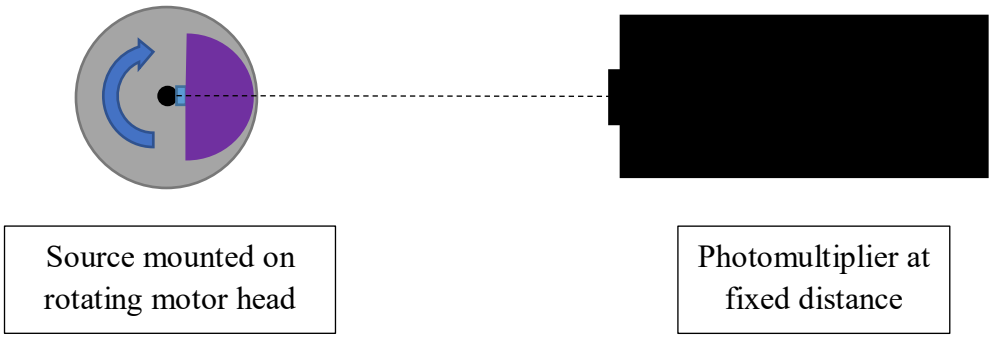


Figure 3.21: Schematic representation of the rotating source experiment. An americium-241 source was mounted onto a 28BYJ-48 stepper motor programmed to rotate at a rate of one revolution per hour. The photomultiplier tube was programmed to observe variation in the intensity observed from a fixed distance from the source. The orientation of the source displayed in the figure corresponds to the zero-degree orientation on figures 3.19 and 3.20.

3.4 Conclusion

The numerical simulations presented in this chapter give rise to a number of interesting findings which has informed work presented later in the thesis. The performance of detectors designed for use with alpha-induced radioluminescence has been shown to differ from other types of radioactivity detectors in a number of ways. Through simulation of the decay process it has been shown that, because photon emissions are spread over a region surrounding the source surface, detection close to a source exhibits more complex behaviour and cannot be considered to behave as a point source.

By analysing the effect of changing the angle between source and detector it was shown that the viewing angle (and physical casing of the source) can affect the light intensity observed by the detector. This is particularly significant when considering the impact of both factors on a device calibration; consideration must also be made to ensure that the viewing angle between source and detector is consistent between measurements. This also applies to

measurements which are to be compared to a calibration standard, and any difference in viewing angle compared to the calibration should be noted as a possible source of error.

Another consideration is the possible effect of the decay energy of different species and their effect on the detector's response. For most purposes, when collecting data from a detector the only observable variables are the count rate recorded by the detector and the distance at which the measurement a taken from an object. Given that the number of photons detected could be affected by either the source's alpha activity or its energy, measurements should be made with consideration of the likely radioisotopes (and therefore alpha decay energy) present during measurement, especially in the near field region. In an industrial context this could be done by consideration of the processing history for a particular plant, sample or piece of machinery.

Given that the model has been based upon a simple concept of an ideal detector with no optical enhancement (e.g. lenses, filters) the results are limited in their relevance to the detection efficiency of real systems, beyond the most basic such as that discussed in the final section. Further work could expand upon the framework discussed above by use of modelling software such as Geant4 or MCNP which are capable of assessing the performance of more sophisticated optical processes. Nevertheless, the results presented give an estimate of the limits of performance for ideal detectors which accurately models two-dimensional emission geometries.

In the following chapter we consider the implications of these results on the design and development of real detector systems.

Chapter 4
Equipment Design: Detector System

This chapter explores the design processes associated with the development of equipment, and most importantly the detector, used in the experiments presented in the later chapters. This process began with a comprehensive survey of available optical focussing technologies - including UV optical concentrators, parabolic mirrors and prefabricated lens systems - and it was decided to prioritise the design of a lens system which matches the properties illustrated to be significant through the literature search and numerical modelling. On this basis an optical detector technology - a single photomultiplier - was chosen and a suitable product was found with high, quantitative sensitivity in the appropriate wavelength region (Hamamatsu H10721-210). Subsequently a lens design was completed, optical filtration was optimised for radioluminescence and a mechanical assembly for housing these was designed and 3D printed.

Consideration was also given to the choice of data acquisition device. Given the nature of the research project a device was chosen based on its ability to operate without the need for preamplification – thus reducing cost – and with high temporal resolution, to enable more detailed analysis of data. A preamplifier was not required given the absence of a requirement for a long distance between data acquisition (DAQ) system and detector head. The decisions which led to the choice of device are explained and it is concluded that for any future commercial product of this type, an off the shelf DAQ solution would suffice.

Finally the interfacing of these two elements required an iterative set of electronic circuit designs, revisions and correctional factors. These systems and corrections were used in all experimental work presented in the thesis.

To conclude an overview is presented of the entire system and its performance in the various developmental stages is evaluated in environments of relevance to decommissioning.

4.1 Detector design

Chapters 2 and 3 – the literature review and numerical modelling – informed the direction pursued in the design of the detector system. The major conclusions of this process can be summarised as –

- Most systems able to produce quantitative measurements in short times (and at reasonable expense) are photomultiplier based
- Performance has so far been limited by environmental factors (e.g. need to confine system from external light while in measurement) and variation between systems' performance is primarily reliant on their mode of optical filtration
- While ability to produce spatially resolved maps of contamination is interesting, for this to be of practical use this needs to be complemented by quantitative, repeatable detection limits for the detection device. This is only possible so far in systems (without imaging capability) which use photomultiplier tubes
- Numerical simulation showed that one of the most significant determinants of detector sensitivity is the physical size of the optical assembly concentrating radioluminescence onto a detector face
- While a relatively large number of photons are emitted in the decay process, for detection systems to be effective systems must employ high sensitivity detector technology and high transmission optics to maximise detection characteristics while not compromising background reduction
- All detectors designed to produce quantitative outputs are currently optimised to operate at a fixed distance only.

Considering these factors it was decided that it was necessary to pursue, for the sake of cost and quality of assessment, a photomultiplier system with an optical concentration assembly capable of operation at a range of distances under one metre.

4.1.1 Components of detector

The conceptual makeup of a detector exploiting radioluminescence can be considered. When compared to other devices used for the detection of ionising radiation - such as scintillation detectors or electronic impact sensors - this technique is unique in that the material with

which the ionising radiation interacts is not an element of the detector design. Ordinarily a large element of the detector's performance would be determined by this scintillator or substrate; instead in this case this element of design is fixed.

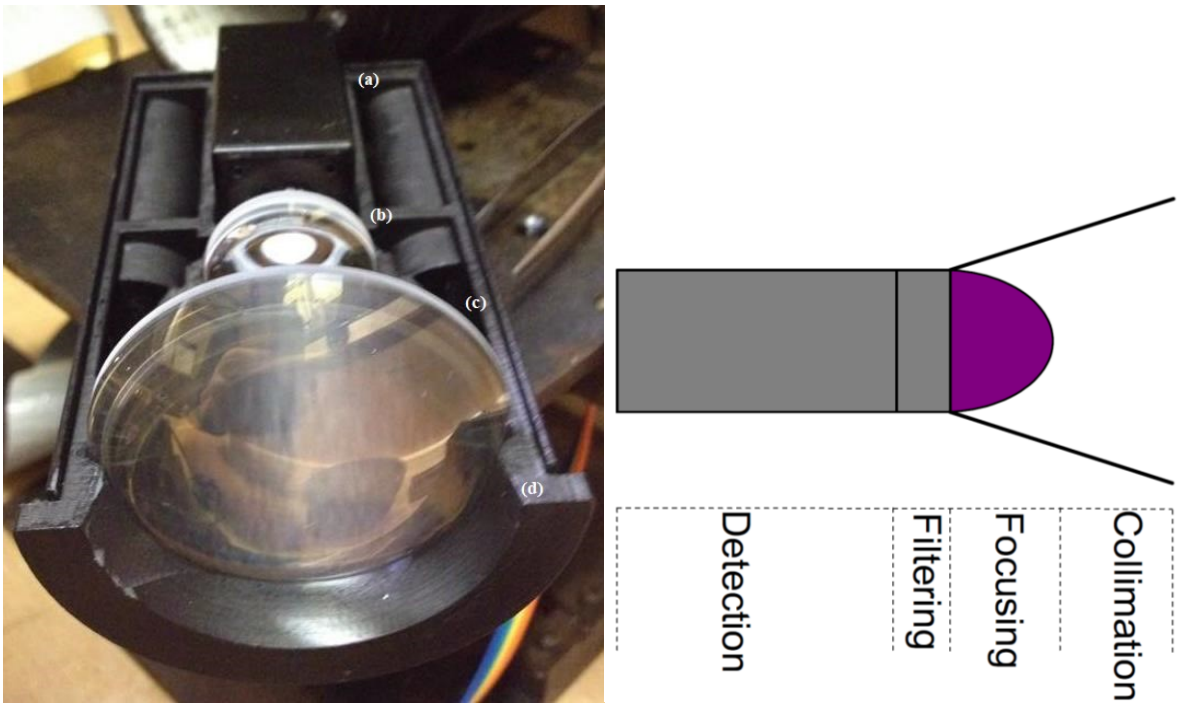


Figure 4.1: Left: Interior of the first edition of the detector prototype. Shown is the interior casing (mat black to reduce reflections) of half of the detector. From top to bottom components include (a) photomultiplier, (b) filter, (c) lens assembly, (d) collimation area.
Right: Conceptual composition of a non-imaging alpha-UV optical detection technology.

Illustrated in figure 4.1 is a conceptual representation of the components of a radioluminescence detector (right) alongside the first edition prototype (left).

From the emission of UV photons from a radioactive source, a detector's first component is typically some form of collimation. Without collimating an input it is challenging to define the directional sensitivity of the detector. In this case, given that the detector relies on the collection of UV photons, collimation is not difficult and can be achieved by a shaped

element of the casing, be it plastic or metallic. A further consideration should be whether collimation materials reflect UV light or not - this could be desirable (if attempting to collect a greater proportion of photons with poor directional refinement) or undesirable, for example where UV interference is observed, and non-reflective materials or coatings can be used.

The next area for consideration is the mechanism of concentrating or focussing the UV photons derived from radioluminescence. Given the likelihood that the optical detector's sensitive area will be relatively small, as illustrated in previous chapters detector systems are advantaged by having a larger effective solid angle relative to the source of emissions. As such optical concentration devices - typically lenses or metallic, reflecting concentrators - are possible choices. If a device seeks imaging capability or the ability to distinguish sources in different regions then the focusing device is of particular importance.

Optical filtration is the principal means of refining detector sensitivity to radioluminescence over other background sources, for example from conventional room lighting (400-700nm). This is one of the most important determinants of device performance, dictating overall detection efficiency (and so detection limits of the detector) and the environments in which a detector can operate. This is achieved using a variety of optical filtration devices, although the most relevant to this application are short pass filters and wide band blocking filters for in and out of band wavelength regions.

Finally after these detection parameters have been established the photo-detection technology must be considered. This is the device which ultimately converts photons into an electrical signal which can be digitised. Optical detection technologies range from photomultipliers of a number of types to CCD detectors to more exotic multi-pixel photomultiplier arrays which combine elements of both. Crucial factors for consideration in choice of detection technology are the sensitivity in the appropriate region of the electromagnetic spectrum and the noise associated with both the detector and any electronics.

Together these components represent the most significant elements of the detector's design. In addition detector design must incorporate an appropriate casing - fabricated to ensure light tightness, optimised to ensure a fixed optical alignment and positioning - which can also have impact on the detector's functionality.

4.1.2 Detector design parameters

Illustrated in table 1 are a set of the parameters used in the design of the detector system.

Component	Design Parameter	Explanation
Photodetector	High Sensitivity	It is necessary for the detector technology to have high sensitivity so it can detect photons in the appropriate wavelengths. This must reflect the desired wavelength band(s) of sensitivity.
	Large photocathode	For the detector to concentrate light effectively it is necessary to have a large photocathode. This enables adaptability in the optical design to a variety of distances as opposed to a single, fixed distance to which it is most sensitive.
	Low noise	Noise has the effect of masking the alpha-derived signal received from the detector, thus reducing detection limits and increasing required acquisition time. This could be derived from: dark counting, readout noise, shot noise, voltage ripple.
	Low rise/fall times	Low rise/fall times mean that consecutive pulses do not either overlap or pile up. This means that linear response rates can be maintained both at high and low input count rates.
	Not sensitive to other radioactive sources (e.g. beta/gamma)	To ensure that the detector is able to operate in mixed radiation environments in a reliable way (and exhibit a specific response to alpha-emitting radionuclides) it must be ensured that the photodetector is not sensitive to beta, gamma or any other form of radiation which it is likely will be encountered.
Focusing	Large area optics	In order to concentrate alpha radioluminescence photons from the largest possible solid angle it is desirable to employ large area optics.
	Made of materials transparent/reflecting at detection wavelength	Materials employed, such as lenses or mirrors, should be transparent at the wavelengths being detected. This typically means, for UV wavelengths, using fused silica lenses or polished aluminium mirrors, both of which have excellent UV performance.

	Optimised to operate over a range of distances	A considerable issue from an operational perspective of devices produced previously is that they operate only in a limited, fixed distance scenario. From an operational perspective this single distance may be either unachievable or inconvenient and so it is desirable that optics function over a range of conditions.
	Sensitive to a refined angular acceptance	As with collimation, the optical design process also determines the directional sensitivity of the detector system. An ideal implementation in this area will ensure that at the minimum anticipated operating distance that the detector will still be sensitive to a region large enough to incorporate the photons emitted by a point source.
Filtration	High transmission	While optical filtration's main role is to block photons of undesired wavelengths, refinement to the specific band desired must also be achieved at high transmissivity.
	Blocking of all interfering wavelengths	Dependent on the sensitivity of the photomultiplier being operated, the entire range of interfering wavelengths must be blocked where they are present in the environment being measured.
	Filters of the appropriate dimension and property	Some filters are often only effective, or only operate at manufacturers specifications, when light is incident at particular angles. This means that if the method of optical concentration includes non-axial light being incident on the filters then the specification of the filters must be appropriate.
Collimation	Ensures incident light from eccentric angles is blocked	Eccentric light is a very large contributor to background and having a physical block on light from certain angles minimises this contribution. It also ensures that sensitivity is refined to a particularly angular spread which is ideal for imaging.
	Does not interfere with operation at short distance	If operating in the near-field region (under 10cm) then it is possible the casing will attenuate alpha emissions from radioactive sources emitted into air. This will reduce with detector sensitivity. As such design of collimation must consider this and optimise apertures to not attenuate alpha particles being emitted.

Table 4.1: Parameters utilised in the detector design process, derived from the modelling and survey of past literature on alpha UV detectors.

4.1.3 Optical detection devices

A wide range of photodetection devices were considered in the detector design phase. As the project was focussed on producing a device capable of producing quantitative measurements of sources (with low detection limits and in relatively short time) this resulted in the choice to use a photomultiplier tube as the photodetector. Had priorities instead been on the ability to image and localise contamination in longer times this process would more likely have considered a UV-sensitive CCD detector or similar. Photomultiplier tubes by contrast offer a positive compromise, allowing with appropriate optical design discussed later the approximate localisation of sources while maintaining speed and quantitative data outputs.

Photomultiplier tubes are a type of vacuum tube containing a photosensitive cathode exploiting the photoelectric effect [32]. After being liberated and repelled from the cathode, photoelectrons are accelerated and multiplied many times by a series of successive dynodes at incrementally larger, positive electrical potential, toward a final anode where a much amplified signal is registered. The performance and efficiency (measured by number of individual pulses recorded per photon incident on the photocathode) of a photomultiplier are primarily determined by the material used in the photocathode and the physical and electronic design of the dynode and anode.

The final choice of photomultiplier tube was based on these considerations. The Hamamatsu H10721-210 photosensor module uses an ’Ultra Bialkali’ photocathode offering up to 43% quantum efficiency in the 300-400nm wavelength range.

The H10721-210 module incorporates the R9880-210 photomultiplier tube and the quantum efficiency of the variant used is reproduced in figure 4.2. This model has an adequate amplification to enable the analysis of individual photons (known as photon counting) and also incorporates the high voltage circuit to amplify a +5V input into a variable anode voltage of up to 1100V. This eliminated the requirement for a separate high voltage power supply.

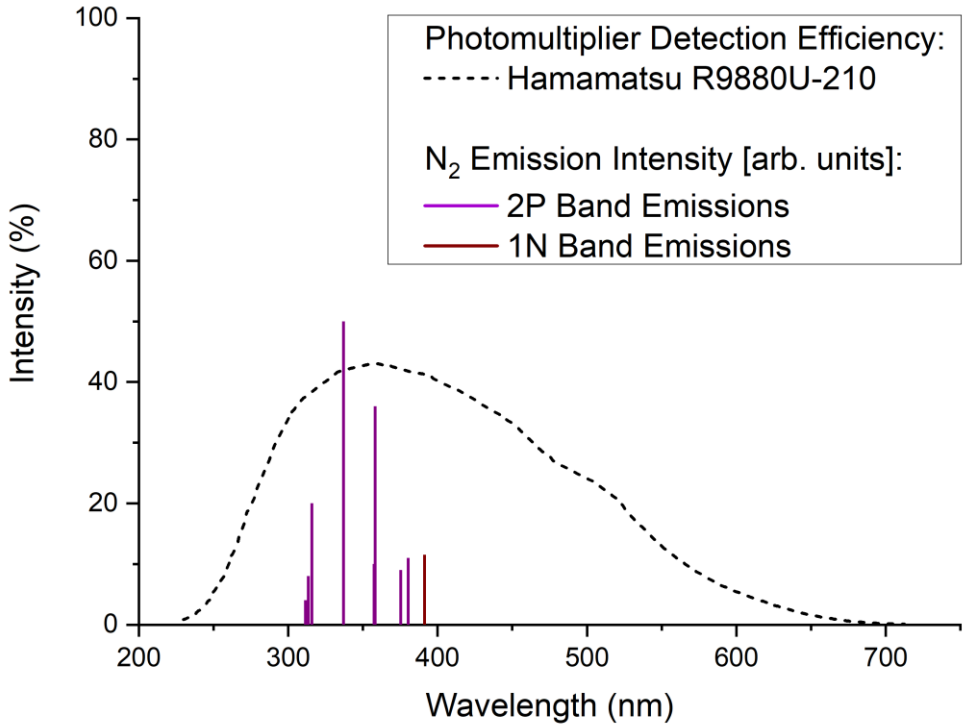


Figure 4.2: Quantum efficiency of the photomultiplier tube used in the detector (dashed) versus peak emission wavelengths in the nitrogen 2P and 1N band systems (purple and brown respectively). The region of peak detection efficiency coincides with the region of maximum emission intensity from 337nm to 380nm. Data obtained from the device's datasheet [78] and emission intensity data [49].

The capability of photon counting is a considerable asset in an engineered detector solution. Supply voltage circuits can be very complicated and suffer from environmental variation, leading to instability in supply voltages. As shown in figure 4.3 photon counting methods - in which the number of voltage pulse larger than a threshold are recorded in certain time periods - are significantly less sensitive to variation in supply voltage than analogue systems, which integrate all current received from a photomultiplier. For this detector this means that the system can be operated in different environments and over time without the need to re-calibrate to the particular environment of measurement.

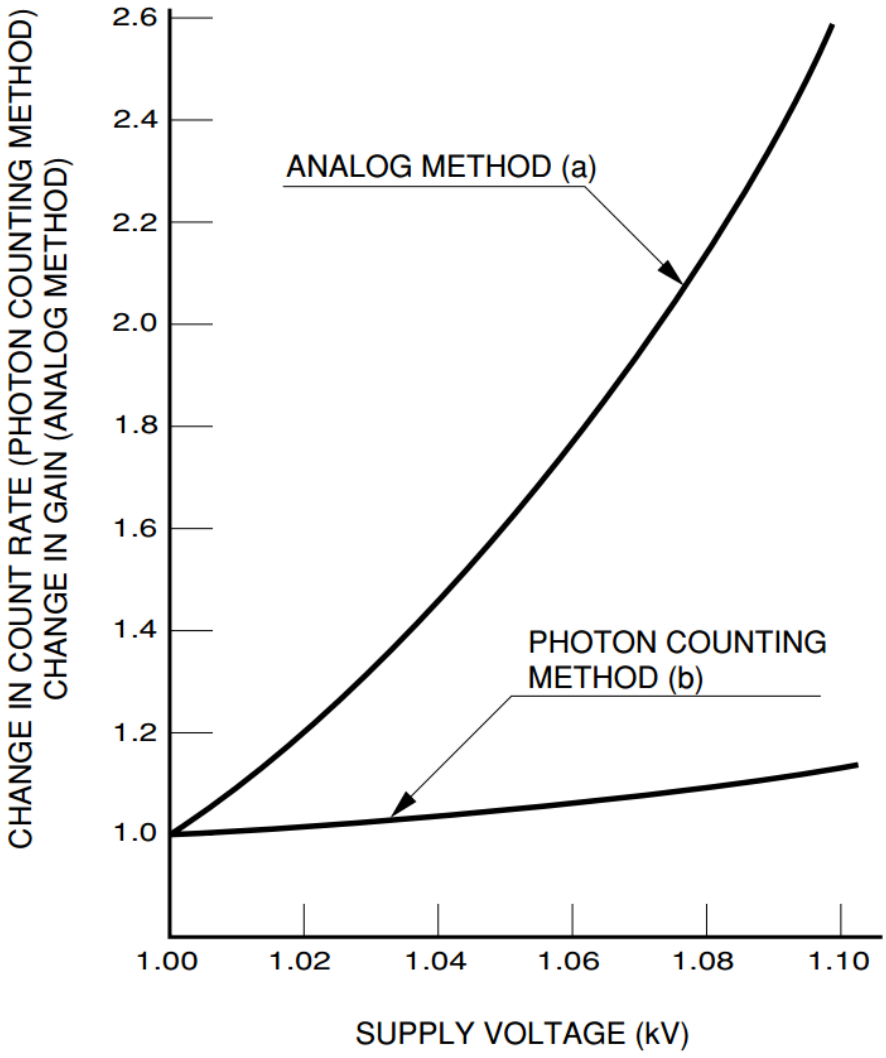


Figure 4.3: Photon counting, as compared to conventional analogue operation, reduces significantly issues associated with sensitivity to change in supply voltage. This means that photon counting methods are more practically useful in an engineered solution - and especially one in which consistency is required between different measurements in a calibrated system [80].

This photomultiplier also featured an 8mm photocathode - sufficiently large to easily focus light - and very low intrinsic noise - caused primarily by thermionic emission from the

cathode and dynodes - measured experimentally as approximately 5 counts per second in a completely dark environment.

The H10721-210 photosensor module meets all photodetector specifications anticipated in table 4.1. The further elements of casing and optical design now hinge on the physical casing dimensions of the chosen optical sensor module.

4.1.4 Optical modelling for lens design

Consideration of the focusing method initially required evaluation of available technologies for optical concentration within the design parameters. The following options were considered:

- Prefabricated, imaging lens assembly made of fused silica (for UV transmissivity)
- Custom designed lens configuration
- Parabolic mirror assembly with UV reflective coating
- Compound parabolic concentrator ("Winston Cone") of adequate aperture crafted out of aluminium

After assessing available options it was decided that a custom designed lens configuration would offer the greatest flexibility in research direction, optical filtering method and lowest cost. The cost of the assembly was also considered given the risk that the device may become contaminated and therefore have to be disposed of and replaced during experimentation. Additionally, while prefabricated imaging assemblies are available from commercial suppliers, it was impossible to find one which would accommodate field of view limiting or bespoke optical filtration.

While parabolic concentrators and mirrors appeared a possible solution it was difficult to optimise acceptance angles sufficiently. Most systems incorporating mirrors tend to operate most efficiently for light rays which are incident planar to the assembly. For alpha-derived UV photons typically light is emitted in all directions from the source. At short ranges (where photons incident on the detector cannot be assumed to be planar) mirrors and concentrators could not be shown to provide adequate focussing power.

As a result it was decided that optical modelling would be performed on lens assemblies with view to a final design meeting design criteria.

Given that the design criteria did not require that the device directly produce images, and instead prioritised having a defined region of angular sensitivity, the process of assembly design was approached differently. Optical modelling software was obtained (OpticalRayTracer, a General Public Licence optical ray tracing software [81]) and an iterative series of optical assembly designs were considered. The primary software used for this purpose was Optical Ray Tracer, a free optical modelling software incorporating all commonly encountered physical processes in optical lens design.

After a period of consideration of mirror-based solutions, a final decision was made to refine the process to purely lens based systems. While mirrors offered a promising ability to concentrate light, the number of options available which also offered specificity in the region of sensitivity was limited, without also incorporating a large lens or array of lenses before light was incident on the mirror.

After a series of revisions, a design was chosen utilising a combination of two lenses. This incorporated a 50mm fused silica (UV transmitting) plano-convex lens and a subsequent 25mm convex lens. The combination of these lenses provided a combination of the design parameters, including most notably the ability to direct eccentric light to the UV-absorbing walls of the detector rather than the photosensitive region of the photomultiplier. In addition for rays originating close to the optical axis of the system it was found that focusing onto the photocathode was still possible despite rays being incident at non-planar angles.

4.1.5 Optical filters

Another consideration addressed in the design of the detector assembly was a method to reduce the amount of light incident on the photomultiplier with wavelengths not arising from alpha-induced fluorescence. Given the increased background which would be caused by seeking to incorporate two peaks of the spectrum it was necessary to refine the detector's optical transmission to a maximum at the peak emission wavelength of the fluorescence - 337nm - and to minimise transmission to almost zero outside of this region, within the limits of the photomultiplier's sensitivity.

Given the H10721-210's sensitivity between 200 and 700nm this required a combination of filters and custom components. An initial design composed a single optical density (OD) 4, 337nm-centred 10nm bandpass filter produced by Edmund Optics. This filter offered peak transmission at 337nm of 90%. While this filter alone performed adequately in environments isolated from external light by black cloth surrounding the detector, it was noticed that if exposed then (visible wavelength) room lighting was interfering, producing spikes of >1000cps upon exposure, meaning that absorbance in the visible spectrum was not adequate.

An additional filter was chosen to reduce this interference in the 400-700nm visible spectrum. A filter glass product (Hoya U340 glass) offering high transmission in the 300-400nm UV range (80%) and adequately low transmission in the visible spectrum (<10^-3 %) was identified. This product was available in custom geometries and was acquired in a 50mm circular geometry to sit behind the plano-convex lens.

Filter	Transmission Wavelengths (nm)	Description
Edmund Optics (337±10)nm filter	332-342	Centred on the most intense emission band of the nitrogen fluorescence spectrum this filter refines transmission to appropriate UV wavelengths and blocks visible to Optical Density 4.
Hoya 2.5mm U340 Glass	300-400	Additional reduction in the transmission of visible light to enable functioning in ambient light conditions
Schott Fused Silica Glass Lenses	250-2000	Fused silica glass capable of transmitting UV photons of appropriate wavelengths. Antireflection coated.

Table 4.2: Optical components incorporated into final detection system.

After addition in combination with the Edmund Optical filter the detector recorded no interference from ambient room lighting. However, in environments with sources of UV light (e.g. external glass windows) and bright white lighting, high levels of interference (>10,000cps) were observed.

Within the final detection system the two optical filters were combined with lenses made out of Schott Fused Silica glass, specifically chosen for its high (90%) UV transmission at the appropriate wavelength (337nm). Final components are summarised in table 4.2.

4.1.6 Theoretical combined efficiency

To analyse overall transmission of 337nm photons arising from alpha-induced fluorescence and the blocking of visible light it is necessary to take manufacturer quantities for individual components.

Displayed in figure 4.4 is the manufacturer published transmission (and detection for the Hamamatsu photomultiplier) data for each component integrated into the final detection system. Using this, by multiplying the individual transmission probabilities for each component it is possible to construct an overall optical transmission probability for photons of each wavelength, and when combined with the detection efficiency of the photomultiplier, an overall detection probability for each wavelength (shown in solid purple colour). Displayed inset is a higher resolution plot for the region between 320-380nm.

This data illustrates that for the system, photons emitted on axis to the system at 337nm can be expected to be detected with a 24% probability, compared to the photomultiplier detection efficiency of 42% at the same wavelength.

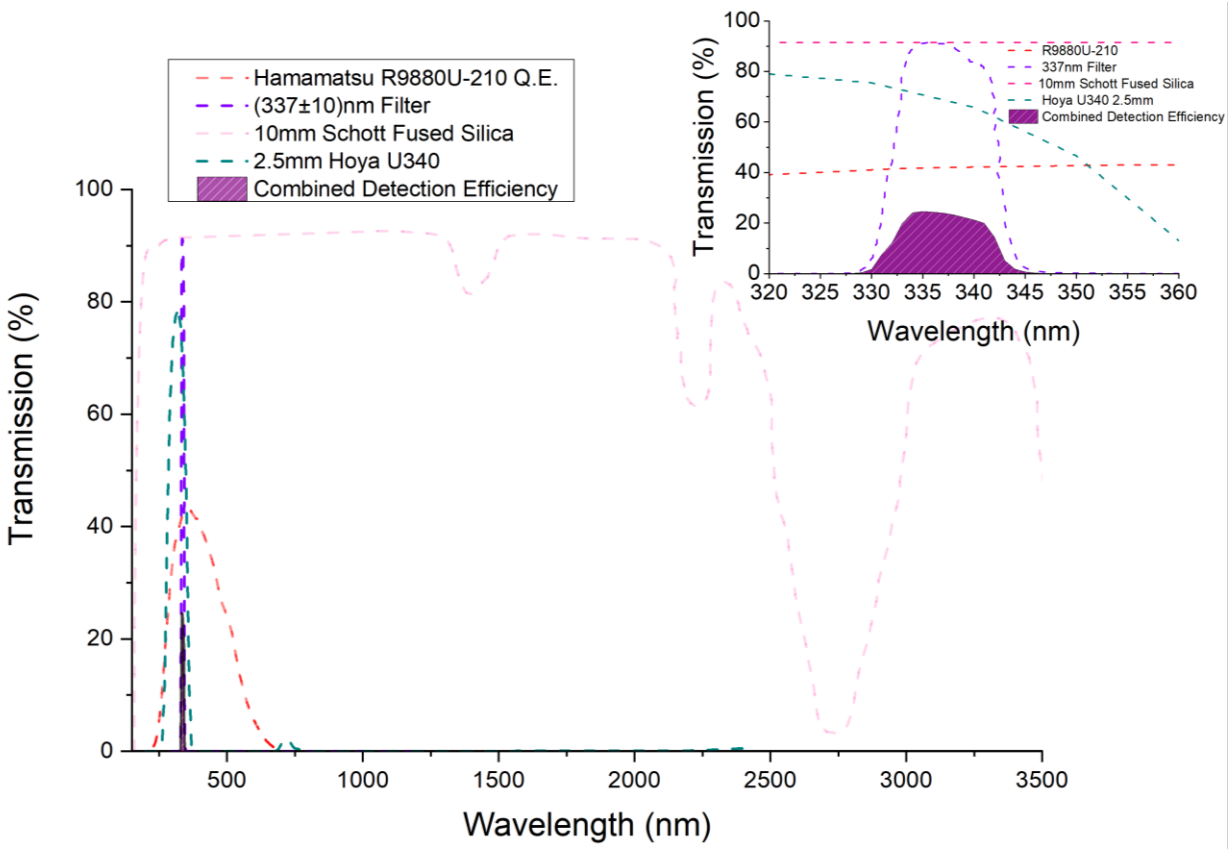


Figure 4.4: Transmission data for optical components of the detector system illustrating the proportion of normally incident photons transmitted through the optical assembly compared to those absorbed for each component (dotted lines), and those detected by the photomultiplier (solid purple). The detection of photons incident on the system is highest for wavelengths between 334-337nm (>20%) and reduces steeply to a negligible (<0.1%) proportion detected outside the 327-347nm range. Given the variety of components incorporated no wavelengths other than those close to the most prominent 337nm nitrogen fluorescence emission contribute in a measurable way to the photomultiplier's output. Inset: rescaled optical system transmission between 320-360nm.

4.1.7 Mechanical casing design: additive manufacturing

After finalising the layout of components it was necessary to design an appropriate casing to house these in place in a fixed and stable environment to ensure consistency between measurements. This was achieved by taking the conceptual layout of components previously discussed and converting this into a design capable of being produced using a 3D printer.

A computer-aided design program, 123 Design (published by AutoDesk), was used to produce a design. Displayed in figure 4.5 is the computer representation of the casing. Each component was fitted to a tolerance of approximately 0.2mm compared to manufacturer values, producing optical tightness. The casing was produced in two halves (see figure 4.6), one with a tapered edge which fit into a groove on the underside casing. Grooves were raised around the photomultiplier edges to ensure no light could pass through the split of the case. The entrance aperture was optimised to contain without attenuation the emissions of an alpha-emitting point source radiating in all directions - with the entrance cone being >8cm wide and approximately 5cm deep. The geometries of the walls of the casing provided collimation of any light incident on the detector at angles in excess of 53 degrees.

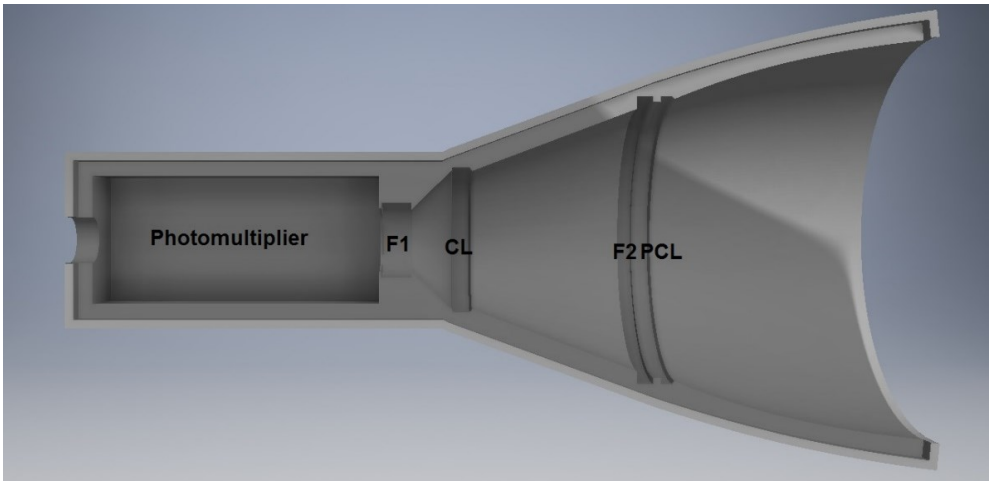


Figure 4.5: Component layout of the second edition detector casing, illustrating the photomultiplier tube, Edmond Optic 337nm filter (F1), convex lens (CL), Hoya U340 filter (F2) and plano-convex lens (PCL). The collimation cone (shown to the right of the plano-convex lens) was sized to accommodate an alpha particle corona for a point source.

Displayed in figure 4.5 is the component layout of the system. In the position labelled F1 is the Edmund Optics 337nm filter placed immediately in front of the photocathode of the photomultiplier tube. The label CL refers to the fused-silica convex lens. F2 is the crafted Hoya U340 filter and PCL refers to the fused-silica plano-convex lens. Each component was sufficiently tightly fitted, according to dimensions quoted on the manufacturer datasheets, that when shook they did not rattle within the casing.

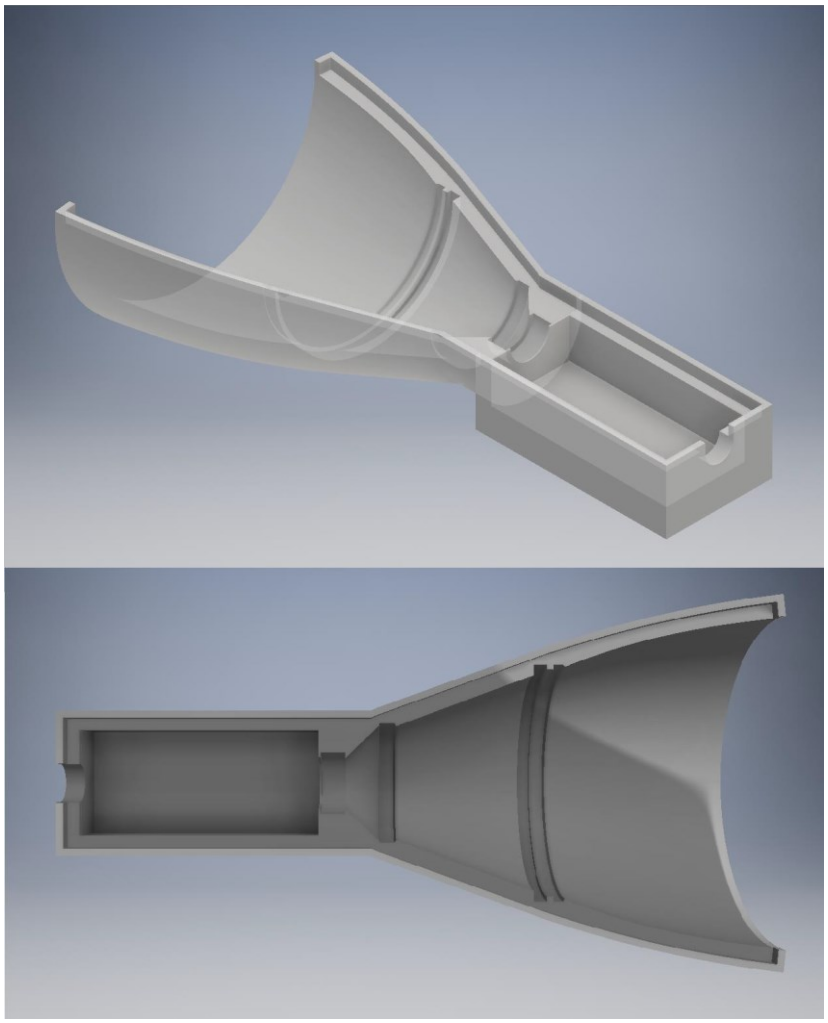


Figure 4.6: CAD drawing of final detector casing layouts displayed illustrating the adjoining edges of the top and bottom half and the cross section of the casing. Images produced using 123 Design, an AutoDesk product used for 3D modelling for 3D printing [82].

4.2 Data acquisition equipment design and selection

4.2.1 Electronic controller design

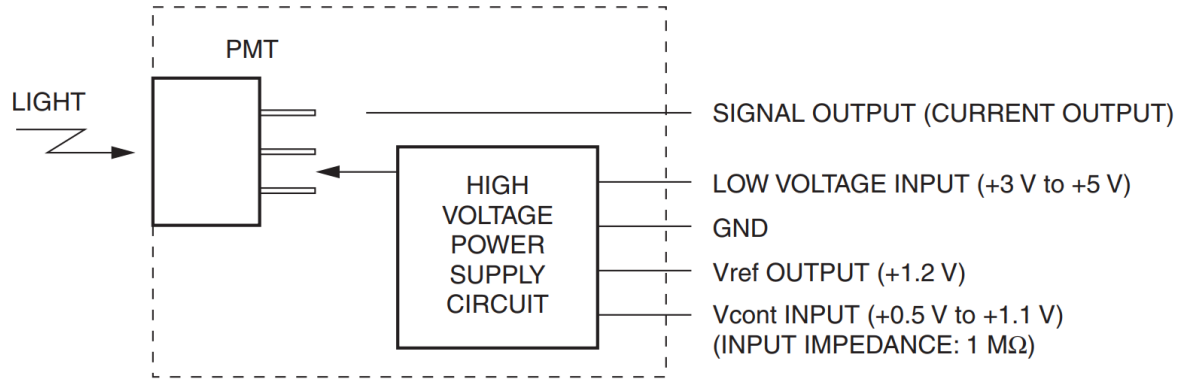


Figure 4.7: Schematic representation of the H10721 photosensor module. In addition to the photomultiplier tube (PMT) it also provides a high voltage power supply circuit which can be driven by a 3-5V while providing the 1000's of volts required for the photomultiplier's operation [83].

A fundamental element of the detector's functionality is the electronic control of the photomultiplier tube and its outputs. The H10721-210 photosensor module contains a high voltage power supply circuit, as illustrated in figure 7, in addition to the R9880U-210 photomultiplier tube [83]. This circuit enables the use of a 3 to 5V power supply rather than the >1000V supply ordinarily required for photomultiplier operation. In addition it provides a simple interface for the control of the sensitivity of the photomultiplier, with an input control voltage of between 0.5 and 1.1V determining levels of sensitivity.

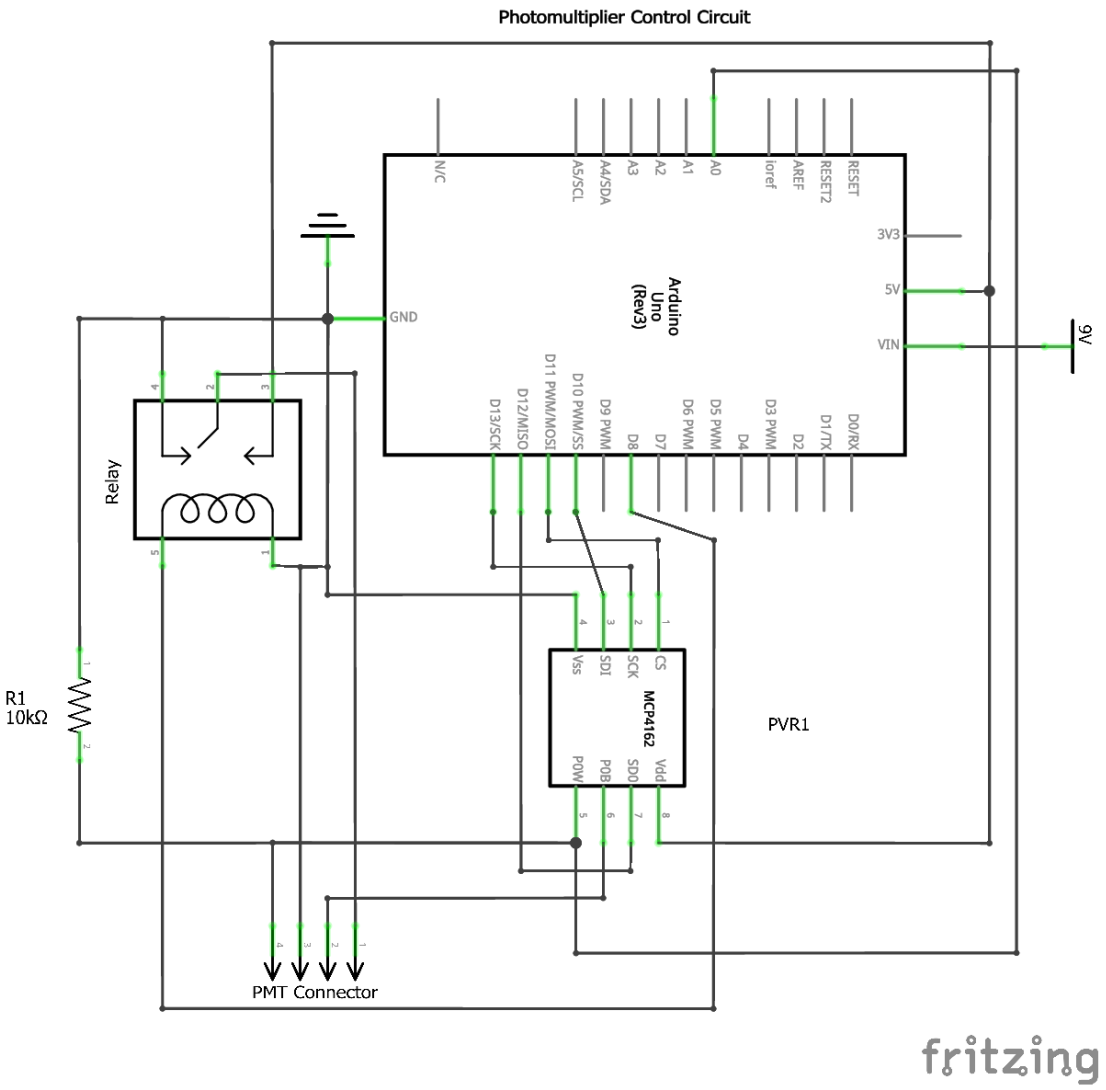


Figure 4.8: Circuit diagram of components used to control power and level of sensitivity of photomultiplier tube. Pins 1,2,3 and 4 of the photomultiplier connector correspond to the (1) low voltage input, (2) *Vref* photomultiplier 1.2V output (3) Ground, and (4) the *Vcont* photomultiplier input. Image produced using fritzing, a computer-aided design program, under a General Public Licence [84].

The manufacturer suggested implementation of this control circuit uses a potential divider circuit between the reference voltage (*Vref*) and a potentiometer. While easy to implement using a manual potentiometer the practical implications of using a physical dial to control

sensitivity has the potential to reduce repeatability of measurements, with difficulty in achieving identical positioning between measurements.

As a result an alternative system was designed for the control of the photomultiplier. Using a digital 10kΩ rheostat integrated circuit, the MCP4162-103E/P, control of the sensitivity of the photomultiplier was achieved using an Arduino microcontroller. With 257 resistance steps the MCP4162 can be controlled using a communications interface to give differing levels of resistance. Illustrated in figure 4.8 is the complete circuit layout of the chip, microprocessor and a relay used to control the on/off state of the photomultiplier tube, in turn controlled by the digital switching output of the Arduino Uno R3.

4.2.2 Microprocessor firmware design

Using an SPI (serial peripheral interface) protocol between the Arduino Uno R3 microprocessor and the MCP4162 it was possible to use an inbuilt Arduino SPI protocol library for the control of the sensitivity. In practice this meant that firmware developed for the Arduino could adjust resistance across the integrated circuit by communicating an integer between 0 and 256, corresponding to the variety of resistances offered by the circuit, across the SPI.

The firmware contained functionality to switch the relay circuit controlling the powering of the system on and off.

A visual interface was created for the system for use during the project, illustrated in figure 4.9. Using a USB-based serial interface this interacted with the Arduino microprocessors firmware to switch on and off the relay controlling the photomultiplier tube's power supply. A slider function was provided to change the MCP4162's 257 levels of resistance using an integer passed over the serial interface, thus in turn adjusting the sensitivity of the photomultiplier. In response the interface would report a voltage measurement assessed by the Arduino's internal voltmeter function to assess the reference voltage being input to the photomultiplier system. The interface provided facility to initiate measurements on the data acquisition system (DAQ) including the threshold at which pulses would be registered, although in practice it was often more practical to use the manufacturer's provided software for this purpose.

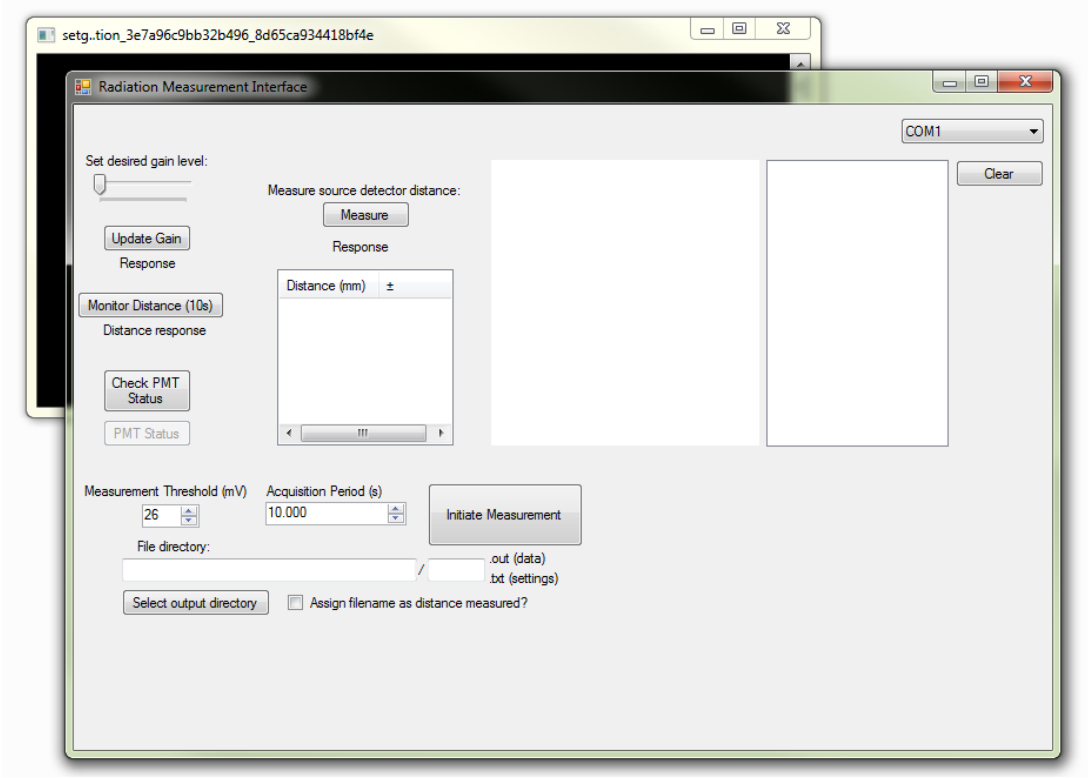


Figure 4.9: An interface made in Visual Studio using the C# programming language to control elements of the detector system. Control of the various components was achieved using a USB-based serial interface to control the Arduino Uno board and bespoke C# libraries to interact with the DAQ controller.

4.2.3 Choice of photomultiplier DAQ unit

A core consideration for practical use of the detector system is the data acquisition (DAQ) unit. This is the unit which converts the output of the photomultiplier tube into a digital format of use to the final user.

The most significant considerations during the choice of data acquisition system were the timing resolution of the system (the minimum time gap between pulses required to distinguish them as distinct), compatibility with the photomultiplier system and whether the system would require preamplification of the photomultiplier tube's output.

After consideration the system meeting these criteria was the PicoQuant TimeHarp 260 Nano. This system offers resolution of 1ns and produces records of pulses registered by the system. This ability provides the option to analyse, identify and extract erroneous data and assess the reliability of observations. In addition, the short dead-time of the system (1ns) means that the risk of counts being missed due to the system being over-exposed is unlikely in intended operation.

The TimeHarp Nano 260 benefits from native compatibility with the Hamamatsu H10721-210 module without the need for a preamplifier. A possible limitation may be the cable length (20cm). If necessary to extend this length then a pre-amplifier would be necessary.

4.2.4 After pulsing correction

An intrinsic property of photomultiplier tubes is afterpulsing. Afterpulsing, the production of multiple electronic cascades in a photomultiplier tube from a single photon, occurs due to the presence of residual gases within the photomultiplier tube being ionised and subsequently interacting with the photomultiplier dynode, thereby producing secondary or tertiary cascades without a corresponding photon.

After connecting the system and verifying that it was functional, the system was evaluated for signs of afterpulsing or any deviation from expected Poisson-distributed inter-arrival statistics.

The Poisson distribution is described by the equation $P(k) = \frac{\lambda^k}{k!} e^{-\lambda}$ where the number of events k=0,1,2,... and λ is the mean rate of occurrence in some period.

For Poisson-distributed processes, such as radioactive decay, the probability that no events (k=0) have occurred after an elapsed time t can be expressed as:

$$P(k(t) = 0) = e^{-\lambda t} \tag{4.1}$$

where λ represents the global mean rate at which such events occur. This time could be measured from any arbitrary start.

Given that the Poisson distribution describes probability of events which occur completely independently of one another it is equally possible that this time could be evaluated as the elapsed time since another event was observed.

This elapsed period between observations of events is a quantity which is readily measured, be it the mean time between customers arriving in a shop or period elapsed between radioactive decays.

As demonstrated in equation 4.1 the probability distribution of these periods of no observation (referred to as interarrival periods) is an exponential decay, meaning the longer the time elapsed the less chance that no events are observed.

Shown in figure 4.10 is the experimental measurements of two americium sources using the detection system as described in section 4.1. The distributions are binned to allow representation of the distribution and are illustrated using a log-normal axes.

The trace illustrated in red is of a source of approximately three times lesser strength than the black source. This has a corresponding impact, as expected, on the gradient of the exponential distribution (represented linearly due to log-normal axes).

An unexpected feature of the detection system is the large deviation from the exponential distribution illustrated at small values on the time axis. This feature indicates that a higher than expected probability of shortly-followed counts is observed. This effect is likely explained by the afterpulsing phenomenon of photomultiplier tubes, by which a single photon can induce multiple discharges of the photomultiplier's dynodes due to ionisation of material within the vacuum tube.

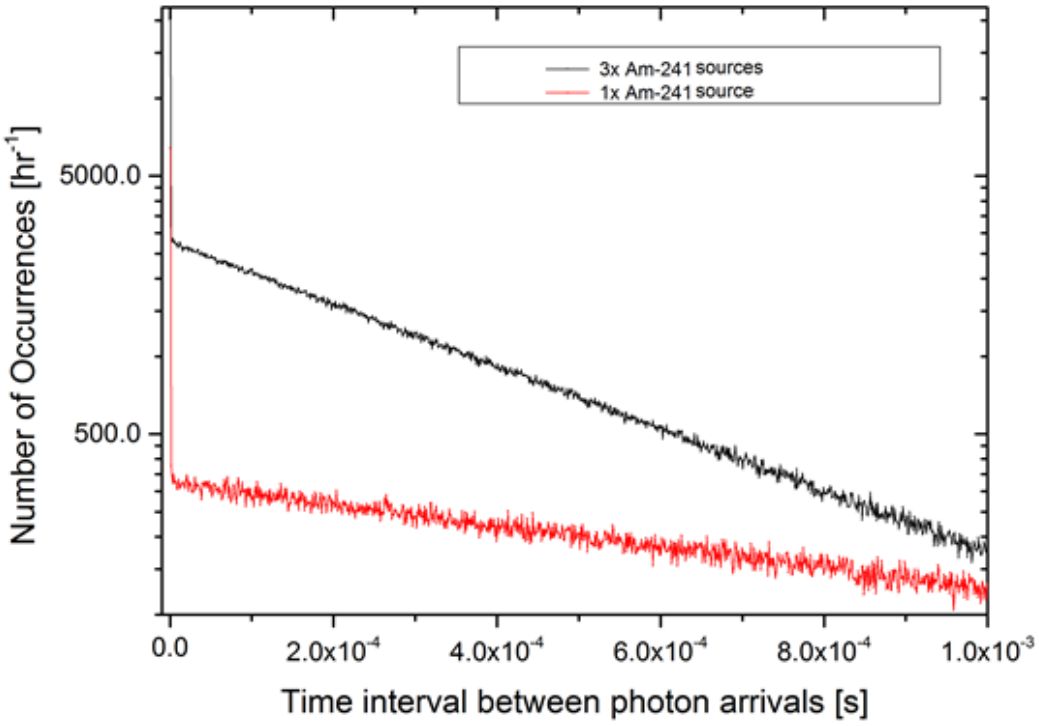


Figure 4.10: 100ns histogram of interarrival periods of two americium sources measured using the detection system illustrated using a log-normal axis.

In its uncorrected form the detection system reported non-linear response to alpha-emitting radioactivity and other sources of light to which it is sensitive. This was demonstrated to be true by measuring six individual radioactive sources on their own, and then again in combination. Due to the tendency for non-Poisson distributed results the results in combination were elevated compared to the additive sum of their components.

This deviation from Poisson-distributed behaviour was observed on all traces produced by the detection system and as such a solution had to be implemented. This was achieved using the simplest solution of imposing an artificial, post-acquisition dead time. Thus for each observed discharge of the photomultiplier a period is initiated in which no further counts are recorded by an algorithm after data is measured by the system. As illustrated in figure

4.10 this process removes completely the segment of the graph which deviated from the linear (exponential on a normal axis) trend.

It is then necessary, in order to produce analytically valid results, to correct this using a conventional non-paralysable dead time correction, as is frequently employed in radiation metrology, to correct for the lost counts. This correction takes the form of:

$$n = \frac{m}{1 - m\tau} \tag{4.2}$$

where n, m and τ represent the true interaction rate, recorded interaction rate (with dead time) and the dead time respectively.

The net effect of doing so is to restore the lost segment to the broader linear trend. The period of dead for the optimal removal of afterpulses from the system, illustrated by the deviating segment, was found to be 20μs. In all subsequent reported measurements this artificial dead time and subsequent correction was applied.

4.3 Conclusion

The system developed under the project took approximately six months for initial development, with further refinements incorporated up to one year. The result was a functional device which can detect alpha-induced radioluminescence in a variety of practical scenarios. The system will be used in later sections to demonstrate the various methods suggested for detector operation and to prove the concept of calibrating detector response.

The use of 3D printing methods, field-programmable microcontrollers and bespoke optical designs meant that revisions to the design of the system were possible in considerably shorter timescales than commercial equivalents. The use of these methods also led to a considerable reduction in cost compared to projects presented earlier, with all equipment incorporated into the detector assembly costing less than £1,000. The major expense was the DAQ system, which was intentionally chosen to provide the highest level of detail possible. For a commercial device this could be replaced with a system at relatively low cost.

The following chapters will propose methods for the assessment of device performance in a wide variety of scenarios and modes of operation.

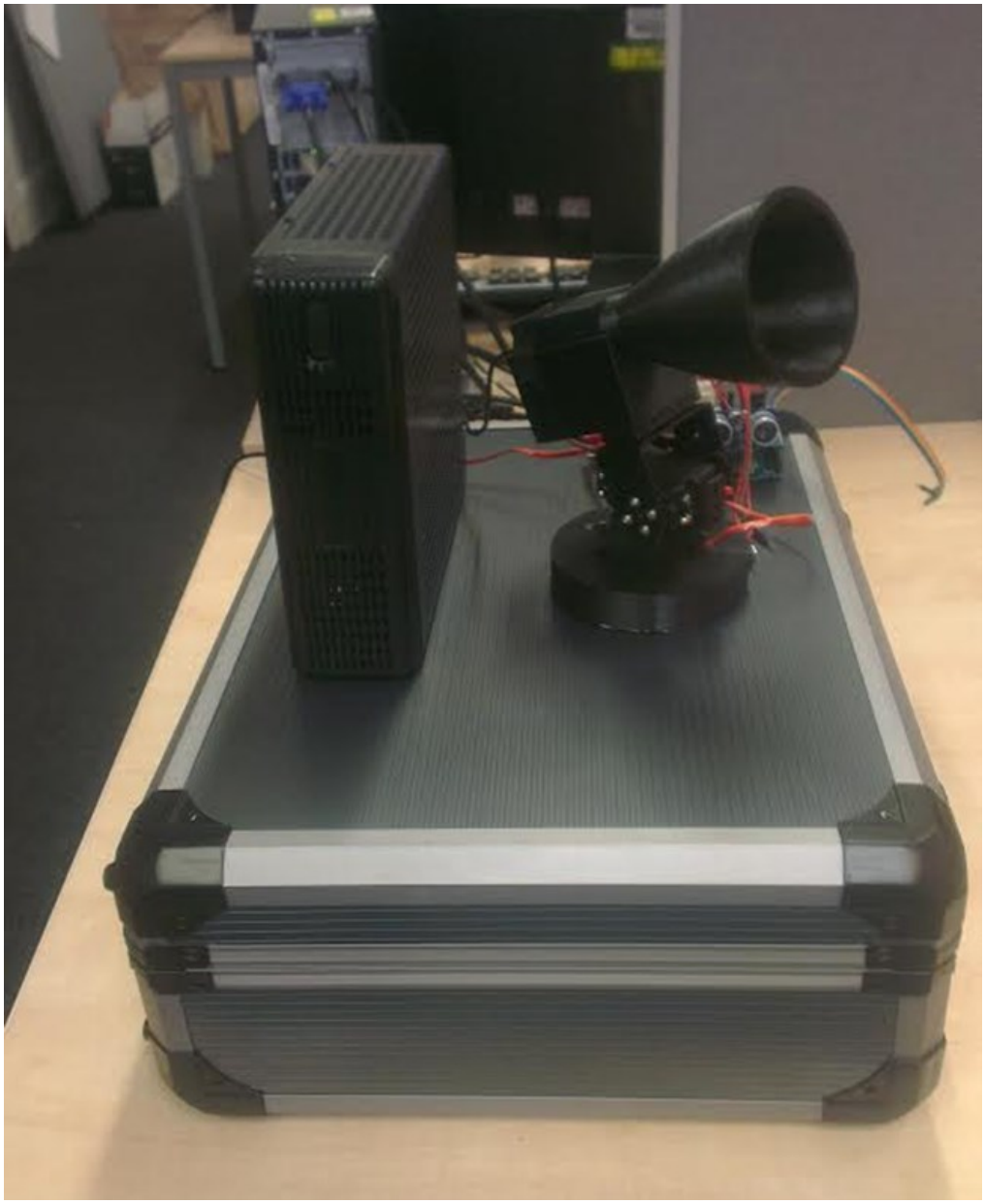


Figure 4.11: The final detector system developed for use in experiments presented in later chapters. The system is shown on top of a briefcase-style case used to transport the system to sites for measurement. From left to right the system incorporates: a miniature PC, the detector on a pan/tilt assembly and a small Arduino-based electronic control board.

Chapter 5
Development of Calibration and Operational Methods

The primary aim of the detector's development in the previous chapter was to produce a device which would be capable of quantitatively measuring the activity of alpha-emitting radioactive sources. To demonstrate this capability, initial measurements were performed using sources of known radioactive composition and geometry to understand the device's response to known conditions. It is intended that after establishment of calibration, sources of unknown levels of contamination can then be presented to the system and its response will indicate a calibrated measurement of the activity of the source.

This chapter outlines the development, testing and comparison of four methods for the calibration and use of detectors sensitive to alpha-induced UV fluorescence. Initial focus is on the most basic method which is currently used for traditional probe detectors – manually placing a source in front of a detector, measuring for a fixed time, removing it and measuring again. A number of limitations are discussed, with the most significant being that any manual interference with the source is likely to adjust the light environment for the second measurement, reducing calibration precision and repeatability.

The second method developed uses an electronically controlled mechanical device to shield the source from the detector, removing the need for human intervention. This was found to alleviate some of the issues identified with the manual method.

Next, the device discussed above is placed on a manoeuvrable platform to establish a calibration over a range of distances between source and detector. This is significant as in the remote measurement of a source or hot spot it may not be possible to accurately fix the distance between source and detector. By applying a calibration which can be applied over a range of distances this method increases the range of potential uses of the technique and reduces the time required to obtain a series of measurements.

The third method outlined is based on the scenario of a conveyor-style scanning system. A radioactive source is passed under a stationary detector held by a stand and clamp. It is concluded that this method could be deployed effectively used in industry so long that the possible limitations are properly understood.

Finally, the chapter looks at how quantitative measurements and a device calibration could be obtained for “imaged” scenes containing potential contamination. It is concluded that while there are methods which could be employed to identify peaks and backgrounds, the limits of detection and accuracy of such measurements are likely to be less favourable than the other methods.

The detector used for experiments was that described in chapter four, but it is intended that these methods are applicable to any detector using radioluminescence to measure alpha-emitting radioactive materials.

While ideally calibration measurements, in keeping with analytical convention, would have been performed using internationally traceable, standard sources of known geometry, limitations of available sources meant that most data presented was obtained using a set of six Americium-241 radioactive sources, nominally of 33kBq activity each.

Results arising from these sources are presented for each calibration method and used to assess the relative validity and accuracy of each, and this is developed in the subsequent chapter using internationally traceable standard sources. For comparisons of each method’s relative merits this data can be considered useful as a metric but should be considered only as made from sources of unknown overall activity and surface contamination, and so no estimate can be made of the detector’s efficiency overall. However, such sources are perfectly acceptable for the purposes of obtaining measurements of the relative changes caused by measurement conditions (e.g. relative detection efficiency of the detector at different measurement distances).

5.1 Motivation for calibration

5.1.1 Established calibration methods

Several established International Standards exist in relation to the calibration and use of devices for radioactive surface contamination measurement. Recent international standards on this topic are ISO 8769:2016 “Reference Sources – Calibration of surface contamination monitors – alpha-, beta- and photon emitters” and ISO 7503:2016 “Measurement of Radioactivity – measurement and evaluation of surface contamination” in relation to the radioactive sources and methods used to calibrate such devices [85][86].

The devices addressed in these standards are detectors which detect radioactivity by the direct interaction of the emission with the detector itself. As such the calibrations discussed in these standards differ from an ideal calibration of a device which detects radioactivity by observation of indirect physical processes remotely.

This distinction can be explored by consideration of the proposed methods for direct calibration outlined in ISO 7503-1 [86]. Annex A of the ISO specifies the following guidelines:

- The calibration programme is determined by the nature of the expected contamination scenarios to be encountered (e.g. particular radionuclides or surfaces)
- It is important that the activity value is traceable to a national standard. Aliquots of this solution can then be allowed to dry on a representative sample of the surface.
- Two calibrations should be used, one representative of a point source and another representing a uniform distribution over an area larger than the detector probe (referred to as a “semi-infinite” source).
    - Using the two it is possible to assess variation of detection efficiency across the entire entrance window.
- Each calibration factor is only relevant for the radionuclide concerned on the particular surface.
- It is recommended that a separation of minimum 3mm, and surface of minimum source attenuation (typically anodised aluminium), is used for comparison to confirm manufacturer calibration factors.

- To determine the calibration factors for an alpha-emitting source, a practical method is to use a fixed 3mm distance. It may be sufficient to use a single radionuclide.

For satisfactory calibration of a conventional probe-type detector these guidelines prescribe a measurement at a single, fixed distance and a combination of sources which can evaluate the uniformity of response across the device's entrance aperture and on average. Using this method, it is possible to compare to manufacturer values to evaluate device performance and compare attenuation of sources on different matrices to consider measurements in different environments.

5.1.2 Establishing a calibration for UV fluorescence

The indirect UV fluorescence detection method differs in a number of ways which motivate a modified approach to calibration. The foremost of these differences is that given the indirect nature of the detection method, and the need for the alpha particles to interact fully with air, a fixed measurement distance of 3mm is not ideal as there is the potential for attenuation of the emissions by the casing of the detector.

Instead, for detectors measuring the UV photons resulting from the fluorescence of nitrogen in air, a more appropriate approach would be to take a fixed distance beyond the radius of emissions of an alpha-emitting source. It is therefore appropriate to consider materials potentially encountered in practical environments where the detector may operate.

Summarised below are a range of alpha-emitting radionuclides commonly encountered in a decommissioning environment. Shown are the decay routes with the largest branching ratio [87][39]. As shown for energies varying between 4.27-6.1MeV particle ranges of between 2.7-4.75cm are encountered:

Radionuclide	Energy (MeV)	Range (cm)
Am^{241}	5.49	4.0
Pu^{238}	5.59	4.15
U^{238}	4.27	2.7
Cm^{242}	6.10	4.75

Given a maximum distance travelled by emissions it is appropriate that a calibration performed using the UV-fluorescence technique must occur at greater than 4.75cm. As such for calibrations against common radionuclides it is advisable that fixed distance measurements occur at >5cm distance.

5.1.3 Attenuation over distance

Another way in which the UV fluorescence technique differs is that alpha-sensitive probes ordinarily operate only at a small range of distances from the contaminant, limited by the range of the alpha particle emissions. By comparison, the UV photons emitted by fluorescence travel until they are absorbed either by the atmosphere or in collision with other objects. This means that while probes have a limited effective range determined by the extent of the particle emissions, UV fluorescence detection has a far greater range determined instead by absorption of photons at further distance.

As such, any calibration of such a device must also account for the variety of relevant scenarios in which the detector could be used – at short or long distance to source. Given that the lower limit of reliable operation is determined by the range of particle emissions (up to 5cm), at ranges greater than this it is appropriate to measure the detector response at practical distances greater than this, and those in which the detector is expected to operate.

Practically this consideration expands the variety of operational scenarios from a single point (for a probe) to a scale of distances. As has been illustrated in previous work in chapter 3 the nature of this relationship is an attenuation, as the peak intensity is reduced over distance by inverse-square laws and other effects. It is anticipated that at the relevant scales (>5cm and up to 1m depending on source) this relationship is to be regular, single valued and well defined for similar source geometries, meaning that the relationship between intensity and distance can be sampled at appropriate intervals, interpolated and approximated using regression analysis to establish the detector's relative effectiveness over this scale for each source.

Considering these differences, it is possible to design a new method accommodating the need for the detector to operate at different distances.

5.2 Method development

5.2.1 Manual Remote Calibration

The simplest method to address the problems outlined is to implement the same type calibration at a fixed distance but to modify the prescribed distance beyond the 5cm alpha particle boundary. The method for implementation is simple and can be outlined as:

- Ensure light conditions will not over-expose detector. Reduce sources of background light.
- Position radioactive source on a non-reflecting surface
- Position detector so that the central axis of the detector is aligned with the source centre
- Initiate measurement for a period appropriate for the strength of the given source to ensure that sufficient counts over background are present
- Remove radioactive source from holder and replace into shielded container
- Initiate measurement for the same period in identical conditions without radioactive source

Using the two measurement scenarios it is possible to analyse the contribution from the radioactive source and other light sources and intrinsic photomultiplier noise (background).

As an illustration of this technique this measurement was performed using 6 americium sources in laboratory conditions. For the purposes of comparison, the same six sources have been used in the same conformation in all measurements presented in this chapter:

68mm	Counts	Period (s)	Observed Count Rate (cps)
Source and background	64233±250	280	229.40±0.91
Background	4399±70	280	15.71±0.24

Table 5.1: Measurement of the UV photons detected during measurement of six americium-241 sources at 68mm using the manual calibration method.

The measurement distance quoted is, in keeping with the prescriptions of ISO-7503, made between the outer edge of the detector casing and the active surface of the source.

This method was utilised considerably in the initial phases of detector operation to understand the device's sensitivity. After many measurements were performed at a variety of measurement distances several conclusions became apparent:

1. Given the need to physically disturb the system between measurement of the background and background with radioactive source measurement discrepancies were observed where the level of background interference changed. This was especially true of measurements performed in environments where the removal/insertion of the source required a change to confinement from the outside environment. An example of this was when measurements were performed inside an aluminium light tight box in which significantly different level of background would be observed after opening and closing it. This meant that the assumption that the background was the same across both measurements did not hold, and so reliable data was difficult to obtain.
2. The process of obtaining a calibration over a wide range of measurement distances is prone to error and requires the operator to perform many manual, repetitive measurements.
3. Given the long duration over which measurements are performed the external environment can often be affected by external environmental changes in light levels (e.g. varying levels of sunlight, need for room lighting) resulting in a background skew across both individual and the series of measurements.
4. It is often practically difficult to assess whether a source is centrally located on the axis of the detector, meaning results can significantly deviate between repeat measurements. For example, if the source is off-axis by 2cm at close measurement distance a reduction in signal of approximately 20% is observed.

These observations highlight the difficulty of applying the standard calibration method for probe detectors to a remote fluorescence device. In particular, the need to confine the system and to fix the external environment of the system between active and background measurements motivates a considerable change in method.

5.2.2 Mechatronic UV confinement

The first method devised to resolve these challenges (and particularly (1)) utilised a mechatronic system to control the physical confinement of the light emission from the source itself. A potential solution to the changes in external light condition between measurements is to create a system which itself confines the source's light emissions, in-situ, from the detector which can be controlled externally.

Given that photons emitted with UV wavelengths are readily attenuated by most optically opaque materials (e.g. coloured plastics) this confinement would not need to be complex and would only have to ensure that the line of sight from the source to detector was obscured. This could be achieved in any number of ways, and even by the attenuation of the alpha particle emissions themselves.

Illustrated in figure 5.1 is a design of the first version of the source confinement device. The device is designed such that if a source planchet is secured using the lip holder it can be rotated using a motor placed within the lower circular platform. During an active measurement the motor can be used to orientate the planchet to face outwards, meaning that radioactive emissions evolve into open air and the resulting fluorescence photons are able to propagate in any direction including toward the detector. Once a background measurement is required the device can be oriented using the motor such that the planchet is confined by the surrounding plastic, effectively confining completely the source from the external environment. This principle is conceptually illustrated in figure 5.2 where the confinement method is shown with radioactive emissions (purple) producing UV photons (arrows) which are either allowed to propagate (b) or are retained within the interior of the confinement device (a).

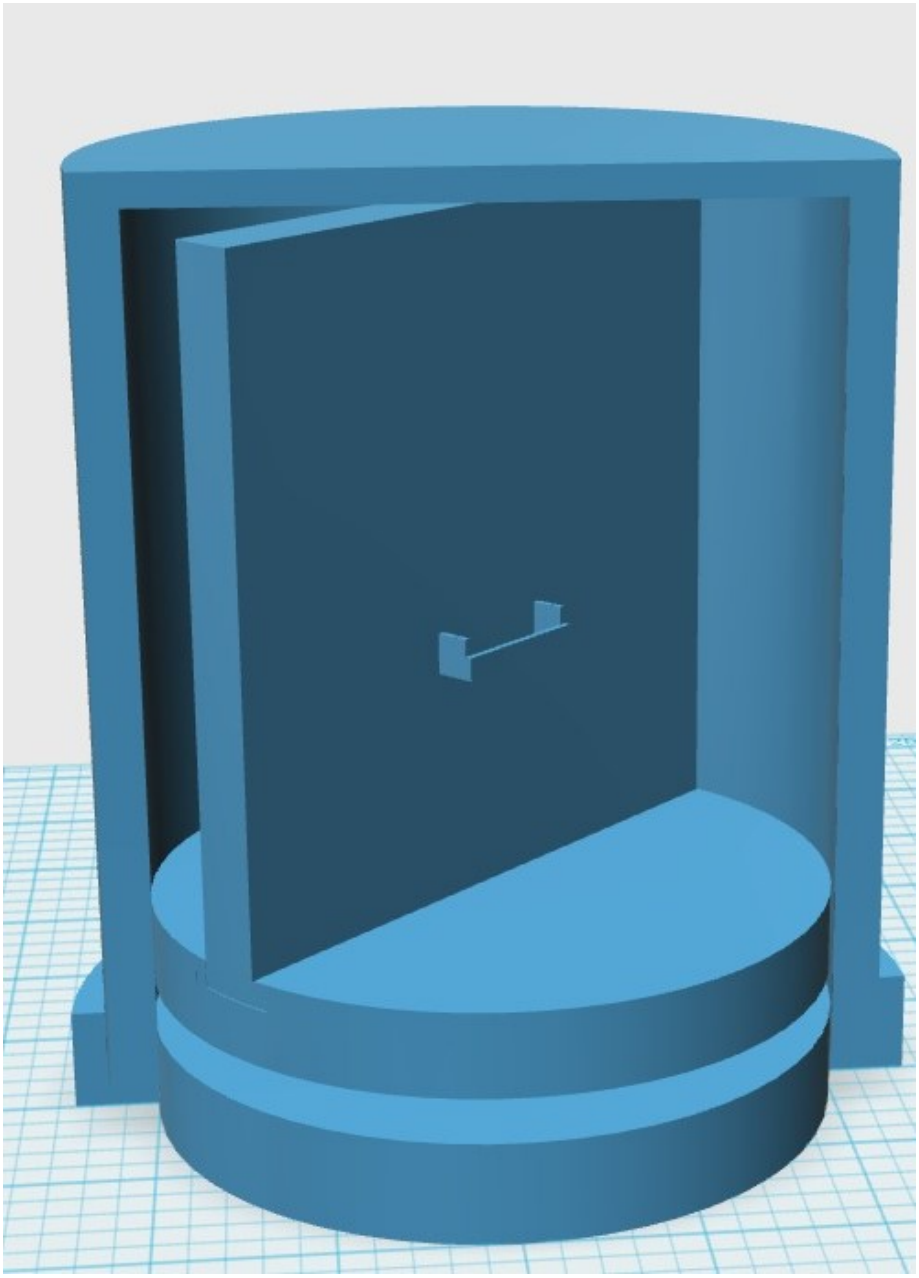


Figure 5.1: Computer aided design representation of the first edition, modular UV confinement device. This device provides a mechanism to perform in-situ measurement of the background contribution to signals derived from sources present at its centre. Using a motor the source is confined into the rear section of the device, from which radioluminescence photons are unable to escape.

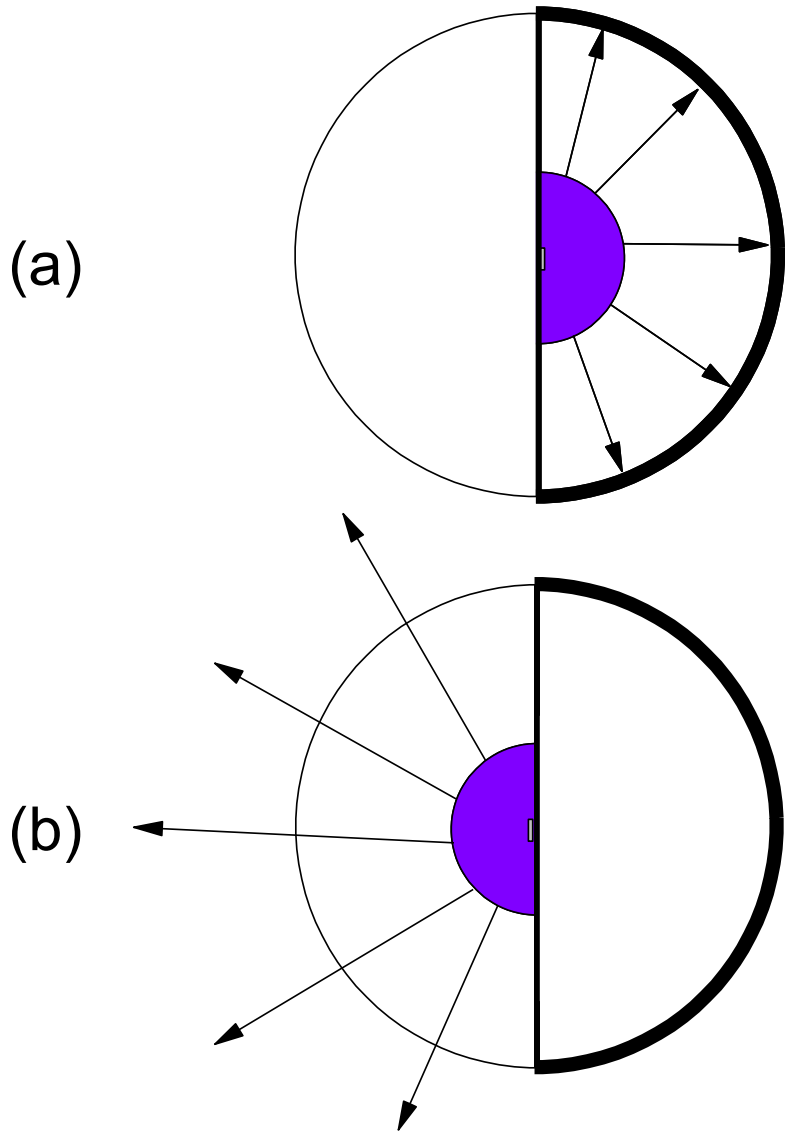


Figure 5.2: Simplified conceptual representation of the UV confinement method showing radioactive emissions (purple) producing photons (arrows) which are either (a) confined or (b) allowed to propagate into the external environment. The semi-circular regions shaded boldly and lightly illustrate the interior of the device and outside respectively. States (a) and (b) are achieved by the rotation of the plastic wall on which the source is mounted through 180 degrees.

This technology also means that during measurements it is not necessary for the operator to physically interfere with the system. This means that this method is also less labour intensive.

Finally, given the ability to pre determine the measurement period, it is possible that long measurements can be performed and if necessary repeat measurements can be organised for validation of the result's repeatability.

The calibration device was constructed by initial design using 123 Design, an Autodesk computer design program. The design was made such that a motor was embedded within the lower circular platform (shown in figure 5.1), the teeth of which fed into an assembly in the bottom of the upper circular platform. Thus once the motor rotated the entire upper circular assembly and its planchet support rotated.

This design was realised using 3D printing and each component illustrated in figure 5.1 was printed separately. This modular design was also intended with application in mind, considering that if some element were contaminated in an operational environment, it would be helpful for the sake of disposal if the contaminated element could be isolated and removed, rather than the entire module, so waste volume can be reduced.

The motor employed within the design was the unipolar stepper motor the BYJ-48. This was driven by the ULN2003 motor driver board, which in turn was controlled, for timing and programming, by an Arduino Mega 2560.

After initial operation it was observed that under free unconstrained motion, the circular platform was difficult to position consistently. This was because no sensor had been placed to verify which position the motor or the platform were in.

As such a modified design was created incorporating limit switches embedded into the lower platform. In addition, on the upper platform a small (2mm thick) piece of plastic was glued such that it would strike the two limit switches when at the appropriate positions, fully enclosed and with the source face perpendicular to the detector axis. The modification of this design is illustrated in figure 5.3 where the grooves in which the limit switches sit are illustrated. The depth of the grooves is refined to allow the upper half of the switch lever to be activated by the piece of plastic on the underside of the upper platform.

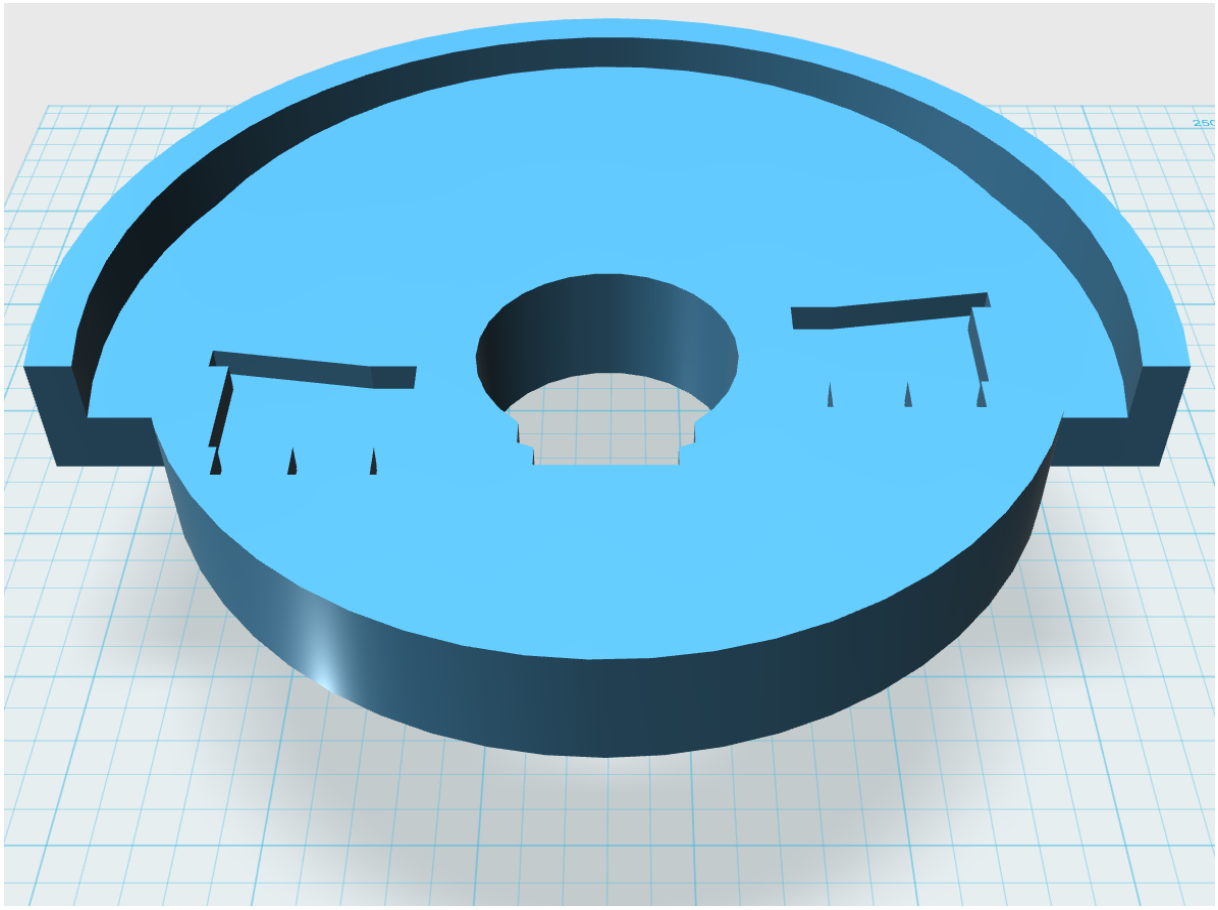


Figure 5.3: Modified lower platform incorporating grooves to fit two limit switches, activated once the upper platform is in positions (a) and (b) illustrated in figure 5.2. The central cavity is designed to accommodate a BYJ48 motor.

The development of the UV confinement device enabled consistent results with fewer anomalous measurements indicating larger background readings than those with sources present. This reduced considerably the time required to perform calibration measurements, although the acquisition of data spanning a variety of measurement distances remained time consuming.

Measurement uncertainty using this method was dominated by the uncertainty caused by physically moving and re-measuring the system. This was especially true when attempting to ensure that each distance remained along a consistent axis relative to the detector.

5.2.3 Development of an automated actuator system

To address these concerns and the initial ones encountered with the manual method it was decided that a system which, in addition to the above functionality, could also move along another axis – toward or away from the detector – would be very helpful. This would ensure that very long measurements could also be automated over long periods and over a range of distances. These could also be convened with ease and with no need for human intervention.

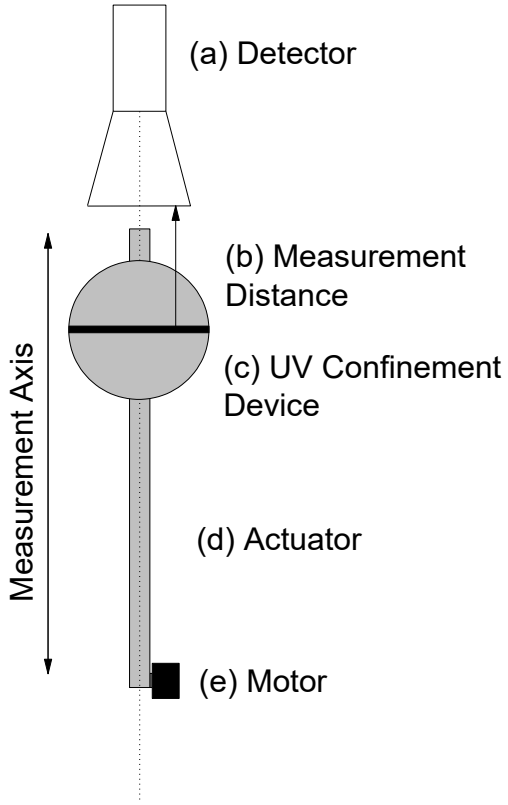


Figure 5.4: Conceptual illustration of the actuated UV confinement measurement system. The system was developed to automate measurements across a series of distances using a belt-driven actuator. This means that by using the motor (e) the operator can vary the measurement distance (b) between the confinement device (c) and the detector (a). This effectively adds an additional measurement axis or dimension to the system of measurements it is possible to obtain.

Illustrated in figure 5.4 is the conceptual realisation. The UV confinement device (c) can be mounted on top of a gantry plate which is moved using another stepper motor (e). This means that the actuator system (d) enables the variation on demand of the measurement distance. This means that measurements can, in addition to being automated in the acquisition of background and active measurements, be acquired along a new measurement axis of varied distance.

The system chosen for this purpose was the OpenBuilds linear belt driven actuator. This product features a NEMA 17 motor which drives a rubber belt, positioning a gantry plate along a 500mm track. Using a Polulu A4988 stepper motor driver it is possible to produce minute variations in the linear position of the gantry plate, theoretically smaller than 0.1mm, although this level of precision is unlikely due to belt elasticity during motion.

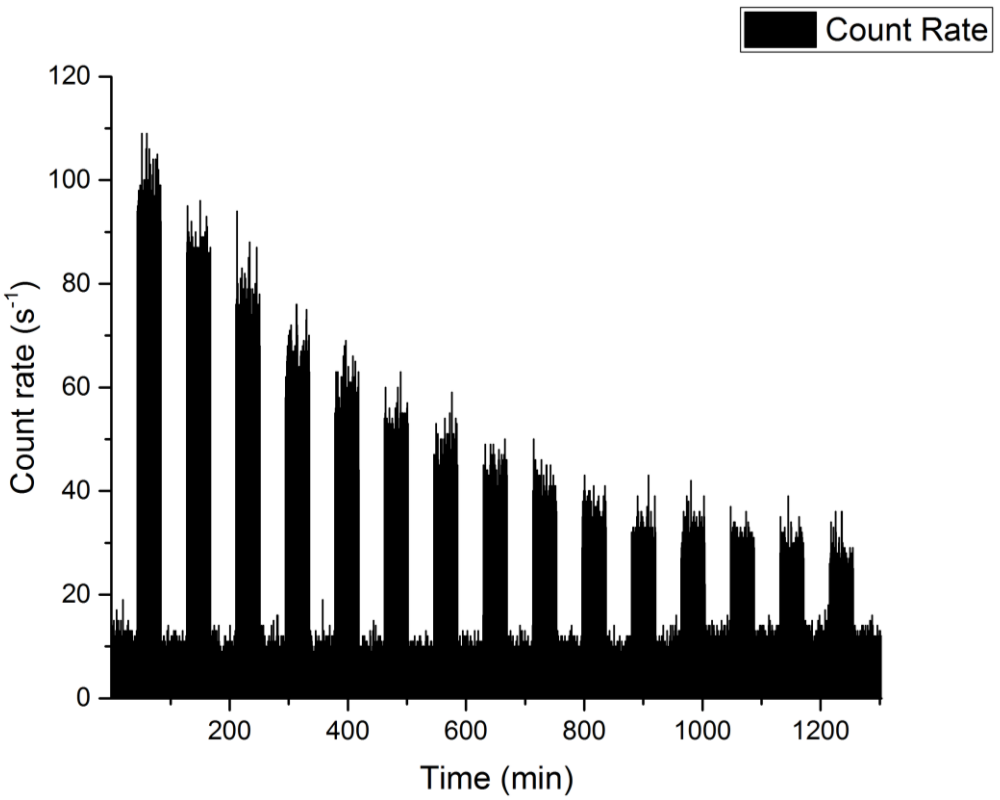


Figure 5.5: Illustration of the detector output of the actuated UV confinement system. Measurements are taken over a set interval (40 minutes) with a background measurement (source confined) followed by a measurement of the same period with the source exposed. The confinement device is then moved to a new position by the actuator's motor.

The UV confinement device was mounted to the actuator by 3D printing a plate matching the dimensions of the confinement device with protrusions fitting the mounting holes of the OpenBuilds system's gantry plate. This plate was then glued onto the bottom surface of the confinement device, meaning the actuator was moved by control of the motor system.

In addition the Arduino controller was primed to operate using a Bluetooth connection, meaning that the measurement sequence discussed could be initiated without any requirement for physical access to the enclosure in which measurements occurred. All power was supplied from within the confinement and no wires were trailed without.

Demonstrated in figure 5.5 is the output of a measurement using this method. The sequence of measurement can be summarised:

1. Background is measured with source enclosed in the confined position
2. Wait for pre-set period
3. Motor orientates source to open position, orientated toward the detector
4. Wait for pre-set period
5. Belt driven actuator is moved pre-determined number of steps, producing motion.

In the specific measurement shown in this figure two of the six americium sources were measured for 40 minutes in each orientation to reduce the associated Possion uncertainty associated with short measurements. The initial distance from source to detector was measured to be (69±0.5)mm and the final distance was (354.5±0.5)mm, with 15 measurement iterations. This means that each successive segment is determined to correspond to distances of 69mm, (69+(354.5-69)/(15-1)), (69+2x(354.5-69)/(15-1)), …, 354.5mm.

The distances (x) in between the start and end points for measurement n can be generalised to the expression:

$$x_n = x_{initial} + (n-1)\frac{x_{final} - x_{initial}}{I-1} \tag{5.1}$$

where n=1,2,…,I, for total number of different distance measurements, I.

Summarised in table 5.2 are the results obtained from the measurement performed using two americium sources.

As shown, by combining the Arduino's data records of when transitions between active and background occur, and in turn when the actuator moves, it is possible to obtain a series of measurements over a long period. The data shown was obtained over a 20-hour period overnight. Interestingly this is reflected by the background trend, with measurements in the middle of the session obtained during night hours, displaying lower levels of background interference than the initial and final stages which occurred during daytime. This measurement was performed within a light tight box in a room within a normally lit room with windows and fluorescence tube lighting.

Distance (mm)	Period (s)	Counts (Source + Background)	Counts (Background)	Net count rate (cps)
69	2363	186996	14864	72.84
89.4	2363	163307	13176	63.53
109.8	2363	140812	12609	54.25
130.2	2363	121420	12465	46.11
150.6	2363	106480	12284	39.86
171.0	2363	93817	12092	34.59
191.4	2363	82442	12158	29.74
211.8	2363	74124	12016	26.28
232.1	2363	66541	11867	23.14
252.5	2363	58607	11730	19.84
272.9	2363	54578	11889	18.07
293.3	2363	52489	12840	16.78
313.7	2363	49028	15182	14.32
334.1	2363	47725	15594	13.60
354.5	2363	43773	16393	11.59

Table 5.2: Measurement of two americium sources in combination using the actuated UV confinement method. Counts represent the number of UV photons detected by the detector.

The counts within the measurement segments were combined using the common time basis of the Arduino system and the PicoQuant device monitoring photomultiplier output. The recorded timings of events (e.g. confinement rotation, actuator motion) initiated by the Arduino control system were mapped onto the output of the records of the photomultiplier system. The corresponding counts within these periods are then summed to provide the appropriate number of counts within certain measurement conditions (particular distances, confined or exposed measurements) and these are presented here.

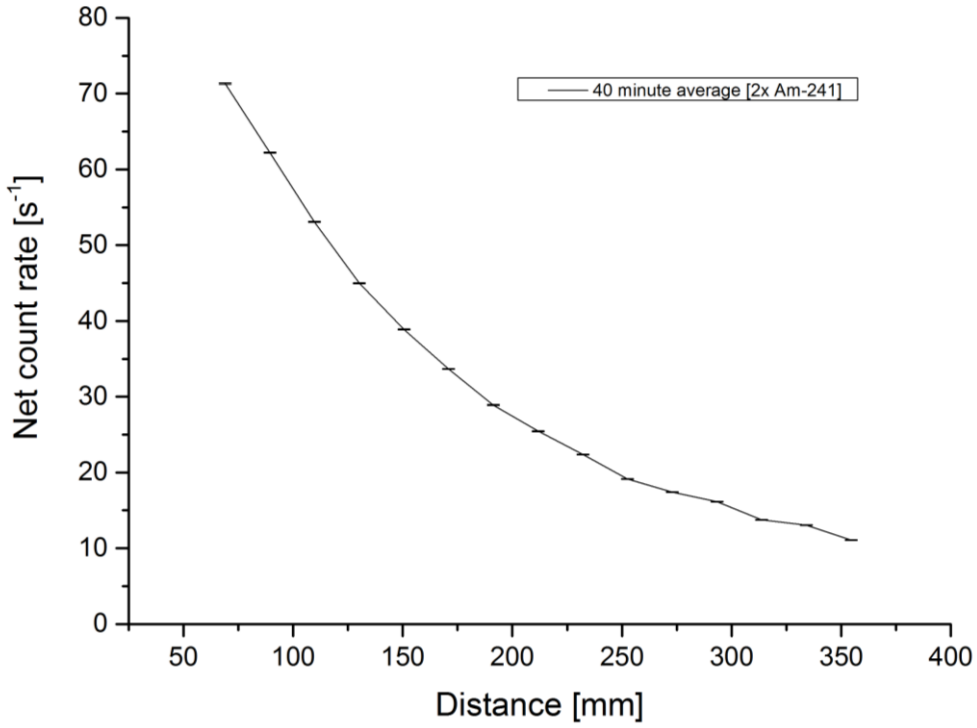


Figure 5.6: The UV photon count rates observed over background for two Americium sources produced using the actuated UV confinement system. Data points are presented as the net count rate of the exposed minus confined result, with the remainder being derived due to the presence of the radioactive source

Displayed in figure 5.6 is the graphical representation of the data presented in table 5.2. As anticipated from previous work the attenuation is described by a negative power law with further distance, as source emissions are spread more finely. The uncertainty in the measurements presented is calculated by the sum in quadrature of the Poisson errors

associated with the number of counts observed in the confined and exposed measurements. As can be seen by the deviations from the broader trend at approximately 310mm this is likely an under-estimation, which could be explained by the considerable change in background count rates within this measurement.

Figure 5.7 shows a simple visualisation of this effect. Within each segment of measurement, both exposed and confined, a simple linear regression trend is analysed. If no trend exists and the light levels observed are consistent throughout measurement then it is expected that the linear regression will yield a straight line, as illustrated by most measurements. For several, however, a downward or upward trend is observed within the 40 minute measurement period, meaning some variation is occurring due to an external change of environment.

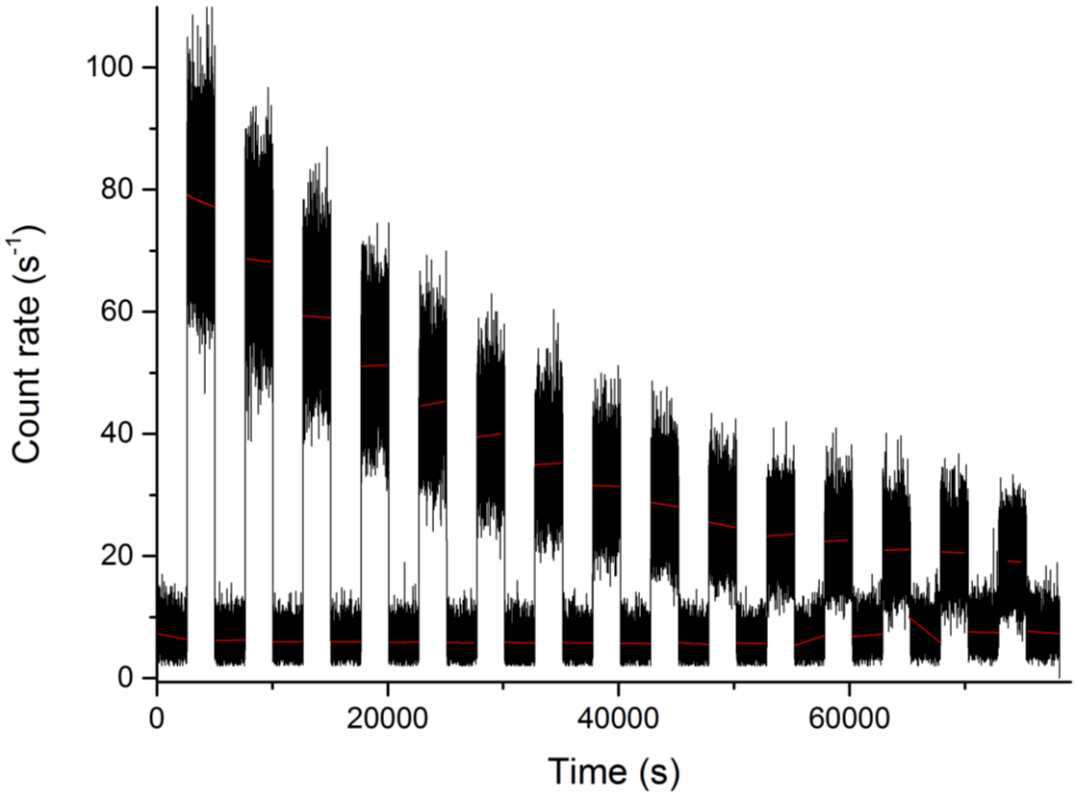


Figure 5.7: Analysis of trends within the segments of 40 minute measurements of UV photons detected from two americium sources (background and exposed). In red are simple linear regression trendlines over the periods analysed for each section. As shown in the first two and last four measurements it seems likely that variation in the level of background within the period of measurement likely increased the uncertainty associated with each measurement.

The most likely origin of this variation is changing levels of external ambient light – for example due to the sunrise or room lights being turned on or off. Clearly for the purpose of the measurement this does, however, enhance the uncertainty in measurement, and so analysis of trends within these segments should be performed before using data of this kind – obtained over long periods in which changes are likely.

As such when using this technique over long measurement intervals the best estimate of the uncertainty in measurement is provided by analysis of the spread of count rates observed throughout the measurement period. If the observed standard deviation of second-wise measurements is greater than the random error indicated by the Poisson statistics then it is likely to have occurred due to interference of this kind.

To assess the repeatability of this method, and for comparison with previous data, a further two measurements over a similar range of distances was obtained using the same two americium sources. These measurements were performed with summing over periods of 20 and 60 seconds, for comparison. The results of this analysis are presented in figure 5.8.

By comparison to the 40-minute data, the observations obtained over shorter periods, as expected, exhibits considerably higher variability. This can be expected due to counting statistics, although its full extent is not quantified by the calculated errors, suggesting some underlying systematic error.

This error could be attributed to the uncertainty associated with the measurement of distance between source and detector and misalignment of the detector and the source axis. At short distances such uncertainty is likely to have a particularly significant effect given that small variations in distance produce the largest variation in net count rate at short distance. The same is also true of source-detector misalignment.

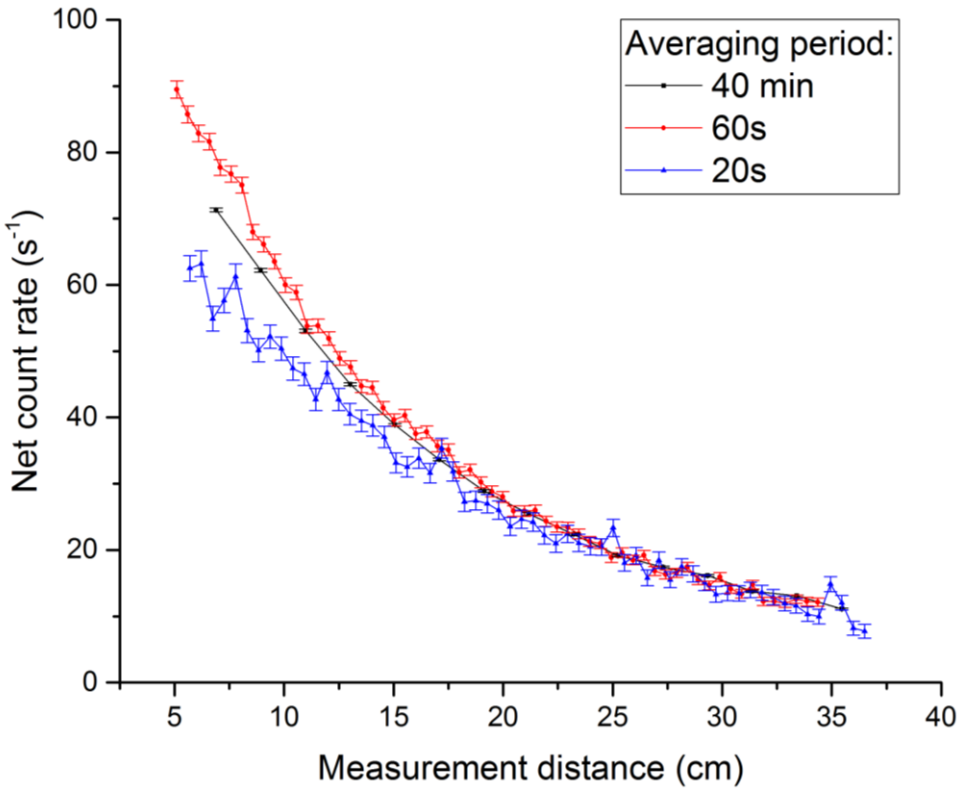


Figure 5.8: Three measurements using the actuated UV confinement method for measuring the attenuation of observed UV photon counts from two americium sources. All measurements were performed in a common environment, within a dark box in a room with normal lighting.

Given the shorter acquisition periods it is unlikely that this is due to variation within the measurement period itself. Another explanation explored was that, given that the deviation appeared most exaggerated in the shortest distances, it could arise due to misalignment of the actuator along the optical axis of the detector. Misalignment could arise if the actuator rail was positioned such that the sources did not lie within the immediate vicinity of the line of the detector's optical axis. This could also explain that at larger distances, where the field of view of the detector system is physically greater in extent, the three measurements converge.

For the purposes of comparison between calibration techniques this method was repeated using the same set of six americium sources discussed in previous sections. This was performed under the same conditions as previous measurements. These results are presented in figure 5.9 and table 5.3.

Distance (mm)	Period (s)	Counts (Source + Background)	Counts (Background)	Net count rate (cps)
69	300	67418	4421	209.99
89	300	62866	6195	188.90
109	300	59370	6913	174.86
129	300	52929	7601	151.09
149	300	46550	7862	128.96
169	300	40116	7874	107.47
189	300	35061	7914	90.49
209	300	30941	7846	76.98
229	300	27637	7564	66.91
249	300	24890	7603	57.62
269	300	22311	7495	49.39
289	300	20324	7425	43.00
309	300	18816	7361	38.18
329	300	17225	7288	33.12
349	300	15760	7420	27.80

Table 5.3: Data obtained from measurements of UV photons detected from six americium sources measured in combination using the actuated UV confinement method.

The measurements obtained from the six sources, on the single point which can be compared, appear to be roughly similar to the figures obtained from the manual measurement method at comparable distances.

The benefits and limitations of the actuated UV confinement method can be summarised as:

Benefits:

- Measurements with radioactive source exposed and confined are automated
- Data is obtained without intervention by the operator throughout measurement
- The process of obtaining data is considerably faster
- Variability in background due to physically breaking the system's enclosure is reduced, meaning background and exposed measurements are comparable

Limitations:

- If taken over long periods levels of background observed by the detector can vary, reducing measurement accuracy.
- Misalignment of the actuator rail relative to the detector's optical axis can product inaccurate data. This effect is hard to identify with a stationary detector, or without knowledge of detector attenuation characteristics.

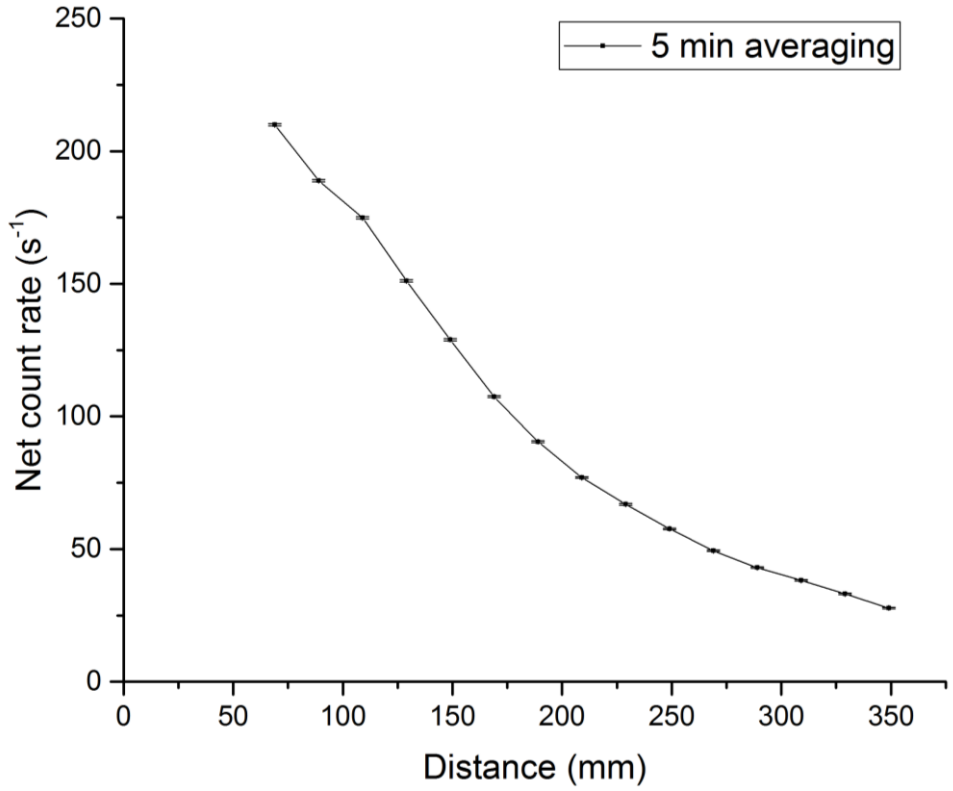


Figure 5.9: Measurement of the UV photons detected at various distances using the actuated UV confinement technique for six americium sources. Each point is the net rate (source over background), averaged over 5 minutes, obtained from the six sources exposed and confined respectively.

5.2.4 Conveyor Scanning

A first attempt to overcome some of the limitations of the previous method involved considering measurements performed instead with a stationary detector and a source in lateral motion. Influenced by a potential operational scenario in which potentially contaminated materials are passed under a stationary detector on a conveyor belt-like system (which could be placed in complete darkness), this method had the advantage that if the detector were to operate at a fixed distance only a single calibration distance would be required. In addition, given that the source was to pass under the detector, it is simple to fix the position of the actuator rail such that the source would pass directly under the central optical axis of the detector.

Displayed in figure 5.10 is a conceptual representation of the equipment layout associated with this method. A radioactive source is placed upon a platform (c) which is driven by the actuator motor (d) along the rail. At some point along the rail the source passes under a stationary, fixed detector (a) at measurement distance (b).

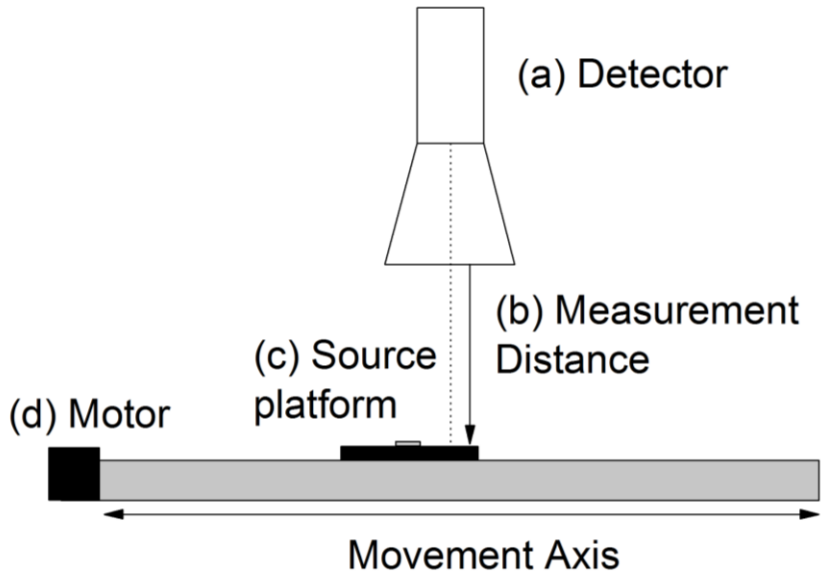


Figure 5.10: Conceptual representation of a conveyor-style calibration measurement in which a source is passed by motor under a fixed detector at a fixed distance.

During the period of operation the detector is set to record all photons observed by the detector. By correlating the timing of the platform's motion (determined by an Arduino board driving the stepper motor as previously) with the recording of the detector it is possible to assign a physical location to the radioactive material and to determine correspondence between peak intensity and radioactive sources.

Before any correspondence can be made between timing and physical location it is necessary to calibrate the actuation system. The most reliable means of achieving this was found to be to drive the motor system from a fixed zero position with a defined number of "steps" – as many as is physically possible while remaining on the rail – and then to measure the overall displacement of the platform using a calliper accurate to 0.1mm. This enables the calculation of the number of steps per mm of platform motion. Thereafter the Arduino system can be set to deliver a fixed number of steps/s, and correspondingly, with calibration, a platform speed in mm/s. Because of the likely changes in the tension of the actuator's driving belt it is necessary to perform this calibration every time the actuation system is moved.

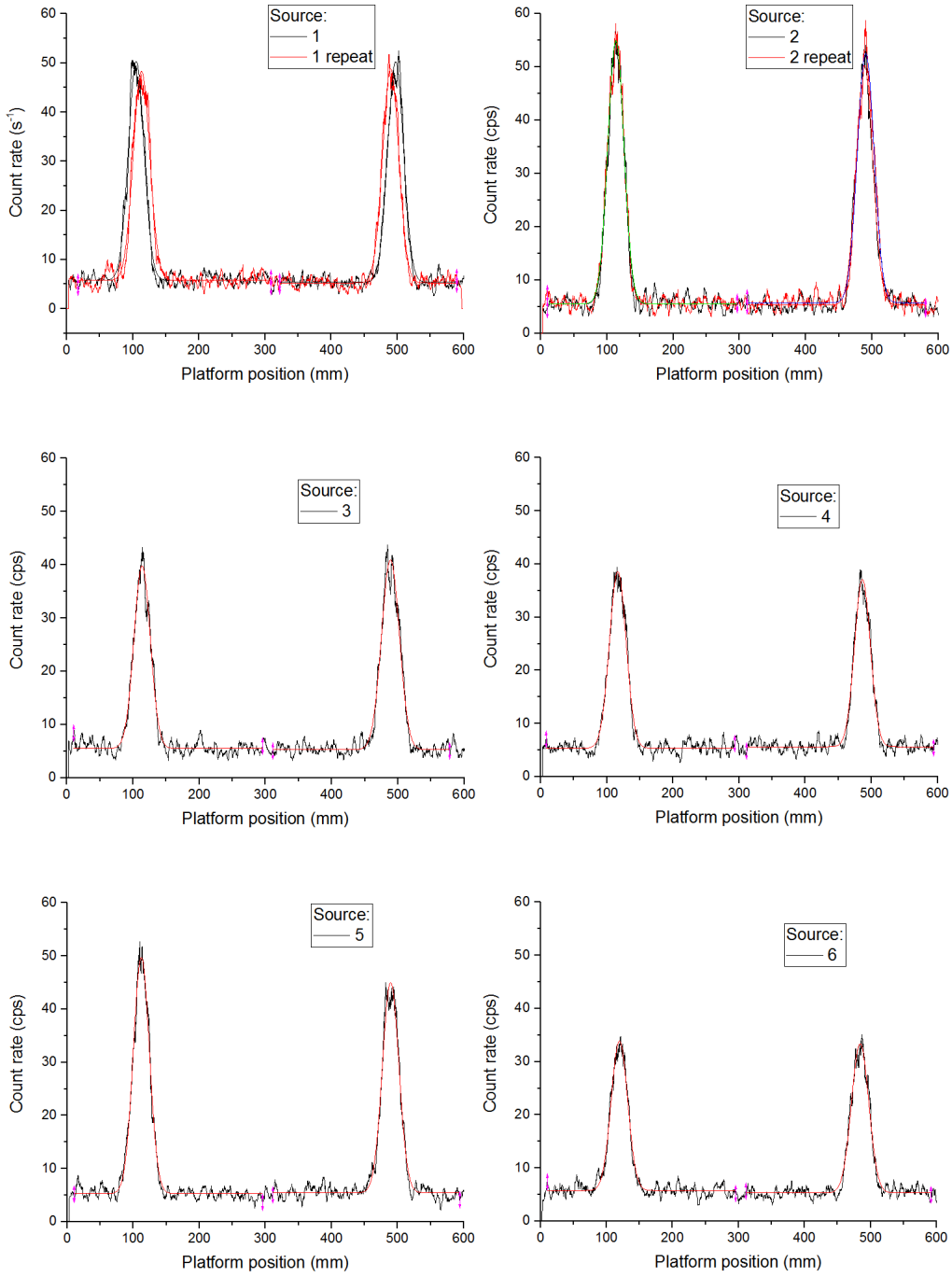


Figure 5.11: Analysis of detection characteristics of 6 individual americium-241 sources sampled at 0.1mm intervals using the conveyor detection method. The UV photon count rate observed as the sources are moved laterally. The overall movement of the platform is 300mm in each case, with the section between 300mm-600m representing the reverse measurement along the rail. Each graph is fitted using a Gaussian function between 0-300mm and 300-600mm.

Displayed in figure 5.11 is a set of results obtained for each individual source within the set of six americium sources with an appropriate label. Each source is of a nominal 33kBq activity although as shown, in reality the surface activity of each source varies considerably. This is likely to have resulted in differences produced in the manufacturing process, with small differences in the source surface resulting in large variation in surface activity – a commonly identified property for alpha-emitting sources [43]. All of the sources are of similar geometry, with a 2mm diameter circular active surface with a metallic overlaying seal and surrounded by a 5mm diameter casing.

Each measurement shown in the figure is derived from the conveyor scanning method. Each individual source was placed on the platform with the detector located 50mm above and, after calibrating the actuator system, the motor was set to operate at a fixed speed of 1mm/s. The actuation system was programmed to operate such that the platform would move 300mm at fixed speed and then to immediately return at the same speed. This resulted in the symmetry displayed in the figures and mean that each individual measurement could be checked for consistency. As such each measurement took a total period of approximately 10 minutes.

Applied to each measurement in the regions of 0-300mm and its reverse, 300-600mm, is a Gaussian fitting function. This fit function was chosen due to the constant baseline and steep peak, which enables effective prediction of background and peak values respectively. This function takes the form:

$$y = y_0 + \frac{A}{w\sqrt{\pi/2}} e^{-2\frac{(x-x_c)^2}{\omega^2}} \tag{5.2}$$

With y_0 representing the baseline level (background), A representing the area under the peak, w the width of the peak at $\pm 1\sigma$ and x_c representing the value of x at which the peak of the Gaussian function is observed.

The net count rate (*NCR*) can be calculated by considering the peak height of the Gaussian above the baseline. This can be obtained by evaluating y at the point $x=x_c$ and subtracting the background, y_0, to provide the expression: $NCR = \frac{A}{w\sqrt{\pi/2}}$.

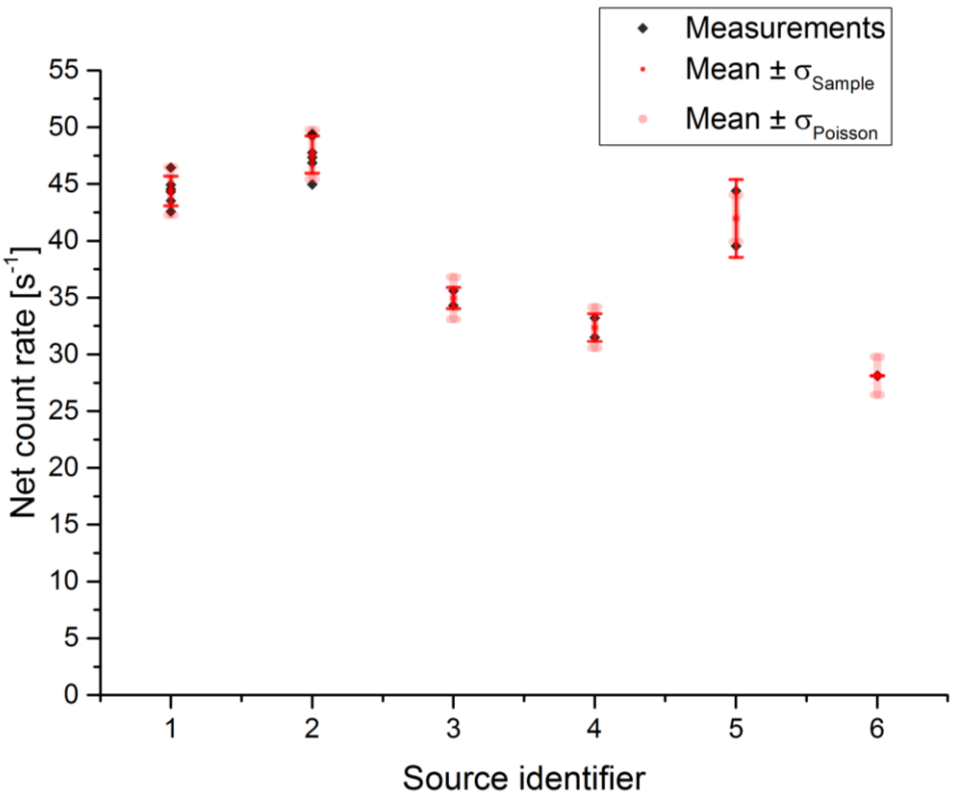


Figure 5.12: Extracted net UV count rates due to the individual sources labelled 1-6 at a measurement distance of 50mm. Each data point is produced from the Gaussian fit of the measurements presented earlier using the conveyor scanning method. Errors are presented using the sample standard deviation (red) of the individual measurements and the expected standard deviation of the observed net count rates due to Poisson statistics (pink).

The net count rate is extracted from the fit parameters of the model applied to the measurements. Displayed in figure 5.12 are the extracted parameters (black), their associated uncertainty and the mean of these measurements taken together (red).

Source Label	Net Count Rate			
	Mean (cps)	± $\sigma_{observed}$	± $\sigma_{expected}$	Measured (cps)
1	44.4	1.3	2.1	42.57
				43.52
				44.55
				44.92
				44.31
				46.43
2	47.6	1.6	2.2	49.41
				49.21
				44.96
				49.41
				46.85
				47.77
3	35.0	0.9	1.9	34.29
				35.61
4	32.4	1.2	1.8	33.22
				31.50
5	42.0	3.4	2.0	44.39
				39.55
6	28.11	0.02	1.7	28.13
				28.10

Table 5.4: Observations using the conveyor scanning method for the individual sources labelled 1-6 at 50mm measurement distance. Count rates are UV photons detected from americium-241 sources using the radioluminescence detector.

As shown this method appears to offer a high degree of repeatability, with measurements taken during separate sessions, such as those presented for sources 1 and 2, yielding net count rates within the expected margins of error.

The data composing figure 5.12 is presented in table 5.4 for clarity. The mean of the individual measurements of the net count rate was calculated for each source and the standard deviation of the sample was calculated, reported as $\sigma_{observed}$. For comparison the expected level of Poisson noise is also calculated ($\sigma_{expected}$) – although the limited number of samples mean it is unlikely that the two figures would be identical – and this indicates the expected boundaries into which most individual measurements would fall based on the observation period for each mean. In figure 5.12 it is possible to see that the majority of measurements do fall within this boundary.

An important feature of this data is that the measurement of individual sources can also be used to prove that the detector response scales linearly versus the amount radioactive activity, and indeed to demonstrate that the amount of UV fluorescence generated by the emission of alpha particle in air is linearly correlated to the amount of activity present.

Given that the component signals have been analysed for each source these sources can also now be measured in combination. When the sources are presented in combination the detector is presented with an activity equivalent to the sum of the individual component activities.

As such, measurement in combination can give a clear demonstration that the detector's response is linear. If the response is linear within the appropriate scales, then the sum of the individual net count rates – presented in table 5.4 – for each component source should equal the observed combined total obtained using the same method.

Presented in figure 5.13 are measurements of the same six sources in combination under the same experimental conditions as the individual measurements – with a 1mm/s speed and the detector at a measurement distance of 50mm. The combination of sources presented to the detector are labelled in each graph. For consistency between the two series of measurements the same Gaussian fitting procedure was applied to the measurements and the peak and background levels were obtained.

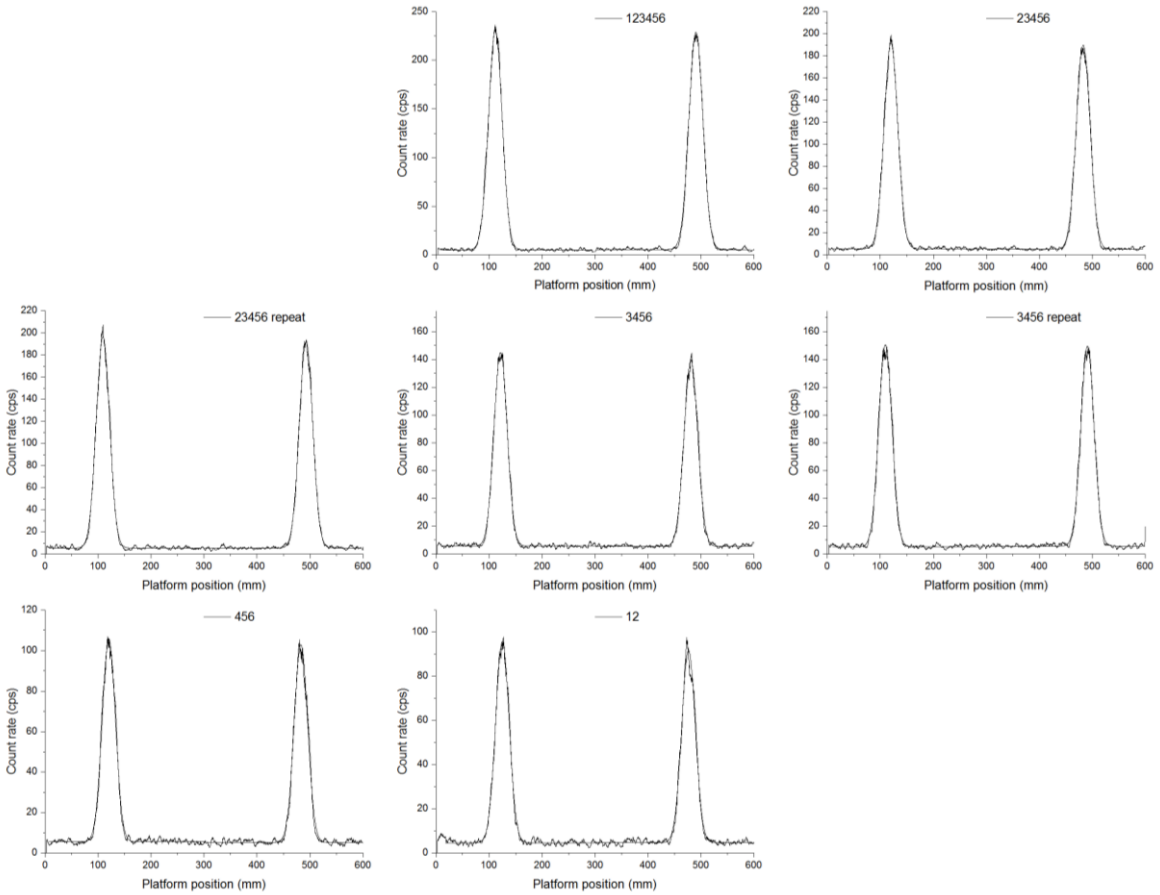


Figure 5.13: Measurements performed on the set of six sources in combination using the conveyor scanning method. The sources (with the identifiers labelled on each graph) were placed on the platform and passed at a speed of 1mm/s under the UV detector located at a measurement distance of 50mm. Results were fit using the Gaussian fit function to extract their peak height and background baseline in order to calculate the net UV photon count rate due to the sources.

In figure 5.14 the resulting net count rates are plotted with the sum of the individual measurements. Shown in black is the mean of the two measurements for each combination of sources shown in figure 5.13 and its corresponding standard deviation. Also displayed in red is the sum of the individual measurements presented in table 5.4, and the associated standard deviation, obtained by calculation of the sum of errors in quadrature.

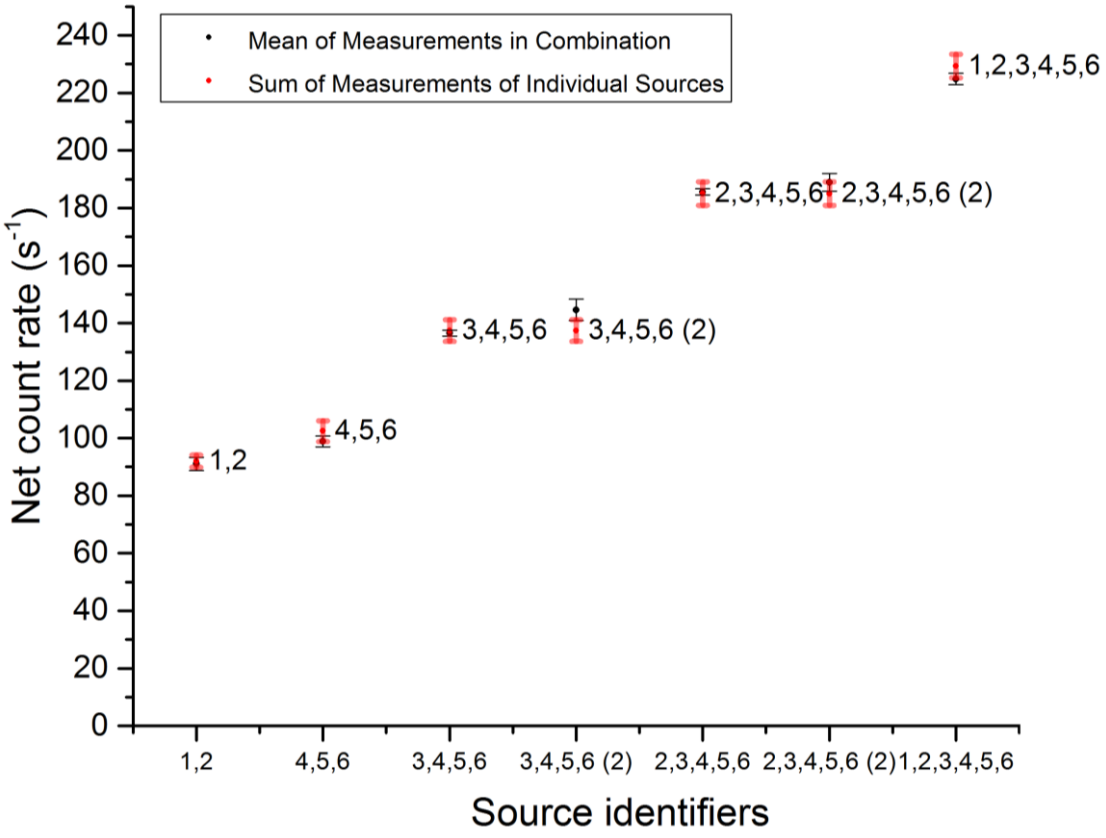


Figure 5.14: The mean net UV photon count rates observed during measurements of sources in combination (black) using the conveyor scanning method compared to the sum of the same sources measured individually (red) under the same conditions. This shows that the detection system responds in a linear, consistent way in measurements of varying amounts of alpha activity.

Demonstrated by the overlapping of the calculated net count rates, obtained from individual measurements, and the measured net count rates in combination is the principle that the detector itself can be used to analyse quantitatively the amount of activity presented in front. This proves the usefulness of calibrating the system against sources of known, quantified activity.

This data is also presented in table 5.5. For the measurements of all sources in combination (1 to 6) and the second measurement of sources 3 to 6 the sum of individual measurements can

be said to be in good agreement with the combined measurement, and all others are in excellent agreement with the expected values.

Source combination	Sum of Individual Measurements (cps)		Measurement in combination (cps)	
	Net count rate	±σ	Mean net count rate	± σ
1 and 2	**92.0**	2.1	**91.0**	2.3
4, 5 and 6	**102.4**	3.6	**98.9**	1.9
3, 4, 5 and 6	**137.4**	3.8	**136.5**	1.1
			144.6	3.7
2, 3, 4, 5 and 6	**185.0**	4.1	**185.6**	1.1
			188.9	3.1
1, 2, 3, 4, 5 and 6	**229.4**	4.3	**224.9**	2.0

Table 5.5: Comparison of the sum of individual measurements of net UV photon count rates compared to those measured by the same sources in combination. All measurements were performed at 50mm measurement distance using americium-241 sources.

The conveyor scanning method can thus be considered a reliable and consistent measurement method in practical scenarios. The practical potential of this technique is discussed further in later chapters, notably in quantifying the minimum detectable amount of activity over a variety of background scenarios.

An additional observation considered when analysing this as an operational scenario is that while measurements have so far been performed for a fixed detector and a moving source, the results discussed here are also valid for the opposite scenario of a moving detector and fixed source (e.g. on a remotely operated vehicle transiting a wall).

As a calibration technique, given the methods repeatability and adaptability to the desired level of accuracy (i.e. by making measurements faster or slower) it has the potential for

practical use. However, the original concerns arising from manual calibration – that it is difficult to achieve a calibration at a wide variety of measurement distances – still continue due to the fixed operational distance.

Some potential methods to overcome this difficulty exist, notably by mounting the detector itself onto an actuated platform which enables the detector to be raised and lowered relative to the platform. This could also enable the acquisition of calibration over a wide range of measurement distances. A system which could be used for this purpose is the OpenBuilds C-Beam Machine, a system designed for a CNC drilling/engraving system based on similar actuators, although this was beyond the scope of this project and thesis.

5.2.5 Imaging method

A final method considered for calibration and the analysis of detector performance was to effectively use the detector to 'image' a source and its surrounding region. This method was intended to address the need for the calibration method to be useful over a range of different measurement distances while overcoming the difficulties of misalignment.

The equipment used in the development of this method is outlined in figure 5.15. Added to the detector is a pan tilt assembly (a). This is composed of two connected servomotors, which, by using an electronic controller, can be programmed to orientate at any angle between 0 and 180 degrees. For experiments presented the servomotors were roughly orientated such that the central (90°,90°) position such that the detector's optical axis was orientated at the centre of the source, thus enabling the full ±90° field of view.

Like the conveyor scanning technique the development of this method is also motivated by a potential operational scenario. If a fluorescence detector were to be used within a decommissioning environment to locate regions of contamination then it would not be known before measurement where these were located. As such an image based scan could be used as the first step to establishing the location and/or approximate magnitude of either contaminants or sources of background. After a map of the area is produced over a span of pan and tilt angles an operator could scrutinise any regions of elevated count rates, find the corresponding position and establish whether it is likely source of background (e.g. if a light bulb or source of light is present) or contamination (e.g. a stain or dirt) and respond

accordingly, either to reduce background or analyse the contaminant further (e.g. by scanning at a fixed distance to establish the amount of activity present).

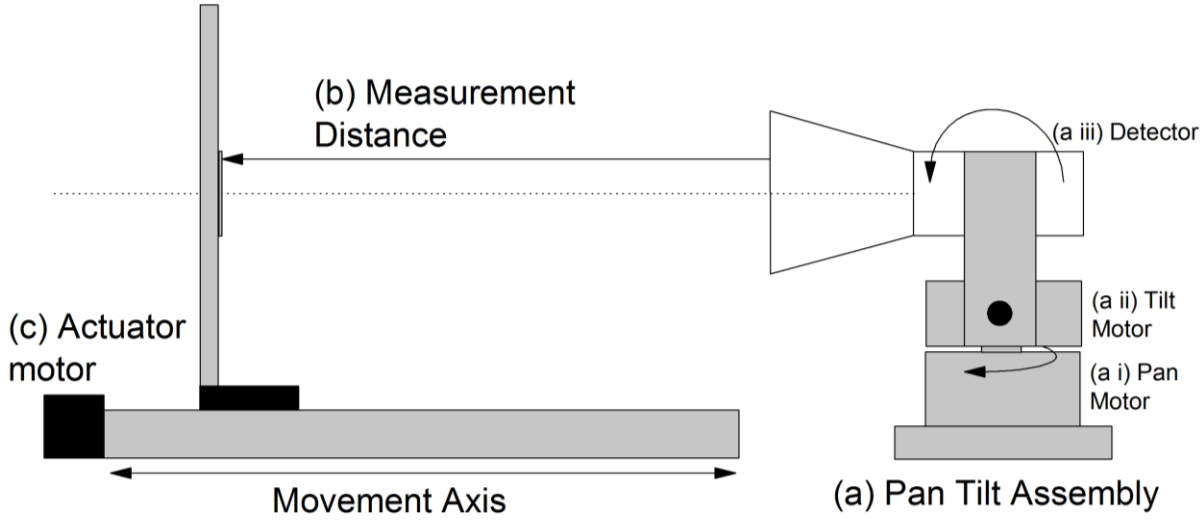


Figure 5.15: Experimental setup for the imaging calibration method. The pan tilt assembly (a) enables the detector to be orientated upward, downward, left or right using two 180 degree servo motors. Movement of the actuator can lead to the automated production of UV images over a wide range of distances.

For the purposes of calibration it was considered that the detector assembly could be used to scan the region surrounding a source. This scanning region was optimised such that at the outer reaches of the image the detector would be oriented outside the region of source, providing an indication of background. As such the resulting output would display an elevated central region in which the influence of the radioactive source was present surrounded by a baseline level of background. Thereafter the central peak would be evaluated to yield the net contribution due to the source over the background baseline.

This method has the advantage that even if the central detector axis is not perfectly aligned with the centre of the source, and so misses the peak contribution due to the activity present, then the central peak will be located at some point within the image. The procedure for data extraction then allows the simple location of this peak and, by considering the symmetry of the output image, it is possible to locate this peak sensitivity regardless of misalignment.

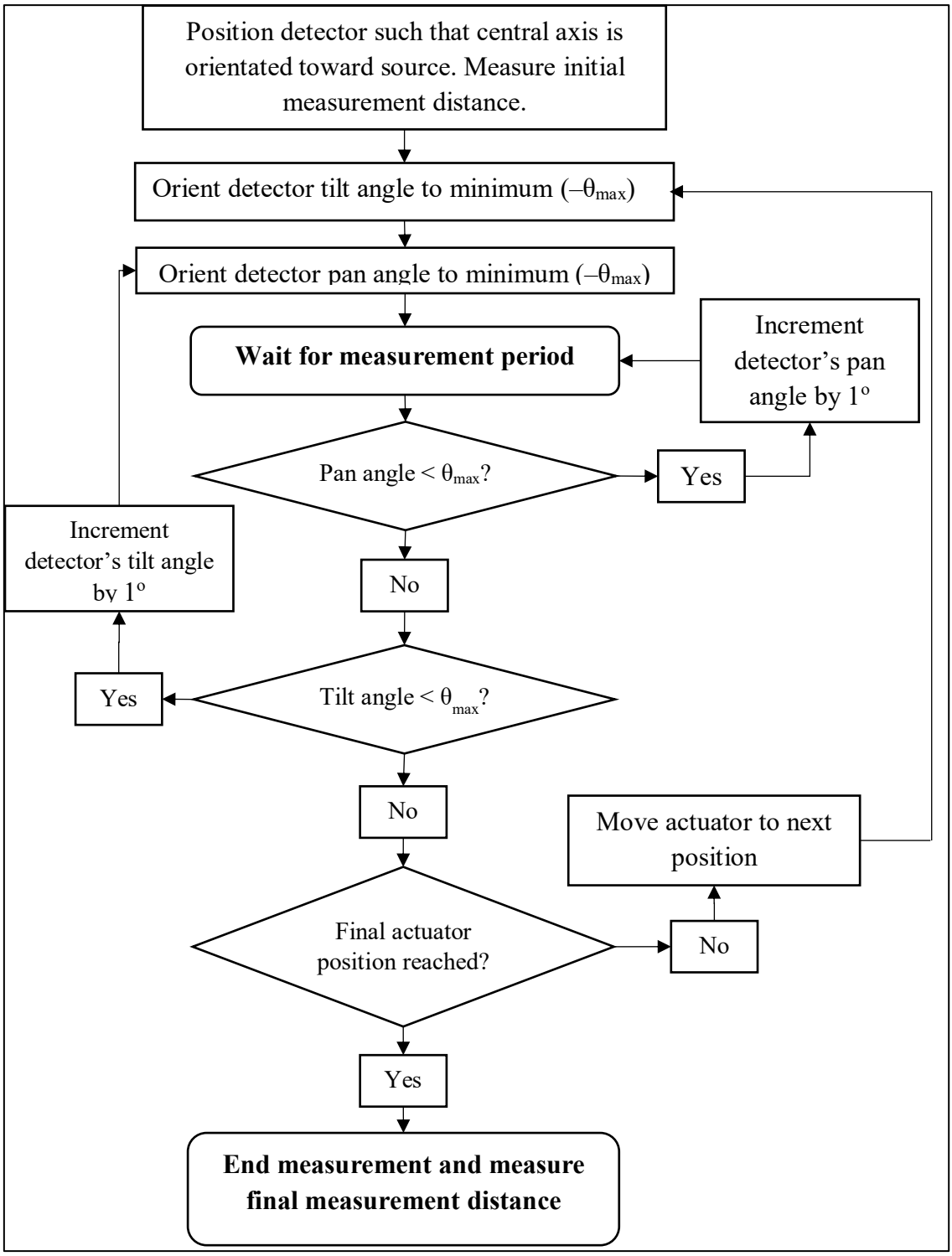


Figure 5.16: Flowchart illustrating the procedure for measurement using the imaging method. Parameters required for the method include θmax, the angular limits of the image, the final actuator position and measurement period per orientation.

The imaging procedure can be summarised as shown in figure 5.16. The detector is in sequence oriented to the outer reaches of some angular space between the angles $\pm\theta_{max}$. As the source being imaged is considered small enough to approximate to a point it is expected that the output will be symmetric, and so the same $\pm\theta_{max}$ angles are used for both the vertical tilt angle and the horizontal panning.

The imaging sequence commences at the orientation ($-\theta_{max}$, $-\theta_{max}$) and incrementally, with wait times at each position, the pan angle is increased until reaching θ_{max}. At this point the tilt angle is incremented and the sequence commences again.

This process is repeated until measurements are obtained discretely at 1° intervals across the entire space between ($-\theta_{max}$, $-\theta_{max}$) and ($+\theta_{max}$, $+\theta_{max}$). The period of measurement at each discrete position is pre-set prior to measurement and determines the expected level of noise, and as a result the sensitivity.

This sequence is also illustrated in figure 5.17 for the example of a $\theta_{max} = 10^{o}$. This results in 21x21 discrete measurements each lasting for the pre-set period.

Given the need for calibration to be performed over a range of distances this sequence is then repeated for each successive position of the actuator until an image is obtained for each position.

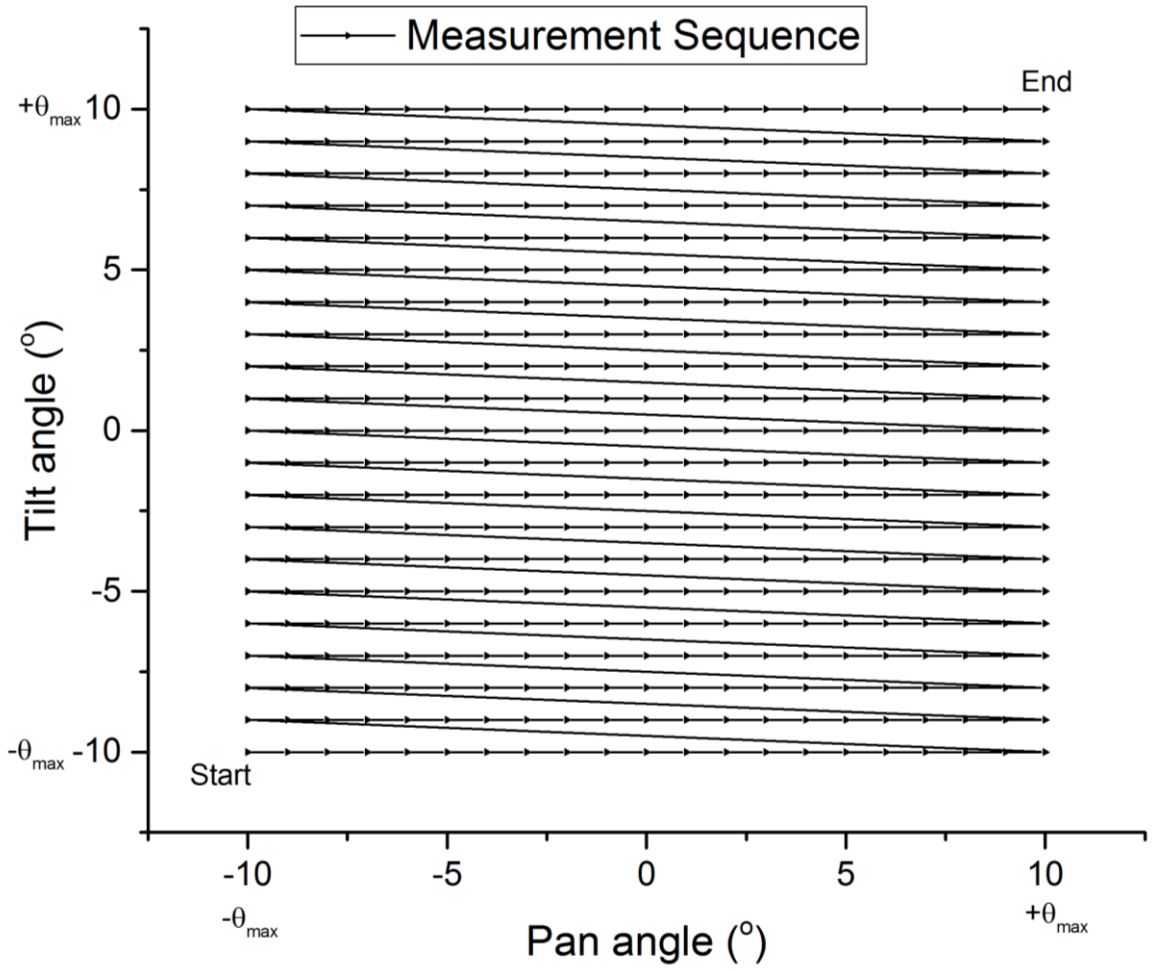


Figure 5.17: Illustration of the sequence of measurements performed using the UV imaging method. Shown is an example of maximum angle, $\theta_{max} = 10^{o}$. Measurement commences at the angular minimum position ($-\theta_{max}$, $-\theta_{max}$), sequences through range of pan angles in succession and then moves to the next tilt angle, at which the pan angle resets to $-\theta_{max}$. This continues until reaching the final position, ($+\theta_{max}$, $+\theta_{max}$).

In figure 5.18 is the output resulting from this measurement sequence. This method was applied to the set of six americium sources for a measurement period of 10s/point over a 27x27 grid, repeated in 10 iterations for measurement distances between 69mm and 339mm. The entire measurement sequence was therefore performed over a period of 75600 seconds (21 hours). As shown there is little variation in the observed levels of background, present in the regions between the clear image structures, compared to the previous confinement

technique. This is attributable to a change of location for this and subsequent measurements with this technique, which were performed in a room without windows.

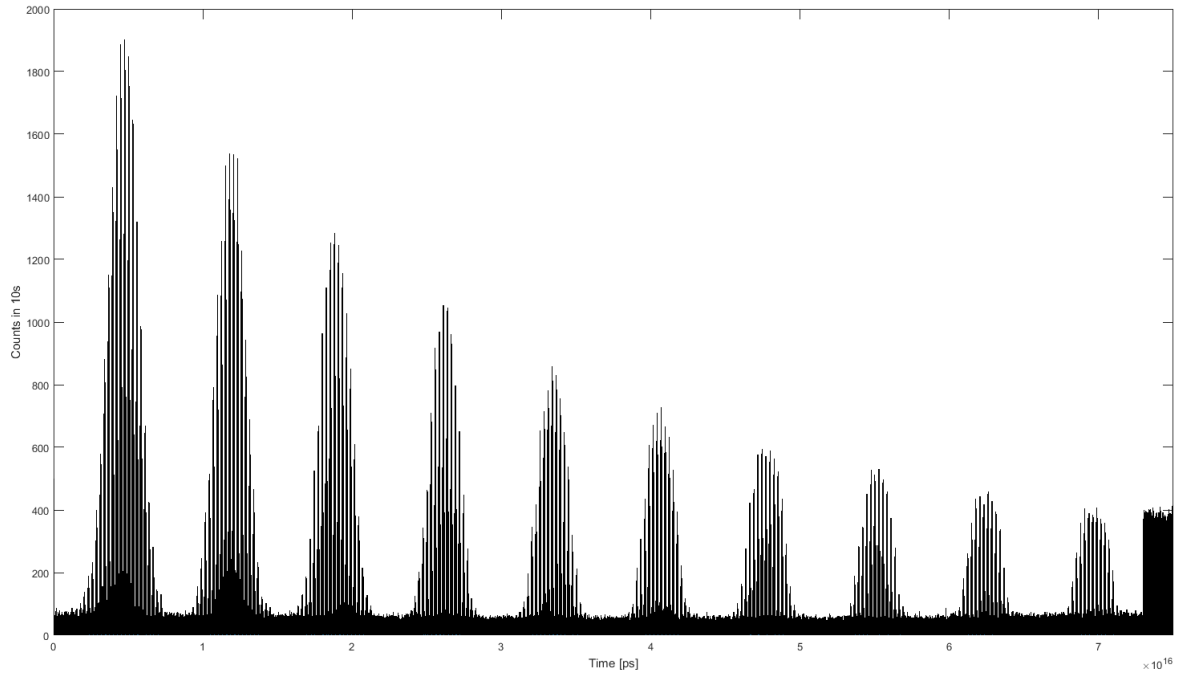


Figure 5.18: Raw data obtained by using the UV photon imaging method over distances of 69mm to 339mm from detector to americium-241 source in 10 iterations. Each measurement was performed over a 27x27 grid (θmax = 13o), with each measurement lasting 10 seconds. Embedded in each shape is an image of the source at distances between. At the end the detector was programmed to end the sequence such that it faced the centre of the source, hence the solid region of relatively constant intensity.

Using an algorithm developed to decode the images derived from the method it is possible to sum the counts observed during each distinct interval and to assign the corresponding pan and tilt angle. The result is a series of matrices each representing an image at a different distance.

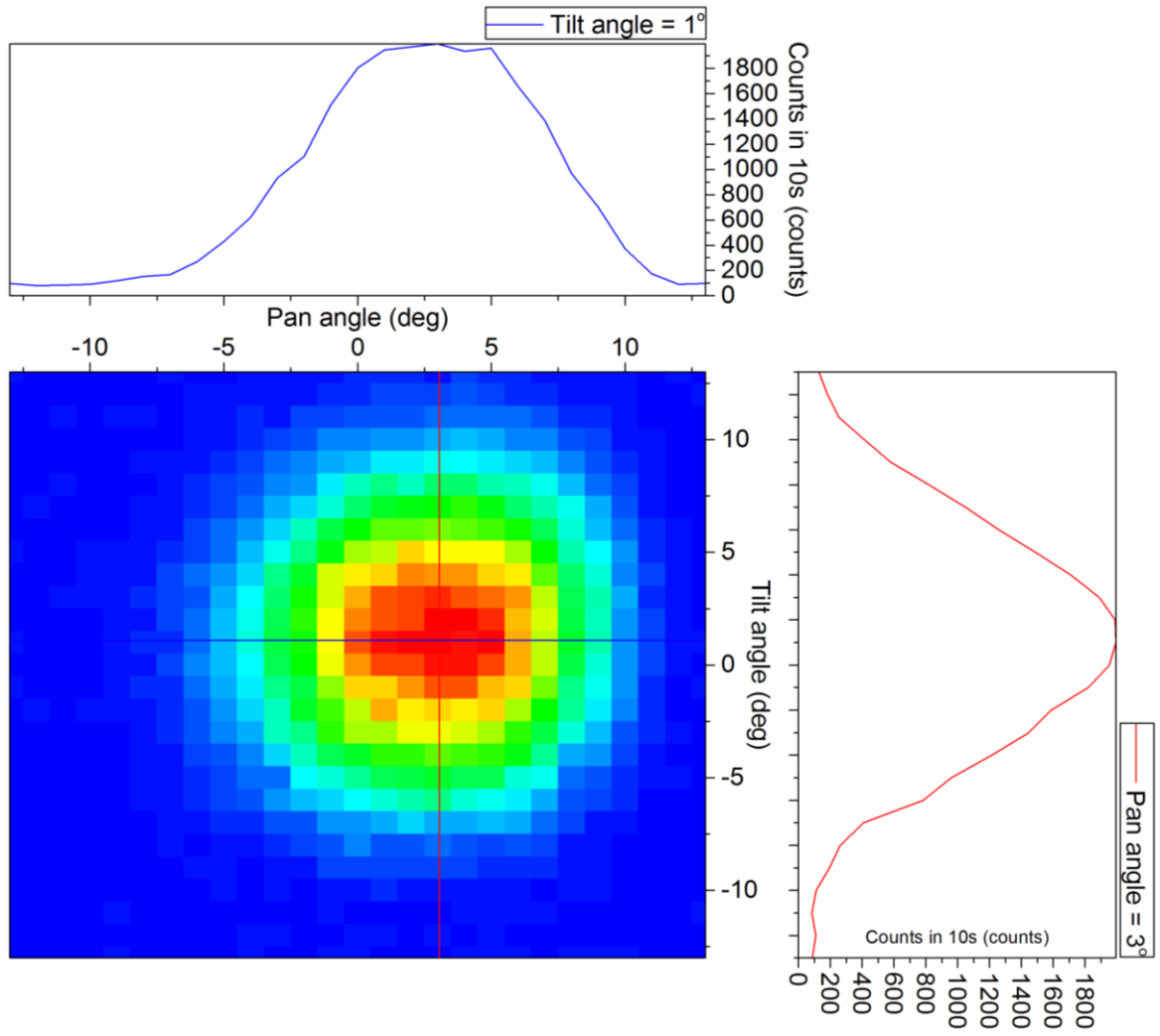


Figure 5.19: The UV image resulting from measurements of americium-241 performed over a 27x27 grid at 69mm measurement distance over an angular range of -13 degrees to 13 degrees. Each pixel displayed represents a distinct 10s measurement. The two profiles displayed above and to the right of the image are graphs representing the two lines shown for fixed tilt and pan angles respectively.

Figure 5.19 graphically represents the matrix output of the measurement obtained for measurement distance 69mm displayed in figure 5.18. Each individual cell represents the sum of the counts observed within the relevant time period. This has then been matched to the relevant pan and tilt angle. As a result it is possible to analyse the count rates over the ranges of angular positions.

Figure 5.19 also displays two cross sectional profiles of the matrix for fixed pan and tilt angles represented by the red and blue lines respectively. The blue line on the image displays the profile shown in the upper graph for the 1° tilt angle. As shown it is possible to identify that the centre of the source did not at the beginning of the measurement lie on the central optical axis of the detector and instead lay at approximately (3°, 1°) pan and tilt angle respectively. This is easily identified by using the imaging method, however, and the measurement also encompassed the central region. For calibration this can be extracted and analysed.

The background regions surrounding the source is also incorporated into the matrix. This is represented by the region of fixed intensity surrounding the peaks on the two cross sectional profiles.

Given the increased level of complexity associated with the large number of measurements obtained a new methodology was developed to extract the necessary net count rates for calibration of the device.

As shown in figure 5.19 the response of the detector over the range of angular orientations varies such that a defined peak can be observed over a constant background. Considering this an appropriate method for the extraction of peak values could also be to fit the surface of the 3D function to an appropriate three dimensional fitting function.

An appropriate fit function was identified as the 2D Gaussian distribution. This function is similar to the one dimensional form used previously and takes the form:

$$z = z_0 + Ae^{-\frac{1}{2}(\frac{x-x_c}{\omega_1})^2-\frac{1}{2}(\frac{y-y_c}{\omega_2})^2} \tag{5.3}$$

With Z_0 representing the constant background level; A, the peak elevation over the background (NCR); x_c and y_c, the central coordinates in x and y of the peak; ω_1 and ω_2 the standard deviations in x and y respectively. The independent parameters ω_1 and ω_2 mean that the fit function can also represent asymmetry between the pan and tilt angle sensitivities, meaning the output can also be used to analyse symmetry of optical response.

This fit function can be applied to the matrix and using the non-linear method of least squares implemented on MATLAB it is possible to extract the appropriate parameters. However, it was noticed upon analysis of this data that the algorithm was consistently over-estimating the

value of the peak of the distribution, and in particular for larger distance images. This was found to arise due to a feature of the detection system which meant that measured sensitivity was found to be relatively flat over angles close to the detector's optical axis. This can be observed for example in figure 5.19 in the cross section presented for the fixed tilt angle = 1°. As shown at the apex of the distribution the curve is comparably flat for a range of approximately 5°.

As such an alternative method had to be devised to overcome this tendency to overestimate. It was observed that the fit function, despite this difficulty representing the apex and net count rate, was however accurately describing the central position of the distribution (x_c and y_c), its width (ω_1 and ω_2) and the surrounding level of background (Z_0). This observation led to the consideration that rather than using the output fit function and the associated parameters, instead direct sampling could be performed upon the matrix to extract a relevant sample of data representing these peak values at the appropriate positions identified by the fit function.

Given the large uncertainty associated with a brief 10s count arising from a single point sample, and the resulting effect on detection limits over background, the number of points which could be incorporated into the sample while maintaining accuracy was investigated.

Two models exploiting the symmetric property of the images of the radioactive sources were considered incorporating 5 and 9 of the meaurements surrounding the central point. Shown in figure 5.20 is the final sampling method adopted for measurements obtained using the imaging method, incorporating samples at 5 points. The five white circles represent the five measurements which are incorporated, including the central point ($\theta_{pan,c}$, $\theta_{tilt,c}$) and the adjascent points represented by ($\theta_{pan,c}\pm1°$, $\theta_{tilt,c}$) and ($\theta_{pan,c}$, $\theta_{tilt,c}\pm1°$).

Four alternative models were analysed: a single central point measurement, a five-point average, a 9 point average (incorporating the five plus the four adjascent represented by ($\theta_{pan,c}\pm1$, $\theta_{tilt,c}\pm1°$)), and the fit parameter A alone.

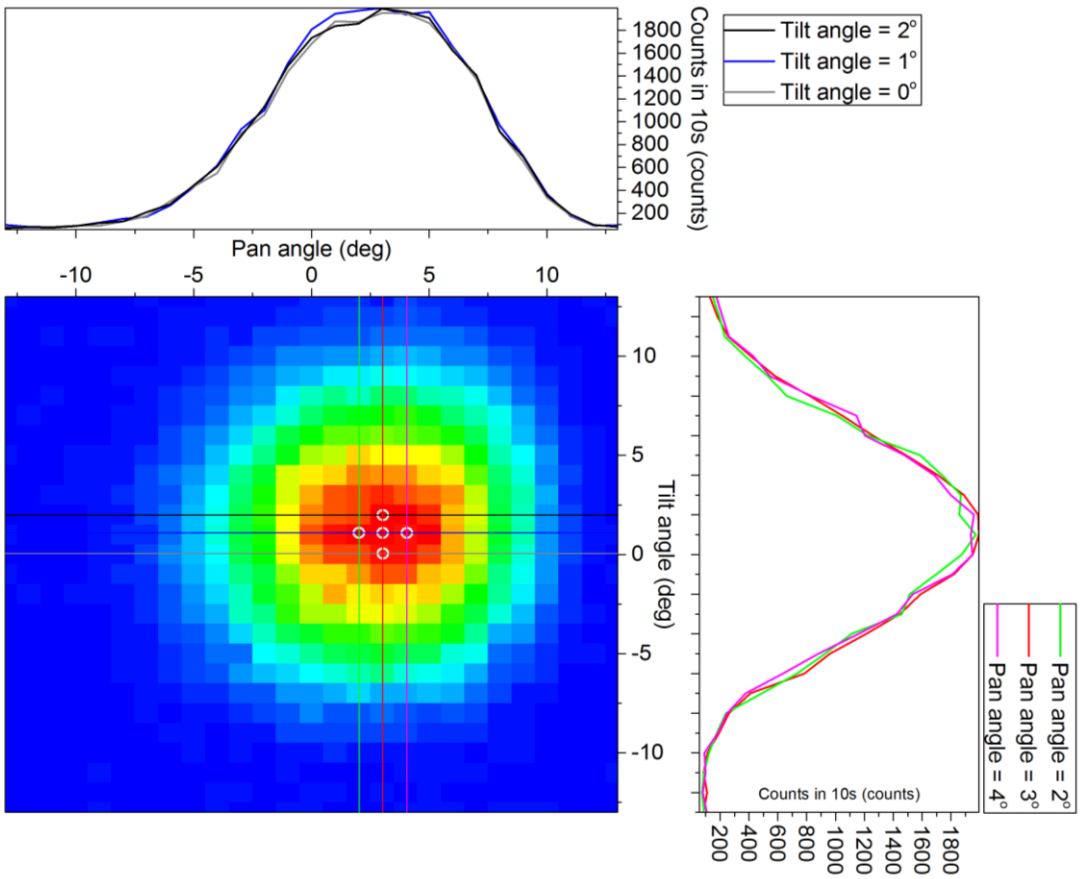


Figure 5.20: UV measurement of six americium-241 sources at 69mm distance from source to detector illustrating a sampling method incorporating five points about the centre, derived from a 2D Gaussian non-linear least squares fitting algorithm. Illustrated are cross sections of six different fixed angles. Samples are taken within the 5 regions indicated by white circles.

The results of this analysis are presented in figure 5.21 using data obtained from 47 images obtained in 8 separate measurement. Initial analysis shows that the parameter extracted from the image fit function is not a reliable metric with high degrees of uncertainty compared to the other metrics. In addition there is no simple way to quantifiably analyse the uncertainty in measurements obtained using this method.

It is possible also to see that the single central point measurement, shown in blue, suffers from a considerably greater measurement error when compared to the 5- and 9-point averages. This is reflected by the deviation from the broader trend exhibited, and in particular in the region between 45-75cm.

By comparison the 5- and 9-point averages are steady and consistent even between different sessions. This is especially true when compared to the measurements shown earlier in figure 5.8 for the actuated UV confinement method.

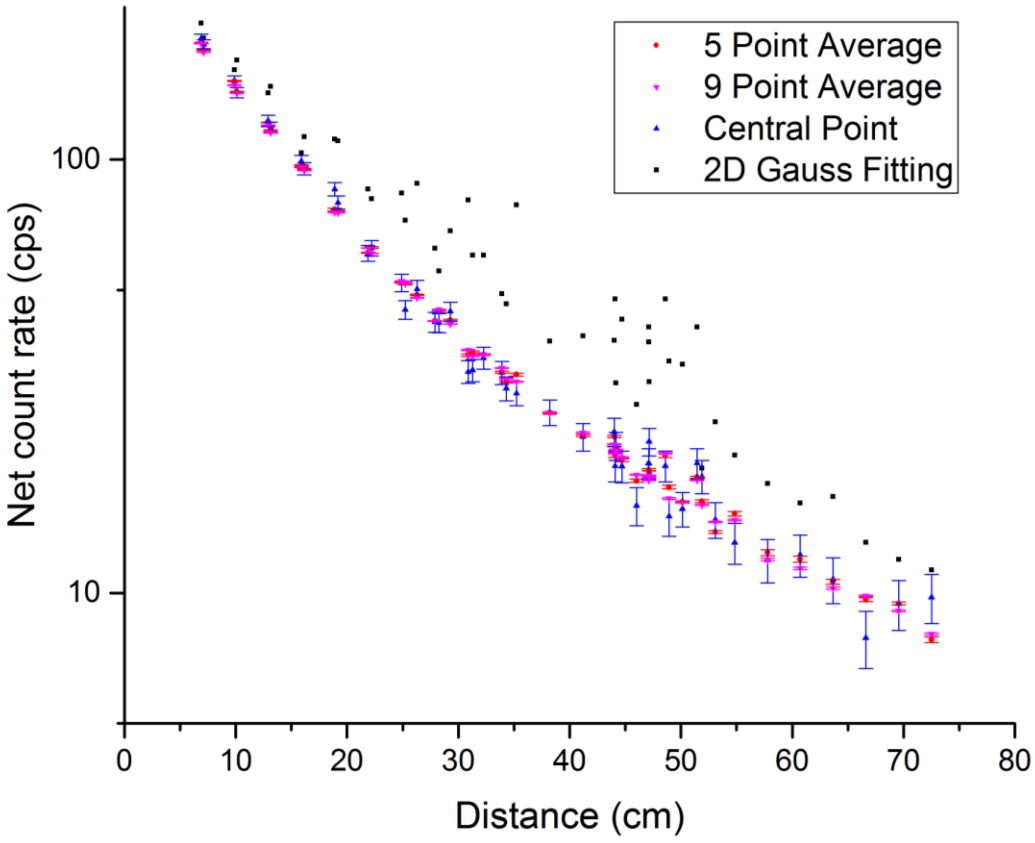


Figure 5.21: Four models of data extraction performed on 47 UV images of six americium-241 sources at various distances under 1m. The 2D Guassian fit parameter is not repeatable and tends to over-estimate. The 1, 5 and 9 point samples produce consistent measurements although the 1-point 10s measurement is dominated by Poisson noise. The 9-point samples were analysed and were found to under-estimate the measurement uncertainty and consistently under-estimate the net count rate when compared to the 5-point measurement.

Little difference was observed between the 5- and 9- point average measurements except at short (up to 20cm) distances – where the sensitivity to angular variation would be most marked – where the 9-point average consistently predicted a lower average net count rate

(*NCR)* than the corresponding 5-point sample. Given the level of variation observed between measurements it appears that the larger standard error calculated for the 5-point mean more accurately represents the associated measurement error. As such it was decided that this was the most appropriate metric for analysis of the broader attenuation trend, and the calibration over distance.

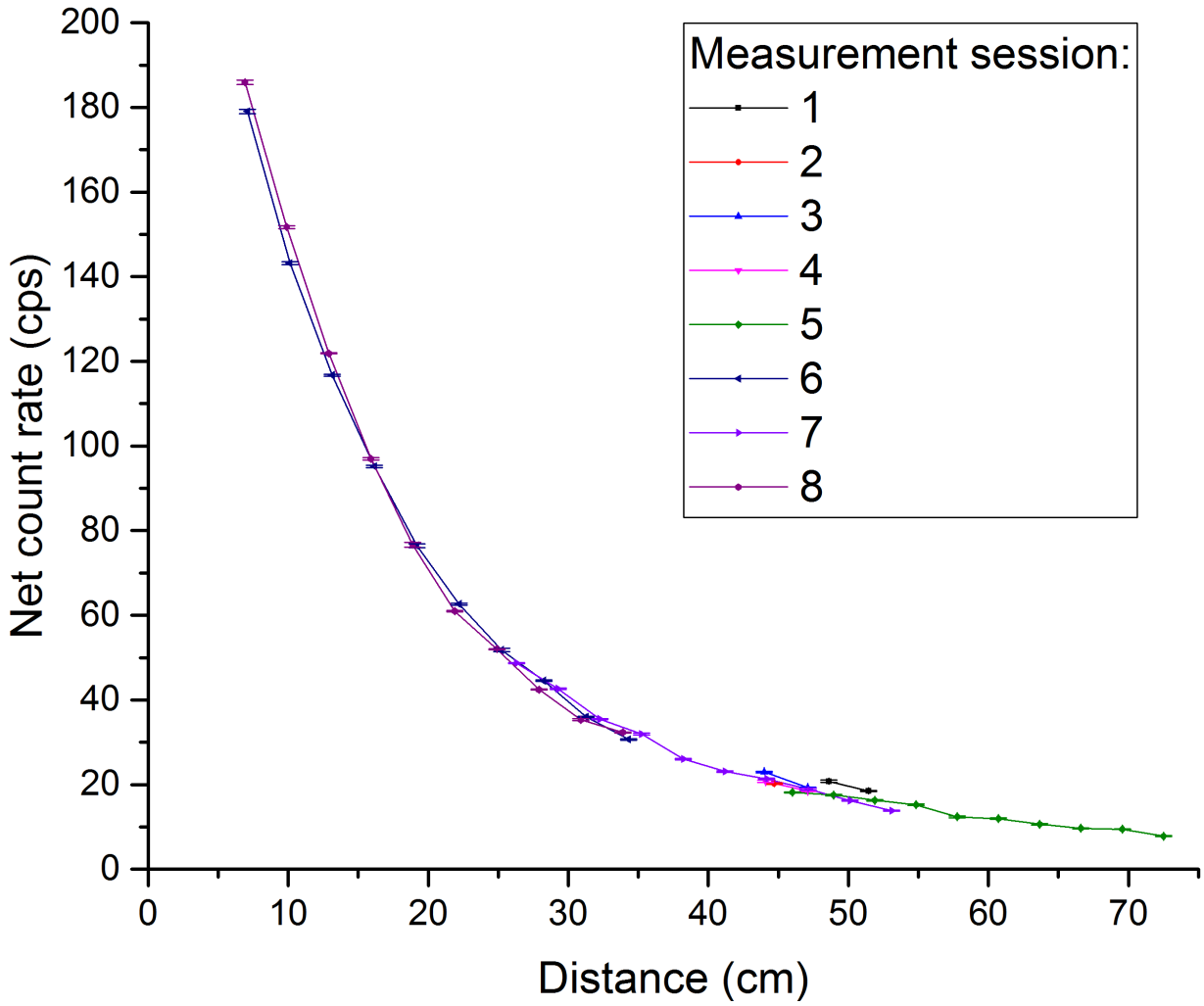


Figure 5.22: Measurements obtained from 47 UV images over 8 measurement sessions for six americium-241 sources showing repeatability of radioluminescence measurements. All were made over the course of a 2 month period for the same six americium sources. Data was extracted using the 5-point averaging method. Images were performed with the following seconds per image point (1-8): 6s; 6s; 6s; 10s; 10s; 10s; 10s; and 10s.

Displayed in figure 5.22 is the full set of data obtained using the imaging method with the 5-point samples to obtain net count rates. As demonstrated this combination of techniques offers excellent consistency between measurements. Sessions 1-8 were performed over a two month period due to the long period required to acquire the full set of calibration data. Some of these contained only 1-2 images.

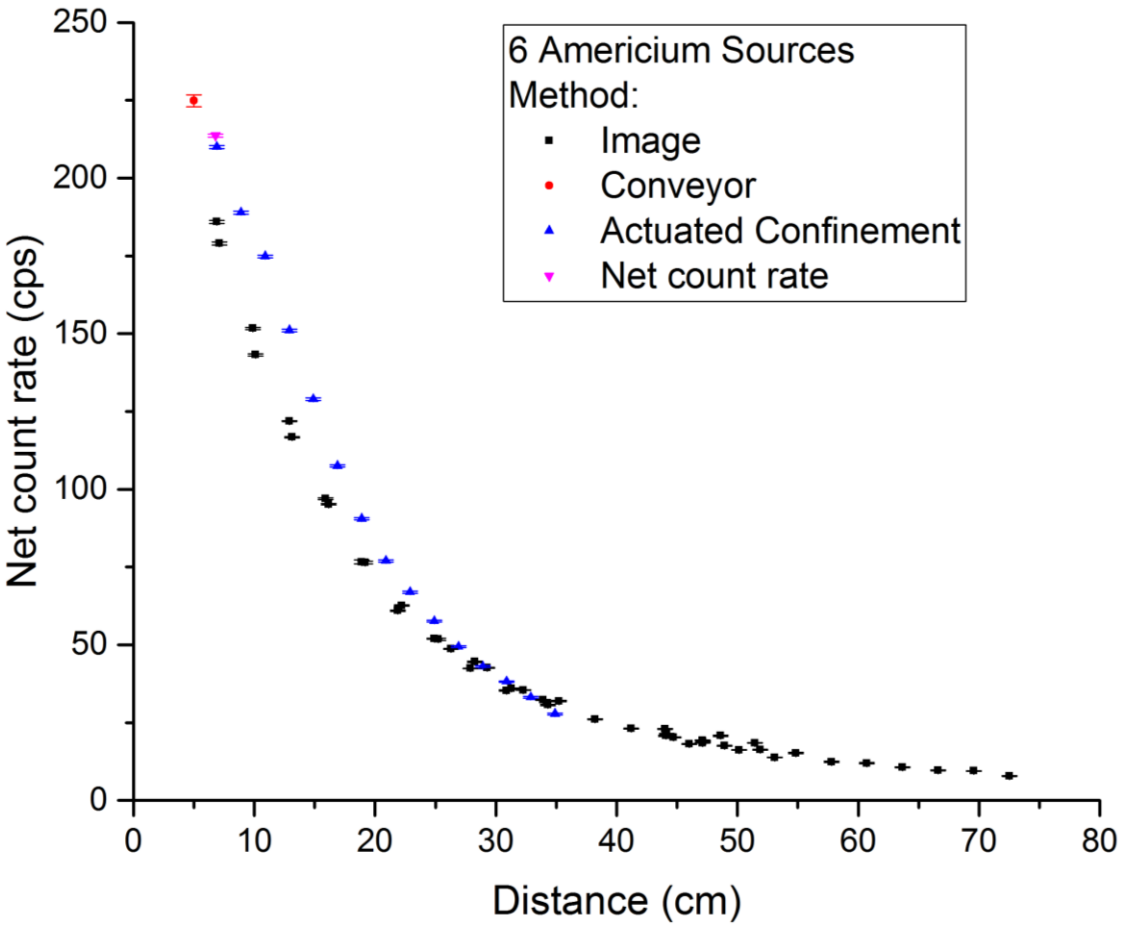


Figure 5.23: Comparison of net count rate measurements obtained using the four alpha-induced radioluminescence calibration methods presented in chapter 5. Measurements were obtained using the same six americium-241 sources in comparable, low UV background conditions.

5.3 Conclusion

Four methods for the analysis of detector performance have been outlined in this chapter, and data has been obtained for each using the same set of radioactive sources measured over a series of measurement distances of under one meter. The difficulties associated with the acquisition of data suitable for calibration over a wide range of distances has been discussed and several methods of potential use have been presented.

Displayed in figure 5.23 is a comparison between all data presented in this chapter for the set of six sources by method. As shown results obtained between measurements appear to be comparable in order of magnitude. Measurement error between different methods does not, however, appear to be commutable. Nevertheless, with baseline analytical requirements for industrial in-situ measurements with radioactive materials typically being measured in 10's of percent the technique has potential for analytical application in industry.

Another conclusion which can be drawn through the comparison of these calibration methods is that measurements appear to be more consistent at distances greater than 20cm. In addition to figure 5.23 this is also observable in the data presented in figure 5.8 for two of the americium sources. This is potentially attributable to the effects of close distance on the detector's angular sensitivity. This effect will be explored in greater depth in the following chapter.

Also discussed in this chapter has been the problem, until now unexplored in an experimental setting, of the linear scaling (or otherwise) of light intensity, as measured by count rates observed or number of photons, with the activity of sources presented. As discussed in depth in relation to the conveyor scanning method evidence has been presented indicating that linear scaling laws exist between light production and activity present, and that the system itself is capable of resolving this effect.

Four methods motivated by practical measurement scenarios, of direct potential application to industry, have been explored. Most notably the conveyor scanning method in its ability to produce repeatable, consistent analytical measurements of bulk alpha activity, holds great promise.

In addition in an operational environment in which the presence or extent of alpha contamination has not been measured – e.g. post-operational nuclear facilities with plutonium contamination such as reprocessing plants – the imaging method has great potential to identify regions which may or may not be contaminated. This could be a very useful development for operators in such an environment, having the potential to reduce dose exposure and expense.

This chapter explored several analogues of these operational scenarios and has yielded useful data which shall be used in the next and final chapter regarding the practical properties of the detection system.

Chapter 6
Methods for Quantitative Analysis of Detector Performance

To evaluate the effectiveness of the methods and equipment developed within the thesis, and indeed the alpha-induced radioluminescence technique itself, it is necessary to assess the limits and performance of the detector system. Research presented so far has focused on the development of methods to extract data relating to the detection system – such as the detector response to differing levels of activity or radioactive sources presented in different ways. This chapter will illustrate the application of these methods in a practical context using sources of known, traceable activity. The UV confinement method and imaging method of calibration were used to illustrate two ways to obtain fundamental, quantitative metrics of detector performance, detection limits and minimum detectable activity, over the appropriate ranges of measurement distances under 1m.

Given that the conveyor scanning method related to measurement of a source in motion. consideration of the detection limits associated with the technique were outside of the scope of this chapter. Further research on the application of metrics of detection for moving sources – such as receiver operator characteristics – to the conveyor scanning method is one of the primary recommendations in the future research discussed in chapter 7.

6.1 Establishing relative detector response over distance

A key finding presented in the previous chapter was a method to establish the attenuation of the detector's response to sources over distance. This is of significance given the detector's unique ability to operate over a range of distances without the need for any change to the optical configuration of the detector system, meaning that measurements can be easily compared in different environments without correction. For the majority of systems, such as those reliant on motors for focusing lenses, this would be more difficult given the requirement to match both measurement distance and the focusing arrangement.

Given that alpha-emitting traceable standard sources tend only to be manufactured up to a maximum activity of a few thousand Becquerel, it would not be practical to consider a full distance attenuation calibration obtained with such a source as presented before for the set of six americium sources. Instead, an approach was devised to use smaller activity sources – which are readily available as traceable to national and/or international standards – to obtain a distance calibration.

An important consideration when establishing a generic calibration - which can be used to compare measurements of activity between environments - is that the calibration must be based on variables which are independent of the change of environment. Discussed in chapter 3 was the relationship between particle emission energy and the relative attenuation of intensity as the source is moved further away from the detector. That discussion concluded that this effect is less significant at the distances under consideration (10cm to 1m), while at shorter ranges (under 5cm), due to the alpha particle's proximity to the detector, it produces significant effects.

Another variable which has been fixed is the radionuclide used for calibration. While the sources used for these measurements were of nominal overall activity, the emitted alpha particles were known to originate from the decay of americium-241. While they may not be useful in the context of calibration for the measurement of activity, they are valid for the analysis of the measurement distance attenuation of americium sources in general and can be considered useful for the comparison of relative response over distance.

Given the difficulty finding sources suitable for simultaneous calibration over both measurement distance and activity, it was considered that the set of americium sources could be used to produce measurements for a generalised attenuation function – valid for relative measurements of americium and most radionuclides which are of similar decay energy – which could in turn be made specific by a point calibration using a source of known activity.

The sources which have a combined activity of approximately 200kBq have enough activity to provide a detector response in measurements at distances up to 1m. While it is possible to measure smaller sources at short distance, the attenuation of net count rate over distance means that longer range measurements of smaller sources are not possible.

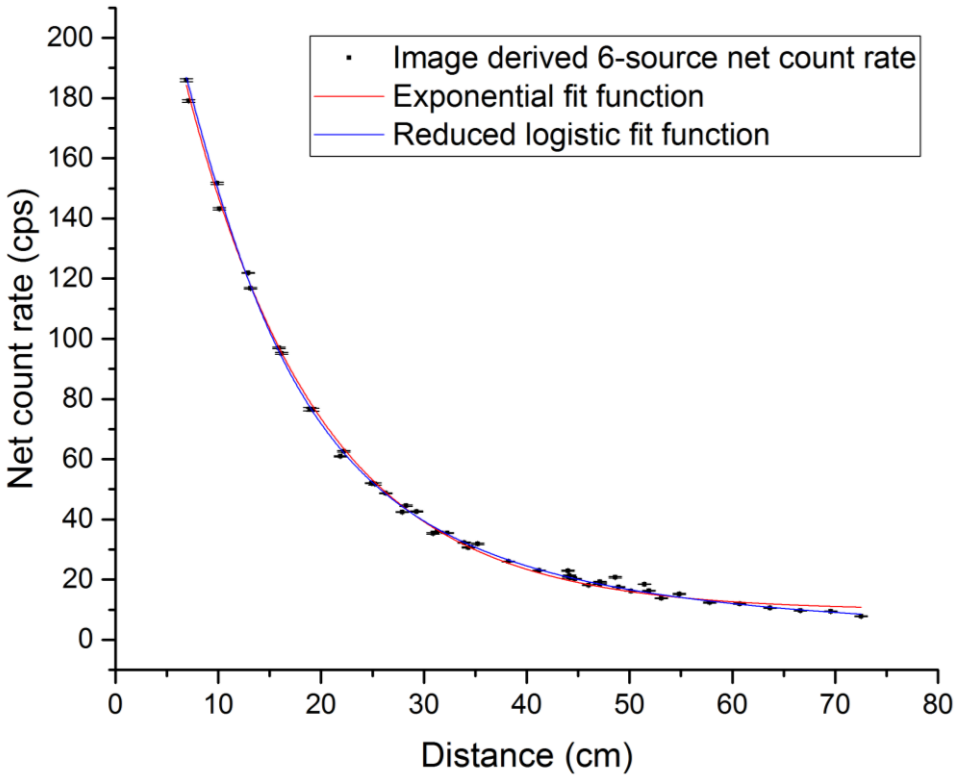


Figure 6.1: Measurements of the set of six americium-241 sources using the imaging calibration method, fitted with logistic and exponential fit functions using a non-linear least squares regression analysis.

Displayed in figure 6.1 is the measurement distance attenuation data produced in the previous chapter using the imaging method, applied to six sources over a range of distances under 1m. Applied to the data are two models, produced using the non-linear least squares method, for the data. An exponential fit function of the form:

$$y = y_0 + Ae^{\frac{-x}{t_1}} \tag{6.1}$$

was first applied. This model converged with an adjusted *R*-squared value of 0.996, and yielded the following fit parameters:

Parameter	Value
$\mathbf{y_0}$	9.7±0.5
A	297±6
$\mathbf{t_1}$	13.0±0.2

While this fit represented the data reasonably well it was considered that the non-zero intercept at $y=\infty$ could not be considered physical. Attempts to fit the data while fixing y_0 to a zero value would not converge. As such this model was rejected for further evaluation.

Another fit function which appeared to accurately represent the data was a reduced form of the logistic function:

$$y = \frac{A}{1+(\frac{x}{x_0})^p} \tag{6.2}$$

Which also converged with a higher adjusted R-squared value of 0.998. The parameters derived from this model were:

Parameter	Value
$\boldsymbol{A}$	248±8
$\boldsymbol{x_0}$	12.4±0.4
$\boldsymbol{p}$	1.89±0.03

This function appeared to accurately map the data within this interval. For the boundary conditions of $y=0$ and $y=\infty$ the function appears to match the expected behaviour, achieving a finite value, A, and 0 respectively. The function tends to infinity when $(x/x_0)^p = -1$ at $x=-x_0$, although the positive value of x_0 means this occurs outside the relevant region.

The parameter A is a quantity which scales the overall magnitude of the distribution to an arbitrary maximum at $x=0$, at which the value of $y=A$ is achieved. Given that the magnitude of the net count rate measured in this distribution is of little significance for the calibration, as it is derived from sources of only nominal activity, it is of little importance. Effectively A is a scaling factor across the function which determines its y-intercept.

The parameters x_0 and p are of more general significance for the calibration. These parameters determine the particular characteristics of the rate of decline of the relative net count rates over increasing measurement distance.

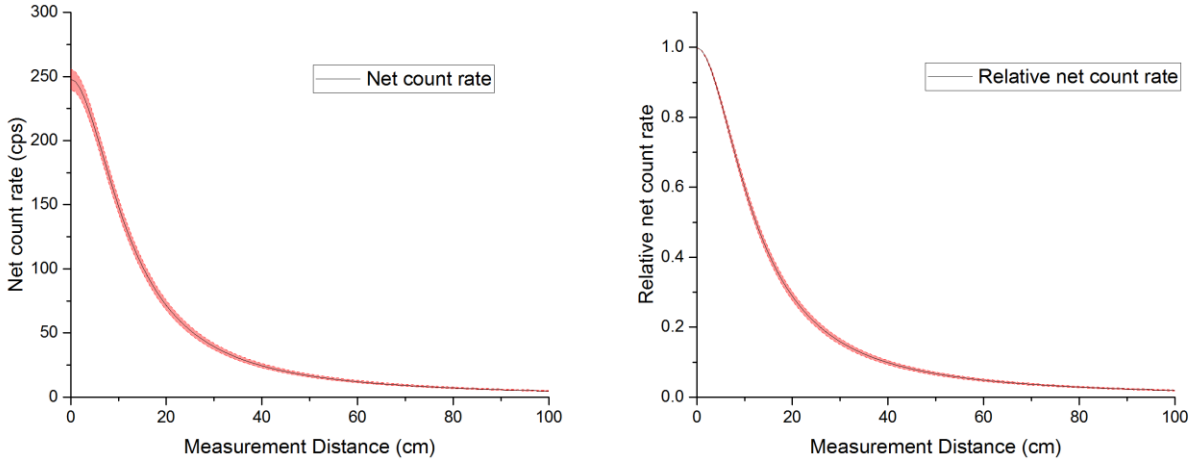


Figure 6.2: Left: Generalised form of the parametrised net count rate distribution for the set of six sources. Right: The relative net count rate observed over measurement distances compared to a fixed y-intercept of 1, resulting from the fixing of parameter A.

Displayed on the left of figure 6.2 is the fit function of the six source image measurements and shown on the right is the same form with the parameter A fixed at a value of 1. Also shown by the red shadow is the error associated with the two functions, based on the error of the associated parameters. Comparing the two figures it is possible to see that the error in A is dominant at short distances, although as it is scaled away its influence reduces and the uncertainty in x_0 and p become more dominant.

Using this relative (dimensionless) attenuation function over distance it is possible to consider the impact of a single fixed point calibration. If a measurement of a source of known activity is performed the relative attenuation function can be fixed at the corresponding point, using its net count rate, to represent the expected decline in net count rate for the particular

source measured over distance. The errors associated with the relative net count rate can also be analysed to yield the uncertainty across the entire function.

The resulting model of net count rate over distance can then also be divided by the activity of the corresponding source. This will yield the net count rate per decay within the source (cps/Bq), which is a quantity which is specific to the detector itself and which can be applied to other sources of known – or unknown – activity.

6.2 Measurements of sources of known activity

For the calibration in activity it was necessary to locate sources of appropriate, known activity and geometry. It was initially anticipated that, based on the response of the detector to the set of six sources, a source of only a few hundred Becquerels would be required. Initial measurements focused on a 50mm circular source of (221±6%)Bq, traceable to international standards (certificate number: 139716-SX214, product: AMR05011; appendix 1), at Imperial College Reactor Centre.

Displayed in figure 6.3 is a measurement of the source obtained using the UV confinement method. The centre of the source was positioned at (51±2)mm measurement distance from the detector optical axis and a measurement was obtained for 4600s (1 hour 20 minutes), although the measurement ended prematurely, as shown at approximately 4400s.

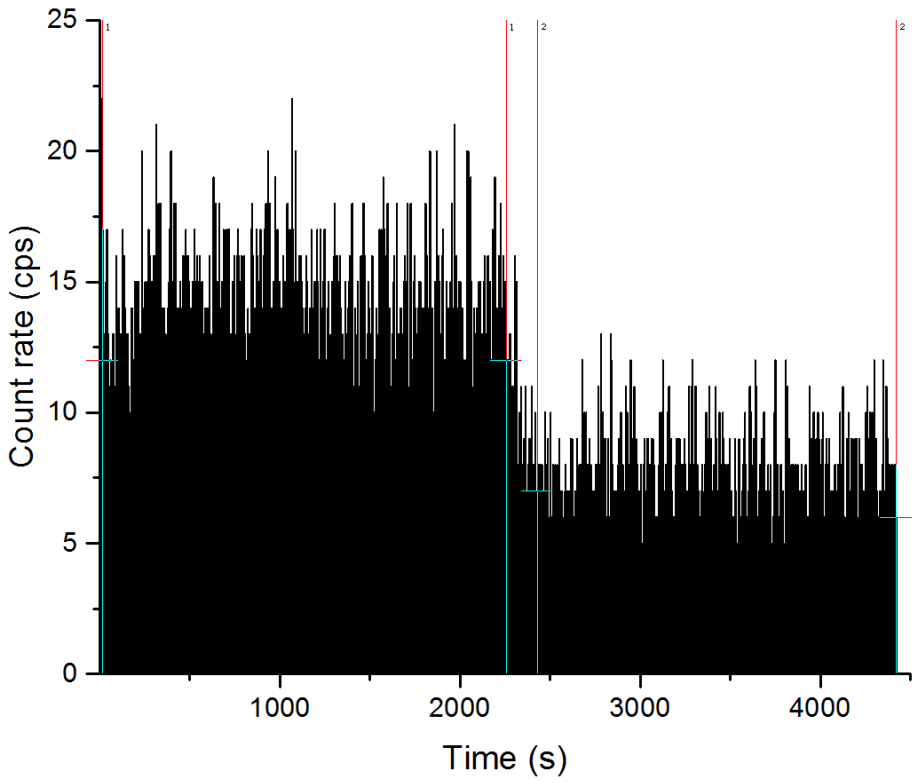


Figure 6.3: UV confinement calibration measurement using a 221Bq source positioned at (51±2)mm measurement distance. Red markers illustrate the regions used in analysis of exposed and confined segments. The exposed and background segments were 2250s each, with a settling time allowed between the two states as shown.

A second measurement was obtained on a later date using the same source at measurement distance (59.5±1)mm, and this is presented in figure 6.4, This measurement was initiated in the reverse sequence, with the background measurement obtained first, as some measurements had indicated slight elevation in the initial period after switch on. This measurement was obtained with two segments of 830s due to time limitations.

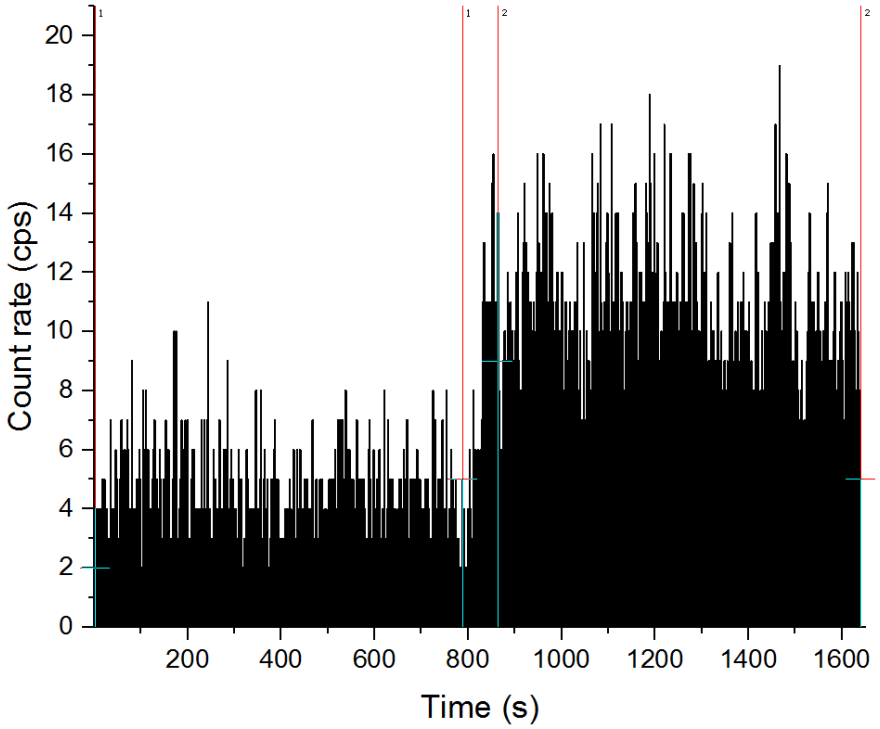


Figure 6.4: UV confinement calibration measurement using (221±13)Bq source at (59.5±1)mm measurement distance. The equipment was programmed to measure the background segment first (lasting 800s) followed by the source exposed (800s). A brief settling period has been allowed as shown by the red markers.

The transition between the the exposed and confined states is visible in both cases by the relative count rates on either side. In order to produce a quantitative estimate of the mean count rates within this measurement the observed counts within the period indicated by the red markers was summed. The period immediately preceding and following the transition were disregarded to ensure that settling effects post-transition were disregarded.

Distance (mm)	**Exposed Measurement**			**Confined Measurement**			**Net count rate ± σ_{calc} (cps)**
	Sum	*Period (s)*	*Mean ± σ_{calc} (cps)*	*Sum*	*Period (s)*	*Mean ± σ_{calc} (cps)*	
51±2	22860	2242	10.20±0.07	9700	1994	4.86±0.05	5.33±0.08
59.5±1	6447	778	8.3±0.1	2472	786	3.14±0.06	5.14±0.1

Table 6.1: Data extracted from the summing of exposed and confined segments of the measurement of a 221Bq americium source.

The results of this analysis are presented in table 1. Given the difference of measurement distance it is challenging to compare the two measurement directly, although they appear to be in good agreement with one another, lying within two standard deviations of one another.

Given that the source used in this measurement is traceable to international standards it is also possible to extract the net count rate per Becquerel of activity for each measurement. Given the 6% uncertainty quoted on the source's calibration certificate – provided in appendix 1 – the activity used for this calculation is (221±13)Bq.

Distance (mm)	**Net count rate (cps)**	**Net count rate / activity (cps/Bq)**
51±2	5.33±0.08	0.024±0.0015
59.5±1	5.14±0.1	0.023±0.0015

Table 6.2: Calculation of the detector's response to a (221±13)Bq americium source at two distances, as measured by the UV confinement method.

The calculation of this property is shown in table 6.2. When factoring in the uncertainty in activity of the source the results are in excellent agreement.

Given the differences observed in the detector response using the UV confinement method and the imaging method of calibration over distance additional measurements were performed using images. Given the short measurement times involved in the acquisition of images (with most in the previous chapter taking place over 10s/point) a source of larger activity would be required. It was initially attempted to produce an image of the 221Bq source at the Imperial College Reactor Centre, however of two attempts neither was successful due to the low signal-to-noise ratio for short period image measurements.

Measurements were obtained with three sources using the imaging method. Firstly a (3±1)kBq americium source used for the calibration of alpha spectrometers was measured at the Imperial College Reactor Centre. Unfortunately the associated documentation had been lost, although records within the College indicate an activity of 3kBq measured in 2003. To represent the uncertainty associated with this source a ±1kBq uncertainty has been applied.

Subsequently two further measurements were made during a visit to NNL Central Laboratory, Sellafield. This involved a certificated americium source (certificate number: 0227744 D-K-15203-01-00, product: AMR02022; appendix 2) of the same geometry with an activity of (912±3%)Bq and is traceable to international NIST standards. The second was with an older (2005) calibration source for which the calibration certificate had been lost. Accounting documentation associated with the source recorded the original activity as 1429Bq spread over an active diameter of 30mm. Given the lack of conclusive documentary evidence a 20% uncertainty has been applied to all measurements presented.

Figure 6.5 displays the output of imaging calibration on the three sources. Given the lower activity of the sources and the requirement that measurements be performed relatively quickly these are notably more affected by noise than those previously presented using this method, as shown by the volatility in count rates shown in the cross sections.

The outcome of the 5-point analysis applied to each image is presented in table 6.3 as follows:

Source (Bq)	Distance (mm)	Timing /Point (s)	5-Point Sum (counts)	Mean active count rate (cps)	Background (cps)	Net count rate (cps)	Net count rate/activity (cps/Bq)
912±27	71.5±1	6	433	14.4±0.5	4.54±0.2	9.9±0.6	0.0109 ±0.0007
1429±280	68±1	5	412	16.5±1	4.51±0.2	12.0±1.1	0.00837 ±0.002
3000±1000	75±1	5	432	17.3±0.5	4.85±0.3	12.4±0.5	0.004 ±0.002

Table 6.3: Calibration data obtained from three sources using the imagining method and a five point analysis as outlined in the previous chapter.

The output of these measurements show considerable variation. As expected the relative uncertainty associated with the measurement of the 3kBq source is considerably larger, at 50% uncertainty. The measurements of the 912Bq source and the 1429Bq source appear to be in good agreement although the 1429Bq source has considerable relative uncertainty of 25%.

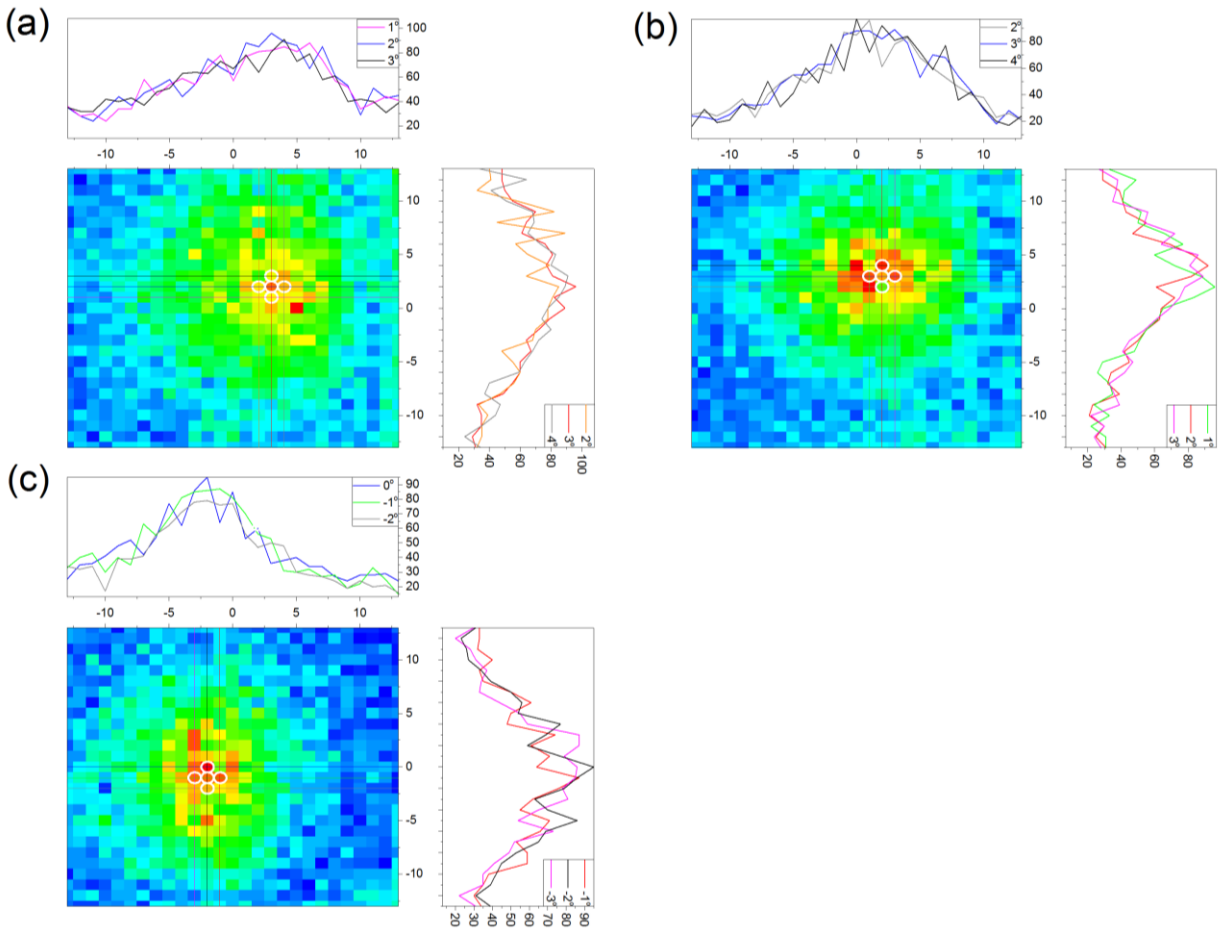


Figure 6.5: Image calibration measurements for (a) (912±27)Bq source at 71.5mm measured with 6s/point; (b) (1429±280) Bq americium source at 68mm at 5s/point and (c) (3±1)kBq americium source at 75mm at 5s/point. Cross sectional profiles illustrate the number of counts observed within each pixel and each is labelled with the angle from which it is derived.

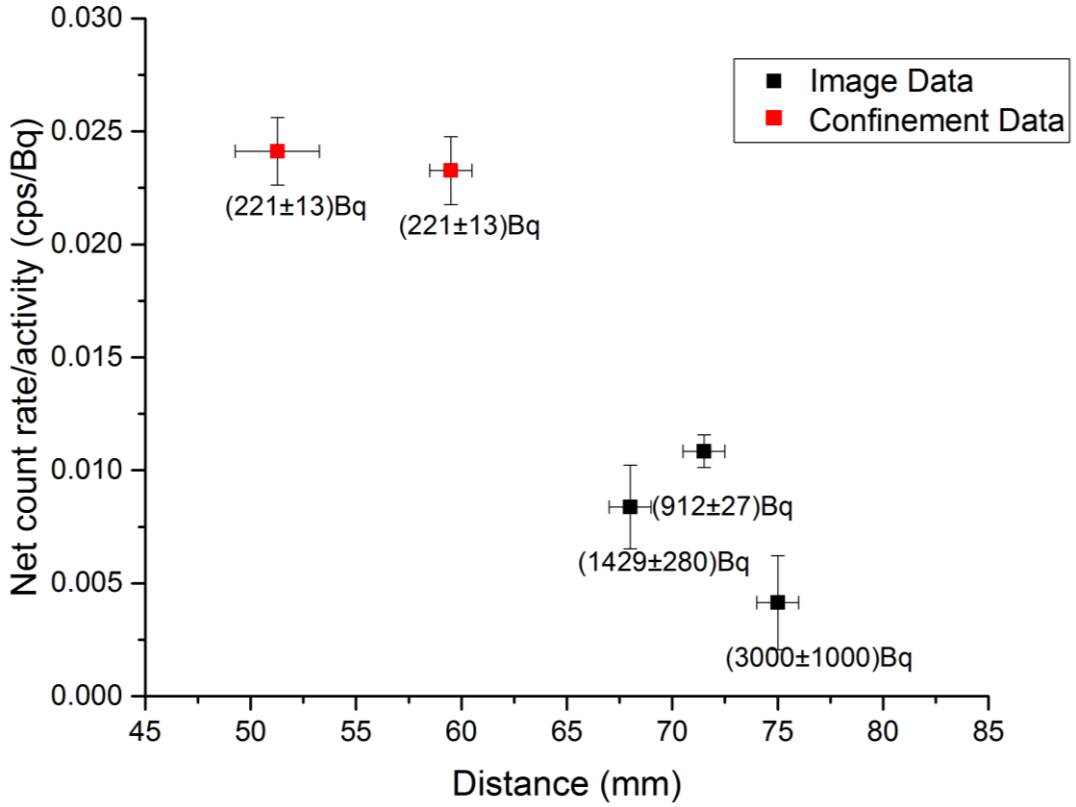


Figure 6.6: Data obtained across measurements of four sources using the imaging (black) and confinement methods (red) to obtain calibration factors. Source activities are labelled.

It is possible to compare the measurements made between the two methods (derived from the imaging method and the mechatronic confinement method), displayed in figure 6.6. In agreement with measurements made using both methods in the previous chapter the confinement method yields higher count rates when the same amount of activity is measured. There is no obvious explanation of this effect and this could warrant further investigation if these methods are to be applied in practise.

For the purpose of establishing a calibration factor for use in measurement, however, clearly the method of measurement must be the same as the method by which calibration is established. For the purposes of measurement it is appropriate that each calibration factor be used only with the attenuation data obtained by the same method.

6.3 Activity calibration over distance

The three measurements obtained using the imaging method can be combined with the attenuation over measurement distance presented earlier in the chapter. As discussed in relation to figure 6.2 it is necessary for each case to establish the value of the y-intercept parameter, A.

The value of the parameter can be established using the data presented in table 6.3. The measurements presented here are indicative of the detector's response to a source at particular measurement distances. For the establishment of the expected response over distance the parameter A can be extracted by using the expression:

$$A = y\,(1 + \left(\frac{x}{x_0}\right)^p) \tag{6.3}$$

The parameters x_0 and p have already been determined with their corresponding uncertainty. The value assigned to y will determine the unit associated, in this case the previously measured net count rate/activity.

Source (Bq Am-241)	**Distance (cm)**	***NCR*/activity (cps/Bq)**	**$A\pm\sigma_A$ (cps/Bq)**	$\sigma_A^{\frac{NCR}{activity}}$ (cps/Bq)	σ_A^x(cm)	σ_A^p	$\sigma_A^{x_0}$ (cm)
912±27	7.15±0.1	0.0109 ±0.0007	0.015± 0.001	0.001	0.0001	0.00006	0.0002
1429±280	6.8±0.1	0.0084 ±0.002	0.011 ± 0.003	0.002	0.00008	0.00005	0.0002
3000±1000	7.5±0.1	0.004 ±0.002	0.0058± 0.004	0.003	0.00004	0.00002	0.00009

Table 6.4: Calculation of the attenuation calibration parameter A using measurements of three sources using the imaging method. A is calculated using the expression in equation 6.3.

The calculated parameter A is corrected for the differences in the distance at which they were measured on the basis of the relative attenuation calibration model derived previously. These

measurements are directly comparable, as they are independent of the distance which they were measured, by comparison to the raw *NCR*/activity measurements discussed before.

The total error associated with the parameter *A* was determined by the sum of the component uncertainties due to *NCR*/activity, x_0, p and x ($\sigma_A^{\overline{activity}^{NCR}}$, $\sigma_A^{x_0}$, σ_A^{p} and σ_A^{x}) in quadrature:

$$(\sigma_A)^2 = (\sigma_A^p)^2 + (\sigma_A^{x_0})^2 + (\sigma_A^x)^2 + (\sigma_A^{\overline{activity}^{NCR}})^2 \quad (6.4)$$

As a result of the lower uncertainty associated with the activity of the traceable, certificated source (912Bq) the resulting uncertainty in the parameter A for this measurement is considerably lower than the others. As such in determination of an accepted figure for the activity response to americium an uncertainty-weighted mean can be used to establish an appropriate value for the parameter *A*.

The error weighted mean, $\hat{\mu}$, can be calculated for measurements x_i of standard deviation σ_i using the formula:

$$\hat{\mu} = \frac{\Sigma\frac{x_i}{\sigma_i^2}}{\Sigma\frac{1}{\sigma_i^2}} \quad (6.5)$$

And the uncertainty associated with the weighted mean of the measurements, $\sigma(\hat{\mu})$, can then be calculated by:

$$\sigma(\hat{\mu}) = \sqrt{\frac{1}{\Sigma\frac{1}{\sigma_i^2}}} \quad (6.6)$$

Using these formulae it is possible to establish a best estimate, based on the observed uncertainties, of the mean detector response to activity. The calculation of this parameter is displayed in table 6.5.

A (cps/Bq)	σ	A/σ^2	$1/\sigma^2$
0.01468	0.00123	9703.2	660982.2
0.01107	0.00307	1174.5	106101.9
0.00575	0.00356	453.7	78904.2
	Sum:	*11331.5*	*845988.3*
	Weighted mean:	**(0.01339±0.00108)cps/Bq**	

Table 6.5: Calculation of the weighted mean for the parameter A, the y-intercept of the measurement distance calibration function. Figures presented are extended to higher precision to prevent rounding errors.

Finally using the calculated best estimate value of A it is possible to evaluate the net count rate per decay over the appropriate range of measurement distances by evaluating the original attenuation model.

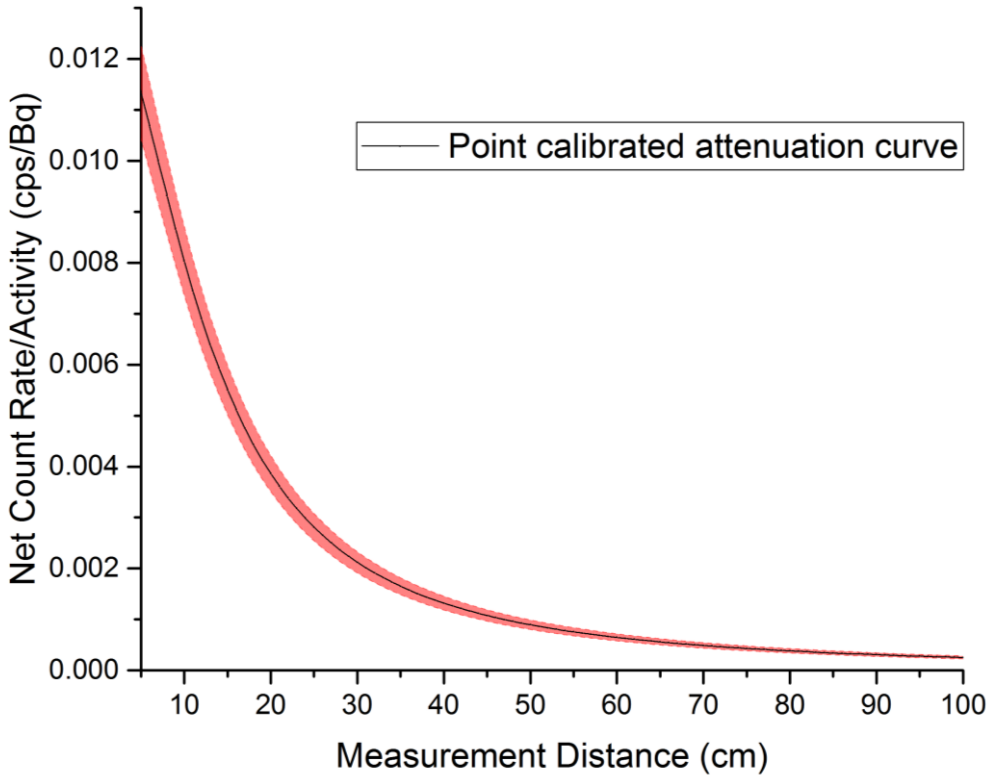


Figure 6.7: Using the parametrised model of relative net count rate attenuation over distance it was possible, using point calibration, to calculate the attenuation of the detector's response using the imaging method over distance. The region shown in red is the standard uncertainty associated with the model calculated to one standard deviation.

Displayed in figure 6.7 is the model derived, evaluated over the appropriate range of 5cm to 1m. This figure represents the expected response of the detector, as measured in counts per second, per Becquerel of americium-241 for distances up to 100cm. This model is also only appropriate for measurements obtained using the image calibration method, as discussed earlier.

6.4 Detection Limits

The most useful outcome of the parametrised model of detector response is that it can be used to evaluate the expected detector response within scenarios, and as a result can be used to establish the performance characteristics of the detector system.

A crucial consideration in the evaluation of the limits of detection of a method is the nature of the blank signal. In this method the background is extracted by the least squares method parameter averaging of regions about some central peak represented by the radioactive source.

By comparison to simple methods such as the manual or UV confinement method the nature of the variance of the background for the imaging method requires more consideration.

Similar methods are used in gamma spectroscopy for evaluation of peaks above Compton baselines in which the contributing background is removed using a peak estimation algorithm. Currie in his paper [88] discusses a procedure for estimation of detection limits in this case, although the procedure for the imaging method is simplified due to the fixed background without a slope.

For evaluation of the appropriate background the 47 images obtained for the calibration of the system over distance were used. These samples have a mean background of (60±10)counts in a 10 s/point measurement, with a replication variance of 118. The variance associated with the non-linear least squares method reported by the algorithm by comparison was only 5. A Chi-squared variance test conclusively rejects the prospect that this is a measure of the variance of this set of samples. This difference arises as the method implemented by the algorithm is only seeking to identify the uncertainty associated with the parameter within this measurement rather than variance between successive measurements. The calculation of the parameter itself takes into consideration many of the individual 10s measurements composing the image background and so the associated Poisson noise would on average be reduced.

An alternative descriptor of variance could be the variance arising due to the Poisson noise associated with the counting method itself (60). However, when evaluating the expected variance due to Poisson noise (59.955) with the Chi-Square variance test, again this hypothesis is rejected (p<0.0002).

As such it can be concluded that the dominant source of variance for observations of background within this method are due to the replication variance. This is readily understood given the variety of conditions in which the system was operated throughout these 47 measurements.

To evaluate the limits of detection it is necessary to evaluate the greatest source of variance in blank measurements, and then to use this to calculate the critical, detection and quantification limits (S_c, S_d, S_q). These are defined for signal S measured in counts in paired measurements of signal-background:

$$\sigma_0 = \sigma_B\sqrt{2}$$

$$S_c = 1.645\sigma_0 \qquad (6.7)$$

$$S_d = z^2{+}2S_c$$

$$S_q \cong 10\sigma_0$$

With σ_B being standard deviation associated with the background. As such it is possible to evaluate, using this observed behaviour across measurements, the limits associated with this method. The expressions illustrated are for a 95% confidence interval. For the calculation the standard uncertainty associated with the replication variance will be used, $\sigma_B = 10\ counts$.

$\sigma_0 = \sigma_B\sqrt{2}$	$\sigma_0 = 10\sqrt{2}$	14.14 counts
$S_c = 1.645\sigma_0$	$S_c = 1.645 \times 14.14$	23.26 counts
$S_d = z^2{+}2S_c$	$S_d = 3.29 + 2 \times 23.26$	49.81 counts
$S_q \cong 10\sigma_0$	$S_q \cong 10 \times 14.14$	141.4 counts

Table 6.6: Calculation of the critical limit, limit of detection and the limit of quantification for measurements obtained using the imaging method based on the replication variance-based standard uncertainty in background (±10 counts).

The figures calculated for S_c, S_d and S_q represent the number of counts in a measurement above background which a detection decision, detection limit and quantification limit can be established. These thus are representative in their formulation of what has until now been termed the net count rate, that is the signal minus background.

It is possible to calculate, on the basis of the model derived in section 6.3, the minimum amount of americium-241 activity which would have to be presented to the detector in order to exceed these thresholds. This quantity is the detector's detection limit specific to the imaging technique, and also to the condition of 10s/point measurement.

This calculation can be approached by considering the value of the net count rate per unit activity (cps/Bq). The activity, A, required for S counts to be recorded in excess of background in measurement period t can be related to the net count rate/activity ($R_{detector}$) by the expression:

$$A = \frac{S}{R_{detector}\, t} \tag{6.8}$$

Which, as shown by evaluation using dimensional analysis, is a measure of activity:

$$[Bq] = \frac{[Counts]}{\frac{[counts]}{[s][Bq]}[s]} = [counts][counts]^{-1}[s][s]^{-1}[Bq] \tag{6.9}$$

Using this equation, we can transform the model illustrated in figure 6.7 to represent the required amounts of activity. This was performed for a measurement period of 10s/point.

Displayed in figure 6.8 and table 6.7 are the minimum activities required for the limits to be reached over distance. Upon initial inspection this appears to corroborate the failed attempts discussed earlier in the chapter to measure using the imaging method the 221Bq source at approximately 7cm distance, in which the source was indistinguishable from the Poisson noise observed in the measurement.

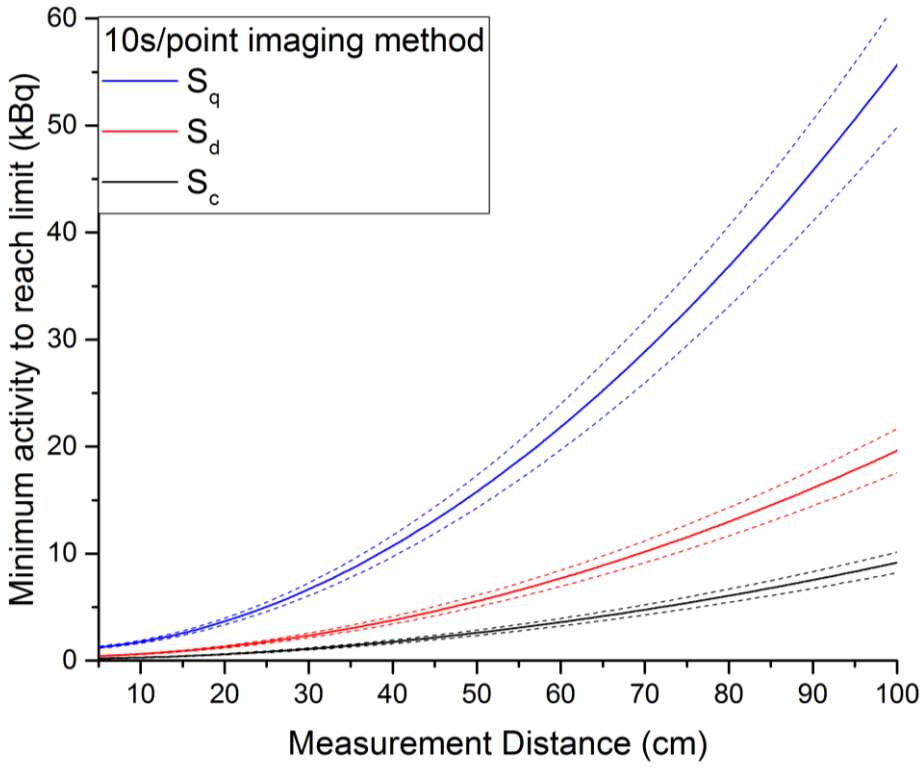


Figure 6.8: The minimum activity required for a net count rate in excess of the limit of quantification, S_q , limit of detection, S_d, and the critical limit, S_c, for an image-based measurement of an americium source.

Limit	Minimum activity (Bq)			
	7cm	10cm	20cm	50cm
L_c	230±20	290±20	600±50	2600±250
L_d	500±40	620±50	1300±100	5600±500
L_q	1400±100	1760±140	3700±300	16000±1500

Table 6.7: Sampled minimum activities required to reach the threshold decision limit, detection limit and limit of quantification in a 10s/point image of americium sources.

6.5 Calculating Detection Limits for the UV Confinement Method

Detection limits and performance metrics apply to the analysis method applied and not to the particular instrument itself. As such, for meaningful discussion and evaluation of the methods it is also necessary to perform a comparable analysis using the UV confinement attenuation data and the point calibration obtained using the 221Bq source.

Figure 6.9 shows a fit function evaluated for net count rates measured over distance using the UV confinement method between 6.9 and 35.45cm for two americium-241 sources. This data was chosen for the evaluation of the fit function as it was of the highest precision obtained, being evaluated in paired 2400s exposed/confined segments, and because it corresponded to the same range of measurement distances as evaluated using the imaging method.

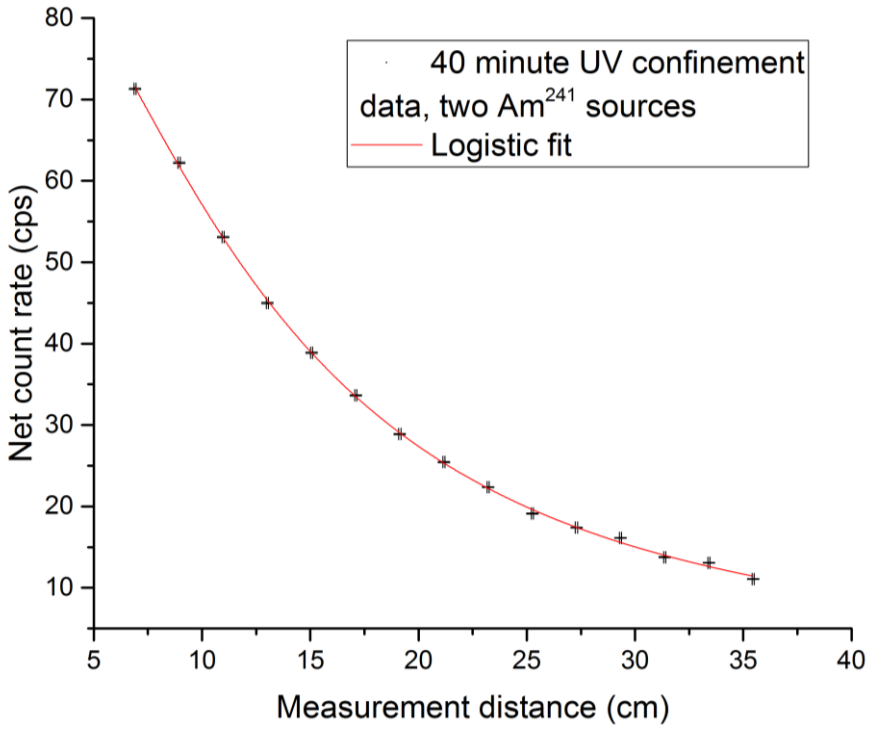


Figure 6.9: Attenuation curve for the confinement method obtained using two americium-241 sources. The data is fit using a logistic function. Net count rates were obtained from 2400s (40 minute) signal-background segments.

This data was also combined with the two other sets of measurements obtained over considerably shorter periods (20s and 60s), presented in the previous chapter, to also evaluate the repeatability of this method, as was also evaluated by the imaging technique. The result is displayed in figure 6.10, clearly illustrating the problem of repeatability associated with the technique, with variability between the three measurements particularly defined at shorter distances.

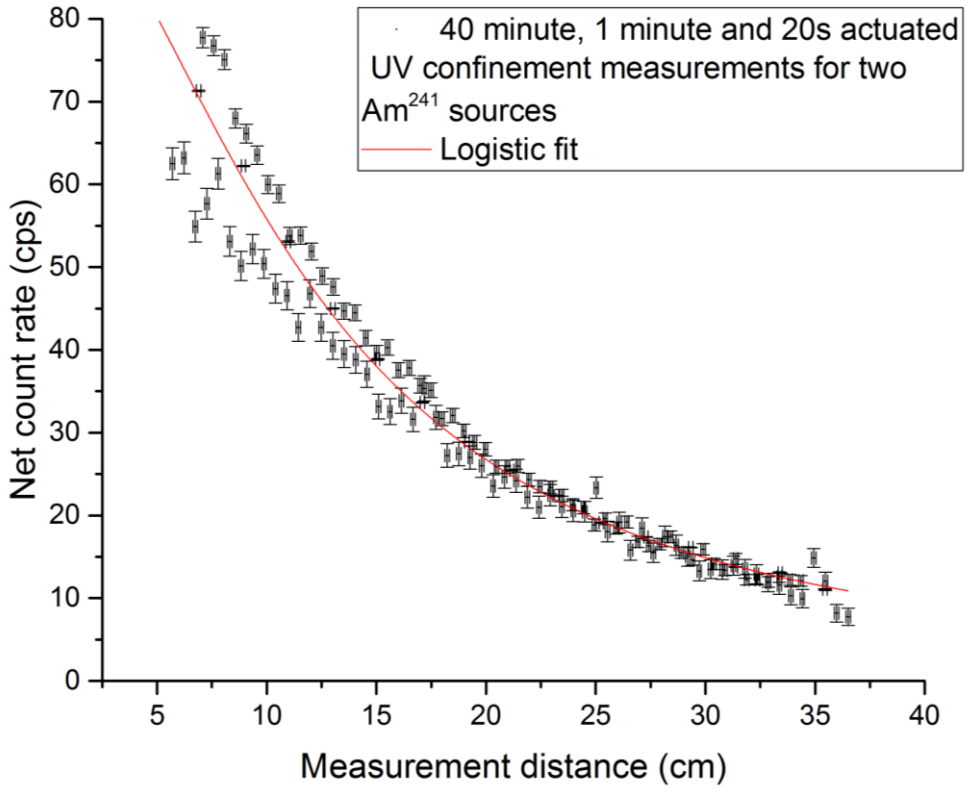


Figure 6.10: Actuated UV confinement measurements of two americium sources modelled using a logistic fit function. Measurements were obtained over paired 40 minute, 1 minute and 20s measurements to assess repeatability and combined into a single dataset.

The fit parameters extracted from the two datasets are summarised in table 6.8. The logistic model applied was as previously discussed for the imaging method, and is reproduced here for clarity:

$$y = \frac{A}{1+(\frac{x}{x_0})^p} \tag{6.10}$$

Parameter	40 minute data	40 minute, 1 minute and 20s.
A	95.0±1.5	97±5
x_0	12.4±0.2	11.8±0.9
p	1.89±0.03	1.83±0.10

Table 6.8: Logistic fitting parameters obtained from actuated UV confinement data evaluated for the periods indicated.

The two methods therefore produced estimates of the parameters in excellent agreement with one another, and also in excellent agreement with the data obtained by the imaging method.

For the comparison of the method performance between the actuated UV confinement method and the imaging method, the combined dataset (40 minute, 1 minute and 20s) will be used to accurately reflect the repetition variance associated with the method.

Using the parameters x_0 and p it is possible to evaluate the new parameter $A_{confinement}$, using the point calibration data obtained for the 221Bq source (figures 6.3, 6.4 and table 6.2).

Source (Bq)	**Distance (cm)**	***NCR*/activity (cps/Bq)**	$A \pm \sigma_A$ **(cps/Bq)**	$\sigma_A^{\frac{NCR}{activity}}$ (cps/Bq)	σ_A^x (cps/Bq)	σ_A^p (cps/Bq)	$\sigma_A^{x_0}$ (cps/Bq)
221±13	5.1±0.1	0.0241 ±0.0015	0.0294 ± 0.0025	0.002	0.0002	0.0004	0.0007
221±13	5.95±0.1	0.0233 ±0.0015	0.0299 ± 0.0026	0.002	0.0002	0.0004	0.0008

Table 6.9: Calculation of the y-intercept of the calibration function for the UV confinement method using a point calibration performed using a 221Bq americium-241 source. Extra decimal places were maintained to reduce rounding errors in subsequent calculations.

Displayed in table 6.9 are the calculated values of the parameter A for the attenuation model over distance, as obtained using the parameters x_0 and p displayed in table 8 combined with the measurements of the 221Bq source. The calculated values of A between the two measurements continue to be in excellent agreement with one another.

***A* (cps/Bq)**	***σ***	***A/σ²***	***1/σ²***
0.0294	0.0025	4704.0	160000.0
0.0299	0.0026	4423.1	147929.0
	Sum:	*9127.1*	*307929.0*
	Weighted mean:	**(0.0296±0.0018)cps/Bq**	

Table 6.10: Calculation of the error weighted mean for the two calculated values of the model parameter A.

Displayed in table 6.10 is the calculation of the error-weighted mean using the same method as used for the imaging method. Using the new set of parameters it is now possible to evaluate the graph of detector response (Bq/cps) over distance as previously.

Figure 6.11 shows the detector response curves calculated for the two methods. The higher net count rate measured using the UV confinement method with the 221Bq source (annex 1) means that the detector response function for the method is considerably elevated.

The difference between the two response functions suggests error associated with the imaging method calibration. Given the considerable uncertainty associated with the measurements used to calculate the intercept (see figure 6.5), the uncertainty associated with source activity (table 6.3) and the age of two of the sources, this is likely be attributable to the point calibration measurements.

The origin of this discrepancy requires further investigation using higher activity sources using longer measurement periods. For future point calibration measurements a minimum

source activity of 1kBq is recommended to reduce uncertainty associated with the point calibration.

Further systematic factors which may have influenced the measurement include differences in field of view for the two methods and the influence of gamma photons on measurements. Data obtained after the project's conclusion has shown that it is highly unlikely that this can be explained by gamma interference as no photomutliplier response to kBq gamma sources has been observed. Testing of response to high activity beta and gamma backgrounds is, however, required before deployment within a decommissioning environment.

It remains unclear whether the field of view of the detector in the two modes of operation could have led to differences in the point calibration measurement. Given that backgrounds are measured from the region surrounding the source in the imaging method this may have had an impact on the measurement.

Consideration of this discrepancy forms one of the recommendations for future work. This will be necessary before a comprehensive assessment of detector performance using the imaging method can be achieved.

Nevertheless International Organisation for Standardisation is clear that a calibration in its enterity – including in relation to data analysis processes – can only be meaningfully compared to measurements obtained using the same underlying method. The method outlined above for the comparison of performance is more suited to the comparison of device performance rather than in relation to methods of measurement.

Given the variance of the set of 40 minute, 1 minute and 20s measurements a higher relative uncertainty is also associated with net count rate per decay for the confinement method.

For consideration of the detection limits associated with the UV confinement method it is necessary to again analyse the variance associated with the background observed in this method.

The UV confinement method is considerably simpler to evaluate than the imaging method due to the lack of a fitting algorithm. Direct analogues also exist for established radioanalytical methods such as counting systems.

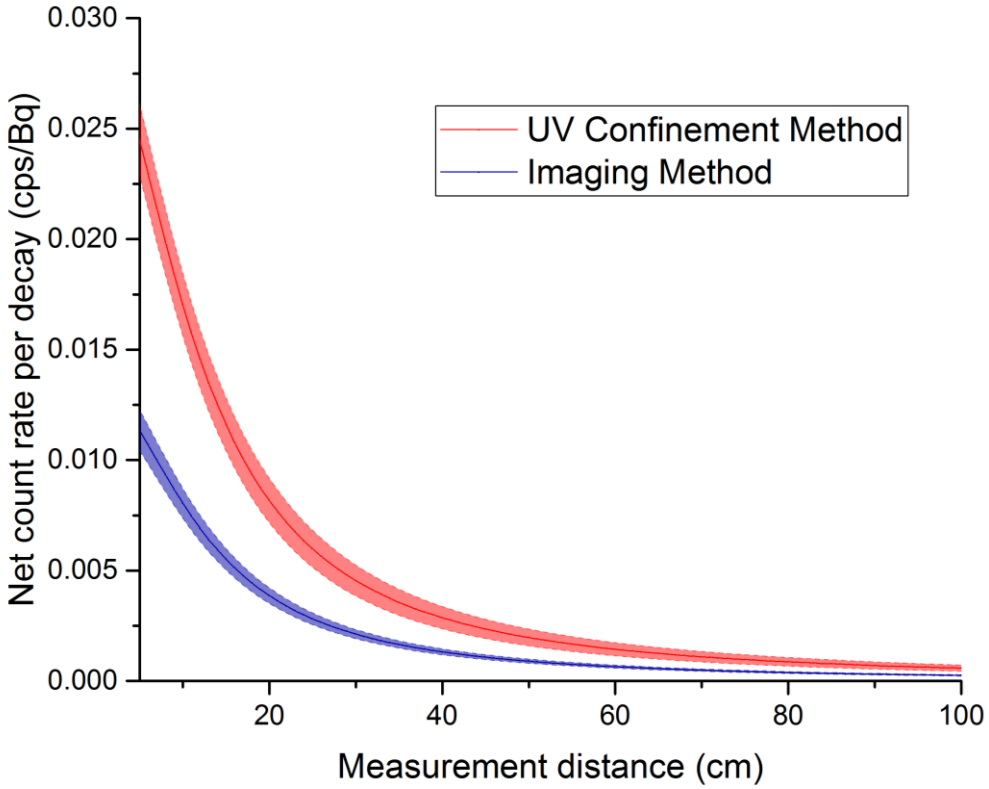


Figure 6.11: Comparison of the detector response using the UV confinement method and the imaging method. For the UV confinement method net count rate is calculated using measurements presented in figure 6.10 and table 6.10. The imaging method curve is identical to that presented in figure 6.7. The two lines represent the output of the parametrised fit model and based on measurements of sources traceable to international standards. Shaded regions around the lines display the ±1σ boundary.

The background measurement used for the calculation of the net count rate is simply the sum of the counts observed within some measurement period. As such the major expected source of noise would be due to the Poisson count statistics.

The three datasets obtained using measurements of 40 minutes, 1 minute and 20s were used to test this hypothesis.

The results of this analysis are presented in table 6.11. The sets of 60, 60 and 15 samples were evaluated for their standard deviations, variance and the corresponding expectation was

calculated on the basis of Poisson noise alone. This was then tested using a Chi-Squared Variance test implemented on MATLAB and the result of this, and the associated p-value, are displayed. As shown the 20s and 40 minute measurement backgrounds exhibit a higher variance than would be expected were the variance only due to Poisson noise.

	20s		60s		40 minutes	
	Observed	Expected	Observed	Expected	Observed	Expected
Number of samples	60		60		15	
Mean Background Rate (cps)	6.22		5.70		5.25	
Standard deviation	0.72	0.56	0.34	0.31	0.63	0.05
Variance	0.51	0.31	0.11	0.095	0.39	0.002
Chi-Squared Variance test: variation due to Poisson?	**No**		**Yes**		**No**	
P-Value	0.0027		0.26		0	

Table 6.11: Evaluation of the background variance associated with measurements using the UV confinement method of various measurement periods.

This is very interesting and illuminates two issues with measurements of either scale. For the twenty second measurements it is likely that the greater than expected level of variance can be explained by the settling period of the photomultiplier tube. The manufacturer quotes a

10s settling period in which higher levels of volatility can be expected after changes in the external light environment.

The variance exhibited by the 40 minute measurements is very interesting and the reason for this is not immediately obvious. As discussed in the previous chapter, however, over measurements performed over such periods changes in the environment (e.g. lights being switched on or sunlight interference) are highly likely. The effect of this is that the background observed between measurements exhibits considerably greater variability than it otherwise would, were there no changes in the external light environment. As such the most dominant source of uncertainty arises within this set of measurements due to replication variance.

The 60s background signals were proven to exhibit variance which is consistent with Poisson variation alone. This is once again readily understood by considering that it is likely that if measurements last only for 60s they are less likely to be affected by such variation in environmental conditions, and are more likely to be obtained over a shorter total period in which such variation is not to be expected.

Quantity	Calculation	10s	60s	300s
$\sigma_0 = \sigma_B\sqrt{2}$	$\sigma_0 = t \times 0.72\sqrt{2}$	10.2 counts	61.1 counts	305.5 counts
$S_c = 1.645\sigma_0$	$S_c = 1.645 \times \sigma_0$	16.7 counts	100.5 counts	502.5 counts
$S_d = z^2{+}2S_c$	$S_d = 3.29 + 2 \times S_c$	36.8 counts	204.3 counts	1008.3 counts
$S_q \cong 10\sigma_0$	$S_q \cong 10 \times \sigma_0$	101.8 counts	610.9 counts	3054.7 counts

Table 6.12: Calculation of the decision limit, detection limit and limit of quantification for the UV confinement method for a measurement of 10s, 60s and 300s using an assumed standard deviation of 0.72cps, scaled to each measurement period.

As such for calculation of the method detection limits the higher replication variance of 0.51, and the associated standard deviation (0.72cps) will be used.

However, as shown in table 6.12 if the variation of the background is assumed to scale linearly with the time period then the detection limits also scale linearly in the same fashion. This means that the same required net count rate applies no matter how long one counts for, and as a result counting for longer does not provide any increase in the detection limit. Instead the corresponding amount of activity is determined only by the minimum activity required to provide a net count rate in excess of σ_0, 0.72cps.

Limit	Minimum activity (Bq)			
	7cm	10cm	20cm	50cm
$\mathbf{L_c}$	78±5	98±8	205±23	851±140
$\mathbf{L_d}$	157±10	197±15	412±45	1708±280
$\mathbf{L_q}$	476±32	598±46	1247±137	5175±840

Table 6.13: Minimum activity at the limits of determination, detection and quantification for the UV confinement technique measured for paired measurements of 300s duration for each active and background segment. Results are displayed for a series of measurement distances.

Displayed in figure 6.12 and table 6.13 are the minimum detectable activities at the limits of determination, detection and quantification over measurement distance. As shown, in spite of the background variance problem the minimum detectable amounts of material for this technique, evaluated here for a 300s measurement, are notably lower than for the imaging method.

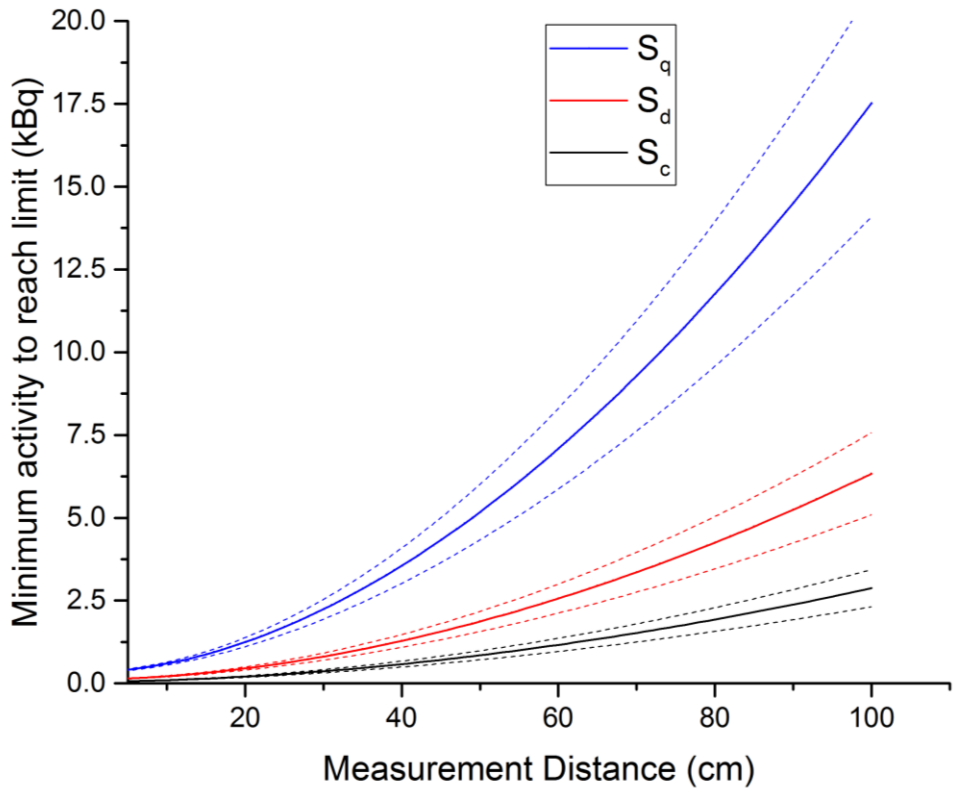


Figure 6.12: Minimum detectable activities at the limits of determination, detection and quantification for the UV confinement method. The results displayed are for a measurement of 300s in an active-background configuration, although these limits have been shown to be independent of the count period.

6.6 Conclusion

Through the quantitative comparison of two modes of operation – the UV confinement method versus the imaging method – this chapter has demonstrated how it is possible to quantitatively evaluate the performance of alpha-induced radioluminescence detectors.

Results have shown that the detection limits for the UV confinement method are considerably lower than those associated with the imaging method, though the underlying reason this result needs to be explored in more detail. Interpretation of the results has indicated that this discrepancy might be attributable to uncertainties in the point calibration measurement and differences in field of view between the two methods. Further work is recommended to

consider this in more depth using higher activity sources measured for longer periods. Nevertheless, the results are promising and indicate that the method proposed for comparison is more suited to analysis of comparative device performance rather than data acquisition methods.

The methods applied to the two modes of operation can be readily used to compare the performance of two detectors. By consideration of the repetition variance for each detector and the response to activity it would be possible to calculate detection limits for particular measurement scenarios.

As has been demonstrated, each device calibration and detection limit must be applied to a particular mode of operation. It is not possible to use a detection limit calculated for one method to infer performance of another. Therefore when comparing detectors they should be compared using the same mode of operation for a like-for-like performance comparison.

It has been demonstrated that an individual point calibration using a traceable source can be combined with measurements of non-traceable alpha-emitting sources of the same radionuclide to infer the response of the detector over distance. This is particularly useful given the difficulty to find traceable sources of sufficiently large activity to produce such calibration measurements at longer distances.

This limitation may be offset for detectors using more sophisticated optical assemblies which are likely to exhibit higher sensitivity, and therefore lower detection limits at comparable distances.

The results presented have only been assessed for americium-241. In a practical industrial scenario it is highly likely that calibrations against other nuclides would be required. Future work should therefore assess the relative detector performance against other radionuclides.

The response to activity (cps/Bq) of the detector constructed in the project has been shown to be lower than equivalent probe-type zinc sulphide detector if comparing ideal operating scenarios. For example, ThermoFisher Scienfic quote a 18% conversion efficiency for americium-241 alpha particles on the HP-380A detector[89], corresponding to average response of 0.18cps/Bq at the standard 3mm calibration length discussed in section 5.1.1. For comparison, in table 6.4 measurements showed the detector to exhibit a net (photon) count

rate above background of (0.0109±0.0007)cps/Bq at (7.15±0.1)cm and (0.0084±0.002)cps/Bq at (6.8±0.1)cm.

Direct comparison at equivalent distances are however not possible given that measurements using alpha-induced radioluminescence are not possible at lengths below the path length of the particles themselves. Likewise probe-type detectors are unable to detect beyond the alpha particle's path length.

Chapter 7
Conclusions and future work

7.1 Review of research problem

The use of alpha-induced radioluminescence for the detection of alpha-emitting radionuclides has considerable potential for use in the nuclear industry. Methods currently available to operators for the measurement of alpha contamination require either direct interaction with contaminated material – posing risk to personnel and Site Licence Companies – or using an indirect measurement of gamma signatures, which is only possible a small range of radionuclides. This work has sought to address a number of the gaps which have limited the adoption of alpha-induced radioluminescence detectors by industry.

Reviewing existing literature in the field highlighted several unknowns which have limited this progress. While a number of devices had been developed in the recent past, the absence of established methods of operation – in terms of the type of measurement performed, the types of source used and the conditions of measurement – made comparison between devices, and indeed modes of operation in like-for-like conditions, impossible. The lack of an established measurement methodology has meant that some of the most fundamental parameters of device performance have not been considered; for example, detection limits, detector response, and measures of performance in different environments. This meant that while it was obvious that the method had potential, it was not possible to establish how such detectors would perform compared to the techniques currently used, or what their possible limitations would be.

The absence of established methods had also led to limited consideration of the types of measurement which might be performed. An obvious gap in the literature was the absence of a method of calibration of detectors against sources of known activity. Given the remote nature of alpha-induced radioluminescence detection it was also clear that any attempt to calibrate the detector would have to think beyond the calibration methods used for other detectors of alpha-emitters, which were performed at a fixed distance. Given that various modes of operation had already been explored by researchers – specifically fixed

measurements and scene scanning – the method used to obtain measurements would also be a key factor in any future calibration.

A limited body of research considered the physical processes underlying the alpha-induced radioluminescence process. This work has sought to build on this by considering the implications for detector function. Given the physical properties of the alpha particle emissions arising from an alpha source, the performance of detectors operating near the source were found to be more complex than has been previously assumed. For any detectors operating in the range under half a metre from source to detector these factors become significant, with a resulting impact on the accuracy of measurements. Any approach to calibration in this region should consider this effect.

7.2 Conclusions

In appropriate conditions, alpha-induced radioluminescence has been shown capable of producing quantitative, accurate, repeatable measurements of the activity of alpha-emitting contaminants. This thesis has sought to prove this to be the case and to address several of the key limitations which have stalled industry interest in the technique so far.

The detector designed and developed in the project was shown to be capable of producing such measurements with a linear response to activity. Within the constraints of the project's budget this detector was comparatively inexpensive and demonstrated an ability to detect sources of similar magnitude to others produced elsewhere. Furthermore the development process was used to outline a number of the key factors which ought to be considered in any effort to produce a similar detector.

A useful feature of the detector was its ability to perform in a broad range of environments. During the project the device was shown to operate effectively in different environments – ranging from an optically sealed laboratory (in the Blackett Laboratory), to active nuclear facilities (NNL's Central Laboratory at Sellafield and the Imperial College Reactor Centre) and an industrial facility with semi-opaque window lighting (Viridian Consultants' workshop in Wales). A limitation on the device's performance was that given the choice to focus on the most intense 337nm emission wavelength, the device was not able to operate effectively in direct view of externally facing windows. Given that most active

facilities handling alpha-emitting materials (e.g. reprocessing, hot cell facilities) do not tend to have such windows this was not a major concern in the relation to the project.

The physical processes underlying alpha-induced radioluminescence have also been evaluated using a novel simulation framework. This has been used to explore the processes underlying the temporal characteristics of alpha decay and the resulting emission of photons. It has been shown that the two elements of this process provide for a convenient timescale upon which measurements can be gated to identify background. A simple model of detection geometry was presented and used to show a first principles method to assess the maximum possible detection efficiency of detectors at different distances between source and detector. This was used to demonstrate the importance of the accuracy in the measurement of this distance when producing quantitative measurements of source activity. It also demonstrated that given the dependency between the detection efficiency and the viewing angle between source and detector, any off-axis measurement at short distance will measure a lesser intensity. These factors illustrate the practical constraints which affect measurement uncertainty and determine the conditions in which valid measurements should be made.

Four methods of operation have been developed and evaluated. These methods have been used to consider how devices could be calibrated with respect to traceable sources of known activity. Each method was demonstrated using sources of americium-241.

Firstly a method comparable to that used to calibrate probe detectors was explored. It was found that the requirement to physically remove the source led to changes in the light environment of the detector, considerably increasing the random uncertainty associated with these measurements. Given that measurements were also required over a several distances (in order to calibrate detector response over the full range of possible measurement distances) it was also found that this was also slow and prone to human error.

The UV confinement method was developed as an extension of the calibration method used for probe type detectors. The new system meant that rather than measuring a calibration at a single, fixed distance, the system could be primed to perform a series of individual calibrations over a range of distances in an automated manner. The method was found to produce a calibration which was repeatable for measurements performed in similar conditions.

A limitation of the experimental setup used was that it was difficult to align the detector axis with the railing of the motorised platform. This could be remedied in future work by defining a fixed geometry between detector and platform for calibrations using this method.

This is indicative of a potential pitfall for practical measurements of unknown sources. It is likely to be difficult to ensure alignment between a detector axis and the centre of a source, meaning any single measurement may not fully incorporate the absolute intensity of the source. This issue is also known to affect standard probe type detectors – for which a series of scanning measurements over a surface must be made in order to isolate the full extent of contamination. An equivalent method for the remote alpha-radioluminescence detector could be to move the detector further away from the surface. Given that the detector is sensitive to a particular solid angle along its axis, by moving further away it is likely that the detector would incorporate a greater proportion of the source corona, leading to a more complete measurement of the source.

The third method presented was conveyor scanning. This method was used to illustrate the potential of the alpha-radioluminescence technique to produce autonomous measurements of materials which were passed underneath the detector. It was shown that a background measurement could be inferred by calculation of the mean count rate during periods when no source was present underneath the detector. It was then shown that using this method linear scaling of count rate versus source activity could be obtained, with the sum of count rate measurements of individual sources being consistent with measurements obtained for the same sources analysed in combination.

The conveyor scanning method was shown to produce quantitative, repeatable measurements. A particularly interesting property of the method was that based on the speed of conveyor motion it was possible to introduce more or less uncertainty into measurement (and by proxy increase or decrease detection limits), depending on the need to scan a greater quantity of material, obtain more accurate measurement of activity or perform measurements with a lower activity clearance threshold.

A quantitative assessment of detection performance for the conveyor scanning method requires consideration of the signal processing of the measurement of a moving source. While this was beyond the scope of the current study – focussed on the adaption of established

metrics of radiometric calibration to remote methods – it is strongly recommended that further research is commissioned in this area.

The final method presented was the imaging method, in which the detector was orientated about a sequence of pan and tilt angles relative to a source. The background present for each measurement was calculated by analysis of measurements obtained at pan and tilt angles beyond the source corona. This baseline could then be subtracted from the peak intensity to obtain the contribution due to the source under measurement.

The imaging method was shown to produce the most consistent measurements of individual sources. The adjustment of pan and tilt angles meant that even if the source was initially misaligned, the centre of the source would still be measured during the scan. A method was also devised to average measurements of the 5 points surrounding the central peak to reduce the uncertainty associated with measurements at longer source to detector distances.

Through comparison of measurements from each of the methods it was shown that the calculated net count rates were of a similar order of magnitude, though not consistent within error. This led to the conclusion that a separate calibration should be obtained for each method used to obtain the most accurate possible measurements. Given that other methods for in-situ alpha measurement are also affected high levels of variability it was concluded that the difference between different methods was not a limiting factor for adoption.

In chapter 6 the measurements obtained from sources of unknown activity were used to obtain a normalised detector response function over distance for the imaging and confinement methods. This normalised function was used to assess the relative performance of the detector at distances over the range measured – from 6 to 75cm.

Measurements using sources traceable to international standards were then presented. In the absence of a traceable source of sufficiently high activity, the normalised response function was then combined with a weighted mean of the measurements of the traceable sources. The resulting curve then gave the detector response (cps/Bq) which was expected over the distance range based on previous measurements of the other americium sources.

Through analysis of the measurements obtained using the detector and presented in chapters 4 and 5 it was possible to calculate the replication variance for the imaging and confinement method. These were in turn used to show the critical limit, limit of detection and limit of quantification for both methods.

By considering the response of the detector to the traceable sources it was then possible to consider the minimum source activity which would produce a detector response of sufficient magnitude to reach the critical limit, the limit of detection and the limit of quantification. It was shown that the UV confinement method, due to its higher detector response to activity and lower repetition variance, was able to detect sources over three times smaller ((157±10)Bq vs (500±40)Bq at 7cm source to detector) than through use of the imaging technique.

Statistical analysis of the backgrounds observed in measurements obtained using the confinement method showed that both short measurements (20 seconds per measurement) and longer measurements (40 minutes) were affected by higher variance than expected. Statistical testing showed that only measurements of 60 seconds had a variance consistent with a Poisson distributed variable.

This finding could suggest that due to the types of background observed using the alpha-radioluminescence technique – which mostly arise from non-radioactive sources such as ambient light and detector noise – that there is an optimum measurement period. It was suggested that this could lie between the settling time of the photomultiplier tube (quoted as 10 seconds by the manufacturer) and the period over which variations in atmospheric sources of background are typically observed (e.g. changes in ambient light due to cloud movement).

These findings highlights that any attempt to derive detection limits for such a detector must consider the environment in which measurements are obtained in. A key conclusion of this analysis is that for the comparison of detector performance (e.g. detection limits or minimum detectable activity) between devices measurements of background must be obtained in standard environments, e.g. windowless rooms under lighting of a particular wavelength. During most experiments presented in this thesis a red LED torch was used which was known to only emit light at wavelengths in excess of 600nm. For detectors which do not have sensitivity at this wavelength this could be adopted as a standard procedure.

Similar constraints would exist for sources of different radiological composition or shape. Sources of differing physical shape, concentration of activity (Bq cm^{-2}), source matrix material or radiological composition will each produce different emission geometries and detector characteristics. As such each of these factors should be considered – as is standard with radiological calibrations – when choosing the most appropriate mode of calibration.

The procedure outlined in chapter 6 is applicable to other methods and detectors and would provide a sound basis for device designers to present parameters of their device performance. Using a metric of the minimum detectable activity (of americium-241) in a windowless room in the presence of (non-interfering) light of known wavelengths over a range of distances it would be possible to quantitatively assess the relative detection capability of different devices.

Further work is also required to fully understand the origin of the discrepancy observed between the two modes of operation considered in chapter 6. While the presented results are promising this will provide a fully comprehensive understanding of detector performance. The results of the analysis serve to illustrate the value of a comprehensive method of comparison for relative performance of detectors and modes of operation.

A clear limitation of this as a metric of device performance is that it does not consider another fundamental parameter of device performance – the detector's ability to operate in different light environments. Given the difficulty of defining a quantitatively repeatable light environment it is likely that any metric of performance would be qualitative. It is suggested that any such metric of performance in imperfect environments could be presented alongside an "ideal" environment defined above.

The detector developed in the project was intended to operate in a broad range of environments and be capable of demonstrating performance using sources available in a basic radiometric laboratory. The detector was successful in achieving this objective, though could be developed further to obtain lower detection limits, greater versatility in operation and further improvement in performance.

7.3 Future work

The conclusions drawn from this work have raised several areas which can be developed to further increase the capability of the alpha-induced radioluminescence technique. By using the proposed modes of operation and calibration methods with different sources and in environments which more closely resemble those encountered in industry it would be possible to further raise confidence in the technique's potential and application in industry. My recommendations for further research following the outcomes of the project are:

1. **Use of the calibration method to compare measurements performed by two detectors operating in the same environment.**
   Given the focus of the project on the establishment of calibration methods which would allow for the quantitative comparison of device performance, the use of the techniques to compare performance between two radioluminescence detectors would also be a valuable development. This could be achieved by using the same source to assess the detection limits over a range of distances for two different detectors.

2. **Further assessment of detector performance in the presence of strong beta and gamma backgrounds to assess alpha differentiation.**
   In the early stages of detector development, measurements were performed using a 2MBq strontium-90 source to ensure that beta (and lower activity gamma) sources were unable to interfere with measurements of alpha-emitting sources. While adequate in the early stages of development and for the purposes of this project, should the design presented in this thesis be taken forward this should be quantitatively assessed as this has been highlighted as a shortcoming in detectors developed by others.

3. **Testing with a larger traceable calibration sources with alpha-emitting radionuclides other than americium-241.**
   A limitation identified during measurements performed in the project was that the traceable sources available under the project were smaller than the (untraceable) 33kBq americium-241 sources used in the laboratory. Given the linear scaling of counts versus activity, for more accurate, quicker calibration measurements to be performed sources of larger activity could be measured.

All measurements presented in this thesis were using sources containing only americium-241. Given that americium is only one of the alpha-emitting radionuclides encountered in the decommissioning of nuclear facilities others should be tested. This would be particularly interesting in the context of calibration – to establish whether the radionuclide under measurement influences the overall detection limit.

4. **Assessment of the detection performance of the conveyor scanning method using ROC curves.**
   Receiver Operator Characteristic (ROC) curves are used extensively in nuclear security related fields to assess the detection performance of radiation portal monitors and similar devices. ROC curves are used to assess the performance of these systems for sources of differing radiological composition, transit speed and in the presence of backgrounds from other sources (e.g. cat litter or recent patients of radiotherapy). Given that the conveyor method performs measurement on a moving source the ROC method may be better suited to assess attributes such as the maximum undetected activity which could evade detection. These kinds of attribute are particularly important in a waste categorisation context, where for site licence companies and regulators to be satisfied the technique must be considered robust. Given the use of ROC characteristics in nuclear security this is would be a familiar, trusted metric of detector performance.

5. **A pilot study to assess detector performance in a realistic industrial environment and to allow an operational comparison to other established methods.**
   A limitation of the results presented was that the radioactive sources available in the course of the project were sealed test sources. A pilot study to assess the performance of a radioluminescence detector versus a probe detector in the assessment of radiologically contaminated material (for example, a hot spot in a facility undergoing decommissioning) would be ideal to demonstrate the relative capability of the technique. Measurements could also be performed to assess detection performance in different environments.

6. **Testing detector performance against sources of differing physical shape and radiological composition.**
   The strength of the technique in producing valid in-situ measurements will depend on its ability to produce measurements of sources of differing radiological composition and physical distribution. This project has only considered in passing the possible use of the technique to measure radiological sources in different geometries, for example contamination spread over a wide region. Given that the detector effectively measures all contamination in view of the optics, the effect of different source geometries on calibration should be considered further.

In the course of the project several further proposals were considered for development but due to the limitations of time, relevance and money were not taken forward. Nevertheless I feel that further research on the following would present opportunity for valuable contributions to the field of study:

- **Extension of the numerical simulation model to 3D emission geometries.**
  Due to limitations on time it was not possible to produce a complete model for 3D alpha emission geometries in chapter 3, with results presented for a two-dimensional emission geometry. As a simple way to obtain the peak theoretical efficiency of a radioluminescence detector it would be worth considering the further development of the model for 3D emission geometries. If this model was developed further, then it would then be possible to validate the preliminary findings relating to the relationship between emission energy and the count rates observed for a rotated source.

- **Development of a two-dimensional X-Y scanning rig based on the conveyor scanning method.**
  The conveyor scanning mode of operation was used to demonstrate linear scaling of counts versus activity and was shown to produce reliable results. One limitation of the method was that it was difficult – when only allowing source motion in one dimension – to establish whether the source was moving directly underneath the detector's measurement axis.

By mounting the detector on computer controllable actuator rig it would be possible to eliminate this risk by performing measurements across the X and Y axis of a potentially contaminated source. This would ensure that any region of maximum contamination would be identified and would provide an operator with a map of the possible regions of contamination on an object.
Development of such a system may present an opportunity to use machine learning approaches to categorise contributions from radiation from alpha, beta and gamma sources.

- **Combination of the imaging method with depth profiles from stereoscopic vision cameras.**
  Stereoscopic vision cameras (such as the Xbox Kinect device) provide a cost effective way to obtain three dimensional depth profiles of surfaces. A limitation of the imaging method is that during measurement of a scene containing a source it may not be immediately possible to identify any surface(s) which are contaminated. This would result in difficulty identifying the relevant calibration distance against which to compare the measurement to. Stereoscopic measurements of the appropriate scene could be combined with such images to produce contamination models containing the most probable locations of contamination. These could then be compared to records of operational activity (or combined with further measurements from different perspectives) to produce a conclusive quantitative assessment of the level of contamination. This method has been demonstrated for other types of radiation detector but has yet to be applied to alpha-induced radioluminescence.

Bibliography

[1] J. Harrison, R. Leggett, D. Lloyd, A. Phipps, and B. Scott, "Polonium-210 as a poison," *Journal of Radiological Protection*, vol. 27, no. 1, p. 17, 2007.

[2] B. Volodarsky, *KGB's Poison Factory: From Lenin to Litvinenko*. Zenith Press, 2010.

[3] M. Oliver, "Radiation found at 12 sites in Litvinenko case," *The Guardian*, November 2006.

[4] F. Lamadie, F. Delmas, C. Mahe, P. Girones, C. Le Goaller, and J. Costes, "Remote alpha imaging in nuclear installations: new results and prospects," *IEEE Transactions on Nuclear Science*, vol. 52, pp. 3035–3039, Dec 2005.

[5] R. Hayward, D. Hoppes, and W. Mann, "Branching ratio in the decay of polonium-210," *Journal of Research of the National Bureau of Standards*, vol. 54, no. 1, 1955.

[6] K. J. Moody, I. D. Hutcheon, and P. M. Grant, *Nuclear forensic analysis*. CRC Press, 2005.

[7] J. Cheung, "NPL (Stand Off) Alpha Detector," tech. rep., National Physical Laboratory, 2007.

[8] V. Hannuksela, J. Toivonen, H. Toivonen, and J. Sand, "Optical remote detection of alpha radiation," in *Proceedings of the Third European IRPA Congress*, pp. 1750–1756, 2010.

[9] M. D. Roberts, "Detection of Ionizing Radiation using Solar Blind Air Fluorescence," tech. rep., Australian Government Department of Defence, June 2013.

[10] E. Inrig, V. Koslowsky, B. Andrews, M. Dick, P. Forget, H. Ing, R. Hugron, and L. Wong, "Development and testing of an air fluorescence imaging system for the detection of radiological contamination," *AIP Conference Proceedings*, vol. 1412, no. 1, pp. 393–400, 2011.

[11] D. Chichester, S. Pozzi, E. Seabury, J. Dolan, M. Flaska, J. Johnson, S. Watson, and J. Wharton, "Fy09 advanced instrumentation and active interrogation research for safeguards," technical report, Technical Information Center Oak Ridge Tennessee, Aug. 2009.

[12] D. Cousins, T. Haslip, “Stand and deliver,” *CBRNe World*, pp. 56–59, 2006.

[13] S. J. Palethorpe, B. Bowen, J. J. Hastings, P. E. Mort, and G. Askew, “Technical challenges, needs and opportunities in decommissioning of the Sellafield Site,” tech. rep., Sellafield Ltd, Oct. 2013.

[14] International Atomic Energy Agency, “Disposal of Radioactive Waste,” tech. rep., IAEA, 2011.

[15] A. Carpio and B. Tapiador, “Analysis of helium bubble growth in radioactive waste,” *Nonlinear Analysis: Real World Applications*, vol. 11, no. 5, pp. 4174 – 4184, 2010.

[16] D. Gosset, P. Trocellier, and Y. Serruys, “Determination of the helium diffusion coefficient in nuclear waste storage ceramics by a nuclear reaction analysis method,” *Journal of Nuclear Materials*, vol. 303, no. 2, pp. 115 – 124, 2002.

[17] H. Bethe and J. Ashkin, “Passage of radiations through matter,” *Experimental Nuclear Physics*, vol. 1, p. 166, 1953.

[18] C. Thompson, E. Barritt, and C. Shenton-Taylor, “Predicting the air fluorescence yield of radioactive sources,” *Radiation Measurements*, vol. 88, pp. 48–54, 2016.

[19] S. M. Baschenko, “Remote optical detection of alpha particle sources,” *Journal of Radiological Protection*, vol. 24, no. 1, p. 75, 2004.

[20] O. Ivanov, A. Danilovich, V. Stepanov, S. Smirnov, and A. Volkovich, “Visualization of radioactive sources without gamma-radiation with uv imaging systems,” in *ASME 2009 12th International Conference on Environmental Remediation and Radioactive Waste Management*, vol. 12, p. 321, 2009.

[21] J. Feener and W. Charlton, “Preliminary results of nuclear fluorescence imaging of alpha and beta emitting sources,” in *Advancements in Nuclear Instrumentation Measurement Methods and their Applications ANIMMA, 2013 3rd International Conference on*, pp. 1–8, June 2013.

[22] T. Kerst, J. Sand, S. Ihantola, K. Perajarvi, A. Nicholl, E. Hrnecek, H. Toivonen, and J. Toivonen, “Standoff alpha radiation detection for hot cell imaging and crime scene investigation,” *Optical Review*, vol. 25, no. 3, pp. 429–436, 2018.

[23] J. Yao, J. Brenizer, R. Hui, and S. Yin, “Standoff alpha radiation detection via excited state absorption of air,” *Applied Physics Letters*, vol. 102, no. 25, 2013.

[24] J. Sand, V. Hannuksela, S. Ihantola, K. Perajarvi, H. Toivonen, and J. Toivonen, “Remote Optical Detection of Alpha Radiation,” tech. rep., IAEA, 2010.

[25] A. J. Crompton, K. A. Gamage, S. Bell, A. P. Wilson, A. Jenkins, and D. Trivedi, “First results of using a uvtron flame sensor to detect alpha-induced air fluorescence in the uvc wavelength range,” *Sensors*, vol. 17, no. 12, p. 2756, 2017.

[26] J. Sand, A. Nicholl, E. Hrnecek, H. Toivonen, J. Toivonen, and K. Perajarvi, “Stand-off radioluminescence mapping of alpha emitters under bright lighting,” *IEEE Transactions on Nuclear Science*, vol. 63, no. 3, pp. 1777–1783, 2016.

[27] R. W. Gurney and E. U. Condon, “Quantum mechanics and radioactive disintegration,” *Phys. Rev.*, vol. 33, pp. 127–140, Feb 1929.

[28] G. Gamow, “Zur quantentheorie des atomkernes,” *Zeitschrift fÃŒr Physik*, vol. 51, no. 3-4, pp. 204–212, 1928.

[29] B. Mattson, “Nasa’s imagine the universe,” June 2014.

[30] B. Martin, *Nuclear and Particle Physics: An Introduction*. Wiley, 2009.

[31] Released under a creative commons license.

[32] J. Lilley, *Nuclear physics: principles and applications*. Manchester physics series, J. Wiley, 2001.

[33] Released under a creative commons license by the University of Southampton.

[34] G. Audi, O. Bersillon, J. Blachot, and A. Wapstra, “The nubase evaluation of nuclear and decay properties,” *Nuclear Physics A*, vol. 624, no. 1, pp. 1 – 124, 1997.

[35] Pöyry Energy Limited and Amec plc, “2013 UK Radioactive Waste Inventory: Radioactivity Contents of Wastes,” tech. rep., Nuclear Decommissioning Authority, 2013.

[36] R. Kinsey, C. Dunford, J. Tuli, and T. Burrows, *The NUDAT/PCNUDAT program for nuclear data*. Oct 1996.

[37] N. Bohr, “I. on the constitution of atoms and molecules,” *Philosophical Magazine Series 6*, vol. 26, no. 151, pp. 1–25, 1913.

[38] J. F. Ziegler, “Stopping of energetic light ions in elemental matter,” *Journal of applied physics*, vol. 85, no. 3, pp. 1249–1272, 1999.

[39] J. F. Ziegler, M. D. Ziegler, and J. P. Biersack, “SRIM - The stopping and range of ions in matter (2010),” *Nuclear Instruments and Methods in Physics Research B*, vol. 268, pp. 1818–1823, June 2010.

[40] K. Yu, C. Yip, D. Nikezic, J. Ho, and V. Koo, “Comparison among alpha-particle energy losses in air obtained from data of SRIM, ICRU and experiments,” *Applied Radiation and Isotopes*, vol. 59, no. 5, pp. 363 – 366, 2003.

[41] International Commission on Radiation Units and Measurements. “Stopping Powers and Ranges for Protons and Alpha Particles,” *ICRU Report 49*, 1993.

[42] M. F. L’Annunziata, *Handbook of radioactivity analysis*. Academic Press, 2012.

[43] Bachelor, Paula, David Jordan, Warren Harper, Bret Cannon, and Erin Finn. "Self-absorption effects on alpha-induced atmospheric nitrogen fluorescence yield." Journal of radioanalytical and nuclear chemistry 282, no. 3 pp. 873-876, 2009.

[44] B. Fahimian, A. Ceballos, S. TÃŒrkcan, D. S. Kapp, and G. Pratx, “Seeing the invisible: Direct visualization of therapeutic radiation beams using air scintillation,” *Medical Physics*, vol. 41, no. 1, p. 1, 2014.

[45] A. N. Bunner, *Cosmic ray detection by atmospheric fluorescence*. PhD thesis, Cornell University, 1967.

[46] T. Waldenmaier, J. BlÃŒmer, and H. Klages, “Spectral resolved measurement of the nitrogen fluorescence emissions in air induced by electrons,” *Astroparticle Physics*, vol. 29, no. 3, pp. 205 – 222, 2008.

[47] W. Huggins and L. Huggins, “On the spectrum of the spontaneous luminous radiation of radium at ordinary temperatures,” *Proceedings of the Royal Society of London*, vol. 72, no. 477-486, pp. 196–199, 1903.

[48] H. Haken and H. C. Wolf, *Molecular physics and elements of quantum chemistry: introduction to experiments and theory*. Springer, 2004.

[49] T. Waldenmaier, *Spectral resolved measurements of the nitrogen fluorescence yield in air induced by electrons*. PhD thesis, Karlsruhe Institute of Technology, 2008.

[50] W. A. Bingel, *Theory of molecular spectra*. J. Wiley & Sons, 1970.

[51] J. I. Steinfeld, *Molecules and radiation: An introduction to modern molecular spectroscopy*. Courier Dover Publications, 2012.

[52] F. Arqueros, F. Blanco, and J. Rosado, "Analysis of the fluorescence emission from atmospheric nitrogen by electron excitation, and its application to fluorescence telescopes," *New Journal of Physics*, vol. 11, no. 6, p. 065011, 2009.

[53] F. R. Gilmore, R. R. Laher, and P. J. Espy, "Franck–condon factors, r-centroids, electronic transition moments, and einstein coefficients for many nitrogen and oxygen band systems," *Journal of physical and chemical reference data*, vol. 21, no. 5, pp. 1005–1107, 1992.

[54] J. Sand, S. Ihantola, K. Perajarvi, H. Toivonen, and J. Toivonen, "Radioluminescence yield of alpha particles in air," *New Journal of Physics*, vol. 16, no. 5, pp. 2–13, 2014.

[55] M. Ave, M. Bohacova, B. Buonomo, N. Busca, L. Cazon, S. Chemerisov, M. Conde, R. Crowell, P. D. Carlo, C. D. Giulio, M. Doubrava, A. Esposito, P. Facal, F. Franchini, J. Gebhardt, T. Graber, J. Horandel, M. Hrabovsky, M. Iarlori, T. Kasprzyk, B. Keilhauer, H. Klages, M. Kleifges, S. Kuhlmann, G. Mazzitelli, M. Meron, L. Nozka, A. Obermeier, M. Palatka, S. Petrera, P. Privitera, J. Ridky, V. Rizi, G. Rodriguez, F. Salamida, P. Schovanek, H. Spinka, E. Strazzeri, A. Ulrich, Z. Yusof, V. Vacek, P. Valente, V. Verzi, J. Viccaro, and T. Waldenmaier, "Energy dependence of air fluorescence yield measured by airfly," *Nuclear Instruments and Methods in Physics Research Section A: Accelerators, Spectrometers, Detectors and Associated Equipment*, vol. 597, no. 1, pp. 46 – 49, 2008. Proceedings of the 5th Fluorescence Workshop.

[56] J. Rosado, F. Blanco, and F. Arqueros, "Comparison of available measurements of the absolute air-fluorescence yield and determination of its global average value," *arXiv preprint arXiv:1104.0894*, 2011.

[57] M. Duquesne, I. Kaplan, *et al.*, “Mesure de la luminescence induite par le rayonnement α du po-210 dans l’air et dans l’eau,” *J. Phys. Radium*, vol. 21, no. 10, pp. 708–716, 1960.

[58] D. L. Chichester and S. M. Watson, “Multispectral uv-visual imaging as a tool for locating and assessing ionizing radiation in air,” in *Nuclear Science Symposium Conference Record (NSS/MIC)*, pp. 447–453, IEEE, 2010.

[59] A. Crompton, K. Gamage, A. Jenkins, and C. Taylor, “Alpha particle detection using alpha-induced air radioluminescence: A review and future prospects for preliminary radiological characterisation for nuclear facilities decommissioning,” *Sensors*, vol. 18, no. 4, p. 1015, 2018.

[60] A. Morozov, M. Fraga, L. Pereira, L. Margato, S. Fetal, B. Guerard, G. Manzin, and F. Fraga, “Photon yield for ultraviolet and visible emission from cf_4 excited with α-particles,” *Nuclear Instruments and Methods in Physics Research Section B: Beam Interactions with Materials and Atoms*, vol. 268, no. 9, pp. 1456–1459, 2010.

[61] A. Crompton, K. Gamage, D. Trivedi, and A. Jenkins, “The effect of gamma and beta radiation on a UVTRON flame sensor: Assessment of the impact on implementation in a mixed radiation field,” *Sensors*, vol. 18, no. 12, p. 4394, 2018.

[62] A. E. Leybourne et al., “Long range detection of radiation-induced air fluorescence,” in *Proceedings of the Institute of Nuclear Materials Management*, p. 1, INMM, 2010.

[63] F. Lamadie, J. R. Costes, F. Delmas, C. Mahe, P. Girones, and C. Le Goaller, “Alpha imaging: first results and prospects,” in *Nuclear Science Symposium Conference Record, 2004 IEEE*, vol. 3, pp. 1594–1598 Vol. 3, Oct 2004.

[64] C. Mahe, “Characterisation and visualisation technologies in dd and r,” in *IAEA Practical training workshop - characterisation and visualisation technologies in DDR and R*, IAEA, 2011.

[65] Peräjärvi, Kari A., Sakari Ihantola, Roy C. Pöllänen, Harri I. Toivonen, and Jani A. Turunen. "Determination of 235U, 239Pu, 240Pu, and 241Am in a nuclear bomb particle using a position-sensitive α-γ coincidence technique." Environmental science & technology 45, no. 4 (2011), pp. 1528-1533, 2011.

[66] Ivanov, Oleg P., Vyacheslav E. Stepanov, Sergey V. Smirnov, and Anatoliy G. Volkovich. "Development of method for detection of alpha contamination with using UV-camera “DayCor” by OFIL." In *2011 IEEE Nuclear Science Symposium Conference Record*, pp. 2192-2194. IEEE, 2011.

[67] J. Sand, S. Ihantola, K. Perajarvi, A. Nicholl, E. Hrnecek, H. Toivonen, and J. Toivonen, “Imaging of alpha emitters in a field environment,” *Nuclear Instruments and Methods in Physics Research Section A: Accelerators, Spectrometers, Detectors and Associated Equipment*, vol. 782, pp. 13–19, 2015.

[68] F. Boschi, S. L. Meo, P. L. Rossi, R. Calandrino, A. Sbarbati, and A. E. Spinelli, “Optical imaging of alpha emitters: simulations, phantom, and in vivo results,” *Journal of Biomedical Optics*, vol. 16, no. 12, pp. 126011–126011–5, 2011.

[69] Government of Canada, “Confidence building measures Canada: 2011 Annual Report of Confidence Building Measures in Biological and Toxin Weapons Convention,” 2011.

[70] Sand, Johan, et al. "Optical detection of radon decay in air." Scientific reports 6 pp. 21532, 2016

[71] S. Ihantola, *Novel approaches to the analysis of nuclear and other radioactive materials-Improving detection capability through alpha-gamma coincidence, alpha-induced optical fluorescence and advanced spectrum analysis*. PhD thesis, Aalto University, 2013.

[72] S. Ihantola, J. Sand, K. Perajarvi, J. Toivonen, and H. Toivonen, “Fluorescence-assisted gamma spectrometry for surface contamination analysis,” *Nuclear Science, IEEE Transactions on*, vol. 60, no. 1, pp. 305–309, 2013.

[73] K. Perajarvi, “Principles of uv gamma coincidence spectrometry,” in *Novel coincidence techniques, detectors and concepts for safety, security and safeguards*, vol. 45, 2014.

[74] N. Gopalsami, H. T. Chien, A. Heifetz, E. R. Koehl, and A. C. Raptis, “Millimeter wave detection of nuclear radiation: An alternative detection mechanism,” *Review of Scientific Instruments*, vol. 80, no. 8, p. 1, 2009.

[75] V. L. Granatstein and G. S. Nusinovich, “Detecting excess ionizing radiation by electromagnetic breakdown of air,” *Journal of Applied Physics*, vol. 108, no. 6, p. 063304, 2010.

[76] Y. Dimant, G. Nusinovich, P. Sprangle, J. Penano, C. Romero-Talamas, and V. Granatstein, “Propagation of gamma rays and production of free electrons in air,” *Journal of Applied Physics*, vol. 112, no. 8, p. 083303, 2012.

[77] G. S. Nusinovich, D. G. Kashyn, Y. Tatematsu, and T. Idehara, “Effect of atmospheric conditions on operation of terahertz systems for remote detection of ionizing materials,” *Physics of Plasmas (1994-present)*, vol. 21, no. 1, p. 1, 2014.

[78] P. Sprangle, B. Hafizi, H. Milchberg, G. Nusinovich, and A. Zigler, “Active remote detection of radioactivity based on electromagnetic signatures,” *Physics of Plasmas (1994-present)*, vol. 21, no. 1, p. 013103, 2014.

[79] Hamamatsu Photonics, “Metal package photomultiplier tube R9880U series,” R9880U datasheet, Mar. 2019.

[80] Hamamatsu Photonics, *Photomultiplier Tubes: Basics and Applications,* 3rd Edition, Hamamatsu Photonics, 2007.

[81] P. Lutus, *Optical Ray Tracer,* Version 9.6, 2017.

[82] Autodesk, *Autodesk 123 Design*. Autodesk, Inc. Accessed January 16, 2017.

[83] Hamamatsu Photonics, “Photosensor modules H10720/H10721 series”, H10721-210 datasheet, Mar. 2019.

[84] Interaction Design Lab Potsdam, “Fritzing”, Version 0.9.3b, 2016.

[85] Stefanik, J. "Reference sources for the calibration of surface contamination monitors-Beta-emitters (maximum beta energy greater than MeV) and alpha-emitters (International Standard Publication ISO 8769: 1988).", 2016.

[86] Stefanik, J. "Evaluation of surface contamination-Part 1: Beta-emitters (maximum beta energy greater than 0, 15 MeV) and alpha-emitters (International Standard Publication ISO 7503-1: 1988).", 2016.

[87] Bhat, M. R. "Evaluated nuclear structure data file (ENSDF)." *Nuclear data for science and technology*. Springer, Berlin, Heidelberg, 1992.

[88] Currie, Lloyd A. "Limits for qualitative detection and quantitative determination. Application to radiochemistry." *Analytical chemistry* 40, no. 3 (1968), pp. 586-593, 1968.

[89] Thermo Electron Corporation, “Probes Selection Guide”, HP-380A datasheet, 2004.

Appendix 1
Eckert & Ziegler Calibration Certificate

Reference: 139716 – SX 214

41, Issue 1, 2009-06-02

Eckert & Ziegler
Nuclitec

Eckert & Ziegler
Nuclitec GmbH

Gieselweg 1
38110 Braunschweig
Germany

Tel. +49 5307 932-0
Fax +49 5307 932-293

5 August 2010

CERTIFICATE

No. 139716 - SX 214

for a Sealed Radioactive Source

Source Type: Alpha Wide Area Reference Source

Product code	AMR05011
Drawing	VZ-1370-001
Dimensions of active surface	Ø 50 mm
Overall dimensions	Ø 60 mm x 3 mm
Source no.	SX 214
Nuclide	Americium-241

Technical Data

Activity	221 Bq
Uncertainty*	6 %
Alpha surface emission rate	105 s^{-1} in 2 π steradian
Uncertainty* of alpha surface emission rate	3 %
Reference date	23 July 2010
Traceability*	Defined on page 2

Leakage and Contamination Test/s

Test method/s*	i
Test/s passed on	4 August 2010

Additional Information

ISO classification*	C.34645
Remark	---

* see page 2 for explanation

Eckert & Ziegler
Nuclitec GmbH

Explanations for Certificates (Page 2 of Certificates)

Uncertainty

The reported uncertainty is based on standard uncertainty multiplied by a coverage factor k = 2, providing a level of confidence of approximately 95 %. (ISO Guide, 1995)

Traceability

This certificate documents the traceability of measurement results to national standards, standard measuring equipment and methods for the realisation of physical units of measurement according to the Inter-national System of Units (SI). Traceability is defined as 'the property of a result of a measurement whereby it can be related to appropriate standards, generally international or national standards, through an unbroken chain of comparisons'.

Eckert & Ziegler Nuclitec GmbH has been accredited as DKD (Deutscher Kalibrierdienst) calibration laboratory by the Physikalisch-Technische Bundesanstalt (PTB) and is authorized to issue reference sources which are traceable to national standards held at the PTB in Germany.
Because of the European co-operation for Accreditation (EA) mutual recognition agreement the certificates are also accepted by all EA-members (e. g. UKAS).

This product complies with the requirements for traceability to NIST specified in the American National Standard "Traceability of Radioactive Sources to the NIST and Associated Instrument Quality Control (ANSI N42.22-1995)".
As a requirement for the ANSI N42.22-1995 **Eckert & Ziegler Nuclitec GmbH** participates in the NEI/NIST Measurements Assurance Program of the Nuclear Power Industry.

Air Kerma Rate

The air kerma rate of a source with an activity A is the sum of the initial kinetic energies of all charged particles created by photons, released per volume element of air and per unit of time.

Leakage and Contamination Tests

Stringent tests for leakage are an essential feature of radioactive sources production. They are based on ISO 9978. Some standard methods used for testing radiation sources are listed below.

Wipe Test I

The source is wiped with a swab or tissue, moistened with ethanol or water, the activity removed is measured.
Limit: 200 Bq, USA: 5 nCi

Immersion Test II

The source is immersed in a suitable liquid at 50 °C for at least 4 hours and the activity removed is measured.
Limit: 200 Bq, USA: 5 nCi

Bubble Test III

The source is immersed in water or a suitable liquid and the pressure in the vessel reduced to 13 kPa (100 mm Hg). No bubbles must be observed.

ISO Classification

The International Organization for Standardization (ISO) has proposed a system of classification of sealed radioactive sources based on safety requirements for typical uses (see ISO 2919 and ANSI N43.6-1997). This system provides a manufacturer of sealed radioactive sources with a set of tests to evaluate the safety of his products. It also assists a user of such sealed sources to select types which suit the application he has in mind. The tests to which specimen sources are subjected are listed in the following table.

Classification of sealed source performance standard according to ISO 2919 and ANSI N43.6-1997

Test	Class 1	2	3	4	5	6	X
Temperature	No test	- 40 °C (20 min) + 80 °C (1 h)	- 40 °C (20 min) + 180 °C (1 h)	- 40 °C (20 min) + 400 °C (1 h) and thermal shock 400 °C to 20 °C	- 40 °C (20 min) + 600 °C (1 h) and thermal shock 600 °C to 20 °C	- 40 °C (20 min) + 800 °C (1 h) and thermal shock 800 °C to 20 °C	Special test
External Pressure	No test	25 kPa absolute	25 kPa absolute to 2 MPa absolute	25 kPa absolute to 7 MPa absolute	25 kPa absolute to 70 MPa absolute	25 kPa absolute to 170 MPa absolute	
Impact	No test	50 g from 1 m	200 g from 1 m	2 kg from 1 m	5 kg from 1 m	20 kg from 1 m	
Vibration	No test	3 x 10 min 25 – 500 Hz at 5 g peak amplitude	3 x 10 min 25 – 50 Hz at 5 g peak amplitude and 50 – 90 Hz at 0.635 mm amplitude peak to peak and 90 – 500 Hz at 10 g peak amplitude	3 x 30 min 25 – 80 Hz at 1.5 mm amplitude peak to peak and 80 – 2000 Hz at 20 g peak amplitude			
Puncture	No test	1 g from 1 m	10 g from 1 m	50 g from 1 m	300 g from 1 m	1 kg from 1 m	

Special Applications

No test programme can cover all possible combinations of environments to which a source may be exposed.
Users should therefore consult our experts before using sources in potentially adverse environments.

IAEA Special Form

'Special Form' is a test specification for sealed sources given in the IAEA transport regulations (IAEA TS-R-1).
It is used in determining the maximum acceptable activities for various types of transport containers.
If nothing else is stated, the reference date is identical with the date of manufacture.

Quality Assurance System

The quality assurance system of **Eckert & Ziegler Nuclitec GmbH** was certified by Lloyd's Register Quality Assurance (LRQA) according to ISO 9001:2000 and according to ISO 13485:2003 for medical devices. Isotrak products meet the requirements of 10CFR50 Appendix B.

NRC Advice

Radioactive Material - not for human use - introduction into foods, beverages, cosmetics, drugs, or medicinals, or into products manufactured for commercial distribution is prohibited - exempt quantities should not be combined

Eckert & Ziegler
Nuclitec

Appendix 2
Eckert & Ziegler Calibration Certificate

Reference: 027744 D-K-15203-01-00

MS015439

Eckert & Ziegler Nuclitec GmbH
Gieselweg 1
38110 Braunschweig
Tel +49 5307 932-0
Fax +49 5307 932-293

Eckert & Ziegler

akkreditiert durch die / *accredited by the*

Deutsche Akkreditierungsstelle GmbH

DAkkS Deutsche Akkreditierungsstelle D-K-15203-01-00

als Kalibrierlaboratorium im / *as calibration laboratory in the*

Deutschen Kalibrierdienst DKD

027744
D-K-15203-01-00
2014-11

Kalibrierzeichen
Calibration mark

Kalibrierschein
Calibration certificate

Strahler Nr. / *Source number* AE-7641

Gegenstand *Object*	**Alpha Wide Area Reference Source**
Hersteller *Manufacturer*	**Eckert & Ziegler Nuclitec GmbH**
Typ *Type*	**AMR05022**
Strahler-Nr. *Source number*	**AE-7641**
Auftraggeber *Customer*	**High Technology Sources Ltd.** **OX11 7HP Didcot** **Great Britain**
Auftragsnummer *Order No.*	**CO00160737**
Anzahl der Seiten des Kalibrierscheines *Number of pages of the certificate*	**2**
Datum der Kalibrierung *Date of calibration*	**28 October 2014**

Dieser Kalibrierschein dokumentiert die Rückführung auf nationale Normale zur Darstellung der Einheiten in Übereinstimmung mit dem Internationalen Einheitensystem (SI).
Die DAkkS ist Unterzeichner der multilateralen Übereinkommen der European co-operation for Accreditation (EA) und der International Laboratory Accreditation Cooperation (ILAC) zur gegenseitigen Anerkennung der Kalibrierscheine.
Für die Einhaltung einer angemessenen Frist zur Wiederholung der Kalibrierung ist der Benutzer verantwortlich.
This calibration certificate documents the traceability to national standards, which realize the units of measurement according to the International System of Units (SI).
The DAkkS is signatory to the multilateral agreements of the European co-operation for Accreditation (EA) and of the International Laboratory Accreditation Cooperation (ILAC) for the mutual recognition of calibration certificates.
The user is obliged to have the object recalibrated at appropriate intervals.

Dieser Kalibrierschein darf nur vollständig und unverändert weiterverbreitet werden. Auszüge oder Änderungen bedürfen der Genehmigung sowohl der Deutschen Akkreditierungsstelle GmbH als auch des ausstellenden Kalibrierlaboratoriums. Kalibrierscheine ohne Unterschrift haben keine Gültigkeit.
This calibration certificate may not be reproduced other than in full except with the permission of both the Deutsche Akkreditierungsstelle GmbH and the issuing laboratory. Calibration certificates without signature are not valid.

Datum *Date*	Leiter des Kalibrierlaboratoriums *Head of the calibration laboratory*	Bearbeiter *Person in charge*

Seite 2
Page

027744
D-K-15203-01-00
2014-11

Alpha Wide Area Reference Source

Source no.	AE-7641
Drawing	VZ-1370-001
Nuclide	Americium-241
Activity	912 Bq
Alpha surface emission rate	431 s^{-1} in 2 π steradian
Reference date	28 October 2014 at 12:00 UTC
Dimensions of active surface	Ø 50 mm
Overall dimensions	Ø 60 mm x 3 mm
Leakage and contamination test	Wipe test according to ISO 9978.
Wipe test passed on	4 November 2014
Construction	Am-241 is incorporated into the surface of an anodized aluminium foil of 0.3 mm thickness. The thickness of the activated layer is approximately 6 µm. The activated foil is mounted into a holder.
Measuring method	The activity was determined by comparison with a reference source of the same construction. The alpha surface emission rate was measured using a windowless proportional counter.
Traceability	Additional to the direct traceability to the PTB through the DAkkS this product complies with the requirements for traceability to NIST specified in the American National Standard "Traceability of Radioactive Sources to the NIST and Associated Instrument Quality Control (ANSI N42.22-1995)". As a requirement of the ANSI N42.22-1995 Eckert & Ziegler Nuclitec GmbH participates in the NRMAP/NIST Measurements Assurance Program of the Nuclear Power Industry.
Uncertainty	The relative uncertainty of the activity is 3 %, the relative uncertainty of the alpha surface emission rate is 3 %. The reported uncertainty, determined according to the DAkkS-DKD-3 report is based on the standard uncertainty multiplied by a coverage factor of k = 2, providing a level of confidence of 95 %. (Ref. NIST Technical Note 1297/"Guide to the Expression of Uncertainty in Measurement" ISO Guide, 1995)
Radioactive impurities	Related to Am-241 (equal 100 %) the following radioactive impurities were detected: none
Quality assurance system	The quality assurance system of Eckert & Ziegler Nuclitec GmbH was certified by Lloyd's Register Quality Assurance (LRQA) according to ISO 9001, issue 2008. Isotrak products meet the requirements of 10CFR50 Appendix B in the USA.
Uniformity	—
Remark	This is an EZN Class 2 equivalent reference source which fulfills all requirements of an EZN Class 2 source except that the active area is smaller than 100 cm^2.

Appendix 3
Permissions to Reproduce Copyrighted Material

Copyright Clearance Center

Back to view orders

Copy order

Print this page
Print terms & conditions
Print citation information
(What's this?)

Confirmation Number: 11818464
Order Date: 05/27/2019

Customer Information

Customer: Benjamin Pearce
Account Number: 3001459934
Organization: Imperial College London
Email: l
Phone:

Search order details by: Choose One Go

This is not an invoice

Order Details

Radiation measurements

Billing Status: **N/A**

Order detail ID: 71909336
ISSN: 1350-4487
Publication Type: Journal
Volume:
Issue:
Start page:
Publisher: PERGAMON

Permission Status: Granted
Permission type: Republish or display content
Type of use: Thesis/Dissertation
Order License Id: 4597020313669

Hide details

Requestor type	Academic institution
Format	Electronic
Portion	image/photo
Number of images/photos requested	1
The requesting person/organization	Benjamin Pearce
Title or numeric reference of the portion(s)	Figure 8.
Title of the article or chapter the portion is from	Thompson, C. I., E. E. Barritt, and Caroline Shenton-Taylor. "Predicting the air fluorescence yield of radioactive sources." Radiation Measurements 88 (2016): 48-54
Editor of portion(s)	N/A
Author of portion(s)	Thompson, C. I., E. E. Barritt, and Caroline Shenton-Taylor.
Volume of serial or monograph	88
Page range of portion	52
Publication date of portion	9 February 2016
Rights for	Main product
Duration of use	Life of current edition
	no

Creation of copies for the disabled	
With minor editing privileges	no
For distribution to	Worldwide
In the following language(s)	Original language of publication
With incidental promotional use	no
Lifetime unit quantity of new product	Up to 499
Title	Design, Calibration and Use of Quantitative Alpha-Induced Radioluminescence Detectors
Institution name	Imperial College London
Expected presentation date	Aug 2019

Note: This item was invoiced separately through our **RightsLink service.** More info **$ 0.00**

Total order items: 1 **Order Total: $0.00**

Copyright Clearance Center

Note: Copyright.com supplies permissions but not the copyrighted content itself.

1 PAYMENT 2 REVIEW **3 CONFIRMATION**

Step 3: Order Confirmation

Thank you for your order! A confirmation for your order will be sent to your account email address. If you have questions about your order, you can call us 24 hrs/day, M-F at +1.855.239.3415 Toll Free, or write to us at info@copyright.com. This is not an invoice.

Confirmation Number: 11818477
Order Date: 05/27/2019

If you paid by credit card, your order will be finalized and your card will be charged within 24 hours. If you choose to be invoiced, you can change or cancel your order until the invoice is generated.

Payment Information

Benjamin Pearce
Imperial College London

Payment Method: n/a

Order Details

Astroparticle physics

Order detail ID:	71909340
Order License Id:	4597050459856
ISSN:	0927-6505
Publication Type:	Journal
Volume:	
Issue:	
Start page:	
Publisher:	ELSEVIER BV

Permission Status:	Granted
Permission type:	Republish or display content
Type of use:	Thesis/Dissertation
Requestor type	Academic institution
Format	Electronic
Portion	image/photo
Number of images/photos requested	1
The requesting person/organization	Benjamin Pearce, Imperial College London
Title or numeric reference of the portion(s)	Figure 2.
Title of the article or chapter the portion is from	Spectral resolved measurement of the nitrogen fluorescence emissions in air induced by electrons
Editor of portion(s)	N/A
Author of portion(s)	T. Waldenmaier, J. Blumer and H. Klages

Volume of serial or monograph	29
Page range of portion	207
Publication date of portion	7 February 2008
Rights for	Main product
Duration of use	Life of current edition
Creation of copies for the disabled	no
With minor editing privileges	no
For distribution to	Worldwide
In the following language(s)	Original language of publication
With incidental promotional use	no
Lifetime unit quantity of new product	Up to 499
Title	Design, Calibration and Use of Quantitative Alpha-Induced Radioluminescence Detectors
Institution name	Imperial College London
Expected presentation date	Aug 2019

Note: This item will be invoiced or charged separately through CCC's **RightsLink** service. More info **$ 0.00**

Molecular physics and elements of quantum chemistry : introduction to experiments and theory

Order detail ID: 71909347
Order License Id: 4597050460963
ISBN: 9783540407928
Publication Type: Book
Publisher: SPRINGER
Author/Editor: HAKEN, H.

Permission Status: Granted
Permission type: Republish or display content
Type of use: Thesis/Dissertation

Requestor type	Academic institution
Format	Electronic
Portion	image/photo
Number of images/photos requested	2

The requesting person/organization	Benjamin Pearce, Imperial College London
Title or numeric reference of the portion(s)	Figures 14.1 and 14.3
Title of the article or chapter the portion is from	Chapter 14: The Electronic Spectra of Molecules
Editor of portion(s)	N/A
Author of portion(s)	Haken, H. (Hermann), Wolf, Hans Christoph.
Volume of serial or monograph	N/A
Issue, if republishing an article from a serial	N/A
Page range of portion	296-297
Publication date of portion	2004
Rights for	Main product
Duration of use	Life of current edition
Creation of copies for the disabled	no
With minor editing privileges	no
For distribution to	Worldwide
In the following language(s)	Original language of publication
With incidental promotional use	no
Lifetime unit quantity of new product	Up to 499
Title	Design, Calibration and Use of Quantitative Alpha-Induced Radioluminescence Detectors
Institution name	Imperial College London
Expected presentation date	Aug 2019

Note: This item will be invoiced or charged separately through CCC's **RightsLink** service. More info **$ 0.00**

Molecular physics and elements of quantum chemistry : introduction to experiments and theory

Order detail ID:	71909348
Order License Id:	4597050462090
ISBN:	9783540407928
Publication Type:	Book
Publisher:	SPRINGER
Author/Editor:	HAKEN, H.

Permission Status: Granted

Permission type: Republish or display content

Type of use: Thesis/Dissertation

Requestor type	Academic institution
Format	Electronic
Portion	image/photo
Number of images/photos requested	1
The requesting person/organization	Benjamin Pearce, Imperial College London
Title or numeric reference of the portion(s)	Figure 14.8
Title of the article or chapter the portion is from	Chapter 14: Rotational Structure in Small Molecules: An Overview
Editor of portion(s)	N/A
Author of portion(s)	Haken, H. (Hermann), Wolf, Hans Christoph.
Volume of serial or monograph	N/A
Issue, if republishing an article from a serial	N/A
Page range of portion	303
Publication date of portion	2004
Rights for	Main product
Duration of use	Life of current edition
Creation of copies for the disabled	no
With minor editing privileges	no
For distribution to	Worldwide
In the following language(s)	Original language of publication
With incidental promotional use	no

Lifetime unit quantity of new product	Up to 499
Title	Design, Calibration and Use of Quantitative Alpha-Induced Radioluminescence Detectors
Institution name	Imperial College London
Expected presentation date	Aug 2019

Note: This item will be invoiced or charged separately through CCC's **RightsLink** service. More info **$ 0.00**

Astroparticle physics

Order detail ID: 71909358
Order License Id: 4597050463219
ISSN: 0927-6505
Publication Type: Journal
Volume:
Issue:
Start page:
Publisher: ELSEVIER BV

Permission Status: Granted
Permission type: Republish or display content
Type of use: Thesis/Dissertation

Requestor type	Academic institution
Format	Electronic
Portion	image/photo
Number of images/photos requested	1
The requesting person/organization	Benjamin Pearce, Imperial College London
Title or numeric reference of the portion(s)	Figure 16.
Title of the article or chapter the portion is from	Spectral resolved measurement of the nitrogen fluorescence emissions in air induced by electrons
Editor of portion(s)	N/A
Author of portion(s)	T. Waldenmaier, J. Blumer and H. Klages
Volume of serial or monograph	29
Issue, if republishing an article from a serial	N/A
Page range of portion	220
Publication date of portion	7 February 2008

Rights for	Main product
Duration of use	Life of current edition
Creation of copies for the disabled	no
With minor editing privileges	no
For distribution to	Worldwide
In the following language(s)	Original language of publication
With incidental promotional use	no
Lifetime unit quantity of new product	Up to 499
Title	Design, Calibration and Use of Quantitative Alpha-Induced Radioluminescence Detectors
Institution name	Imperial College London
Expected presentation date	Aug 2019

Note: This item will be invoiced or charged separately through CCC's **RightsLink** service. More info **$ 0.00**

This is not an invoice.

Total order items: 4 **Order Total: 0.00 USD**

Confirmation Number: 11818477

Special Rightsholder Terms & Conditions

The following terms & conditions apply to the specific publication under which they are listed

Astroparticle physics
Permission type: Republish or display content
Type of use: Thesis/Dissertation

TERMS AND CONDITIONS

The following terms are individual to this publisher:

None

Other Terms and Conditions:

STANDARD TERMS AND CONDITIONS

1. Description of Service; Defined Terms. This Republication License enables the User to obtain licenses for republication of one or more copyrighted works as described in detail on the relevant Order Confirmation (the "Work(s)"). Copyright Clearance Center, Inc. ("CCC") grants licenses through the Service on behalf of the rightsholder identified on the Order Confirmation (the "Rightsholder"). "Republication", as used herein, generally means the inclusion of a Work, in whole or in part, in a new work or works, also as described on the Order Confirmation. "User", as used herein, means the person or entity making such republication.

2. The terms set forth in the relevant Order Confirmation, and any terms set by the Rightsholder with respect to a particular Work, govern the terms of use of Works in connection with the Service. By using the Service, the person transacting for a republication license on behalf of the User represents and warrants that he/she/it (a) has been duly authorized by the User to accept, and hereby does accept, all such terms and conditions on behalf of User, and (b) shall inform User of all such terms and conditions. In the event such person is a "freelancer" or other third party independent of User and CCC, such party shall be deemed jointly a "User" for purposes of these terms and conditions. In any event, User shall be deemed to have accepted and agreed to all such terms and conditions if User republishes the Work in any fashion.

3. Scope of License; Limitations and Obligations.

3.1 All Works and all rights therein, including copyright rights, remain the sole and exclusive property of the Rightsholder. The license created by the exchange of an Order Confirmation (and/or any invoice) and payment by User of the full amount set forth on that document includes only those rights expressly set forth in the Order Confirmation and in these terms and conditions, and conveys no other rights in the Work(s) to User. All rights not expressly granted are hereby reserved.

3.2 General Payment Terms: You may pay by credit card or through an account with us payable at the end of the month. If you and we agree that you may establish a standing account with CCC, then the following terms apply: Remit Payment to: Copyright Clearance Center, 29118 Network Place, Chicago, IL 60673-1291. Payments Due: Invoices are payable upon their delivery to you (or upon our notice to you that they are available to you for downloading). After 30 days, outstanding amounts will be subject to a service charge of 1-1/2% per month or, if less, the maximum rate allowed by applicable law. Unless otherwise specifically set forth in the Order Confirmation or in a separate written agreement signed by CCC, invoices are due and payable on "net 30" terms. While User may exercise the rights licensed immediately upon issuance of the Order Confirmation, the license is automatically revoked and is null and void, as if it had never been issued, if complete payment for the license is not received on a timely basis either from User directly or through a payment agent, such as a credit card company.

3.3 Unless otherwise provided in the Order Confirmation, any grant of rights to User (i) is "one-time" (including the editions and product family specified in the license), (ii) is non-exclusive and non-transferable and (iii) is subject to any and all limitations and restrictions (such as, but not limited to, limitations on duration of use or circulation) included in the Order Confirmation or invoice and/or in these terms and conditions. Upon completion of the licensed use, User shall either secure a new permission for further use of the Work(s) or immediately cease any new use of the Work(s) and shall render inaccessible (such as by deleting or by removing or severing links or other locators) any further copies of the Work (except for copies printed on paper in accordance with this license and still in User's stock at the end of such period).

3.4 In the event that the material for which a republication license is sought includes third party materials (such as photographs, illustrations, graphs, inserts and similar materials) which are identified in such material as having been used by permission, User is responsible for identifying, and seeking separate licenses (under this Service or otherwise) for, any of such third party materials; without a separate license, such third party materials may not be used.

3.5 Use of proper copyright notice for a Work is required as a condition of any license granted under the Service. Unless otherwise provided in the Order Confirmation, a proper copyright notice will read substantially as follows: "Republished with permission of [Rightsholder's name], from [Work's title, author, volume, edition number and year of copyright]; permission conveyed through Copyright Clearance Center, Inc. " Such notice must be provided in a reasonably legible font size and must be placed either immediately adjacent to the Work as used (for example, as part of a by-line or footnote but not as a separate electronic link) or in the place where substantially all other credits or notices for the new work containing the republished Work are located. Failure to include the required notice results in loss to the Rightsholder and CCC, and the User shall be liable to pay liquidated damages for each such failure equal to twice the use fee specified in the Order Confirmation, in addition to the use fee itself and any other fees and charges specified.

3.6 User may only make alterations to the Work if and as expressly set forth in the Order Confirmation. No Work may be used in any way that is defamatory, violates the rights of third parties (including such third parties' rights of copyright, privacy, publicity, or other tangible or intangible property), or is otherwise illegal, sexually explicit or obscene. In

addition, User may not conjoin a Work with any other material that may result in damage to the reputation of the Rightsholder. User agrees to inform CCC if it becomes aware of any infringement of any rights in a Work and to cooperate with any reasonable request of CCC or the Rightsholder in connection therewith.

4. Indemnity. User hereby indemnifies and agrees to defend the Rightsholder and CCC, and their respective employees and directors, against all claims, liability, damages, costs and expenses, including legal fees and expenses, arising out of any use of a Work beyond the scope of the rights granted herein, or any use of a Work which has been altered in any unauthorized way by User, including claims of defamation or infringement of rights of copyright, publicity, privacy or other tangible or intangible property.

5. Limitation of Liability. UNDER NO CIRCUMSTANCES WILL CCC OR THE RIGHTSHOLDER BE LIABLE FOR ANY DIRECT, INDIRECT, CONSEQUENTIAL OR INCIDENTAL DAMAGES (INCLUDING WITHOUT LIMITATION DAMAGES FOR LOSS OF BUSINESS PROFITS OR INFORMATION, OR FOR BUSINESS INTERRUPTION) ARISING OUT OF THE USE OR INABILITY TO USE A WORK, EVEN IF ONE OF THEM HAS BEEN ADVISED OF THE POSSIBILITY OF SUCH DAMAGES. In any event, the total liability of the Rightsholder and CCC (including their respective employees and directors) shall not exceed the total amount actually paid by User for this license. User assumes full liability for the actions and omissions of its principals, employees, agents, affiliates, successors and assigns.

6. Limited Warranties. THE WORK(S) AND RIGHT(S) ARE PROVIDED "AS IS". CCC HAS THE RIGHT TO GRANT TO USER THE RIGHTS GRANTED IN THE ORDER CONFIRMATION DOCUMENT. CCC AND THE RIGHTSHOLDER DISCLAIM ALL OTHER WARRANTIES RELATING TO THE WORK(S) AND RIGHT(S), EITHER EXPRESS OR IMPLIED, INCLUDING WITHOUT LIMITATION IMPLIED WARRANTIES OF MERCHANTABILITY OR FITNESS FOR A PARTICULAR PURPOSE. ADDITIONAL RIGHTS MAY BE REQUIRED TO USE ILLUSTRATIONS, GRAPHS, PHOTOGRAPHS, ABSTRACTS, INSERTS OR OTHER PORTIONS OF THE WORK (AS OPPOSED TO THE ENTIRE WORK) IN A MANNER CONTEMPLATED BY USER; USER UNDERSTANDS AND AGREES THAT NEITHER CCC NOR THE RIGHTSHOLDER MAY HAVE SUCH ADDITIONAL RIGHTS TO GRANT.

7. Effect of Breach. Any failure by User to pay any amount when due, or any use by User of a Work beyond the scope of the license set forth in the Order Confirmation and/or these terms and conditions, shall be a material breach of the license created by the Order Confirmation and these terms and conditions. Any breach not cured within 30 days of written notice thereof shall result in immediate termination of such license without further notice. Any unauthorized (but licensable) use of a Work that is terminated immediately upon notice thereof may be liquidated by payment of the Rightsholder's ordinary license price therefor; any unauthorized (and unlicensable) use that is not terminated immediately for any reason (including, for example, because materials containing the Work cannot reasonably be recalled) will be subject to all remedies available at law or in equity, but in no event to a payment of less than three times the Rightsholder's ordinary license price for the most closely analogous licensable use plus Rightsholder's and/or CCC's costs and expenses incurred in collecting such payment.

8. **Miscellaneous.**

8.1 User acknowledges that CCC may, from time to time, make changes or additions to the Service or to these terms and conditions, and CCC reserves the right to send notice to the User by electronic mail or otherwise for the purposes of notifying User of such changes or additions; provided that any such changes or additions shall not apply to permissions already secured and paid for.

8.2 Use of User-related information collected through the Service is governed by CCC's privacy policy, available online here: http://www.copyright.com/content/cc3/en/tools/footer/privacypolicy.html.

8.3 The licensing transaction described in the Order Confirmation is personal to User. Therefore, User may not assign or transfer to any other person (whether a natural person or an organization of any kind) the license created by the Order Confirmation and these terms and conditions or any rights granted hereunder; provided, however, that User may assign such license in its entirety on written notice to CCC in the event of a transfer of all or substantially all of User's rights in the new material which includes the Work(s) licensed under this Service.

8.4 No amendment or waiver of any terms is binding unless set forth in writing and signed by the parties. The Rightsholder and CCC hereby object to any terms contained in any writing prepared by the User or its principals, employees, agents or affiliates and purporting to govern or otherwise relate to the licensing transaction described in the Order Confirmation, which terms are in any way inconsistent with any terms set forth in the Order Confirmation and/or in these terms and conditions or CCC's standard operating procedures, whether such writing is prepared prior to, simultaneously with or subsequent to the Order Confirmation, and whether such writing appears on a copy of the Order Confirmation or in a separate instrument.

8.5 The licensing transaction described in the Order Confirmation document shall be governed by and construed under the law of the State of New York, USA, without regard to the principles thereof of conflicts of law. Any case, controversy, suit, action, or proceeding arising out of, in connection with, or related to such licensing transaction shall be brought, at CCC's sole discretion, in any federal or state court located in the County of New York, State of New York, USA, or in any federal or state court whose geographical jurisdiction covers the location of the Rightsholder set forth in the Order Confirmation. The parties expressly submit to the personal jurisdiction and venue of each such federal or state court.If you have any comments or questions about the Service or Copyright Clearance Center, please contact us at 978-750-8400 or send an e-mail to info@copyright.com.

v 1.1

Molecular physics and elements of quantum chemistry : introduction to experiments and theory
Permission type: Republish or display content
Type of use: Thesis/Dissertation

TERMS AND CONDITIONS

The following terms are individual to this publisher:

A maximum of 10% of the content may be licensed for republication.

The user is responsible for identifying and seeking separate licenses for any third party materials that are identified anywhere in the work. Without a separate license, such third party materials may not be reused.

Other Terms and Conditions:

STANDARD TERMS AND CONDITIONS

1. Description of Service; Defined Terms. This Republication License enables the User to obtain licenses for republication of one or more copyrighted works as described in detail on the relevant Order Confirmation (the "Work(s)"). Copyright Clearance Center, Inc. ("CCC") grants licenses through the Service on behalf of the rightsholder identified on the Order Confirmation (the "Rightsholder"). "Republication", as used herein, generally means the inclusion of a Work, in whole or in part, in a new work or works, also as described on the Order Confirmation. "User", as used herein, means the person or entity making such republication.

2. The terms set forth in the relevant Order Confirmation, and any terms set by the Rightsholder with respect to a particular Work, govern the terms of use of Works in connection with the Service. By using the Service, the person transacting for a republication license on behalf of the User represents and warrants that he/she/it (a) has been duly authorized by the User to accept, and hereby does accept, all such terms and conditions on behalf of User, and (b) shall inform User of all such terms and conditions. In the event such person is a "freelancer" or other third party independent of User and CCC, such party shall be deemed jointly a "User" for purposes of these terms and conditions. In any event, User shall be deemed to have accepted and agreed to all such terms and conditions if User republishes the Work in any fashion.

3. Scope of License; Limitations and Obligations.

3.1 All Works and all rights therein, including copyright rights, remain the sole and exclusive property of the Rightsholder. The license created by the exchange of an Order Confirmation (and/or any invoice) and payment by User of the full amount set forth on that document includes only those rights expressly set forth in the Order Confirmation and in these terms and conditions, and conveys no other rights in the Work(s) to User. All rights not expressly granted are hereby reserved.

3.2 General Payment Terms: You may pay by credit card or through an account with us payable at the end of the month. If you and we agree that you may establish a standing account with CCC, then the following terms apply: Remit Payment to: Copyright Clearance Center, 29118 Network Place, Chicago, IL 60673-1291. Payments Due: Invoices are payable upon their delivery to you (or upon our notice to you that they are available to you for downloading). After 30 days, outstanding amounts will be subject to a service charge of 1-1/2% per month or, if less, the maximum rate allowed by applicable law. Unless otherwise specifically set forth in the Order Confirmation or in a separate written agreement signed by CCC, invoices are due and payable on "net 30" terms. While User may exercise the rights licensed immediately upon issuance of the Order Confirmation, the license is automatically revoked and is null and void, as if it had never been issued, if complete payment for the license is not received on a timely basis either from User directly or through a payment agent, such as a credit card company.

3.3 Unless otherwise provided in the Order Confirmation, any grant of rights to User (i) is "one-time" (including the editions and product family specified in the license), (ii) is non-exclusive and non-transferable and (iii) is subject to any and all limitations and restrictions (such as, but not limited to, limitations on duration of use or circulation) included in the Order Confirmation or invoice and/or in these terms and conditions. Upon completion of the licensed use, User shall either secure a new permission for further use of the Work(s) or immediately cease any new use of the Work(s) and shall render inaccessible (such as by deleting or by removing or severing links or other locators) any further copies of the Work (except for copies printed on paper in accordance with this license and still in User's stock at the end of such period).

3.4 In the event that the material for which a republication license is sought includes third party materials (such as photographs, illustrations, graphs, inserts and similar materials) which are identified in such material as having been used by permission, User is responsible for identifying, and seeking separate licenses (under this Service or otherwise) for, any of such third party materials; without a separate license, such third party materials may not be used.

3.5 Use of proper copyright notice for a Work is required as a condition of any license granted under the Service. Unless otherwise provided in the Order Confirmation, a proper copyright notice will read substantially as follows: "Republished with permission of [Rightsholder's name], from [Work's title, author, volume, edition number and year of copyright]; permission conveyed through Copyright Clearance Center, Inc. " Such notice must be provided in a reasonably legible font size and must be placed either immediately adjacent to the Work as used (for example, as part of a by-line or footnote but not as a separate electronic link) or in the place where substantially all other credits or notices for the new work containing the republished Work are located. Failure to include the required notice results in loss to the Rightsholder and CCC, and the User shall be liable to pay liquidated damages for each such failure equal to twice the use fee specified in the Order Confirmation, in addition to the use fee itself and any other fees and charges specified.

3.6 User may only make alterations to the Work if and as expressly set forth in the Order Confirmation. No Work may be used in any way that is defamatory, violates the rights of third parties (including such third parties' rights of copyright, privacy, publicity, or other tangible or intangible property), or is otherwise illegal, sexually explicit or obscene. In addition, User may not conjoin a Work with any other material that may result in damage to the reputation of the Rightsholder. User agrees to inform CCC if it becomes aware of any infringement of any rights in a Work and to cooperate with any reasonable request of CCC or the Rightsholder in connection therewith.

4. Indemnity. User hereby indemnifies and agrees to defend the Rightsholder and CCC, and their respective employees and directors, against all claims, liability, damages, costs and expenses, including legal fees and expenses, arising out of any use of a Work beyond the scope of the rights granted herein, or any use of a Work which has been altered in any unauthorized way by User, including claims of defamation or infringement of rights of copyright, publicity, privacy or other tangible or intangible property.

5. Limitation of Liability. UNDER NO CIRCUMSTANCES WILL CCC OR THE RIGHTSHOLDER BE LIABLE FOR ANY DIRECT, INDIRECT, CONSEQUENTIAL OR INCIDENTAL DAMAGES (INCLUDING WITHOUT LIMITATION DAMAGES FOR LOSS OF BUSINESS PROFITS OR INFORMATION, OR FOR BUSINESS INTERRUPTION) ARISING OUT OF THE USE OR INABILITY TO USE A WORK, EVEN IF ONE OF THEM HAS BEEN ADVISED OF THE POSSIBILITY OF SUCH DAMAGES. In any event, the total liability of the Rightsholder and CCC (including their respective employees and directors) shall not exceed the total

amount actually paid by User for this license. User assumes full liability for the actions and omissions of its principals, employees, agents, affiliates, successors and assigns.

6. Limited Warranties. THE WORK(S) AND RIGHT(S) ARE PROVIDED "AS IS". CCC HAS THE RIGHT TO GRANT TO USER THE RIGHTS GRANTED IN THE ORDER CONFIRMATION DOCUMENT. CCC AND THE RIGHTSHOLDER DISCLAIM ALL OTHER WARRANTIES RELATING TO THE WORK(S) AND RIGHT(S), EITHER EXPRESS OR IMPLIED, INCLUDING WITHOUT LIMITATION IMPLIED WARRANTIES OF MERCHANTABILITY OR FITNESS FOR A PARTICULAR PURPOSE. ADDITIONAL RIGHTS MAY BE REQUIRED TO USE ILLUSTRATIONS, GRAPHS, PHOTOGRAPHS, ABSTRACTS, INSERTS OR OTHER PORTIONS OF THE WORK (AS OPPOSED TO THE ENTIRE WORK) IN A MANNER CONTEMPLATED BY USER; USER UNDERSTANDS AND AGREES THAT NEITHER CCC NOR THE RIGHTSHOLDER MAY HAVE SUCH ADDITIONAL RIGHTS TO GRANT.

7. Effect of Breach. Any failure by User to pay any amount when due, or any use by User of a Work beyond the scope of the license set forth in the Order Confirmation and/or these terms and conditions, shall be a material breach of the license created by the Order Confirmation and these terms and conditions. Any breach not cured within 30 days of written notice thereof shall result in immediate termination of such license without further notice. Any unauthorized (but licensable) use of a Work that is terminated immediately upon notice thereof may be liquidated by payment of the Rightsholder's ordinary license price therefor; any unauthorized (and unlicensable) use that is not terminated immediately for any reason (including, for example, because materials containing the Work cannot reasonably be recalled) will be subject to all remedies available at law or in equity, but in no event to a payment of less than three times the Rightsholder's ordinary license price for the most closely analogous licensable use plus Rightsholder's and/or CCC's costs and expenses incurred in collecting such payment.

8. **Miscellaneous.**

8.1 User acknowledges that CCC may, from time to time, make changes or additions to the Service or to these terms and conditions, and CCC reserves the right to send notice to the User by electronic mail or otherwise for the purposes of notifying User of such changes or additions; provided that any such changes or additions shall not apply to permissions already secured and paid for.

8.2 Use of User-related information collected through the Service is governed by CCC's privacy policy, available online here: http://www.copyright.com/content/cc3/en/tools/footer/privacypolicy.html.

8.3 The licensing transaction described in the Order Confirmation is personal to User. Therefore, User may not assign or transfer to any other person (whether a natural person or an organization of any kind) the license created by the Order Confirmation and these terms and conditions or any rights granted hereunder; provided, however, that User may assign such license in its entirety on written notice to CCC in the event of a transfer of all or substantially all of User's rights in the new material which includes the Work(s) licensed under this Service.

8.4 No amendment or waiver of any terms is binding unless set forth in writing and signed by the parties. The Rightsholder and CCC hereby object to any terms contained in any writing prepared by the User or its principals, employees, agents or affiliates and purporting to govern or otherwise relate to the licensing transaction described in the Order Confirmation, which terms are in any way inconsistent with any terms set forth in the Order Confirmation and/or in these terms and conditions or CCC's standard operating procedures, whether such writing is prepared prior to, simultaneously with or subsequent to the Order Confirmation, and whether such writing appears on a copy of the Order Confirmation or in a separate instrument.

8.5 The licensing transaction described in the Order Confirmation document shall be governed by and construed under the law of the State of New York, USA, without regard to the principles thereof of conflicts of law. Any case, controversy, suit, action, or proceeding arising out of, in connection with, or related to such licensing transaction shall be brought, at CCC's sole discretion, in any federal or state court located in the County of New York, State of New York, USA, or in any federal or state court whose geographical jurisdiction covers the location of the Rightsholder set forth in the Order Confirmation. The parties expressly submit to the personal jurisdiction and venue of each such federal or state court.If you have any comments or questions about the Service or Copyright Clearance Center, please contact us at 978-750-8400 or send an e-mail to info@copyright.com.

v 1.1

Molecular physics and elements of quantum chemistry : introduction to experiments and theory
Permission type: Republish or display content
Type of use: Thesis/Dissertation

TERMS AND CONDITIONS

The following terms are individual to this publisher:

A maximum of 10% of the content may be licensed for republication.

The user is responsible for identifying and seeking separate licenses for any third party materials that are identified anywhere in the work. Without a separate license, such third party materials may not be reused.

Other Terms and Conditions:

STANDARD TERMS AND CONDITIONS

1. Description of Service; Defined Terms. This Republication License enables the User to obtain licenses for republication of one or more copyrighted works as described in detail on the relevant Order Confirmation (the "Work(s)"). Copyright Clearance Center, Inc. ("CCC") grants licenses through the Service on behalf of the rightsholder identified on the Order Confirmation (the "Rightsholder"). "Republication", as used herein, generally means the inclusion of a Work, in whole or in

part, in a new work or works, also as described on the Order Confirmation. "User", as used herein, means the person or entity making such republication.

2. The terms set forth in the relevant Order Confirmation, and any terms set by the Rightsholder with respect to a particular Work, govern the terms of use of Works in connection with the Service. By using the Service, the person transacting for a republication license on behalf of the User represents and warrants that he/she/it (a) has been duly authorized by the User to accept, and hereby does accept, all such terms and conditions on behalf of User, and (b) shall inform User of all such terms and conditions. In the event such person is a "freelancer" or other third party independent of User and CCC, such party shall be deemed jointly a "User" for purposes of these terms and conditions. In any event, User shall be deemed to have accepted and agreed to all such terms and conditions if User republishes the Work in any fashion.

3. Scope of License; Limitations and Obligations.

3.1 All Works and all rights therein, including copyright rights, remain the sole and exclusive property of the Rightsholder. The license created by the exchange of an Order Confirmation (and/or any invoice) and payment by User of the full amount set forth on that document includes only those rights expressly set forth in the Order Confirmation and in these terms and conditions, and conveys no other rights in the Work(s) to User. All rights not expressly granted are hereby reserved.

3.2 General Payment Terms: You may pay by credit card or through an account with us payable at the end of the month. If you and we agree that you may establish a standing account with CCC, then the following terms apply: Remit Payment to: Copyright Clearance Center, 29118 Network Place, Chicago, IL 60673-1291. Payments Due: Invoices are payable upon their delivery to you (or upon our notice to you that they are available to you for downloading). After 30 days, outstanding amounts will be subject to a service charge of 1-1/2% per month or, if less, the maximum rate allowed by applicable law. Unless otherwise specifically set forth in the Order Confirmation or in a separate written agreement signed by CCC, invoices are due and payable on "net 30" terms. While User may exercise the rights licensed immediately upon issuance of the Order Confirmation, the license is automatically revoked and is null and void, as if it had never been issued, if complete payment for the license is not received on a timely basis either from User directly or through a payment agent, such as a credit card company.

3.3 Unless otherwise provided in the Order Confirmation, any grant of rights to User (i) is "one-time" (including the editions and product family specified in the license), (ii) is non-exclusive and non-transferable and (iii) is subject to any and all limitations and restrictions (such as, but not limited to, limitations on duration of use or circulation) included in the Order Confirmation or invoice and/or in these terms and conditions. Upon completion of the licensed use, User shall either secure a new permission for further use of the Work(s) or immediately cease any new use of the Work(s) and shall render inaccessible (such as by deleting or by removing or severing links or other locators) any further copies of the Work (except for copies printed on paper in accordance with this license and still in User's stock at the end of such period).

3.4 In the event that the material for which a republication license is sought includes third party materials (such as photographs, illustrations, graphs, inserts and similar materials) which are identified in such material as having been used by permission, User is responsible for identifying, and seeking separate licenses (under this Service or otherwise) for, any of such third party materials; without a separate license, such third party materials may not be used.

3.5 Use of proper copyright notice for a Work is required as a condition of any license granted under the Service. Unless otherwise provided in the Order Confirmation, a proper copyright notice will read substantially as follows: "Republished with permission of [Rightsholder's name], from [Work's title, author, volume, edition number and year of copyright]; permission conveyed through Copyright Clearance Center, Inc. " Such notice must be provided in a reasonably legible font size and must be placed either immediately adjacent to the Work as used (for example, as part of a by-line or footnote but not as a separate electronic link) or in the place where substantially all other credits or notices for the new work containing the republished Work are located. Failure to include the required notice results in loss to the Rightsholder and CCC, and the User shall be liable to pay liquidated damages for each such failure equal to twice the use fee specified in the Order Confirmation, in addition to the use fee itself and any other fees and charges specified.

3.6 User may only make alterations to the Work if and as expressly set forth in the Order Confirmation. No Work may be used in any way that is defamatory, violates the rights of third parties (including such third parties' rights of copyright, privacy, publicity, or other tangible or intangible property), or is otherwise illegal, sexually explicit or obscene. In addition, User may not conjoin a Work with any other material that may result in damage to the reputation of the Rightsholder. User agrees to inform CCC if it becomes aware of any infringement of any rights in a Work and to cooperate with any reasonable request of CCC or the Rightsholder in connection therewith.

4. Indemnity. User hereby indemnifies and agrees to defend the Rightsholder and CCC, and their respective employees and directors, against all claims, liability, damages, costs and expenses, including legal fees and expenses, arising out of any use of a Work beyond the scope of the rights granted herein, or any use of a Work which has been altered in any unauthorized way by User, including claims of defamation or infringement of rights of copyright, publicity, privacy or other tangible or intangible property.

5. Limitation of Liability. UNDER NO CIRCUMSTANCES WILL CCC OR THE RIGHTSHOLDER BE LIABLE FOR ANY DIRECT, INDIRECT, CONSEQUENTIAL OR INCIDENTAL DAMAGES (INCLUDING WITHOUT LIMITATION DAMAGES FOR LOSS OF BUSINESS PROFITS OR INFORMATION, OR FOR BUSINESS INTERRUPTION) ARISING OUT OF THE USE OR INABILITY TO USE A WORK, EVEN IF ONE OF THEM HAS BEEN ADVISED OF THE POSSIBILITY OF SUCH DAMAGES. In any event, the total liability of the Rightsholder and CCC (including their respective employees and directors) shall not exceed the total amount actually paid by User for this license. User assumes full liability for the actions and omissions of its principals, employees, agents, affiliates, successors and assigns.

6. Limited Warranties. THE WORK(S) AND RIGHT(S) ARE PROVIDED "AS IS". CCC HAS THE RIGHT TO GRANT TO USER THE RIGHTS GRANTED IN THE ORDER CONFIRMATION DOCUMENT. CCC AND THE RIGHTSHOLDER DISCLAIM ALL OTHER WARRANTIES RELATING TO THE WORK(S) AND RIGHT(S), EITHER EXPRESS OR IMPLIED, INCLUDING WITHOUT LIMITATION IMPLIED WARRANTIES OF MERCHANTABILITY OR FITNESS FOR A PARTICULAR PURPOSE. ADDITIONAL RIGHTS MAY BE REQUIRED TO USE ILLUSTRATIONS, GRAPHS, PHOTOGRAPHS, ABSTRACTS, INSERTS OR OTHER PORTIONS OF THE WORK (AS OPPOSED TO THE ENTIRE WORK) IN A MANNER CONTEMPLATED BY USER; USER UNDERSTANDS AND AGREES THAT NEITHER CCC NOR THE RIGHTSHOLDER MAY HAVE SUCH ADDITIONAL RIGHTS TO GRANT.

7. Effect of Breach. Any failure by User to pay any amount when due, or any use by User of a Work beyond the scope of the license set forth in the Order Confirmation and/or these terms and conditions, shall be a material breach of the license created by the Order Confirmation and these terms and conditions. Any breach not cured within 30 days of written

notice thereof shall result in immediate termination of such license without further notice. Any unauthorized (but licensable) use of a Work that is terminated immediately upon notice thereof may be liquidated by payment of the Rightsholder's ordinary license price therefor; any unauthorized (and unlicensable) use that is not terminated immediately for any reason (including, for example, because materials containing the Work cannot reasonably be recalled) will be subject to all remedies available at law or in equity, but in no event to a payment of less than three times the Rightsholder's ordinary license price for the most closely analogous licensable use plus Rightsholder's and/or CCC's costs and expenses incurred in collecting such payment.

8. **Miscellaneous.**

8.1 User acknowledges that CCC may, from time to time, make changes or additions to the Service or to these terms and conditions, and CCC reserves the right to send notice to the User by electronic mail or otherwise for the purposes of notifying User of such changes or additions; provided that any such changes or additions shall not apply to permissions already secured and paid for.

8.2 Use of User-related information collected through the Service is governed by CCC's privacy policy, available online here: http://www.copyright.com/content/cc3/en/tools/footer/privacypolicy.html.

8.3 The licensing transaction described in the Order Confirmation is personal to User. Therefore, User may not assign or transfer to any other person (whether a natural person or an organization of any kind) the license created by the Order Confirmation and these terms and conditions or any rights granted hereunder; provided, however, that User may assign such license in its entirety on written notice to CCC in the event of a transfer of all or substantially all of User's rights in the new material which includes the Work(s) licensed under this Service.

8.4 No amendment or waiver of any terms is binding unless set forth in writing and signed by the parties. The Rightsholder and CCC hereby object to any terms contained in any writing prepared by the User or its principals, employees, agents or affiliates and purporting to govern or otherwise relate to the licensing transaction described in the Order Confirmation, which terms are in any way inconsistent with any terms set forth in the Order Confirmation and/or in these terms and conditions or CCC's standard operating procedures, whether such writing is prepared prior to, simultaneously with or subsequent to the Order Confirmation, and whether such writing appears on a copy of the Order Confirmation or in a separate instrument.

8.5 The licensing transaction described in the Order Confirmation document shall be governed by and construed under the law of the State of New York, USA, without regard to the principles thereof of conflicts of law. Any case, controversy, suit, action, or proceeding arising out of, in connection with, or related to such licensing transaction shall be brought, at CCC's sole discretion, in any federal or state court located in the County of New York, State of New York, USA, or in any federal or state court whose geographical jurisdiction covers the location of the Rightsholder set forth in the Order Confirmation. The parties expressly submit to the personal jurisdiction and venue of each such federal or state court.If you have any comments or questions about the Service or Copyright Clearance Center, please contact us at 978-750-8400 or send an e-mail to info@copyright.com.

v 1.1

Astroparticle physics
Permission type: Republish or display content
Type of use: Thesis/Dissertation

TERMS AND CONDITIONS

The following terms are individual to this publisher:

None

Other Terms and Conditions:

STANDARD TERMS AND CONDITIONS

1. Description of Service; Defined Terms. This Republication License enables the User to obtain licenses for republication of one or more copyrighted works as described in detail on the relevant Order Confirmation (the "Work(s)"). Copyright Clearance Center, Inc. ("CCC") grants licenses through the Service on behalf of the rightsholder identified on the Order Confirmation (the "Rightsholder"). "Republication", as used herein, generally means the inclusion of a Work, in whole or in part, in a new work or works, also as described on the Order Confirmation. "User", as used herein, means the person or entity making such republication.

2. The terms set forth in the relevant Order Confirmation, and any terms set by the Rightsholder with respect to a particular Work, govern the terms of use of Works in connection with the Service. By using the Service, the person transacting for a republication license on behalf of the User represents and warrants that he/she/it (a) has been duly authorized by the User to accept, and hereby does accept, all such terms and conditions on behalf of User, and (b) shall inform User of all such terms and conditions. In the event such person is a "freelancer" or other third party independent of User and CCC, such party shall be deemed jointly a "User" for purposes of these terms and conditions. In any event, User shall be deemed to have accepted and agreed to all such terms and conditions if User republishes the Work in any fashion.

3. Scope of License; Limitations and Obligations.

3.1 All Works and all rights therein, including copyright rights, remain the sole and exclusive property of the Rightsholder. The license created by the exchange of an Order Confirmation (and/or any invoice) and payment by User of the full amount set forth on that document includes only those rights expressly set forth in the Order Confirmation and in these terms and conditions, and conveys no other rights in the Work(s) to User. All rights not expressly granted are hereby reserved.

3.2 General Payment Terms: You may pay by credit card or through an account with us payable at the end of the month. If you and we agree that you may establish a standing account with CCC, then the following terms apply: Remit Payment to: Copyright Clearance Center, 29118 Network Place, Chicago, IL 60673-1291. Payments Due: Invoices are payable upon their delivery to you (or upon our notice to you that they are available to you for downloading). After 30 days, outstanding amounts will be subject to a service charge of 1-1/2% per month or, if less, the maximum rate allowed by applicable law. Unless otherwise specifically set forth in the Order Confirmation or in a separate written agreement signed by CCC, invoices are due and payable on "net 30" terms. While User may exercise the rights licensed immediately upon issuance of the Order Confirmation, the license is automatically revoked and is null and void, as if it had never been issued, if complete payment for the license is not received on a timely basis either from User directly or through a payment agent, such as a credit card company.

3.3 Unless otherwise provided in the Order Confirmation, any grant of rights to User (i) is "one-time" (including the editions and product family specified in the license), (ii) is non-exclusive and non-transferable and (iii) is subject to any and all limitations and restrictions (such as, but not limited to, limitations on duration of use or circulation) included in the Order Confirmation or invoice and/or in these terms and conditions. Upon completion of the licensed use, User shall either secure a new permission for further use of the Work(s) or immediately cease any new use of the Work(s) and shall render inaccessible (such as by deleting or by removing or severing links or other locators) any further copies of the Work (except for copies printed on paper in accordance with this license and still in User's stock at the end of such period).

3.4 In the event that the material for which a republication license is sought includes third party materials (such as photographs, illustrations, graphs, inserts and similar materials) which are identified in such material as having been used by permission, User is responsible for identifying, and seeking separate licenses (under this Service or otherwise) for, any of such third party materials; without a separate license, such third party materials may not be used.

3.5 Use of proper copyright notice for a Work is required as a condition of any license granted under the Service. Unless otherwise provided in the Order Confirmation, a proper copyright notice will read substantially as follows: "Republished with permission of [Rightsholder's name], from [Work's title, author, volume, edition number and year of copyright]; permission conveyed through Copyright Clearance Center, Inc. " Such notice must be provided in a reasonably legible font size and must be placed either immediately adjacent to the Work as used (for example, as part of a by-line or footnote but not as a separate electronic link) or in the place where substantially all other credits or notices for the new work containing the republished Work are located. Failure to include the required notice results in loss to the Rightsholder and CCC, and the User shall be liable to pay liquidated damages for each such failure equal to twice the use fee specified in the Order Confirmation, in addition to the use fee itself and any other fees and charges specified.

3.6 User may only make alterations to the Work if and as expressly set forth in the Order Confirmation. No Work may be used in any way that is defamatory, violates the rights of third parties (including such third parties' rights of copyright, privacy, publicity, or other tangible or intangible property), or is otherwise illegal, sexually explicit or obscene. In addition, User may not conjoin a Work with any other material that may result in damage to the reputation of the Rightsholder. User agrees to inform CCC if it becomes aware of any infringement of any rights in a Work and to cooperate with any reasonable request of CCC or the Rightsholder in connection therewith.

4. Indemnity. User hereby indemnifies and agrees to defend the Rightsholder and CCC, and their respective employees and directors, against all claims, liability, damages, costs and expenses, including legal fees and expenses, arising out of any use of a Work beyond the scope of the rights granted herein, or any use of a Work which has been altered in any unauthorized way by User, including claims of defamation or infringement of rights of copyright, publicity, privacy or other tangible or intangible property.

5. Limitation of Liability. UNDER NO CIRCUMSTANCES WILL CCC OR THE RIGHTSHOLDER BE LIABLE FOR ANY DIRECT, INDIRECT, CONSEQUENTIAL OR INCIDENTAL DAMAGES (INCLUDING WITHOUT LIMITATION DAMAGES FOR LOSS OF BUSINESS PROFITS OR INFORMATION, OR FOR BUSINESS INTERRUPTION) ARISING OUT OF THE USE OR INABILITY TO USE A WORK, EVEN IF ONE OF THEM HAS BEEN ADVISED OF THE POSSIBILITY OF SUCH DAMAGES. In any event, the total liability of the Rightsholder and CCC (including their respective employees and directors) shall not exceed the total amount actually paid by User for this license. User assumes full liability for the actions and omissions of its principals, employees, agents, affiliates, successors and assigns.

6. Limited Warranties. THE WORK(S) AND RIGHT(S) ARE PROVIDED "AS IS". CCC HAS THE RIGHT TO GRANT TO USER THE RIGHTS GRANTED IN THE ORDER CONFIRMATION DOCUMENT. CCC AND THE RIGHTSHOLDER DISCLAIM ALL OTHER WARRANTIES RELATING TO THE WORK(S) AND RIGHT(S), EITHER EXPRESS OR IMPLIED, INCLUDING WITHOUT LIMITATION IMPLIED WARRANTIES OF MERCHANTABILITY OR FITNESS FOR A PARTICULAR PURPOSE. ADDITIONAL RIGHTS MAY BE REQUIRED TO USE ILLUSTRATIONS, GRAPHS, PHOTOGRAPHS, ABSTRACTS, INSERTS OR OTHER PORTIONS OF THE WORK (AS OPPOSED TO THE ENTIRE WORK) IN A MANNER CONTEMPLATED BY USER; USER UNDERSTANDS AND AGREES THAT NEITHER CCC NOR THE RIGHTSHOLDER MAY HAVE SUCH ADDITIONAL RIGHTS TO GRANT.

7. Effect of Breach. Any failure by User to pay any amount when due, or any use by User of a Work beyond the scope of the license set forth in the Order Confirmation and/or these terms and conditions, shall be a material breach of the license created by the Order Confirmation and these terms and conditions. Any breach not cured within 30 days of written notice thereof shall result in immediate termination of such license without further notice. Any unauthorized (but licensable) use of a Work that is terminated immediately upon notice thereof may be liquidated by payment of the Rightsholder's ordinary license price therefor; any unauthorized (and unlicensable) use that is not terminated immediately for any reason (including, for example, because materials containing the Work cannot reasonably be recalled) will be subject to all remedies available at law or in equity, but in no event to a payment of less than three times the Rightsholder's ordinary license price for the most closely analogous licensable use plus Rightsholder's and/or CCC's costs and expenses incurred in collecting such payment.

8. **Miscellaneous.**

8.1 User acknowledges that CCC may, from time to time, make changes or additions to the Service or to these terms and conditions, and CCC reserves the right to send notice to the User by electronic mail or otherwise for the purposes of notifying User of such changes or additions; provided that any such changes or additions shall not apply to permissions already secured and paid for.

8.2 Use of User-related information collected through the Service is governed by CCC's privacy policy, available online here: http://www.copyright.com/content/cc3/en/tools/footer/privacypolicy.html.

8.3 The licensing transaction described in the Order Confirmation is personal to User. Therefore, User may not assign or transfer to any other person (whether a natural person or an organization of any kind) the license created by the Order

Confirmation and these terms and conditions or any rights granted hereunder; provided, however, that User may assign such license in its entirety on written notice to CCC in the event of a transfer of all or substantially all of User's rights in the new material which includes the Work(s) licensed under this Service.

8.4 No amendment or waiver of any terms is binding unless set forth in writing and signed by the parties. The Rightsholder and CCC hereby object to any terms contained in any writing prepared by the User or its principals, employees, agents or affiliates and purporting to govern or otherwise relate to the licensing transaction described in the Order Confirmation, which terms are in any way inconsistent with any terms set forth in the Order Confirmation and/or in these terms and conditions or CCC's standard operating procedures, whether such writing is prepared prior to, simultaneously with or subsequent to the Order Confirmation, and whether such writing appears on a copy of the Order Confirmation or in a separate instrument.

8.5 The licensing transaction described in the Order Confirmation document shall be governed by and construed under the law of the State of New York, USA, without regard to the principles thereof of conflicts of law. Any case, controversy, suit, action, or proceeding arising out of, in connection with, or related to such licensing transaction shall be brought, at CCC's sole discretion, in any federal or state court located in the County of New York, State of New York, USA, or in any federal or state court whose geographical jurisdiction covers the location of the Rightsholder set forth in the Order Confirmation. The parties expressly submit to the personal jurisdiction and venue of each such federal or state court.If you have any comments or questions about the Service or Copyright Clearance Center, please contact us at 978-750-8400 or send an e-mail to info@copyright.com.

v 1.1

Close

Confirmation Number: 11818477

Citation Information

Order Detail ID: 71909340

Astroparticle physics by ELSEVIER BV. Reproduced with permission of ELSEVIER BV in the format Thesis/Dissertation via Copyright Clearance Center.

Order Detail ID: 71909347

Molecular physics and elements of quantum chemistry : introduction to experiments and theory by HAKEN, H. Reproduced with permission of SPRINGER in the format Thesis/Dissertation via Copyright Clearance Center.

Order Detail ID: 71909348

Molecular physics and elements of quantum chemistry : introduction to experiments and theory by HAKEN, H. Reproduced with permission of SPRINGER in the format Thesis/Dissertation via Copyright Clearance Center.

Order Detail ID: 71909358

Astroparticle physics by ELSEVIER BV. Reproduced with permission of ELSEVIER BV in the format Thesis/Dissertation via Copyright Clearance Center.

Close

Copyright Clearance Center RightsLink®

Home | Account Info | Help

IEEE Requesting permission to reuse content from an IEEE publication

Title: Remote alpha imaging in nuclear installations: new results and prospects
Author: F. Lamadie
Publication: Nuclear Science, IEEE Transactions on
Publisher: IEEE
Date: Dec. 2005
Copyright © 2005, IEEE

Logged in as:
Benjamin Pearce
Imperial College London
Account #:
3001459934
LOGOUT

Thesis / Dissertation Reuse

The IEEE does not require individuals working on a thesis to obtain a formal reuse license, however, you may print out this statement to be used as a permission grant:

Requirements to be followed when using any portion (e.g., figure, graph, table, or textual material) of an IEEE copyrighted paper in a thesis:

1) In the case of textual material (e.g., using short quotes or referring to the work within these papers) users must give full credit to the original source (author, paper, publication) followed by the IEEE copyright line © 2011 IEEE.
2) In the case of illustrations or tabular material, we require that the copyright line © [Year of original publication] IEEE appear prominently with each reprinted figure and/or table.
3) If a substantial portion of the original paper is to be used, and if you are not the senior author, also obtain the senior author's approval.

Requirements to be followed when using an entire IEEE copyrighted paper in a thesis:

1) The following IEEE copyright/ credit notice should be placed prominently in the references: © [year of original publication] IEEE. Reprinted, with permission, from [author names, paper title, IEEE publication title, and month/year of publication]
2) Only the accepted version of an IEEE copyrighted paper can be used when posting the paper or your thesis on-line.
3) In placing the thesis on the author's university website, please display the following message in a prominent place on the website: In reference to IEEE copyrighted material which is used with permission in this thesis, the IEEE does not endorse any of [university/educational entity's name goes here]'s products or services. Internal or personal use of this material is permitted. If interested in reprinting/republishing IEEE copyrighted material for advertising or promotional purposes or for creating new collective works for resale or redistribution, please go to http://www.ieee.org/publications_standards/publications/rights/rights_link.html to learn how to obtain a License from RightsLink.

If applicable, University Microfilms and/or ProQuest Library, or the Archives of Canada may supply single copies of the dissertation.

BACK CLOSE WINDOW

Copyright © 2019 Copyright Clearance Center, Inc. All Rights Reserved. Privacy statement. Terms and Conditions.
Comments? We would like to hear from you. E-mail us at customercare@copyright.com